MAGNETIC FIELD-INDUCED PHASE TRANSFORMATION AND POWER HARVESTING CAPABILITIES IN MAGNETIC SHAPE MEMORY ALLOYS

A Dissertation

by

BURAK BASARAN

Submitted to the Office of Graduate Studies of
Texas A&M University
in partial fulfillment of the requirements for the degree of

DOCTOR OF PHILOSOPHY

December 2009

Major Subject: Materials Science and Engineering

MAGNETIC FIELD-INDUCED PHASE TRANSFORMATION AND POWER HARVESTING CAPABILITIES IN MAGNETIC SHAPE MEMORY ALLOYS

A Dissertation

by

BURAK BASARAN

Submitted to the Office of Graduate Studies of
Texas A&M University
in partial fulfillment of the requirements for the degree of

DOCTOR OF PHILOSOPHY

Approved by:

Chair of Committee,	Ibrahim Karaman
Committee Members,	K. Theodore Hartwig, Jr.
	Joseph H. Ross, Jr.
	Richard B. Griffin
Intercollegiate Faculty Chair,	Tahir Cagin

December 2009

Major Subject: Materials Science and Engineering

ABSTRACT

Magnetic Field-Induced Phase Transformation and Power Harvesting Capabilities in
Magnetic Shape Memory Alloys. (December 2009)
Burak Basaran, B.S., Osmangazi University, Eskisehir, Turkey;
M.S., Gazi University, Ankara, Turkey;
M.S., Texas A&M University,
Chair of Advisory Committee: Dr. Ibrahim Karaman

Magnetic Shape Memory Alloys (MSMAs) combine shape-change/deformation-recovery abilities of heat driven conventional shape memory alloys (SMA) and magnetic field driven magnetostrictives through martensitic transformation. They are promising for actuator applications, and can be employed as sensors/power-harvesters due to their capability to convert mechanical stimuli into magnetic response or vice versa.

The purpose of the present work was to investigate magneto-thermo-mechanical (MTM) response of various MSMAs, under simultaneously applied magnetic field, heat and stress. To accomplish this, two novel testing systems which allowed absolute control on magnetic field and stress/strain in a wide and stable range of temperature were designed and manufactured.

MTM characterization of MSMAs enabled us to determine the effects of main parameters on reversible magnetic field-induced phase transformation (FIPT), such as magnetocrystalline anisotropy energy, Zeeman energy, stress hysteresis, thermal hysteresis, critical stress to start stress induced phase transformation and crystal orientation. Conventional SMA characteristics of single crystalline Ni_2MnGa and NiMnCoIn and polycrystalline NiMnCoAl and NiMnCoSn MSMAs were investigated using the macroscopic MTM testing system to reveal how these conventional properties were linked to magnetic-field-induced actuation. An actuation stress of 5 MPa and a work output of 157 kJm^{-3} were obtained by the field-induced martensite variant reorientation (VR) in NiMnGa alloys. FIPT was investigated both in Ni$_2$MnGa MSMA and in NiMnCoIn metamagnetic SMA. It proved as an alternative governing mechanism of field-induced shape change to VR in Ni$_2$MnGa single crystals: one-way and reversible (0.5% cyclic magnetic field induced strain (MFIS) under 22 MPa) stress-assisted FIPTs were realized under low field magnitudes (< 0.7 Tesla) resulting in at least an order of magnitude higher actuation stress levels than those in shape memory alloys literature.

The possibility of harvesting waste mechanical work as electrical power by means of VR in NiMnGa MSMAs was explored: without enhanced pickup coil parameters or optimized power conditioning circuitry, 280 mV was harvested at 10 Hz frequency within a strain range of 4.9%.

For the first time in magnetic shape memory alloys literature, a fully recoverable MFIS of 3% under 125 MPa was attained on single crystalline metamagnetic SMA NiMnCoIn by means of our microscopic MTM testing system to understand the evolution of FIPT under simultaneously applied magnetic field and stress.

Conventional SMA characteristics of polycrystalline bulk NiMnCoAl and sintered compacted-powder NiMnCoSn metamagnetic SMAs were also investigated, with and without applied field.

DEDICATED TO
MY FIANCÉE YETZIRAH URTHALER,
PARENTS ALHAS AND ATIYE BASARAN,
AND
SISTER F. BANU OZDEMIR;
FOR THEIR UNCONDITIONAL LOVE AND SUPPORT…

ACKNOWLEDGEMENTS

I would like to thank my academic advisor, Prof. Ibrahim Karaman, for the opportunity to pursue a doctoral degree at this prominent university by involving me in his world pioneer magnetic shape memory research and for the uninterrupted funding throughout my studies. His proofreading the whole dissertation manuscript, despite his busy schedule, is also much appreciated.

I would like to extend my appreciation to all of my committee members; Prof. Ted Hartwig, Prof. Joe Ross and Prof. Richard Griffin, for their precious support and understanding during my Ph.D. related exams. I also would like to thank Prof. Tahir Cagin for participating in my defense.

I would like to express my gratefulness to Prof. Yuriy Chumlyakov for his guidance and inspiring discussions as he shared his deep knowledge on materials science with me. Without the single crystals he had provided for us, my Ph.D. research would not have been.

As he is a dear friend and a mentor to me, I will never forget Mr. Robert Barber's invaluable contributions to both my masters and PhD studies. I did learn a lot from him and always enjoyed our stimulating conversations on mechanical design and other issues of life.

Physics Department's Electronics Shop personnel; Mr. Steve Payne, Mr. Erwin Thomas, Mr. Jason Caswell and Mr. James Kirby are gratefully acknowledged for their kind assistance and patience with my never ending research related questions.

A major part of the accomplishments on NiMnCoIn presented in this book is based on our collaboration with Prof. Ryosuke Kainuma of Tohoku University, Japan. In Kainuma Research Group, along with Prof. Kainuma himself, I would like to extend my most sincere thanks to Dr. Rie Y. Umetsu and Dr. Wataru Ito for their excellent assistance, kindest hospitality and most cordial friendship. Without them, I would never be able to accomplish this part of my research. I also would like to thankfully acknowledge the contributions and hospitality of Prof. Keiichi Koyama of High Field

Laboratory for Superconducting Magnets in Tohoku University. The other colleagues in Kainuma Group, Dr. Nagasako, Mr. Okubo, Mr. Minakuchi, Mr. Miyamoto and Mr. Kyo are also acknowledged for being profound friends and taking me out to great sightseeing tours. Finally, I would like to express my deepest gratitude to Prof. Kiyohito Ishida for sponsoring both of my trips to Tohoku University. By visiting Japan not only did I realize one of my dreams in life but also set foundations of life long friendships with Prof. Kainuma, Dr. Umetsu and Dr. Ito.

I have spent nine long years at Texas A&M University in the course of my masters and PhD studies combined. I consider myself very lucky to have shared them with many dear friends. Among these, Dr. Haluk Ersin Karaca has been my ultimate partner in crime (i.e., research) for ages; we carried almost all of the research narrated in this book together, except for the part handled in Japan. He has always been a beloved and trustworthy friend. Mr. Kadri Can Atli has also been an exceptional friend to me, whose consistent encouragement helped a lot. In the Karaman Research group, my other past/present colleagues; Mr. Ruixian Zhu, Mr. James Monroe, Mr. Majid al Maharbi, Ms. Nevin Ozdemir, Ms. Fatmata Barrie, Mr. Andy Brewer, Mr. Ebubekir Dogan and Dr. Mohammed Haouaoui all deserve my most sincere thanks for being there whenever I needed them. Mr. Steven Rios also deserves my gratitude for being a good friend and sharing the research related workload with me while I was typing my dissertation.

Last but not least, I would like to thank my family: My parents Mr. Alhas and Mrs. Atiye Basaran, my sister Banu, brother in law Cem Ozdemir (and their little son, Demir). They all sacrificed a lot for me during my ongoing quest abroad; my parents endured their only son being away from home for ages, I missed the wedding ceremony of my one and the only sister due to visa related issues, etc... Nevertheless, they have always provided me with their unconditional love and support. The most special appreciation and love from the bottom of my heart go to my fiancée, my beautiful, Ms. Yetzirah Urthaler, without whom I would not have been complete. She very patiently waited and continuously encouraged me to finalize this tough phase of my life for a glamorous future together. God bless them all.

TABLE OF CONTENTS

LIST OF FIGURES

Page

Page

Page

Page

Page

Page

LIST OF TABLES

CHAPTER I
INTRODUCTION

I.1 Motivation & Objectives

In this Ph.D. study, Ferromagnetic Shape Memory Alloys (FSMA) are put under investigation. This newly discovered class of smart materials combines the shape changing/deformation recovery abilities of heat driven conventional shape memory alloys (SMA) and the magnetic field driven magnetostrictives through martensitic transformation. Besides being promising for actuation applications by making up for the sluggish response of heat driven SMAs, they can also be employed as sensors and/or power harvesters due to their capability to convert mechanical stimuli into magnetic response.

The coupled effects of stress, magnetic field and temperature on the magnetic field induced strain response and cyclic repeatability should be explored in detail before allowing these materials in service. Moreover, it is critical to establish a clear understanding of the microstructural mechanisms responsible for macroscopic behavior to tailor microstructures for improved magneto-thermo-mechanical response.

To shed light on the aforementioned issues, the study was planned to consist of these main objectives:

1. Design, build and verify the functionality of and experimentation system to magneto-thermo-mechanically characterize recently invented magnetic shape memory alloys (MSMAs) in bulk form while maintaining complete control on simultaneously applied magnetic field and stress/strain in a wide and stable temperature range.

This dissertation follows style and format of Acta Materialia.

2. Evaluate the magneto-thermo-mechanical (MTM) response of Ni_2MnGa single crystal MSMA utilizing this test setup and reveal materials parameters critical for increasing the actuation stress for NiMnGa actuator applications.
3. Determine conventional shape memory alloy (SMA) characteristics of single crystalline Ni_2MnGa and NiMnCoIn, and polycrystalline NiMnCoAl and NiMnCoSn MSMAs to find out how these conventional properties are linked to magnetic-field-induced actuation and actuation stress.
4. Explore the possibility of harvesting waste mechanical work as electrical power by means of NiMnGa MSMAs.
5. Investigate the magnetic-field-induced martensitic phase transformation (FIPT) in Ni_2MnGa MSMA and recently discovered NiMnCoIn metamagnetic SMA as an alternative mechanism to field-induced martensite reorientation as the governing mechanism of field-induced shape change.
6. Design, manufacture and verify the functionality of the miniature MTM system which would fit into superconducting magnet bearing magnetometer test setups to understand magneto-thermo-mechanical coupling in metamagnetic SMAs by simultaneous measurement of strain and magnetization under precisely applied stress, magnetic field and temperature.
7. Characterize metamagnetic SMAs including single crystalline NiMnCoIn by means of this miniature MTM system to understand the fundamentals of field-induced martensitic phase transformation under simultaneously applied magnetic field and stress.

Essential parameters to be derived from our experimental studies will guide us to:

1. Figure out how to increase the actuation stress in MSMAs,
2. Determine how reversible field-induced phase transformation is influenced by magnetocrystalline anisotropy energy (MAE), Zeeman energy (ZE), transformation hystereses, saturation magnetization and crystal orientation.

I.2 Smart (Active) Materials

In order to understand the magnetic and conventional shape memory materials, it is best to have a brief background on the class of materials they belong to. Smart (a.k.a., active) materials exhibit coupling between multiple physical domains and thus can convert energy from one form into another. A domain is any physical quantity that consists of a set of two state variables. A pair of state variables is a means of defining size or location within a physical domain. For instance, a mechanical domain can be identified through state variables stress and strain in a material. Electrical, thermal, magnetic and chemical domains can be cited among other examples for physical domains. Coupling occurs when alteration of a state variable in one physical domain gives way to a change in a state variable which belongs to a separate physical domain. As an example thermomechanical coupling can be given; i.e., changing the temperature (state variable in the thermal domain) of a material can lead to a change in the strain (state variable of the mechanical domain) [1].

Active materials experience a significant change in one or more of their properties in response to a variation in external conditions such as applied loads, altering temperature, electrical or magnetic fields. Piezoelectrics, magnetostrictives, shape memory alloys (SMAs) and recently discovered magnetic shape memory alloys (MSMAs) are the main groups of active materials which have found use in commercial industrial applications. They are capable of transforming one type of energy into another. In addition, they are able to display direct and inverse effects which lead to applications such as actuators and sensors, respectively. An ideal active material, in this sense, should exhibit high-frequency response, large strain and force outputs, high durability and low cost.

I.2.1 Piezoelectric Materials

Piezoelectric materials are among the most commonly employed smart materials. At microscopic scale, the movement of the off-center charged-ion in a tetragonal unit cell from one axis to another upon the application of an electric field or stress causes the piezoelectric phenomenon [2, 3]. As this ion changes its position, strain occurs in the material. Poling is necessary to observe bulk strain in piezoelectrics [2]. They present two unique characteristics:

a) The "direct" piezoelectric effect, which occurs when a piezoelectric material is subjected to a mechanical stress and the material becomes electrically charged,
b) The "converse" piezoelectric effect, which occurs when the piezoelectric material becomes strained upon being placed in an electric field [2, 4].

By utilizing the direct piezoelectric effect, they can be used to detect strain, movement, force, pressure, or vibration by developing appropriate electrical responses. By means of the converse piezoelectric effect, they can be used to generate a movement, force, pressure, or vibration by applying a suitable electric field.

The most popular commercial piezoelectric materials are lead Zirconate-Titanate (PZT) and Polyvinylidene-Fluoride (PVDF) [2]. Piezoelectric materials can perform strains up to 0.18% (PZT) and 0.1% (PVDF) under an electric field in the frequency range of up to 100 kHz [2]. They are available for numerous applications as both actuators and sensors such as accelerometers, force transducers, ultrasonic motors, helicopter rotor blades [4].

I.2.2 Magnetostrictive Materials

Magnetostrictive materials can convert energy between the magnetic and mechanical (elastic) domains. Due to the bidirectional nature of this energy exchange, magnetostrictive materials can also be employed for both actuation and sensing, just like piezoelectrics. Alloys based on the transition metals such as, Iron, Nickel, and Cobalt, in combination with certain rare-earth elements, are currently employed in actuator and sensor systems in a broad range of industrial, biomedical, and defense applications [2, 4].

In magnetostrictive materials, at a microscopic scale, when a magnetic field is applied, an electron spin tries to align with it. Then, the orbit of that electron also tends to be reoriented with the applied field. However, because the orbit is strongly coupled to the crystal lattice, the orbit resists the rotation of the spin axis. Therefore, the energy required to rotate the spin system of a domain away from the preferred orientations is the energy required to overcome spin–orbit coupling. When magnetic field rotates the spins, the orbital moments rotate, and this results in significant distortion, which is called as magnetostriction [2, 5]. The change in sample dimensions in the direction of applied field is called the Joule magnetostriction. The Villari effect is the change in magnetization due to applied stress and is the inverse of Joule magnetostriction. Magnetostrictives can be employed in sensors and power harvesting applications due to the Villari effect [2].

Since magnetostriction is an inherent property of ferromagnetic materials, on contrary to some poled piezoelectric substances, it does not degrade over time. Due to the required solenoid and related magnetic circuit components, magnetostrictive transducers are usually larger and bulkier than their piezoelectric or electrostrictive equivalents. That’s why; they are employed mostly in applications that require high strains and forces where weight is not of problem. Advanced magnetostrictive materials are costly due to their complex manufacturing needs [4].

Terfenol-D is the most popular commercially available magnetostrictive material. The best magnetostriction based strain for Terfenol-D is 1,6 % under a saturation field of 0.16 MA/m at room temperature [2]. Terfenol-D is expensive and highly brittle [3, 4].

Recently discovered magnetostrictive, Galfenol, sounds promising. It is more ductile and displays higher strength compared to Terfenol-D. However, lower strain levels of about 0.03 % stand out as a major drawback, besides, its high permeability results in low cut-off frequencies due to eddy currents [6].

I.2.3 Shape Memory Alloys & Fundamentals of Shape Memory Phenomenon

Some metallic alloys undergo a solid to solid first order phase transformation in their metastable solid state and display many unique functional properties. After deformation, recovery of the original shape of the alloy upon heating, perhaps, is the most well-known of these properties. The aforementioned diffusionless, shear-like transformation is called Martensitic Transformation (MT) and the metallic alloys which can recover their undeformed shape through this reversible MT are called as Shape Memory Alloys (SMAs) [7, 8]. Since it is reversible, MT is also termed as thermoelastic transformation and does not cause any change in the composition of the alloy. SMAs can produce very high recoverable strains (up to 20%) through reversible MT. Although the same type MT can occur in steels during hardening when quenched, no shape memory exists since there is no reversibility, i.e., the MT in steels is not thermoelastic. In the course of forward MT, the low symmetry/low temperature solid phase obtained upon cooling is named martensite (M) and the high symmetry/high temperature parent phase which transforms into martensite is named austenite (A). The critical temperatures at which forward ($A \rightarrow M$) and reverse ($M \rightarrow A$) martensitic transformations start and finish are known as martensite start (M_S), martensite finish (M_F) and austenite start (A_S), austenite finish (A_F) temperatures, respectively (see Figure I.1). These temperatures are functions of alloy composition and microstructural constitution, and the microstructure can be affected by thermomechanical processing [7, 8].

In an ordered alloy, different species of atoms occupy particular, distinct atomic sites. Since MT is diffusionless, the product phase, martensite, is ordered just like the parent phase, austenite. The SMA martensite phase manifests itself in a plate-shaped (as opposed to lath-shaped) morphology.

In thermoelastic transformations, an incremental decrease in temperature between M_S and M_F results in a slight growth of existing martensite plates and the nucleation of new ones. However, as the temperature is incrementally raised, those newly nucleated martensitic plates disappear and the grown ones shrink back some, accordingly. That is, the martensitic plate undergoes a backward (reverse) shear as it diminishes. Reversal of the given plate on heating is just the inverse of the formation process upon cooling as a consequence of thermoelastic nature of the MT in SMAs. These martensite plates self-accommodate each other and as a whole they produce no net microscopic shape change.

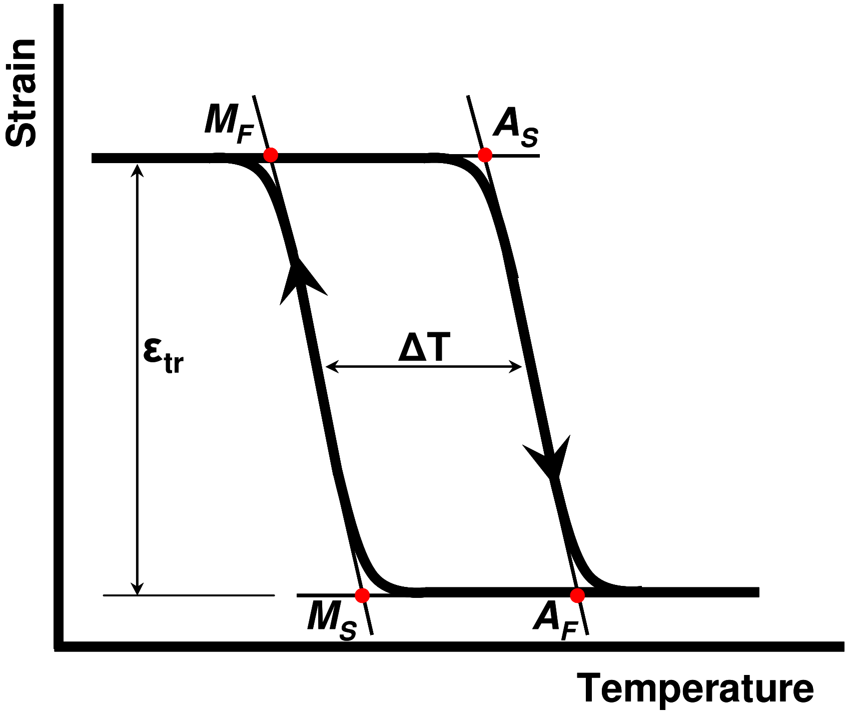

Figure I.1. Schematic representation of isobaric thermal cycling curve and the critical temperatures of forward and reverse martensitic transformations. ε_{tr} is transformation strain, ΔT is temperature hysteresis.

Each individual plate shows a characteristic crystallographic habit plane. By definition, a habit plane is the interface between *A* and *M* phases and coincides with the plane that accommodates the occurring transformation shear [7]. Figure I.2 shows the habit plane separating martensite and austenite phases. The crystallographic transformation associated with the martensite formation takes place in such a way that, provided the martensite displays a tetragonal structure, the c-axis of this tetragonal martensite can be parallel to any one of the several equivalent crystallographic directions in the cubic austenite phase.

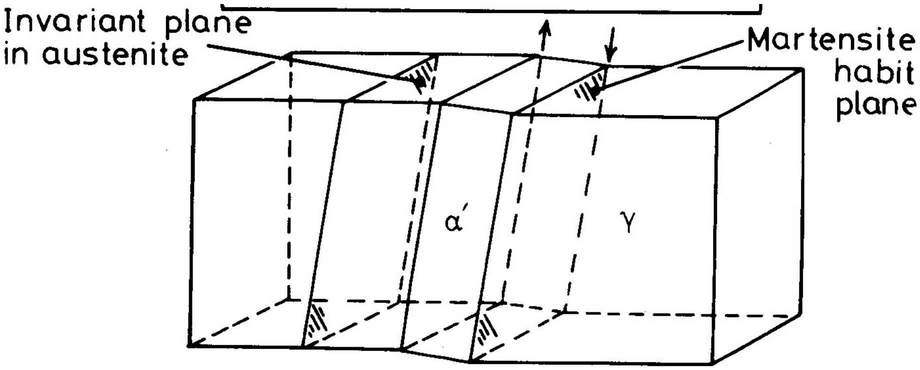

Figure I.2. Schematic representation of habit plane [9].

Therefore, as many as two or three different martensite variants come about within a single martensitic plate. These variants can be related with twins and can yield to formation of internally twinned martensite plates. As the martensite forms within the austenite, misfit strains associated with shear can be accommodated internally within each plate by different deformation mechanisms such as slip or twinning as seen in Figure I.3. The detail view (encircled by the interrupted-line ellipse) shown on the twinned structure represents the four possible ways to generate a rhombic martensite from the cubic austenite. Each of these rhombic orientations (symbolized by arrows) can return to its parent condition in only one way; by going through the inverse transformation distortion [7, 10].

Basically, a SMA is deformed in the martensitic condition and the shape recovery occurs during heating when the specimen undergoes the reverse MT. This is the essence of shape memory effect (SME). SME is only possible when transformation strain is relatively small. Otherwise, a large scale strain associated with an irreversible deformation mechanism such as plastic flow is accommodated without thermoelastic transformation. There occurs no change in the shape of the SMA specimen when cooled from above A_F to below M_F. As the specimen is deformed below M_F temperature, it remains deformed until it is heated. The shape change occurs by favoring of one twin variant over the others, and/or by the growth of those martensite plates in which the favored variant is predominant at the expense of the neighboring plates provided that the corresponding boundaries and interfaces are mobile. Recovery of the shape starts at A_S temperature and gets completed at A_F. Once it is fully recovered, there is no further change observed in the shape of the specimen even when cooled below M_F. The shape memory mechanism can be only activated again by deforming the specimen in its martensitic state. This means that SME is a one-time-only happening and hence referred to as one way shape memory (see figure on page 11), as well [7].

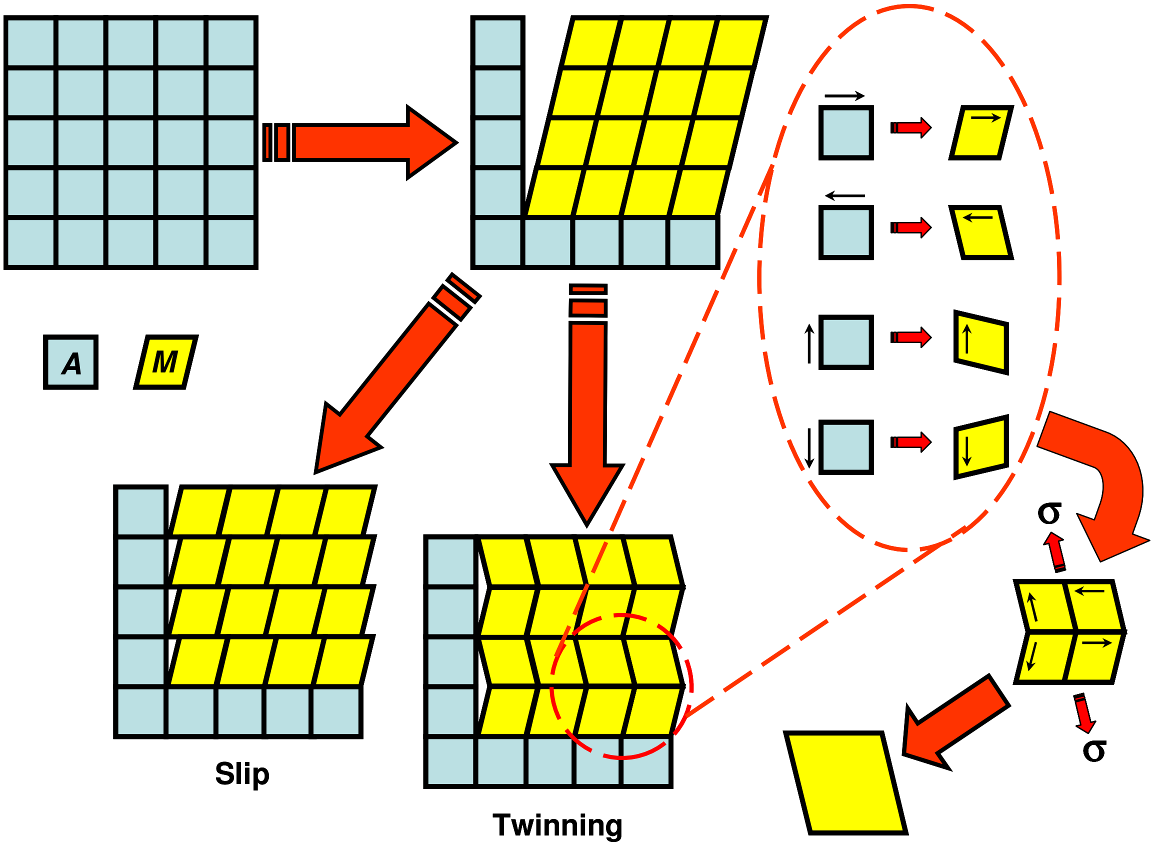

Figure I.3. Schematic representation of martensitic transformation and the alternative accommodation mechanisms for the associated misfit strains. Blue cubes represent austenite and yellow rhombohedra represent martensite. See text for details.

Because of self-accommodation, the four rhombic variants given in detail of Figure I.3 tend to group and fit together in more or less equal portions. Figure I.4 shows self-accommodated martensite plates in 3D. If such a self-accommodated martensite structure is put under tension in the sense of the arrows shown right below the detail view in Figure I.3, three of the variants out of the total of four will be unstable with respect to the application direction of tensile stress. The variant aligned parallel to the direction of the applied stress will be favored and grow at the expense of the others. Eventually, a single crystal of martensite of this favored-direction-variant will be formed. In summary, the initially formed martensite must be deformed below M_F in order to obtain a select variant, which then displays SME when heated to above A_F so that the austenite phase is recreated [7, 8].

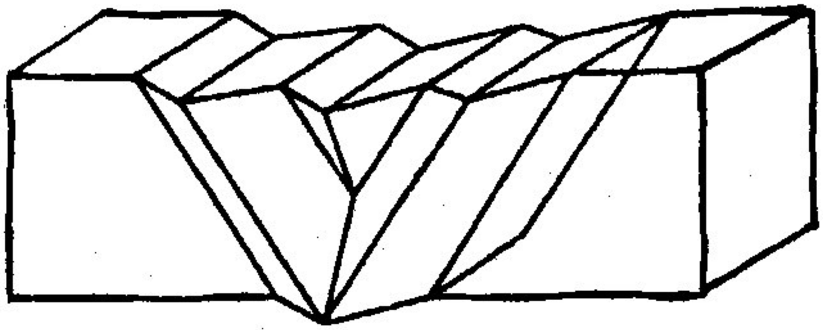

Figure I.4. 3D schematic representation of self-accommodating martensite plates with habit plane variants grouped together to yield a net transformation distortion of zero [7].

Temperature independent shape memory is also possible. As mentioned before, martensite forms at M_S upon cooling without stress. The very same material can produce martensite above M_S temperature when external stress is applied and it reaches a critical level (σ_C). This type of martensite is termed as stress induced martensite (SIM). SIM transfers back into the parent phase upon unloading of stress. As opposed to the thermally driven shape memory mechanism, then, this can be named as mechanically driven shape memory mechanism. Figure I.5 shows (see also the third figure on page 15) a schematic representation of pseudoelastic (or superelastic) behavior (stress vs. strain loop). The upper plateau corresponds to formation of SIM from austenite upon loading. At the end of the plateau, the linear region is the elastic deformation of martensite. The lower plateau represents back transformation from SIM to parent austenite phase when the load is released [7, 8].

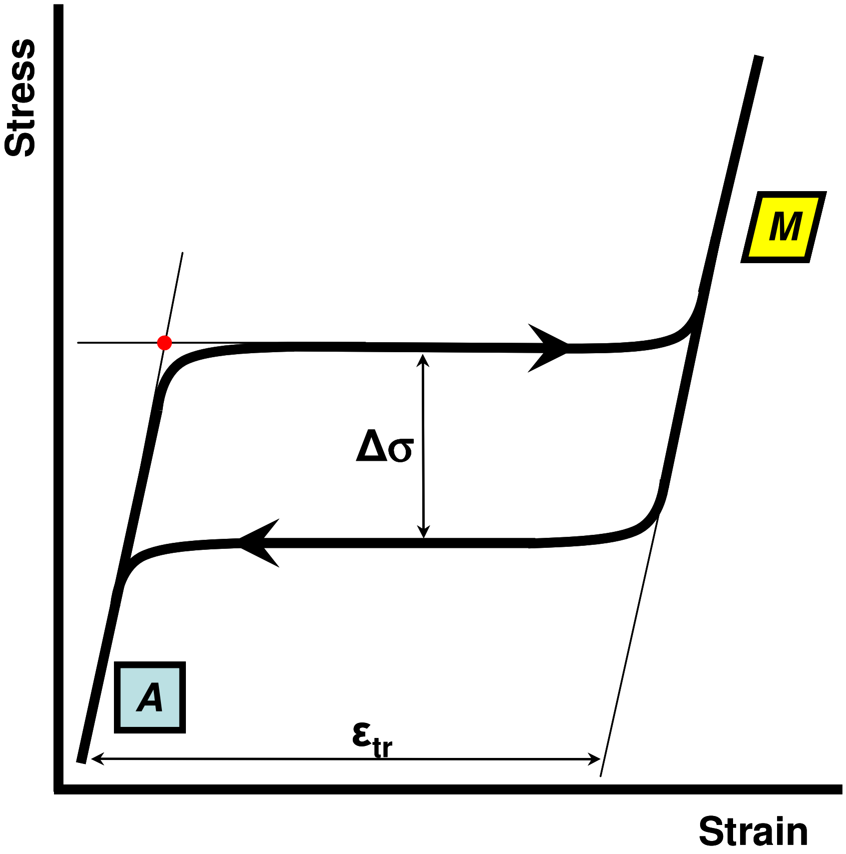

Figure I.5. Schematic representation of pseudoelastic (superelastic) behavior (stress-strain loop). Δσ is stress hysteresis, ε_{tr} is transformation strain and the red dot represents critical stress level, σ_C, at which *A* →*M* transformation starts.

SIM consists of only one variant of martensitic plates which has a habit plane sympathetic with the direction of the applied stress. Since only one martensite variant occurs due to the applied stress, the consequence is a net shape change associated with this single variant. This is different than the self-accommodated martensitic structure which consists of many variants and thus yields to no net shape change. When applied above M_S, the critical stress required to create SIM increases linearly with increasing temperature.

This trend in stress to induce martensite as a function of temperature obeys Clausius-Clapeyron relationship; $\frac{dP}{dT} = \frac{\Delta H}{T\Delta V}$ where, P is pressure, T is temperature, ΔH is transformation latent heat and ΔV is change in volume during transformation. As an alternative the same relationship can be written in the following form for convenience: $\frac{d\sigma_{applied}}{dM_S} = \frac{-\Delta H}{T\varepsilon_O}$ where σ_{applied} is applied stress, ε_O is transformation strain resolved along the direction of applied stress and M_S is the martensite start temperature [7]. There exists a critical temperature, M_d, above which stress cannot induce martensite formation but the parent phase undergoes common plastic deformation. It is noteworthy that the stress required to deform the parent phase above M_d temperature is approximately ten times more than the stress needed to deform martensite at temperatures below M_F.

If the self-accommodated structure is permanently biased (generally by forming dislocations and internal stresses through training), a large fully recoverable macroscopic strain can be induced in the course of consecutive forward and back transformations upon heating/cooling. This is called two-way shape memory effect (TWSME) [11].

In summary, shape memory phenomenon manifests itself in the form of there major effects:

1) One way shape memory effect as explained in 3D space (strain, temperature, stress) in Figure I.6. At a temperature less than M_F, the SMA spring is in the martensitic state (A). Upon application of stress (B), the martensite is deformed and when the load is removed, the deformation is preserved (C). The spring transforms from martensite to austenite and recovers the deformation when heated above A_F (D). There happens no change in the shape if it is cooled below M_F once again (D→A).

2) Two way shape memory effect as explained in 3D space (strain, temperature, stress) in Figure I.7. Besides one way shape memory, SMAs are also capable of

demonstrating indefinitely repeatable recovery through two-way shape memory effect provided they are trained, i.e., the same spring can show shape change upon heating/cooling without external load. After being compressed in martensite condition (below M_F), the spring can be mechanically constrained, then thermally cycled between M_F and A_F several times. This training treatment builds micro-stresses in the parent phase and they bias the MT by dictating a preferred variant in martensite. In Figure I.7, the difference of two-way SME from one way SME is depicted clearly.

3) Pseudoelastic (or superelastic) effect, as mentioned previously, is another mechanism that allows SMAs to perform indefinitely repeatable recovery by SIM formation. In Figure I.8, at a constant temperature above A_F, the spring is loaded and deformed (A→B), then unloaded (C). The pre-deformed shape is fully recovered upon unloading and the area enclosed by the loop is a measure of energy dissipation in one pseudoelastic cycle.

Many distinct alloy systems exhibit MT and they are generally classified as ferrous or non-ferrous martensites. Tables I.1 and I.2 present lists of Nonferrous and Ferrous Martensites, respectively [12]. Among all conventional SMAs, Fe based, Cu based and Ni-Ti alloys have found the most employment in industrial applications.

Table I.1. Classification of nonferrous alloys that display martensitic transformation [12].

Group	Alloy System
A. Terminal Solid Solutions based on an element that has allotropic phases	1. Cobalt and its alloys 2. Rare-earth metals and their alloys 3. Titanium, Zirconium and their alloys 4. Alkali metals and their alloys and Thallium 5. Other metals such as Pu, Ur, Hg and their alloys
B. Intermetallic solid solutions that have a bcc parent phase	1. β-Hume-Rothery phases of Cu, Ag and Au based alloys 2. β-Ni-Al alloys 2. Ni-Ti-X alloys
C. Alloys that show cubic to tetragonal transformation (including quasi martensite)	1. Indium based alloys 2. Manganese based alloys (paramag.←→antiferromag.) 3. A15 compounds 4. Miscellaneous: La-Ag_X-In_{1-x}, Ru-Ta, Ru-Nb, Y-Cu, La-Cd

Table I.2. Classification of ferrous alloys which exhibit complete or nearly complete shape memory effect [12].

Alloy System	Composition	Crystal Structure	Nature of transformation
1. Fe-Pt	25 at. % Pt 25 at. % Pt	bct (α') fct	Thermoelastic Thermoelastic
2. Fe-Pd	30 at. %	fct	Thermoelastic
3. Fe-Ni-Co-Ti	23% Ni-10%Co-4%Ti 33% Ni-10%Co-4%Ti	bct (α') bct (α')	--- Thermoelastic
4. Fe-Ni-C	31% Ni-0.4%C	bct (α')	Non-thermoelastic
5. Fe-Mn-Si	31% Ni-0.4%C 31% Ni-0.4%C	hcp (ε) hcp (ε)	Non-thermoelastic Non-thermoelastic

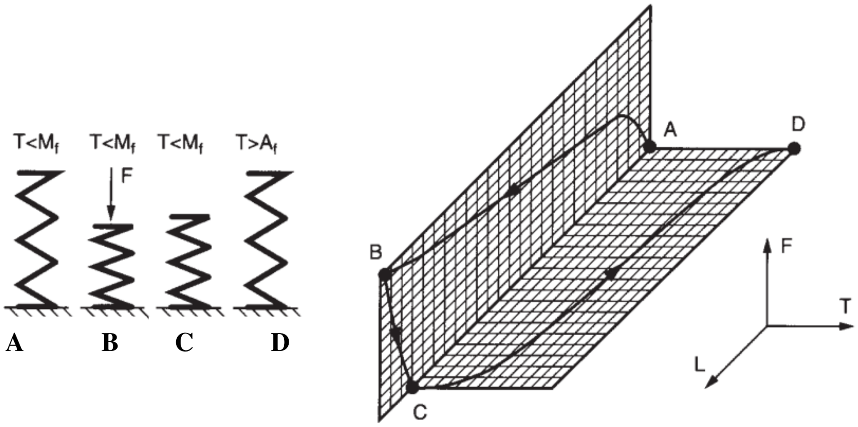

Figure I.6. 3D illustration of one way SME; at a temperature below M_F, sample is loaded and deformed (A→B), then unloaded (C). Upon heating to a temperature above A_F, the pre-deformed shape is recovered. Axes L, T and F stand for strain, temperature and stress, respectively [8].

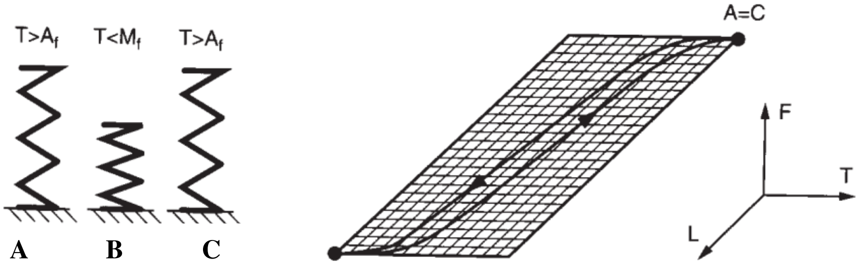

Figure I.7. 3D illustration of two-way SME; spontaneous shape change occurs during cooling the sample from a temperature above A_F to a temperature below M_F (A→B) without any external stress involved. Upon heating back to a temperature above A_F, the pre-deformed shape is recovered. Axes L, T and F stand for strain, temperature and stress, respectively [8].

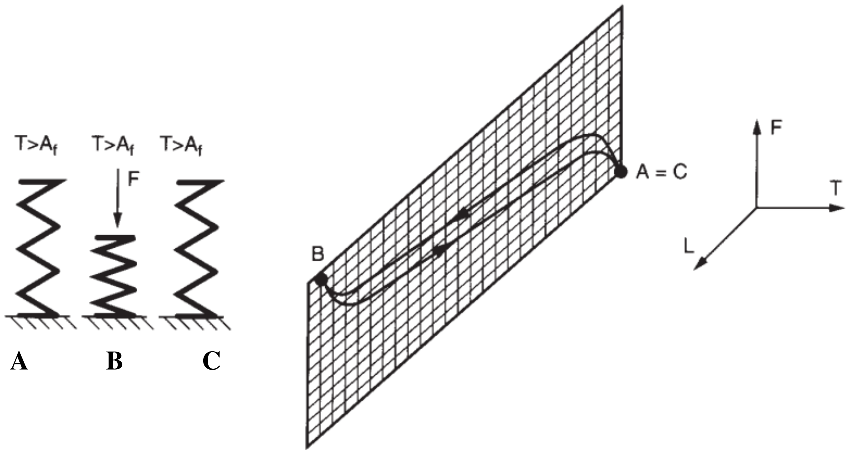

Figure I.8. 3D illustration of pseudoelasticity; at a temperature above A_F, sample is loaded and deformed (A→B), then unloaded (C). The pre-deformed shape is fully recovered upon unloading and the area enclosed by the loop is a measure of energy dissipation in one superelastic cycle. Axes L, T and F stand for strain, temperature and stress, respectively [8].

I.2.3.1 Iron Based Shape Memory Alloys

The austenite (fcc-γ phase) in ferrous alloys can be transformed to these three kinds of martensites, depending on composition or stress: γ-α' (bcc), γ→ε (hcp) and γ→fct martensite. Although a shape-memory effect has been observed in all three types of transformation, most attention in developing a commercial alloy has been given to the alloys that have a γ→ε transformation. These alloys have a low stacking fault energy in austenite (Fe–Cr–Ni, Fe–high Mn alloys). The austenite to ε-martensite transformation proceeds through Shockley partial dislocations and change the crystal. The shape memory effect (only one-way) results mainly from reverse motion of the Shockley partial dislocations during heating [12].

Complete shape-memory effect has been reached in both single-crystal and polycrystalline Fe–Mn–Si alloys that contain suitable amounts of Mn and Si. Shape-memory strains of 9% in single crystals and 5% in polycrystals have been reported. Any factors that impede the reversibility of the motion of partial dislocations lead to incomplete recovery and in turn a poor shape-memory effect. The internal factors that hamper recovery include alloy composition, Neel temperature, transformation temperature, and lattice defects. External factors are applied stress and strain, deformation, recovery annealing temperature, and thermomechanical treatment. Fe-based alloys exhibit only a (limited) one-way shape-memory effect after a labor-intensive thermomechanical training treatment. No significant two-way effect or pseudoelastic properties have been reported, whereas only moderate damping capacity might have attracted some interest. Therefore the only reported successful applications of these Fe-based alloys are couplings. This type of application is based on the one-way effect. The recovery stresses are moderate but sufficient [12].

I.2.3.2 Copper Based Shape Memory Alloys

Copper-based shape-memory alloys are derived from Cu–Zn, Cu–Al, and Cu–Sn systems. The composition range of these alloys corresponds to that of the well-known β-Hume–Rothery phase. In most shape-memory alloys, this phase has a disordered bcc structure at high temperatures but orders to a B2, $D0_3$ or $L2_1$ form at lower temperatures. The temperature of the transformation to martensite, M_S, varies with the alloy composition. Cu–Zn and Cu–Al martensites are of three types α', β' or γ'. Some conversion from one martensitic structure to another, for example β'→γ', may also take place. The net result is a coalescence of plates within a self-accommodating group and even coalescence of groups. Heating this deformed martensitic microstructure transforms it to the β phase, and the shape-memory effect accompanies the structural change [12].

In Cu based alloys, two criteria are important when selecting an alloy composition to obtain a complete β microstructure that transforms to martensite. The first one is having the β phase stable across as wide a temperature range as possible. The less wide this temperature range, the faster the cooling rate required to retain the β phase without diffusional decomposition. The second one is having transformation temperatures fall within a range that satisfies the requirement for the shape-memory application (−150 to 200 ^{o}C) [12].

Copper-based shape-memory alloys presently used are derived from Cu–Zn and Cu–Al systems, and for their ternary alloys, elements are added for various metallurgical reasons. The working martensite in these alloys is only or predominantly the β' with $D0_3$, B2 or $L2_1$ structure [12].

I.2.3.3 Nickel–Titanium Shape Memory Alloys

Nitinol (Ni-Ti) is the most well known SMA which has been discovered by Buehler and his co-workers at the U.S Naval Ordinance Laboratory (NOL) in 1962 [13]. Ni50–Ti50 and near equiatomic Ni–Ti alloys are the best explored system of all shape-memory alloys and occupy almost the whole SMA market. Ni50–Ti50 is an intermetallic phase that has some solubility at higher temperature.

The basic concept of processing Ni-Ti alloys is that the martensitic and β phases have to be strengthened to avoid plastic deformation during shape-memory or pseudoelastic loading. This occurs by classic methods such as strain hardening (during cold deformation), solution hardening, and precipitation hardening. Ni–Ti alloys have the significant advantage that these techniques can be easily applied due to excellent ductility and a very interesting but complicated precipitation process [12].

The compositions of Ni–Ti SMA are approximately between 48 and 52 at. % Ni and the transformation temperatures of the B2 structure to the martensitic phase that has a monoclinic B19' structure are very sensitive to the nickel content (a decrease of about 150 ^{o}C for an increase of 1 at. % Ni). Transformation temperatures can be chosen between −40 and +100 ^{o}C.

Ni–Ti alloys have the best shape-memory behavior of all SMA. Even in the polycrystalline state, 8% shape recovery is possible. Furthermore, 8% pseudoelastic strain is completely reversible above A_F and the recovery stress is of the order of 800 MPa [12].

In some cases, the martensitic transformation is preceded by the so-called R-phase transition. The R transition is a B2 $\leftrightarrow$ rhombohedral transformation that also has second-order characteristics. The most specific characteristics of this R-phase transition are that it shows clear one- and two-way shape memory effects of the order of 1% recoverable strain with very small hysteresis of only a few degrees, which creates possibilities for applications involving accurate regulating devices. Note that, further cooling transforms the R phase into B19' martensite. During heating, generally only the reverse martensitic transformation is observed. It has been shown that the appearance of the R phase depends on composition, alloying elements, and thermomechanical processing. The major common point is that all effects that depress the martensitic forward transformation below room temperature favor the appearance of the R-phase transition that is quite stable near 30 ^{o}C [12].

Addition of a third element and thus having relative replacement of Ni and/or Ti influences the transformation temperatures and also affects hysteresis, strength, ductility, shape-memory characteristics, and the B2 $\rightarrow$ (R) $\rightarrow$ B19' sequence. Although more application oriented, one can distinguish four purposes to add third elements [12]:

1. To decrease (Cu) or increase (Nb) hysteresis,

2. To lower transformation temperatures (Fe, Cr, Co, Al),
3. To increase transformation temperatures (Hf, Zr, Pd, Pt, Au), and
4. To strengthen the matrix (Mo, W, O, C).

Some ternary alloys including Ni–Ti–Cu and Ni–Ti–Nb have been developed for large-scale applications. Among these especially, pseudoelastic Ni–Ti–Nb alloys have significant superiorities from the binary alloy such as much lower stress rate, much higher critical stress levels to start *A*→*M* forward transformation and much larger pseudoelastic window [12].

I.2.4 A Comparison of Ferromagnetic Shape Memory Alloys with Other Smart Materials as Potential Actuator Materials

Figure I.9 depicts a comparison of some active materials against pneumatic and hydraulic systems in regard with their actuation frequencies and actuation strains.

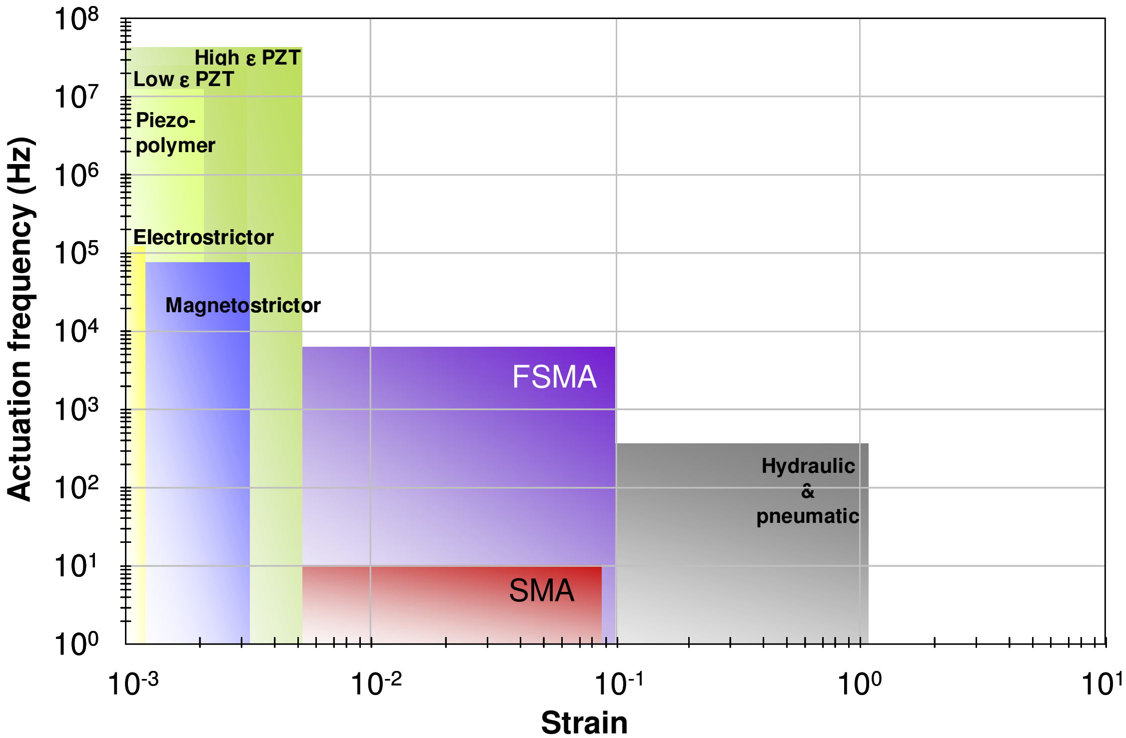

Figure I.9. A comparison of active materials potentially to be used as actuators against pneumatic and hydraulic systems in terms of actuation frequency and actuation strain.

As mentioned in section I.2.1, piezoelectric materials (PZT) are compact and light weight, can operate over a large temperature range, and can function at high frequencies. They have excellent stability and fast response to applied voltage and show no wear or tear. However they are brittle, can only produce small strains compared to SMAs and magnetostrictives, also cannot withstand high shear and tension, and can become depolarized under high voltage and/or temperature [4, 14].

Magnetostrictive material Terfenol-D, as narrated in detail in section I.2.2, displays fast response time (μsec), high Curie temperature, relatively high strain and force capabilities compared to piezoelectrics. It shows no aging effect, and it can operate over a large temperature range. However, its low tensile strength, brittle structure and high cost due to the rare earth metals involved are major drawbacks. Furthermore, Terfenol-D requires intensive equipment in order to produce the magnetic field under which it can function [4, 14].

Conventional SMA NiTi, displays good ductility, large stroke, substantial actuation force and good work output levels, however its frequency range is very low [4, 14, 15] (see section I.2.3 for a detailed discussion).

Table I.3 provides a quantification of the aforementioned properties for all active materials we discussed so far [14]. Obviously, a new class of smart materials, magnetic shape memory alloys surpasses the actuation frequency capabilities of conventional SMAs by almost three orders of magnitude as they provide the same amount of superior strain. Following chapters will tell us the reasons behind this unique capability.

Table I.3 Comparison of actuation strain, stress and operating frequencies of active materials [14]. PT: phase transformation, VR: Variant reorientation.

Driving Force	***Active Material***		***Strain %***	***Stress MPa***	***Operating Frequency Hz***
Heat	Shape-Memory Alloy (NiTi)		2-8	400	1
Electric Field	Ferroelectric		0.1	3	100.000
	Piezoelectric (PZT)		0.2	70	100.000
Magnetic Field	Magnetostrictive (Terfenol-D)		0.2	80	10.000
	MSMA (Ni_2MnGa)	VR	5-10	5	1.000
		PT	0.5-4	20-100	

I.2.5 Magnetic Shape Memory Alloys

A brief look into the history of magnetic shape memory alloys (MSMAs) development is enough to clearly see that for a long time, researchers have been speculating on achieving relatively larger strains (in comparison with magnetostriction) via thermoelastic shape memory effect (just like in conventional SMA Ni-Ti), but through stimulation by magnetic field instead of heat in some certain martensites which also demonstrate ferromagnetism [16-18].

In 1996, when Ullakko *et al* reported 0.2% magnetic field induced strain in Heusler alloy Ni_2MnGa [19], ferromagnetic shape memory alloys emerged as a potential family of active materials to challenge the long existing magnetostrictives and piezoelectrics. Just like heat driven SMAs, MSMAs can display large reversible strains by rearrangement of martensites, this time not only by means of the thermo-mechanical coupling but by magneto-mechanical coupling as well, i.e., by the effect of magnetic field on the magnetic domain structure of ferromagnetic martensites. Magnetization through displacement of magnetic domain walls is possible in the presence of high magnetocrystalline anisotropy energy, when martensitic structure rearrangement is energetically favorable over the reorientation of magnetic moments (a.k.a. magnetization rotation) [20].

All the shape memory related effects we described in section I.2.3 are realized in the stress vs. temperature plane. Thanks to the presence of the magnetic subsystem in MSMAs, the martensitic transformation phenomena they undergo require the use of three coordinates for analysis: stress, magnetic field, and temperature. A magnetic field can be used to shift the temperatures of the structural phase transformations and to affect the structure of the martensitic phase where the parameters of the magnetic subsystem of the ferromagnet play a leading role. The difference in the magnetization of austenite and martensite determines the size of the shift in the critical temperatures of a phase transformation in the presence of a magnetic field [20].

The magnetoelastic coupling and magnetocrystalline-anisotropy constants determine the possibility of having the martensitic variants transform by magnetic field application. Therefore, the same phenomena that are observed in conventional nonmagnetic SMAs in the load vs. temperature plane can, in principle, be realized in the magnetic field vs. temperature plane in MSMAs [20]. Magnetically induced strains (up to 10% [21]) that are two orders of magnitude greater than simple single-ion magnetostriction have been observed in some alloys and in a number of intermetallic compounds, such as the Heusler alloy Ni_2MnGa.

I.2.5.1 Crystal Structure of MSMA NiMnGa

Heusler alloys are ternary intermetallic compounds with the general formula X_2YZ. Ni_2MnGa alloy belongs to this family and has $L2_1$ structure at room temperature [20]. As shown in Figure I.10, $L2_1$ structure can be represented by a bcc lattice in which Ni atoms occupy the position at the center of the cube, while Mn and Ga atoms alternatively occupy the positions at the apexes [22].

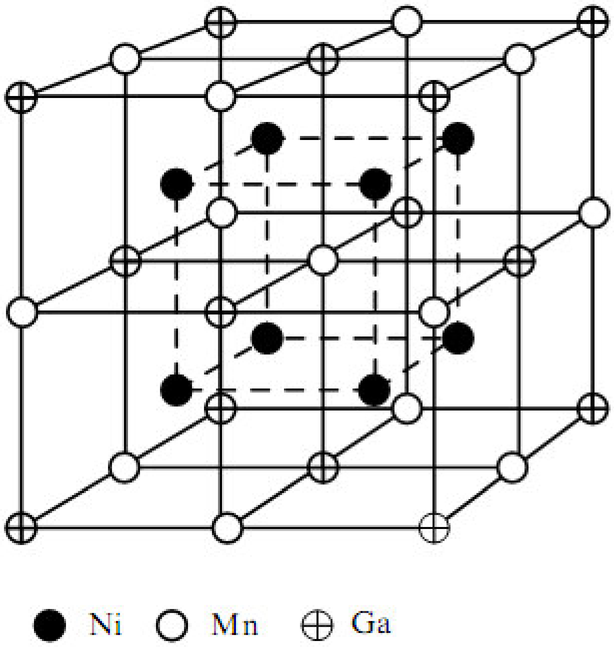

Figure I.10. $L2_1$ structure of the high temperature austenitic parent phase of Ni_2MnGa MSMA [22].

In principle, the formation of such a structure from the melt (the melting point of Ni_2MnGa is 1380 K) is possible either from the fully disordered phase A2 ($A2 \rightarrow L2_1$) or through the partially ordered intermediate phase B2’ ($A2 \rightarrow B2' \rightarrow L2_1$), in which Ni atoms already form the frame of the lattice, while Mn and Ga atoms still occupy arbitrary positions as seen in Figure I.11 [20, 23].

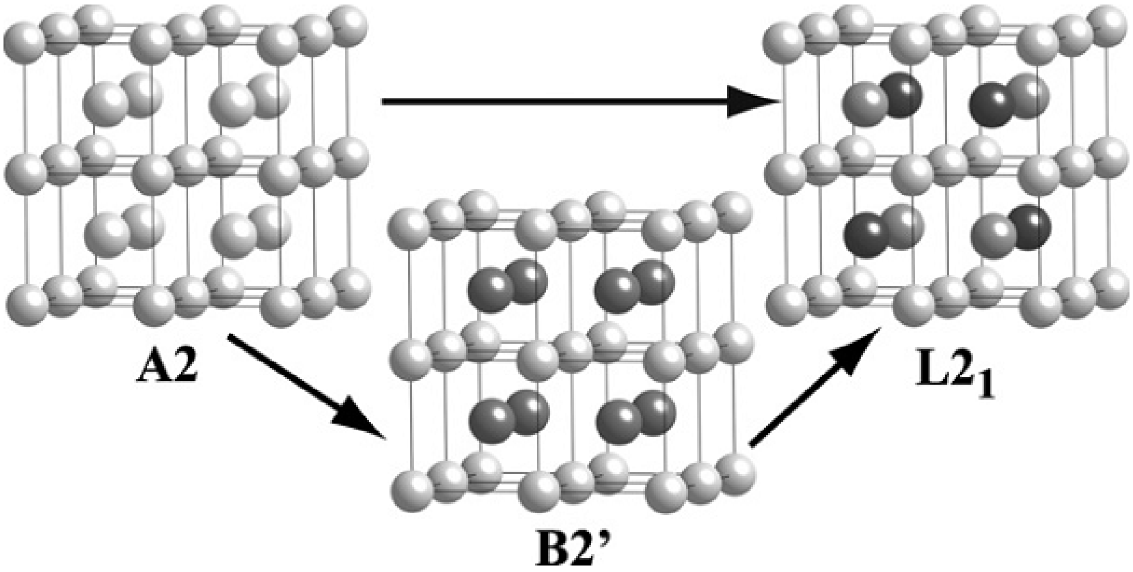

Figure I.11. Schematic representations of the disordered A2, ordered B2' and $L2_1$ structures. In the A2 structure, three atom species are randomly distributed over all lattice sites. In B2' , two sub-lattices are present, with, for Ni_2MnGa, Ni on one lattice (light gray) and Mn/Ga disordered on the other sub-lattice. In the $L2_1$ structure, further ordering occurs on the second sub-lattice [23].

However, formation of Ni_2MnGa is different from both of the above-mentioned scenarios. With decreasing temperature, this compound passes from the melt directly into the partially ordered phase B2', and this phase then experiences a second-order phase transition of the disorder-order type [24, 25]. The B2' → $L2_1$ transition temperature for Ni_2MnGa is about 1070 K. Down to $T_m \sim 200$ K, Ni_2MnGa remains in the $L2_1$ phase, and this Heusler alloy then undergoes a first- order phase transition to a martensitic tetragonal phase, with $c/a < 1$. At room temperature the cubic lattice constant of Ni_2MnGa is $a = 5.825$ Å and the unit cell volume $V_{austenite} = 198$ Å^3 (the number of formula units per unit cell is Z = 4). At low temperatures the parameters of the tetragonal lattice are $a = b = 5.920$ Å and c = 5:566 Å, with c/a = 0:94, and the unit cell volume is 195 Å^3 [22]. Ni_2MnGa alloys can experience premartensitic and intermartensitic transformations. It must also be noted that for samples of nonstoichiometric composition a martensitic phase with orthorhombic and monoclinic distortions has been reported.

Almost all parameters of Ni_2MnGa have proven to be very sensitive to the chemical composition of the specimens; for instance, the transformation temperatures and the formation of super-structures in the austenitic and martensitic states [20].

X-ray and neutron diffraction studies on Ni_2MnGa reveal the presence of super-structural reflections, in addition to the main reflections of the low-temperature martensitic phase. In the neutron diffraction studies of a sample of stoichiometric composition it was found that there are additional reflections of the tetragonal phase and it was assumed that this phase is modulated along the $[100]$ direction [22]. Further studies of the crystal structure of the low temperature phase in nonstoichiometric compounds revealed a complex pattern of formation of different martensitic phases and the presence of intermartensitic phase transitions in the system $Ni_{2+x+y}Mn_{1-x}Ga_{1-y}$. In the early stages of such studies the super-structural motifs were described as static displacement waves (modulations) [26], although an alternative approach was then developed, in which the super-structural reflections of martensite are interpreted as long-period rearrangements of closely packed planes of the $\{100\}$ type [27-29]. A comparative analysis of these two approaches in describing the crystal structure of martensite in NiMnGa is given in reference [30], where it is shown that they often lead to the same results.

The schematic representation of martensite with five- and seven-layered modulations (10M and 14M) along the crystallographic direction $[110]$ can be seen in Figure I.12. There have also been reports about observations of longer-period modulations and about intermartensitic transformations in $Ni_{2+x+y}Mn_{1-x}Ga_{1-y}$ induced by temperature or uniaxial strain.

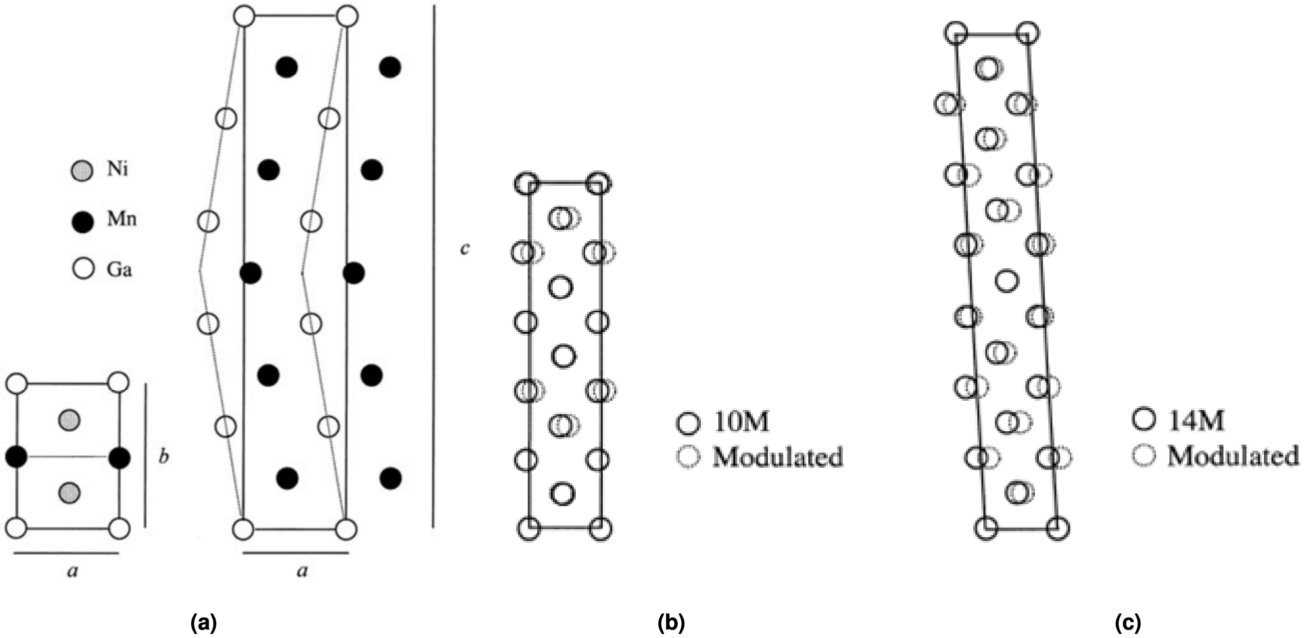

Figure I.12. (a) Detail schematic of the unit cell corresponding to the 10-layered martensite. Comparison of the unit cells obtained from the modulated lattice approach and Ni-Al-type approach for the five-layered (b) and seven-layered (c) martensites [30].

Five-layered modulation of the low-temperature tetragonal phase was observed by the method of diffraction of electrons and X-rays on single crystals of $Ni_{51.5}Mn_{23.6}Ga_{24.9}$ (M_S = 293 K) [26], $Ni_{49.2}Mn_{26.6}Ga_{24.2}$ (M_S = 180K) [31], $Ni_{52.6}Mn_{23.5}Ga_{23.9}$ (M_S = 283 K) [32], $Ni_{52}Mn_{23}Ga_{25}$ (M_S = 227 K) [27, 33], and $Ni_{48.5}Mn_{30.3}Ga_{21.2}$ (M_S = 307 K) [33]. In the process of formation of superstructures in the martensitic phase of these Heusler alloys, the X-ray patterns showed, besides the main diffraction reflections, a number of additional reflections. Modulation occurs in such a way that each fifth (110) plane does not undergo displacements, while the other four are displaced from their regular positions in the body-centered tetragonal lattice along the $[110]$ direction [20].

Seven-layered modulation of the martensitic phase was observed in single crystals of $Ni_{52}Mn_{25}Ga_{23}$ (M_S = 333 K) [26] and $Ni_{48.8}Mn_{29.7}Ga_{21.5}$ (M_S = 337 K) [34]. X-ray studies of $Ni_{48.8}Mn_{29.7}Ga_{21.5}$ have shown that, as in the case of five-layered martensite, besides the main reflections there are additional diffraction reflections that lie along the $[110]$ direction. The crystal structure of the seven-layered martensite in $Ni_{48.8}Mn_{29.7}Ga_{21.5}$ was found to be rhombic with the lattice parameters a = 6.19 Å, b = 5.80 Å, and c = 5.53 Å [34]. In contrast to this, the crystal structure of seven-layered martensite in $Ni_{52}Mn_{25}Ga_{23}$ was interpreted as monoclinic with the lattice parameters a = 6.14 Å, b = 5.78 Å, and c = 5.51 Å with $\gamma = 90.5^{o}$ [26]. Unmodulated martensite was observed in single-crystal samples and thin films of alloys of the following compositions: $Ni_{53.1}Mn_{26.6}Ga_{20.3}$ (M_S = 380 K) [35, 36] and $Ni_{48.5}Mn_{30.3}Ga_{21.2}$ (M_S = 307 K) [33]. The crystal structure of the unmodulated martensitic phase proved to be tetragonal, but the ratio c/a = 1.18 for it is much higher than for the tetragonal martensitic phases considered above. The experimental data on modulations of the crystal lattice in the martensitic phase suggest that the type of martensite (modulation period) depends on the composition of the alloys [20]. It is convenient to classify these types according to the martensitic transition temperature M_S [30]. Five-layered martensite has a crystal lattice of tetragonal symmetry and is formed in the process of cooling in alloys that have M_S < 270 K. Seven-layered martensite is formed in alloys with a higher M_S and has a crystal structure differing from the tetragonal one [20].

I.2.5.2 Magnetics Fundamentals for Magnetic Shape Memory Alloys

To understand the origins of magneto-mechanical coupling (the effect of magnetic field on the magnetic domain structure of ferromagnetic martensites as a function of applied stress) in MSMAs, in the next sections we will look at the magnetization phenomenon in its manifestation in ferromagnetics.

I.2.5.2.1 A Brief Survey on Physical Origins of Magnetization & Types of Magnetic Materials

The macroscopic magnetic properties of materials are a result of magnetic moments associated with individual electrons. Magnetic moments rise from two distinct sources:

The first one comes from the assumption that each electron can be taken as spinning around an axis: The magnetic moment originates from this electron spin, which is directed along the spin axis as shown in Figure I.13a. Spin magnetic moments may be only in an “up” direction or in an antiparallel “down” direction. Thus each electron in an atom may be thought of as being a small magnet having permanent orbital and spin magnetic moments [37-39].

The second one is the electron’s orbital motion around the nucleus. Since it is a moving charge, an electron may be considered as a small current loop, generating a very small magnetic field, and having a magnetic moment along its axis of rotation, as schematically illustrated in Figure I.13b [37-39].

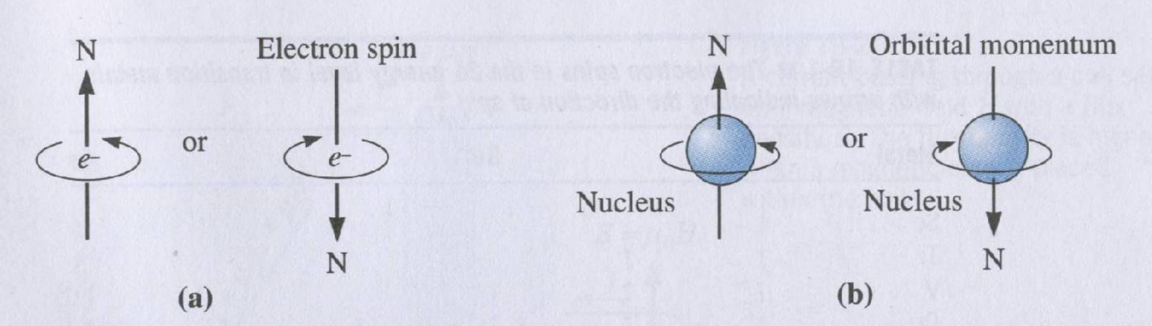

Figure I.13. Schematic demonstration of the magnetic moments associated with (a) a spinning electron and (b) an orbiting electron [38].

Bohr magneton, μ_B, is the most fundamental magnetic moment and its magnitude is 9.27 x 10^{-24} A.m^2 [39]. For each electron in an atom, the spin magnetic moment is designated as $\mp \mu_B$ (plus for spin up, minus for spin down). In addition, the orbital magnetic moment contribution is equal to $m_l * \mu_B$, where m_l is the magnetic quantum number of the electron [39, 40].

The externally applied magnetic field is at times called the magnetic field strength, and is designated by *H*. The magnetic induction, or magnetic flux density, denoted by *B*, represents the magnitude of the internal field strength within a substance that is subjected to an *H* field. Both *B* and *H* are field vectors. They are characterized not only by magnitude, but also by direction in space. Another field quantity, *M*, called the magnetization (response) of the solid, is defined by the expression [40, 41];

$$B = \mu_0 H + \mu_0 M \qquad \text{(Eqn. I.1)}$$

where μ_0 is the permeability of a vacuum, a universal constant, which has a value of $4\pi \times 10^{-7}$ (1.257×10^{-6}) H/m [37, 40].

Diamagnetism (see Figure I.14) is a very weak form of magnetism that is nonpermanent and persists only while an external field is being applied. It is induced by a change in the orbital motion of electrons due to an applied magnetic field. The magnitude of the induced magnetic moment is extremely small, and in a direction opposite to that of the applied field [37, 38].

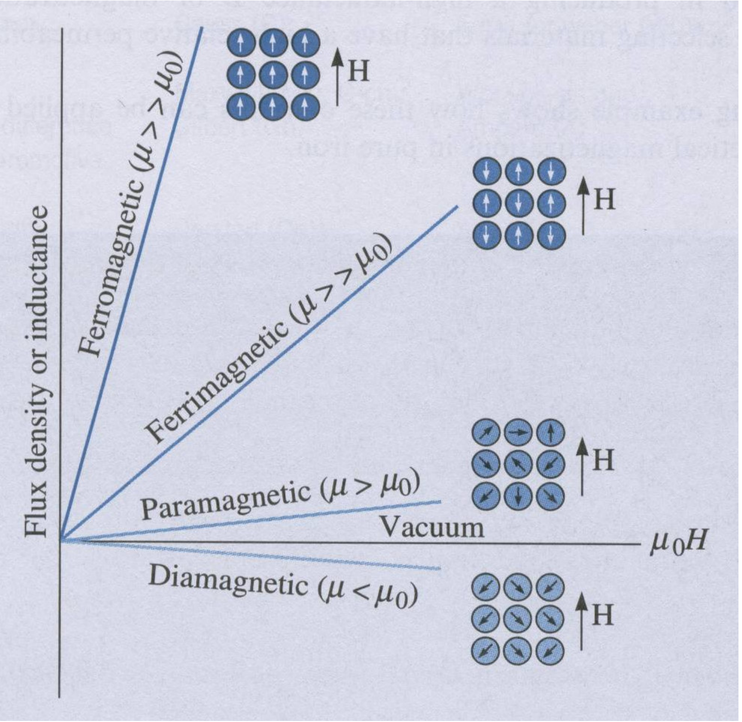

Figure I.14. Comparison among magnetization responses of ferro, ferri, para and diamagnetic materials when magnetic field is applied [38].

Paramagnetic materials (see Figure I.14) have only partial cancellation of their magnetic moments leaving the atom with a net moment [38, 40]. In the absence of an external magnetic field, the orientations of these atomic magnetic moments are random, such that a piece of material possesses no net macroscopic magnetization. When a field is applied to a paramagnetic material, the atomic moments align themselves with the field to an extent determined by the magnitude of the field and the temperature.

In ferromagnetic materials (see Figure I.14), an additional alignment of the moments due to quantum mechanical exchange forces occurs when the material is cooled below a critical temperature, T_C, the Curie temperature [37, 40, 41]. They possess a permanent magnetic moment even in the absence of an external field, and manifest very large permanent magnetizations (spontaneous magnetization) [5, 40, 41]. Ferromagnetic materials are composed of small-volume regions, named as magnetic domains in which there is a mutual alignment in the same direction of all magnetic dipole moments and they magnetized to their saturation magnetization (M^S) [40, 41]. Adjacent domains are separated by domain boundaries or domain walls, across which the direction of magnetization gradually changes. In an unmagnetized state, the total magnetization of samples is zero due to formation of multiple magnetic domain formation where the magnetization vectors cancel each other.

I.2.5.2.2 Magnetic Domains in Ferromagnetic Materials

A ferromagnetic material, as demagnetized, i.e., when there is no applied magnetic field, is divided into a number of small regions (Figure I.15a). These regions are called magnetic domains [5].

Each domain is spontaneously magnetized to the saturation value M^S. The total magnetization of a ferromagnetic material is zero due to the presence of these magnetic domains since their existence reduces the magnetization of the material by reducing the sum of exchange, magnetostatic, magnetocrystalline, and domain wall energies. This happens because the directions of magnetization of various domains are directed such that the specimen, as a whole, has no net magnetization [5, 40].

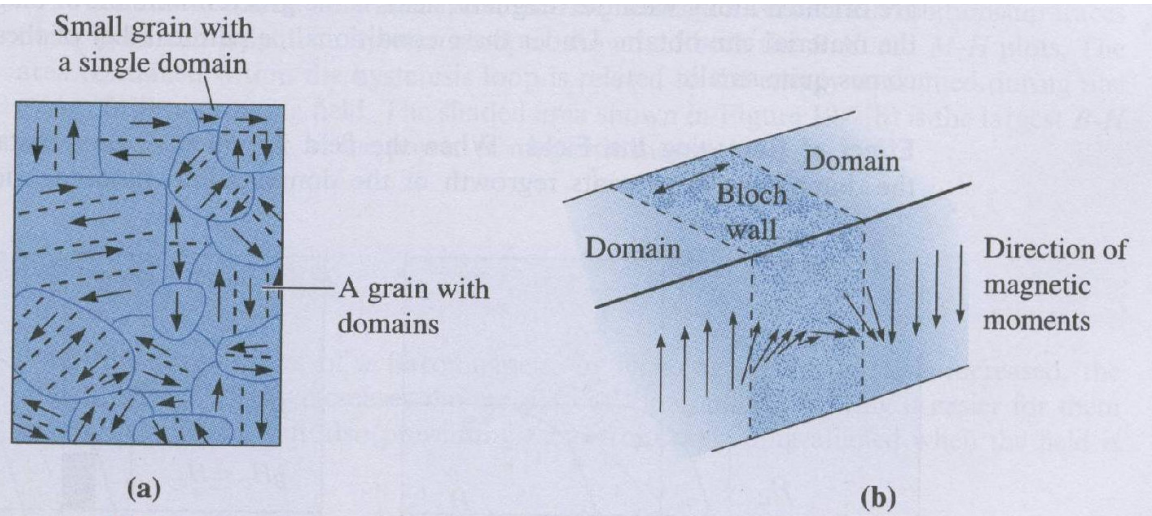

Figure I.15 Schematic representation of (a) general view of magnetic domains and the random magnetization directions within (b) change in orientation of magnetic dipoles in a 180^o twist boundary or domain (Bloch) wall [38].

The process of magnetization is then, converting the material from a multi-domain structure to a single domain with one magnetization direction parallel to that of the applied field. On the other hand, the formation of a magnetic domain results in an increase in domain wall length which costs energy. Domain walls are the boundary regions that separate two magnetic domains with spontaneous magnetizations in opposite directions (Figure I.15b). They are virtual regions of a crystal in which the net magnetization is zero. Also, at or within the wall, the magnetization needs to change direction from one easy crystallographic direction to another. The thickness of domains walls are determined by the exchange and anisotropy energies and can range from 10 nm to several μm [5, 39, 41].

Generally domain walls can be classified into 180^o or non-180^o domain walls. 180^o domain walls occur in almost all materials and are not affected by applied stress. In 180^o domain walls, the directions of magnetization in the neighboring domains are antiparallel and consequently the moments in these two domains lie in equivalent crystallographic directions [40]. In cubic materials, when $K > 0$, the non-180^o walls are all 90^o walls. This assures that the directions of the moments in neighboring domains are at right angles with respect to one another. Thus in iron, where the easy axes are $\langle 100 \rangle$, the domain walls between $[100]$ and $[\bar{1}00]$ directions are 180° domain walls. The walls between $[100]$ and $[010]$ are 90° walls. On the other hand, when $K < 0$ such as in nickel, where the easy axes are $\langle 111 \rangle$, the non-180° domain walls will be either 71° or 109° but not 90° [40].

I.2.5.2.3 Definition & Origins of Magnetocrystalline Anisotropy

One of the factors which dictate the magnetization response of a magnetic material when subjected to an applied magnetic field (M-H curves) is magnetic anisotropy. Simply, it means the dependence of the magnetic properties of the material on the crystallographic directions in which they are measured. Crystal anisotropy or magnetocrystalline anisotropy is an intrinsic property of a magnetic material. Ferromagnetic materials with higher anisotropy display greater magnetic hysteresis. In an isotropic solid, certain crystallographic axes are favored by the magnetic moments to attain minimization of energy. Magnetic moments can be dislodged from the direction they occupy by application of a magnetic field; this happens by jumping to crystallographically equivalent axes closer to the direction of the applied field, hence with lower energy. This process yields a discontinuous and irreversible rotation of the magnetic moments with a switching action [40].

Results of magnetization measurements along $\langle 100 \rangle$, $\langle 110 \rangle$ and $\langle 111 \rangle$ directions for bcc iron and fcc nickel is shown in Figures I.16a and I.16b, respectively. As evident by the figure, saturation of magnetization for iron can be achieved with quite low fields in the $\langle 100 \rangle$ direction where the same is valid in the $\langle 111 \rangle$ direction for nickel. Accordingly, these special directions are called the easy axis of magnetization for these respective metals. A domain wall separates two magnetic domains in a crystal, and can be moved by a magnetic field.

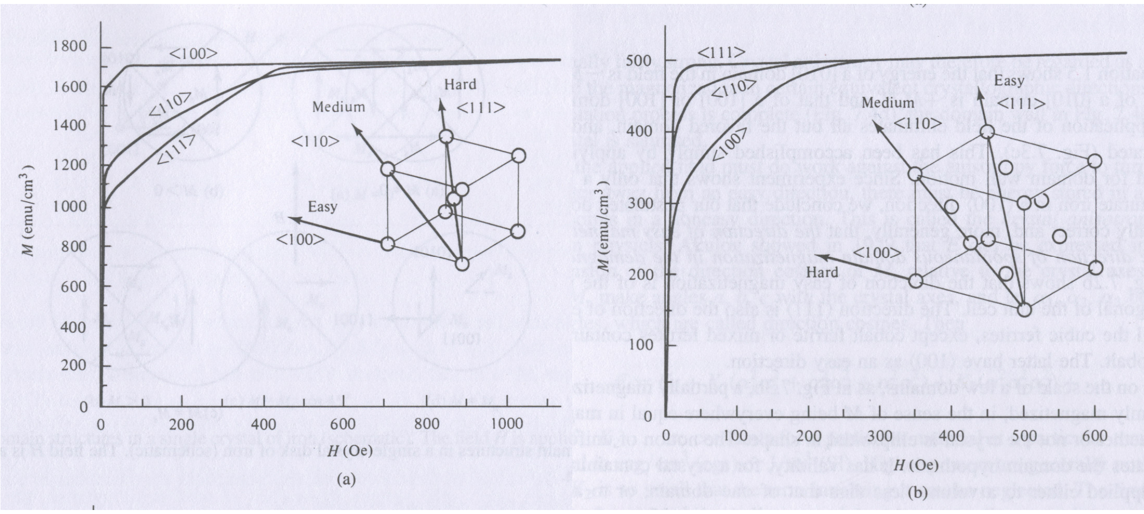

Figure I.16. Magnetization vs. magnetic field curves for single crystalline (a) iron and (b) nickel [5].

Figure I.17 shows a possible domain structure for a demagnetized iron crystal disk cut parallel to (001) plane with the assumption that the domains in the demagnetized state of iron are spontaneously magnetized to saturation in directions of $\langle 100 \rangle$. The schematic in (a) shows four different partitions in the main domain with magnetization vectors M_s of each directing along $[010]$, $[100]$, $[0\bar{1}0]$ and $[\bar{1}00]$ directions, respectively. When a magnetic field is applied in $[010]$ direction as shown in (b), the partition with its magnetization vector in the same direction as the magnetic field will start growing at the expense of the others by the motion of the domain walls in order to lower the magnetic potential energy of the crystal. Continued application of the field finally eliminates all but the favored partition and thus the crystal reaches saturation. The direction of easy magnetization of a crystal then, can also be identified as the direction of spontaneous domain magnetization in the demagnetized state [5].

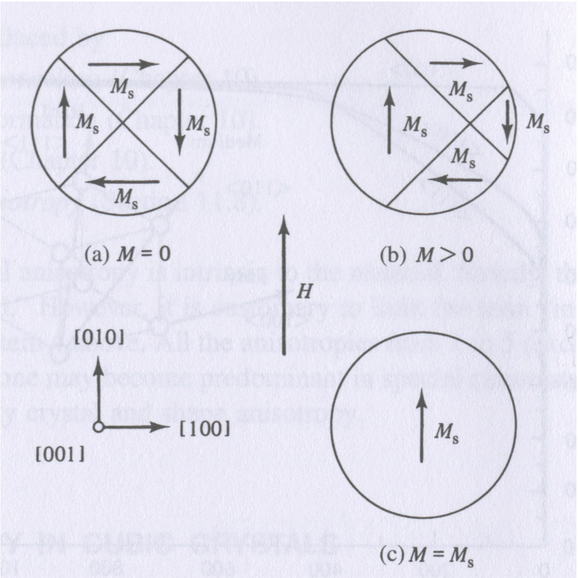

Figure I.17. Evolution in magnetic domain structure in single crystalline iron specimen under applied magnetic field in $[010]$ easy direction, (a) before application of magnetic field, (b) onset of domain wall motion under magnetic field (c) saturation of magnetization [5].

As can be seen in Figure I.16a, more magnetic field is necessary to saturate iron in $\langle 110 \rangle$ medium magnetization direction compared to that of in $\langle 100 \rangle$. The change in domain structure of iron under an applied field in $[110]$ is depicted by Figure I.18. Domain wall motion proceeds until there are only two partitions left as seen in (c) where each of them has equal potential energies. For the magnetization to increase further and reach the level of saturation, the magnetization vectors M_s of both domains need to rotate until they are parallel to the direction of the applied field, i.e., $[110]$. This process is named domain magnetization rotation. The domain itself, which is a group of atoms, does not rotate. It is merely the net magnetic moment of each atom that rotates. Domain magnetization rotation is only possible at relatively higher fields since the field is then acting against the force of crystal anisotropy which is usually fairly strong. Crystal anisotropy may therefore be regarded as a force which tends to conserve the magnetization in certain equivalent crystallographic directions. When the rotation process is complete (d), the domain wall disappears and crystal becomes saturated [5].

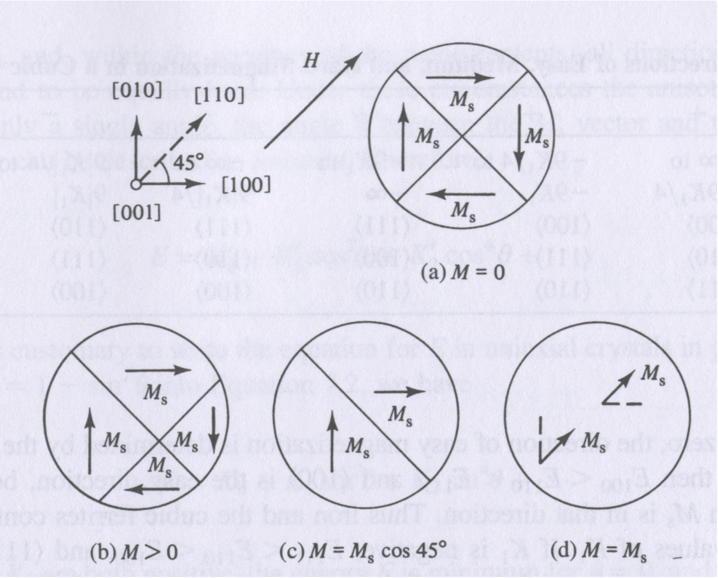

Figure I.18. Evolution in magnetic domain structure in single crystalline iron specimen under applied magnetic field in $[110]$ medium direction, (a) before application of magnetic field, (b) onset of domain wall motion under magnetic field, (c) energetically equipotent two domain structure (d) achievement of saturation following domain magnetization rotation [5].

The applied field must do work against the anisotropy force to turn the magnetization vector M_s away from any easy direction. This means, there must be some energy stored in any crystal in which M_s points towards any non-easy direction. This energy is called magnetocrystalline anisotropy energy (MAE) and denoted by $E_{anisotropy}$. It is possible to express MAE in terms of a series expansion of the direction cosines of M_s that are relative to the crystal axes. In a cubic crystal, if M_s is assumed to make angles *a, b, c* with the crystal axes *x, y, z* and to have $\alpha_1, \alpha_2, \alpha_3$ as the direction cosines of these angles, then,

$$E_{anisotropy} = K_0 + K_1(\alpha_1^2\alpha_2^2 + \alpha_1^2\alpha_3^2 + \alpha_2^2\alpha_3^2) + K_2(\alpha_1^2\alpha_2^2\alpha_3^2) \qquad \text{(Eqn.I.2)}$$

where, K_0, K_1, K_2, …. are constants for a particular materials at a particular temperature and have the unit erg/cm^3 or J/m^3 [5].

Usually higher terms are not necessary in Eqn.I.2. Sometimes even K_2 can be too small to not be neglected. K_0 is not dependent of the angles and is usually neglected since the main interest is in the change of MAE when magnetization vector M$_s$ rotates from one direction into another. When K_2 is zero, direction of easy magnetization is determined by the sign of K_1. If K_1 is positive, then $E^{[100]}_{anisotropy} < E^{[110]}_{anisotropy} < E^{[111]}_{anisotropy}$. This means, $\langle 100 \rangle$ is the easy direction (like in bcc iron) and MAE is minimum when M$_s$ is aligned in this direction. If K_1 is negative, then $E^{[100]}_{anisotropy} > E^{[110]}_{anisotropy} > E^{[111]}_{anisotropy}$. This means, $\langle 111 \rangle$ is the easy direction (like in fcc nickel) and MAE is minimum when M$_s$ is aligned in this direction. When K_2 is nonzero, then the easy direction depends on the values of both K_2 and K_1 [5].

Exchange interaction is between two neighboring spins and can be expressed as spin-spin coupling. It can be very strong and dictates these neighboring spins parallel or antiparallel to each other. However, the associated exchange energy is isotropic and only depends on the angle between adjacent spins. It does not depend on the direction of the spin axis relative to the crystal lattice. Spin-spin coupling does not contribute to magnetocrystalline anisotropy [5, 39, 40].

The orbit-lattice coupling is also strong. The orientations of the orbits are fixed very strongly to the lattice since the orbital magnetic moments are almost entirely quenched [5, 39, 40].

There also exists a coupling between the spin and orbital motion of each electron. Crystal anisotropy mainly stems from this spin-orbit coupling. When a magnetic field is applied not only does it attempt to reorient the spin of an electron but also the orbit of that same electron. The orbit is strongly coupled to the lattice and thus the attempt to rotate the spin axis faces strong resistance. MAE, which is the energy required to rotate the spin system of a domain away from the easy magnetization direction, is just the energy to overcome the spin-orbit coupling. This coupling is relatively weak compared to the aforementioned two [5, 39, 40].

The strength of the anisotropy is measured by the magnitude of the anisotropy constants. The magnitude of crystal anisotropy usually diminishes with temperature more rapidly than magnetization and vanishes at Curie temperature [5, 39, 40].

I.2.5.3 Structure of Magnetic Domains in MSMA NiMnGa

The structure of the magnetic domains in $Ni_{2+x+y}Mn_{1-x}Ga_{1-y}$ studied in bulk single crystals [42] was reported to be faceted along $\{100\}$ planes. Different methods were used for investigation including magnetic force microscopy [43]. The results of these studies show that the domain structure of the austenitic phase is formed primarily by 180° domains with magnetization vectors M_s parallel to $[100]$. The magnetic domain structure changes dramatically in the course of a martensitic transformation, upon formation of the martensitic variants. In the low-temperature phase several magnetic domains are located within a single martensitic variant. Since adjacent martensitic variants are separated by a twin boundary, this leads to the appearance of a relief on the sample's surface, and the magnetization vectors in adjacent martensitic variants prove to be directed at a certain angle with respect to each other [44]. The domain structure within a single martensitic variant consists of 180° domains, just as in the austenitic phase. Pan *et al.* [44] studied the evolution of a hierarchical domain structure. They reported that when a small magnetic field (1-2 kOe) is applied to the sample, the ferromagnetic and martensitic domain structures change, resulting in a formation of a fir-tree pattern meeting at the twin boundaries such as shown in Figure I.19a. As the field is increased to an intermediate level, it changes the topology of the ferromagnetic domains which come to resemble a ‘herringbone’ structure (Figure I.19b) with a common domain wall coinciding with the twin boundary [44]. As the magnetic field strength is increased further, the process of reorientation of the magnetic moments in the ferromagnetic domains and the process of displacement of the boundaries between the martensitic variants begin to compete. With larger fields (8-9 kOe), the magnetization vector that was previously orthogonal to the field will rotate in the field direction and eliminate domain structure within a variant, so each twin band coincides with one magnetic domain.

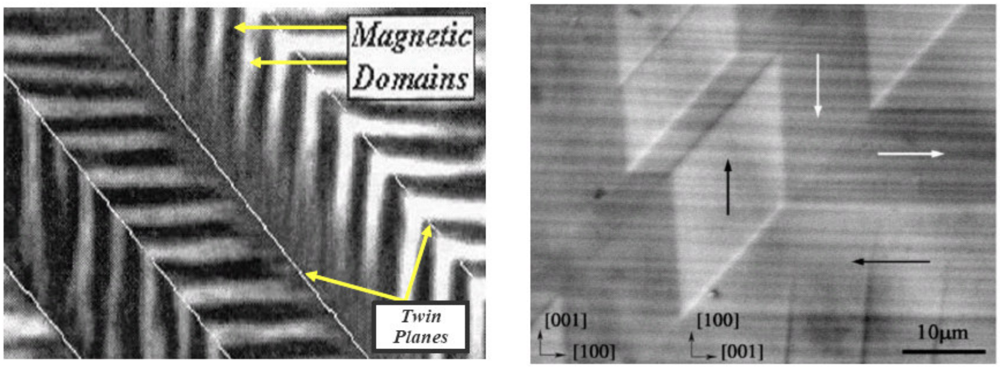

(a) (b)

Figure I.19. Domain structures of NiMnGa alloys determined using a) the magnetic garnet film technique [45] and b) scanning electron microscopy images [46].

A martensite magnetic domain structure phase reconstruction of a Fresnel through-focus series obtained from the martensite plates whose c-axis is oriented in the plane of a foil with a nominal composition of $Ni_{50}Mn_{27}Ga_{23}$ is shown in Figure I.20 [47]. The input Fresnel images I.20a – I.20c show a few domain walls coincident with the twin plate boundaries and others within the twin plates. The reconstructed phase in I.20d clearly shows a pair of white and black phase ridges, similar to a herringbone structure. The gray scale induction components in I.20e and I.20f show the different directions of magnetic induction [47].

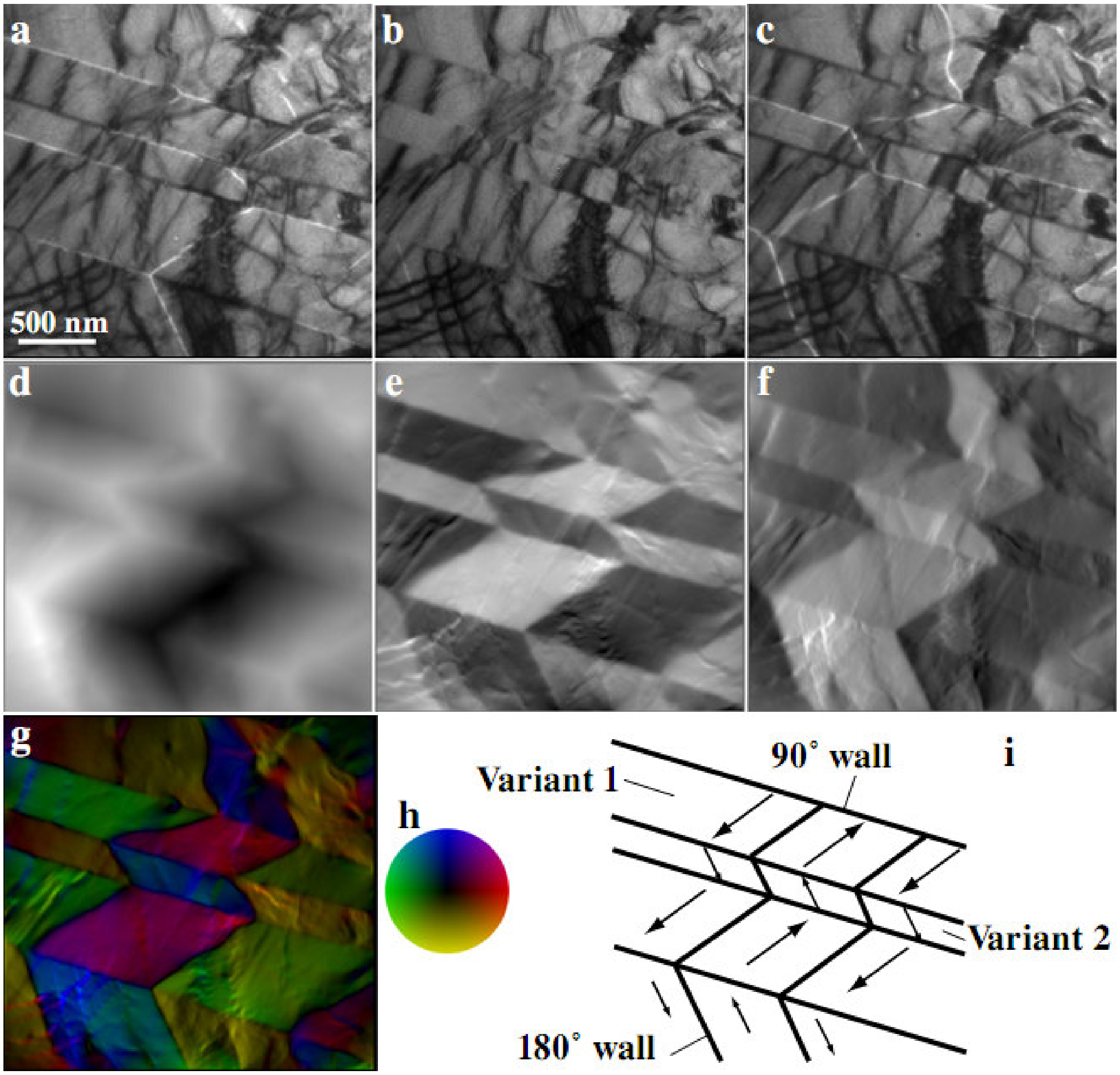

Figure I.20. Phase reconstruction of herringbone martensite domain structure [47]**.**

The integrated induction orientations are more clearly seen in the color plot I.20g that is indexed with the color map I.20h. The color profile delineates two types of domain walls, a 90° wall and a 180° wall, similar to observations of some other researchers [48-50]. While the walls coincident with the twin boundaries have a 90° character, those within the twin variants are 180° walls. The schematic representation of the domain structure (Figure I.20i) is drawn from the color map and shows both the 90° and 180° domain walls. Magnetic measurements in the 5-period modulated martensite phase (10M) have indicated that the easy axis of magnetization is along the $[001]$ direction, i.e., along the shorter c-axis [19, 22]. The 180^o domain walls within a single variant correspond to two magnetic domains whose c-axes are oriented in opposite directions. The twin boundaries separate variants oriented along different cubic axes, resulting in the 90^o walls [47].

I.2.5.4 Magnetocrystalline Anisotropy in MSMA NiMnGa

Magnetocrystalline anisotropy can be considered as the determining parameter for the realization of MFIS in shape memory ferromagnets since the formation and growth of the structural domains (variants) favorably oriented with respect to the application direction of the magnetic field are directly related to it. Magnetocrystalline anisotropy determines the path along which the ferromagnetic system proceeds and reaches the state with the lowest possible energy as the variant reorient. Measurements of magnetization in single-crystalline $Ni_{51.3}Mn_{24.0}Ga_{24.7}$ showed that the easy magnetization axis in the cubic austenite phase is oriented along the crystallographic $[100]$ axis and that the magnetocrystalline anisotropy constant K_1 in this phase is relatively moderate. As a result of the transition to the martensitic phase the magnetocrystalline anisotropy changes significantly [51].

The field dependences of the magnetization of $Ni_{51.3}Mn_{24.0}Ga_{24.7}$ in the martensitic phase are given in Figure I.21a. In order to measure the magnetocrystalline anisotropy, Tickle and James [51] employed a thin single-crystal plate whose faces coincided with the crystallographic planes of the $\{100\}$ type. They compressed the sample to a single variant state in a spring driven mini-press. Measurements of the M vs. H dependence were done in a magnetic field that was parallel or perpendicular to the direction along which the sample was compressed. The sample was first cooled below the martensitic transformation temperature in a 6 kOe magnetic field directed along the compression axis in such a way that both the magnetic field and the applied stress facilitated the formation of a single variant of martensite. The sample size in the direction of compression was selected such that in the martensitic phase the sample would be of square shape. In this case the demagnetization factors for two orientations of the magnetic field proved to be the same, and the uniaxial anisotropy constant K_u could be evaluated by the area between the curves. The field dependences of the magnetization of the single-variant martensite in Figure I.21b show that the *c* axis is indeed the easy magnetization axis and that the curves demonstrate uniaxial anisotropy. The results of measurements under a 1.9 MPa load were used to calculate the areas between the *M* axis and the curves of magnetization along the easy and hard axes. The uniaxial anisotropy constant in the martensitic phase calculated in this manner ($K_u = 2.45x10^6$ erg/cm^3 at T = 256 K) proved to be greater than the constant K_1 in the austenitic phase by a factor of 100.

Studies of the magnetocrystalline anisotropy of single-crystals with different compositions (the samples were converted to a single-domain state) have shown that the values of K_u at room temperature vary from $1.7x10^6$ erg/cm^3 for $Ni_{48}Mn_{31}Ga_{21}$ [52] to $2.48x10^6$ erg/cm^3 for $Ni_{49.7}Mn_{28.7}Mn_{21.6}$ [53]. The temperature dependences of the uniaxial magnetocrystalline anisotropy constant for martensite have been measured for polycrystalline Ni_2MnGa [54] and for single-crystal $Ni4_{8.8}Mn_{28.8}Ga_{22.6}$ [55]. For the polycrystalline sample it was found that $K_u = 2.5$ $x10^6$ erg/cm^3 at T = 220 K.

It is important to note that saturation magnetization is temperature dependent and decreases with increasing temperature so does the anisotropy constants [56, 57]. Sozinov *et al.* [56] reported the room temperature anisotropy constants, lattice parameters, theoretical detwinning strain, detwinning stresses and observed MFIS values of three martensite types of NiMnGa alloys as shown in Table I.4. As the temperature is lowered, the value of K_u increases linearly and at 77 K reaches the value of $3.8x10^6$ erg/cm^3. The increase in K_u with decreasing temperature has also been observed for a single-domain single-crystal sample of $Ni_{48.8}Mn_{28.6}Ga_{22.6}$. At 283 K the magnetocrystalline anisotropy constant $K_u = 2x10^6$ erg/cm^3, while at 130 K its value proved to be equal to $2.65x10^6$ erg/cm^3.

Table I.4. Summary of lattice parameters, cell volume, transformation strain, detwinning stress, MAE and MFIS of three types of martensite structures [56]. In the table, 5M, T and 7M stand for 10M, non-modulated, and 14M martensitic structures.

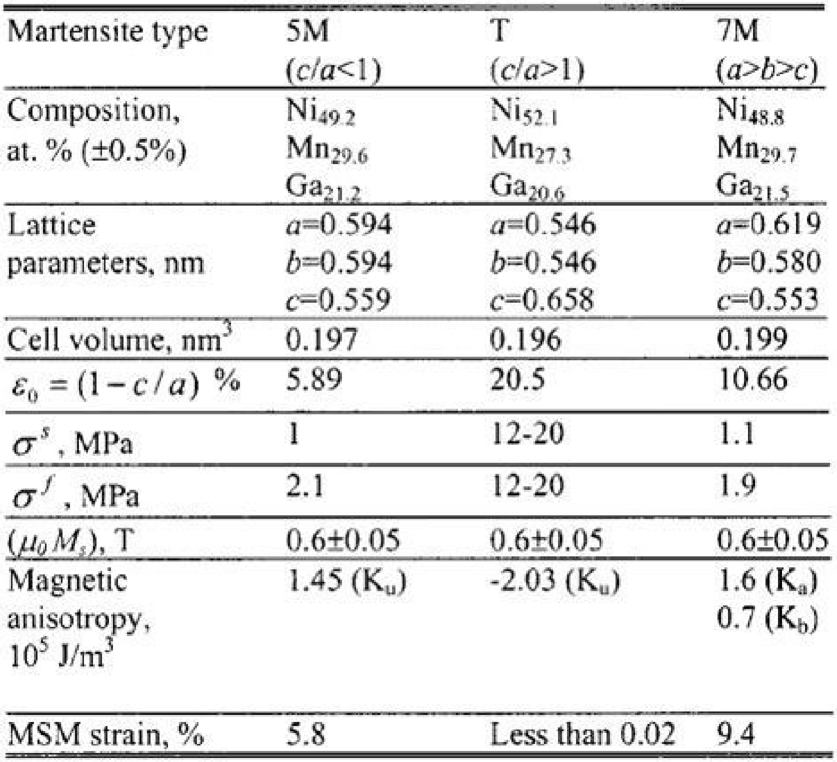

Martensite type	5M ($c/a<1$)	T ($c/a>1$)	7M ($a>b>c$)
Composition, at. % (±0.5%)	$Ni_{49.2}$ $Mn_{29.6}$ $Ga_{21.2}$	$Ni_{52.1}$ $Mn_{27.3}$ $Ga_{20.6}$	$Ni_{48.8}$ $Mn_{29.7}$ $Ga_{21.5}$
Lattice parameters, nm	a=0.594 b=0.594 c=0.559	a=0.546 b=0.546 c=0.658	a=0.619 b=0.580 c=0.553
Cell volume, nm^3	0.197	0.196	0.199
$\varepsilon_0 = (1-c/a)$ %	5.89	20.5	10.66
σ^s, MPa	1	12-20	1.1
σ^f, MPa	2.1	12-20	1.9
$(\mu_0 M_s)$, T	0.6±0.05	0.6±0.05	0.6±0.05
Magnetic anisotropy, 10^5 J/m^3	1.45 (K_u)	-2.03 (K_u)	1.6 (K_a) 0.7 (K_b)
MSM strain, %	5.8	Less than 0.02	9.4

The theoretical analysis of magnetocrystalline anisotropy done by Enkovaara et al. [58] showed that magnetic anisotropy changes sign at c/a = 1, which corresponds to a change in the easy magnetization axis from $[100]$ for c/a < 1 to $[110]$ for c/a > 1. Just as the other physical parameters, the magnetocrystalline anisotropy of the $Ni_{2+x+y}Mn_{1-x}Ga_{1-y}$ alloys varies with the chemical composition of these compounds.

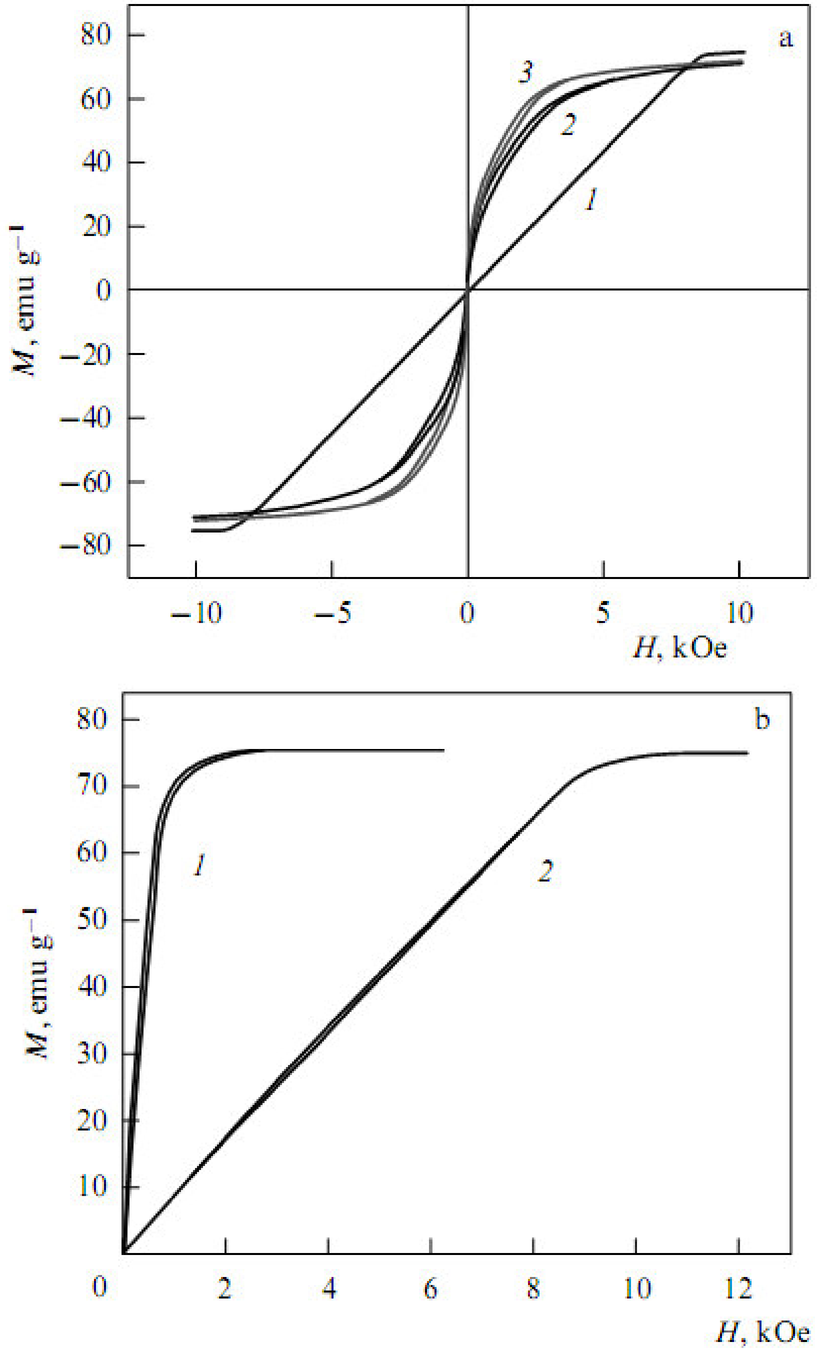

Figure I.21. (a) Field dependences of magnetization of $Ni_{51.3}Mn_{24.0}Ga_{24.7}$ single crystal for a multi variant martensitic state; 1) H parallel to $[100]$, 2) H parallel to $[110]$, and 3) H parallel to $[111]$. The orientation of the single crystal was done in the austenitic phase. (b) Field dependences of magnetization of the $Ni_{51.3}Mn_{24.0}Ga_{24.7}$ single crystal for a single- variant martensitic state: 1) easy magnetization axis, and 2) hard magnetization axis [51].

I.2.5.5 A Potential Substitute for NiMnGa: Concise History & Crystal Structure of NiMnCoIn Metamagnetic Shape Memory Alloys

Recently, a new group of Heusler alloys was introduced as a potential replacement for NiMnGa. Meta-magnetic shape memory alloys, Ni_2MnX, were invented by substitution of Ga with In, Sn or Sb and sometimes with the addition of Co as the fourth element [59-63]. They have been under investigation to reveal their peculiar magnetism related properties [64]. In 2004, Sutou *et al.* [63] investigated these alloys for their potential to demonstrate MFIS. In 2006, Kainuma *et al.* [61] reported that in a NiMnCoIn alloy, a ferromagnetic parent phase transformed to a paramagnetic martensite phase and with increased applied magnetic field the transformation temperatures decreased. In this study, they also showed that NiMnCoIn was capable of reversible phase transformation under the magnetic fields larger than 4 Tesla where martensite transformed to austenite and the critical magnetic field for phase transformation was temperature dependent. One-way 3% MFIS in a pre-deformed single crystal sample was achieved with an applied field of 4T. They reported that the parent and martensite phases had $L2_1$ Heusler-type ordered (a = 0.5978 nm) and 14M modulated (a = 0.4349 nm, b = 0.2811 nm, c = 2.9892 nm and β= 93.24°) structures, respectively [61]. Later, they have also observed the same behavior in NiMnCoSn polycrystalline alloy and reported about 1% one-way and 0.3% reversible MFIS [62]. Wang *et al.* [65] observed reversible MFIS in a NiMnCoIn alloy under 50 MPa which is one orders of magnitude higher than the actuation stress in NiMnGa alloys and they determined the martensite to be 14M. Recently Krenke *et al.* [66] reported 0.12 % reversible MFIS in NiMnIn alloys with the required applied magnetic field of 4T. They have also reported the crystal structure is similar to NiMnGa where the parent phase has $L2_1$ structure with a=0.6011 nm and martensite has 10M modulated martensite structure having a monoclinic unit cell with γ=86.97° and lattice constants a=0.4398 nm, b=0.5635 nm, and c=2.1720 nm [66].

In the later chapters, experimental results pertaining conventional shape memory and magnetic field governed responses of NiMnCoIn metamagnetic shape memory alloy will be given in detail in a comparative manner with those of NiMnGa.

CHAPTER II
EXPERIMENTAL PROCEDURES

Methods employed for the synthesis and preparation of our NiMnGa and NiMnCoIn MSMA specimens are narrated in this chapter. Furthermore, a detailed explanation of the successful computer-aided-design and manufacturing processes of two different novel testing systems (macroscopic and microscopic MTMs) utilized to attain the response of MSMA specimens in the course of simultaneously applied magnetic, thermal and mechanical stimulations is provided.

II.1 Specimen Synthesis & Preparation

Ingots of NiMnGa with a nominal composition of 50Ni-25Mn-25Ga (at. %) and NiMnCoIn with a nominal composition of Ni45-Mn36.5-Co5-In13.5 (at. %) were synthesized using vacuum induction melting. Single crystals were grown using the Bridgman technique in a He atmosphere. The compositions were determined as $Ni_{51.1}Mn_{24.0}Ga_{24.9}$ (using inductively coupled plasma-atomic emission spectrometry) and as $Ni_{45.7}Mn_{35.6}Co_{4.8}In_{13.8}$ for the matrix and $Ni_{42.0}Mn_{40.3}Co_{16.0}In_{1.6}$ for the second phase (using wavelength-dispersive spectroscopy). The difference between the nominal and actual compositions is thought to be due to the Mn evaporation during single crystal growth [67]. The single crystal samples were then cut into rectangular prisms with dimensions of 4 mm x 4 mm x 8 mm using electro-discharge machining to assure that both magnetic field and stress can be applied along known crystallographic directions. As an exception, the specimens used in NiMnGa energy harvesting tests were 16 mm long.

The face normal of the NiMnGa samples were along $[100]$, $[011]$, and $[01\bar{1}]$ directions in the austenite phase ($L2_1$ ordered structure). Compressive stress was applied along the $[100]$ orientation, while the field was applied along the $[011]$ direction.

NiMnGa single crystals have a 10M tetragonal structure in martensite as evidenced by the strain levels achieved in our martensite reorientation experiment which will be reported in the subsequent chapters.

For the NiMnCoIn single crystals, the austenite orientations also are used to describe the directions of the single crystal samples even if the sample might be in martensitic phase. We had four different orientations in hand as $[100]$, $[110]$, $[123]$ and $[111]$, each indicating the long axis of the rectangular prisms. After homogenization at 900 ^{o}C for 24 h in vacuum and water quenching, second-phase particles inherited from the as-grown crystals are detected in the microstructure [68].

The $Ni_{40}Mn_{33}$ $Co_{10}Al_{17}$ (at. %) polycrystalline bulk specimen was prepared by induction melting under an argon atmosphere. The polycrystalline ingot was annealed at 1373 K for 168 hours in vacuum and quenched in ice water. Several compression specimens with dimensions near to $3.0\times2.5\times5.5$ mm^3 were cut out of the annealed ingot by wire-electrical discharge machining [69].

The $Ni_{43}Mn_{39}Co_{7}Sn_{11}$ (at. %) polycrystalline compacted-powder specimen was prepared through a process which consisted of multiple steps. The first step was melting of the ingot by high frequency induction. Next, the powders with particle diameters of 10 to 250 μm were obtained using conventional nitrogen gas atomization under argon atmosphere (1.5 to 5 MPa pressure). For the present study, a powder with particle diameter sizes between 25 to 63 μm was compacted into pellets by pressure application. The compacted powder was sealed in quartz tubes under argon atmosphere and annealed at 1173 K for 6 days and then quenched in ice water. Several compression specimens with dimensions close to $3.0\times2.5\times5.5$ mm^3 were cut out of the sintered pellets by wire-electrical discharge machining [70].

II.2 Development of Novel Testing Systems for Characterization of Magnetic Shape Memory Alloys

In order to understand the variant reorientation and phase transformation based behaviors of MSMAs sourcing from their magneto-mechanically and thermo-mechanically coupled nature, development of original, robust test systems which would allow simultaneous magnetic, mechanical, thermal control and measurements was required. For this purpose two different magnetomechanical testing systems, one macroscopic and one miniature, were designed and manufactured in the course of this research.

II.2.1. Magneto-Thermo-Mechanical (MTM) Macroscopic Testing System

The first of the aforementioned custom designed and manufactured two novel systems is the ***magneto-thermo-mechanical macroscopic testing system*** (macro MTM) (Figure II.1) which consists of seven different subsystems:

1) Servo-hydraulic tension/compression load platform (MTS 810, 50 kip) with hydraulic collet grips and custom load cell,
2) Interchangeable head/easy alignment titanium alloy tension and compression custom design grips,
3) Thermal control subsystem consisting of heating/cooling assembly with optimized number/no slack 3/16 diameter copper tube windings surrounded by mica SS band heaters (Watlow 240V, model STB2CAA4), step-up transformers (ACME model T-2-53007-S, 120V→240V), 160 liter liquid Nitrogen dewar (Warton), solenoid on/off valves (Jefferson, cryogenic grade brass) and PID temperature controllers (Omega model CN8202-R1-CD2-C2),
4) Temperature feedback and data logging assembly with T type thermocouples (Omega) and RS-232 connection data logger (Hotmux),
5) Magnetic field application assembly with a 3 Tesla capable electromagnet (LakeShore model EM4-CS), gaussmeter (LakeShore model 450), transverse Hall sensor and DC power supply (LakeShore model 662),
6) High degree of freedom, electric motor driven custom design carrier frame for electromagnet,
7) Cryogenic grade capacitive displacement sensor (Capacitec model HPC-75) and its peripherals.

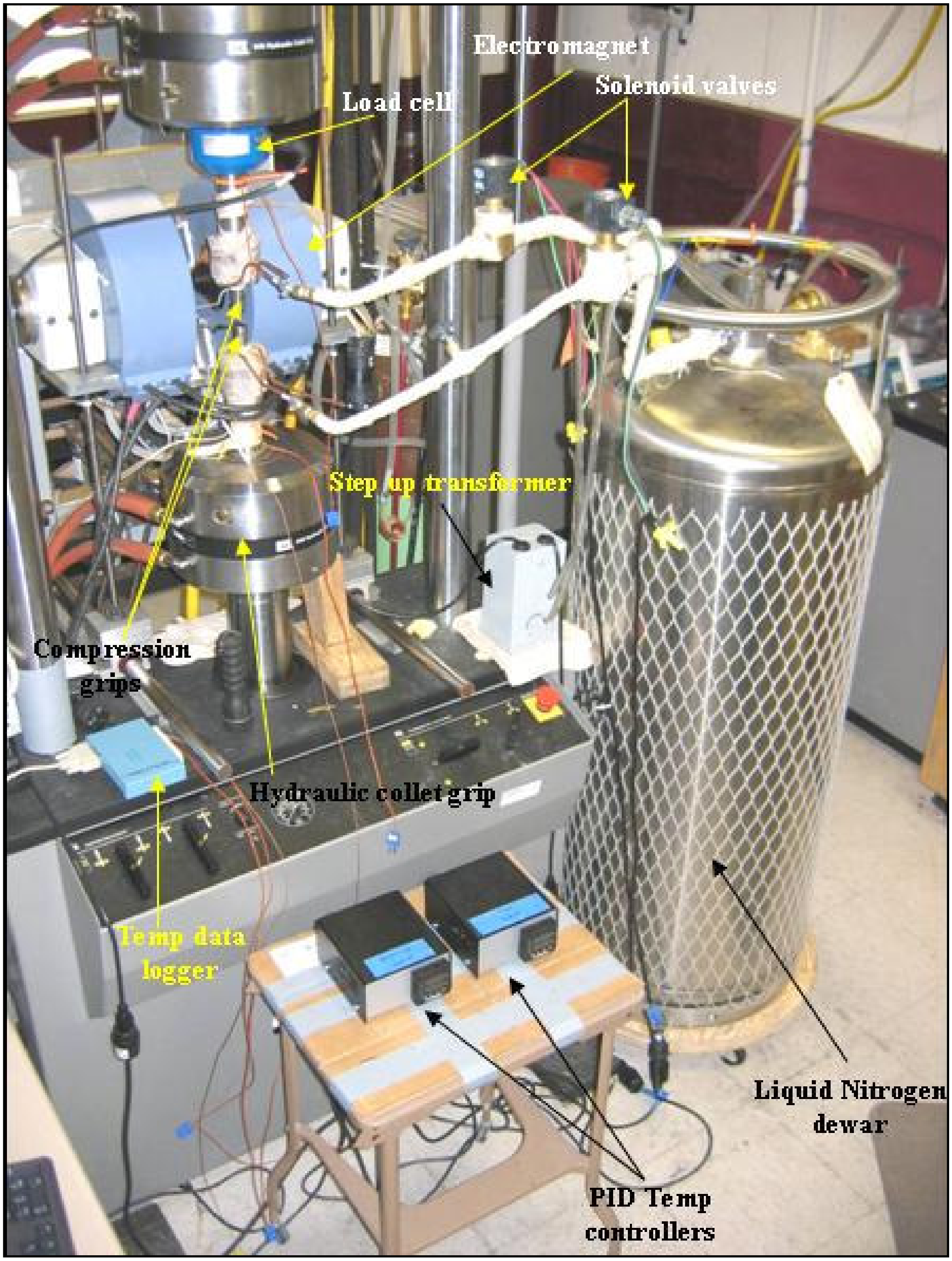

Figure II.1. General view of the components that compose the Magneto-Thermo-Mechanical (MTM) macroscopic testing system.

II.2.1.1 Servo-Hydraulic Tension/Compression Load Platform

As the main component in the experimental setup, the servo-hydraulic load platform, an MTS 810 Material Testing System, is capable of producing approximately 250 kN of force. Force is measured using an array of different load cells depending upon the type of experiment to be conducted. The MTS brand 250 kN load cell came integrated with the platform. For pseudoelasticity tests, where large stresses are required, an Interface model 1010ACK-2.5K-B load cell rated to 2500 lbf. is used to measure force. Meanwhile, for the thermal cycling experiments where low, constant stress levels are needed 500 lbf. Interface model 1010ACK-500-B load cell is employed. For these load cells to be properly attached to the load train, custom design steel adaptors were manufactured. Crosshead displacement and load data is recorded using the MTS controller and data acquisition systems. The system is retrofit with both upper and lower hydraulic collet grips. An overall view of the system can be seen in Figure II.1.

II.2.1.2 Custom-Design Compression &Tension Grips

In order not to have interference between the compression/tension grip material and the applied magnetic field, custom nonmagnetic grips bodies and heads were designed and fabricated out of Ti6Al-4V. The actual photos and 3D CAD models of the custom grip heads for compression can be seen in Figures II.2a and II.2b, respectively.

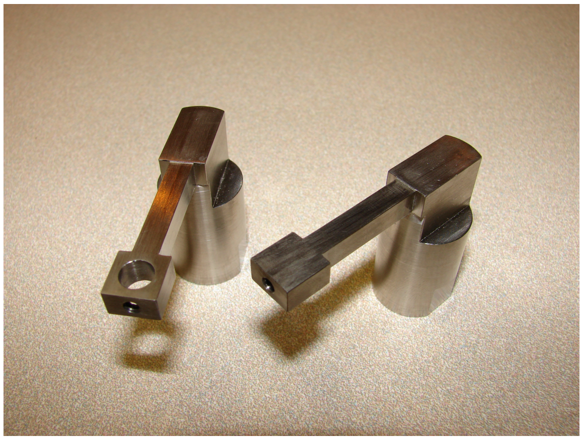

Figure II.2a. Actual photograph of the custom narrow grip heads for compression.

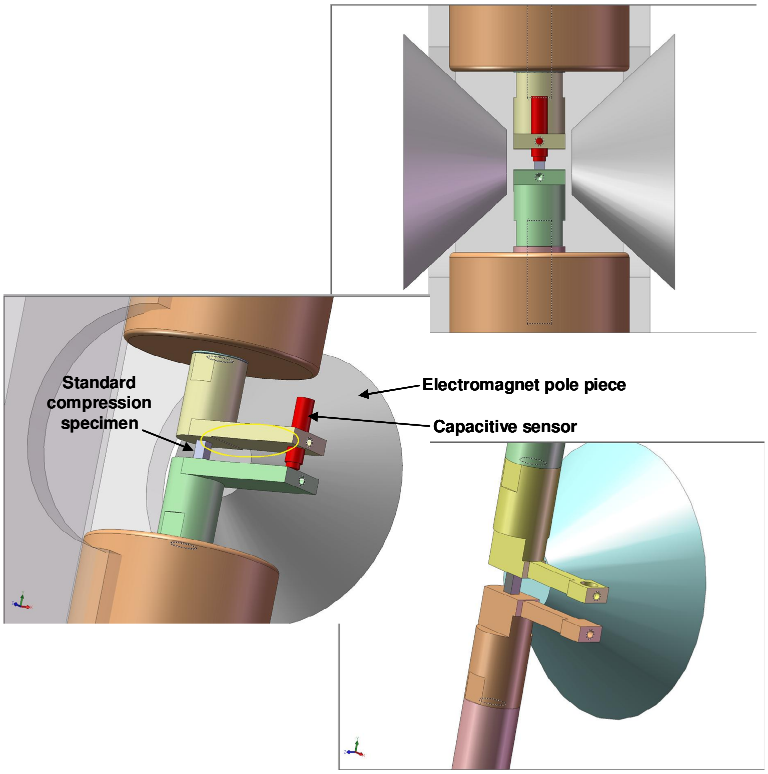

Figure II.2b. 3D CAD models assembly consisting of the magnet pole pieces, capacitive displacement sensor, grip body, grip head, heating/cooing assembly and polymer chamber half created during the design phase of the custom narrow grip heads for compression.

Each titanium alloy grip was designed as an assembly of two pieces, grip body and grip head, to constitute a pair to work together. For easy switch between different grip systems (tension or compression) the head parts are connected to the grip bodies by titanium studs. The top assembly pair fits into the top hydraulic collet grip on the crosshead of the MTS platform, stays rigidly in place upon application of pressure by the collet, and is also responsible to harbor the capacitive displacement sensor. In the design phase, various grip geometries were taken into consideration to achieve the optimum heating/cooling performance by conduction. The narrow compression grip head design was stimulated by the need to increase the magnitude of the available magnetic field through decreasing the air gap between the magnet pole pieces.

Figure II.3 shows a pair of tension grips retrofitted with the heating/cooling assembly. This specific design employs the concept of contoured groove to smoothly accommodate the bone shaped tension specimens without any stress concentrations. The groove fits the contours of the specimen like a glove and supports the specimen at its pits by the groove shoulders. Furthermore, to compensate for the instantaneous misalignment in the axis of the load train due to the deformation of the specimen in the course of the martensitic transformation, a universal joint is introduced at the end of the bottom grip body. The universal joint increases the degree of freedom of the bottom grip assembly and helps avoid premature failure of the specimen.

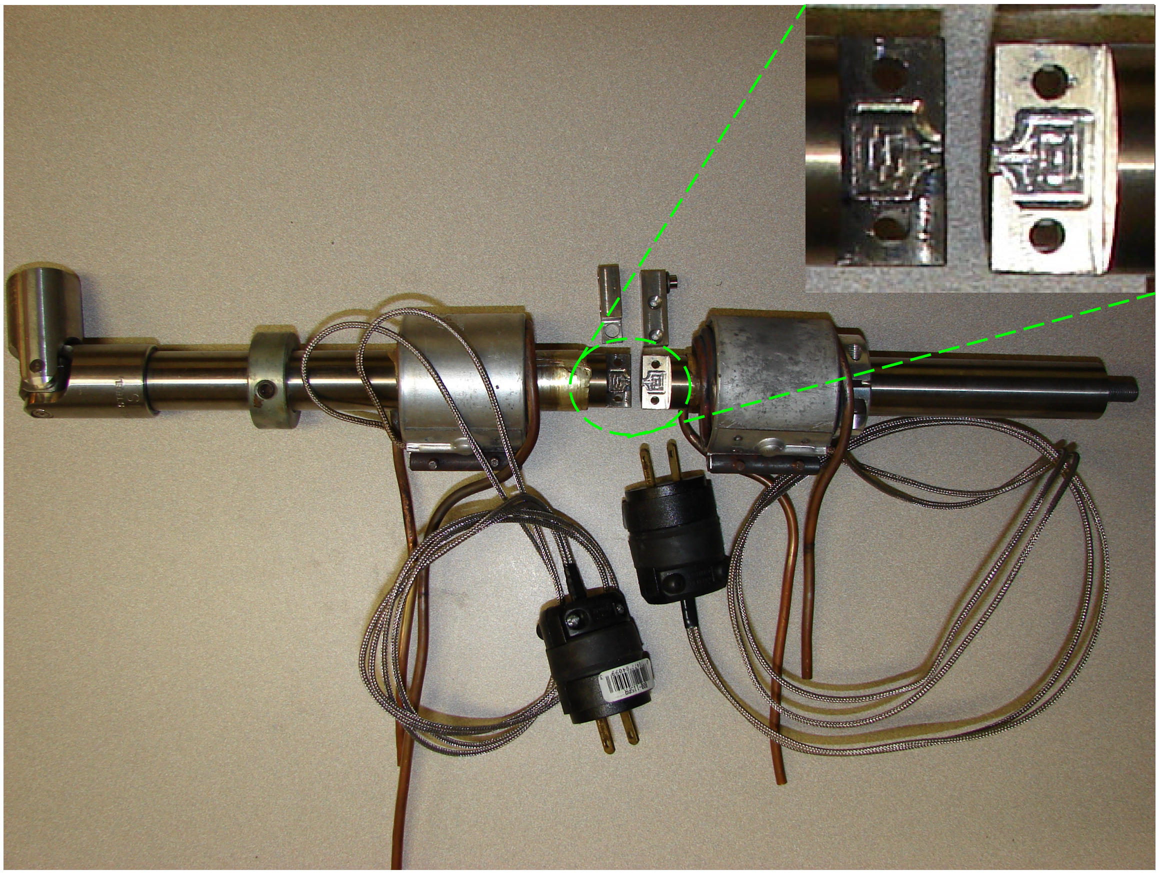

Figure II.3. Actual photograph of the custom grip heads for tension featuring the concepts of contoured groove and universal joint.

II.2.1.3 Custom Thermal Control Subsystem

In order to experimentally observe martensitic transformation and accurately identify the associated transformation temperatures, the thermal control system, components of which are shown in the subsequent figures, was engineered to meet the following requirements:

- Capable of cooling the samples down to approximately -120°C.
- Capable of heating sample to approximately 300°C.
- Capable of heating/cooling at a rate of approximately 10°C/min.
- Capable of maintaining set temperature within ±1°C.

In this system, the sample temperature is controlled by either heating or cooling the compression grips since mode of heat transfer employed is conduction. In order to ensure the stability of the rate of change of temperature in the specimen, conduction must remain as the sole mechanism of heat transfer during testing.

To provide a control volume around the specimen, a transparent polymer chamber was built and successfully employed to minimize the heat transfer by the air surrounding the sample, ultimately reducing the temperature fluctuation due to convection. This custom built chamber was made out of Lexan and is displayed in Figure II.4. Lexan was chosen as the material of the chamber since it is durable to extreme heat/cold and is easy to machine. The chamber consists of two identical halves, which fit and securely stay on the electromagnet pole pieces and between the magnet coils. The recess holes at the top and the bottom of the chamber allow for unrestricted movement of the grip assemblies in the course of testing. Extra holes on the front and back of the chamber assembly provide access for the Hall probe, thermocouples, Cu tube extensions form the heating/cooling assembly and many other various cabling therein. Each half of the chamber was covered with self sticking reflector foil to increase the durability of Lexan where it gets close to the heating source.

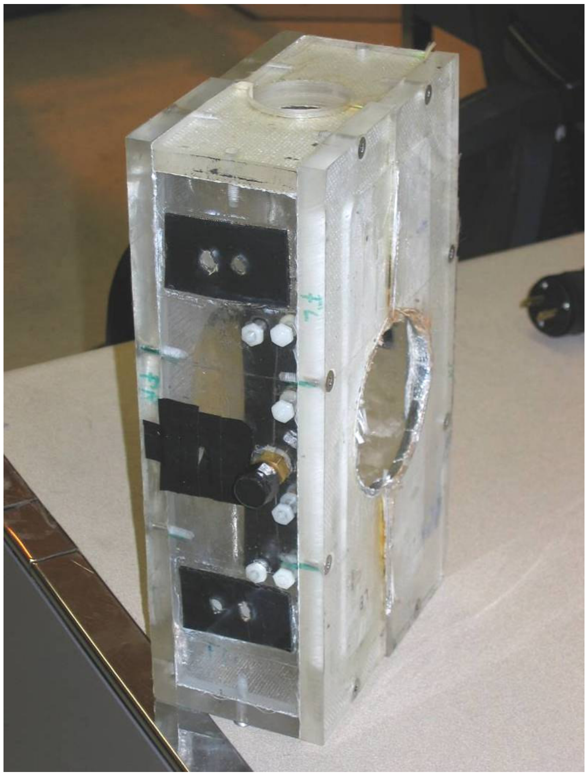

Figure II.4. Lexan was used to build the custom polymer chamber to have a transparent view of the specimen inside. The recess holes on the sides nest the pole pieces of the electromagnet while the ones at the top and the bottom allow the grips to function freely.

In order to achieve a minimum operating temperature of approximately -120°C, the compression grips are cooled using liquid nitrogen. The liquid nitrogen flow is regulated via two Jefferson brand, brass, ON/OFF solenoid valves (see Figure II.1). They are corrosion resistant, and compatible with cryogenic fluids such as liquid oxygen, nitrogen, argon, and carbon dioxide. Temperature range for dependable service is -200 to +50 ^{o}C. The piston inside is type 304 stainless steel, and seal is PTFE. Valves are closed until electrically energized (normally closed) and operates on 120 VAC, 60 Hz. The pipe connections are NPT female.

Past the valves, the liquid nitrogen is then channeled through a pair of Cu coil windings press-fit to both the upper and lower grip bodies. The Cu coil windings were made out of 3/16 in diameter Cu tubing (Figure II.5).

Figure II.5. Cu coil windings used to channel liquid nitrogen.

The sample is heated using a pair of austenitic stainless steel thin-band mica heaters (Watlow, STB2C2AA-4) securely fastened around the Cu coil windings on both the upper and lower grip bodies. The thin-band mica heaters can be seen in Figure II.6.

Figure II.6. Watlow thin-band mica heater used to heat compression grips.

These thin-band mica heaters are approximately 2 inch wide and have a thickness of about 1/16 inch. For maximum power output, the heaters require 1A current and 240V. In order to supply sufficient power to the heaters, wall outlet voltage was increased from 120V to roughly 240V using two step-up transformers at 1A each. The transformers (ACME, T-2-53007-S) are shown in Figure II.7. Under maximum operating conditions, the heaters are capable of reaching nearly 500°C.

Figure II.7. ACME step-up transformer used to increase the voltage supplied to heaters.

In order to administer the heating/cooling assembly during testing, a custom thermal management system, utilizing Proportional-Integral-Derivative (PID) control, was designed and fabricated. The thermal management system consists of two separate circuits, each consisting of an Omega brand temperature controller (model CN8202-R1-DC2-C2), which has multiple output capability. To maintain better thermal control and response, the temperature of each grip assembly is controlled separately via one temperature controller, which can be seen in Figure II.8.

Figure II.8. Temperature controller used to control thermal management system.

The temperature controller's first output manages the cooling system, while the second output dictates the heating system. Nonmagnetic T-type thermocouples are affixed to the top and bottom grips at locations very near to the heating/cooling assemblies and each provides feedback to its respective temperature controller. If the input temperature is greater than the user-defined setpoint temperature, then the cooling system is activated. Likewise, if the input temperature is lower than the setpoint temperature, then the heating system is activated. After auto-tuning, the thermal management system is capable of maintaining the temperature of the specimen to within ±1°C. Also, by using the temperature controller's ramp-soak function, a heating-cooling recipe can be programmed resulting in user-defined heating/cooling rate of 10°C/min.

II.2.1.4 Temperature Feedback & Data Logging Subassembly

Five different T type nonmagnetic thermocouples (Omega) are used as a part of the heating/cooling assembly. As mentioned in the previous section, two of these provide feedback from the top and the bottom grips to their respective temperature controllers. Out of the remaining three, two more are also affixed to the top and the bottom grips, and they go into the temperature data logger, Hotmux. Through an RS-232 connection the data logger saves the temperature data taken from the grips to the harddisk of the dedicated computer. The last thermocouple is directly in contact with the specimen and is solely used for the purpose of logging the specimen temperature.

II.2.1.5. Magnetic Field Application Subassembly

A LakeShore Model EM4-CS electromagnet was combined with the MTS servo-hydraulic load frame and utilized to generate uniform magnetic fields up to 1.6 Tesla in a 2.5 cm x 2.5 cm x 2.5 cm control volume. The maximum attainable level of magnetic field is inversely proportional to the gap (standard is 1 inch) between the pole pieces. The electromagnet is energized by a LakeShore switching power supply (model 662) which is capable of producing ±35V and ±70A. The electromagnet is pictured in Figure II.9.

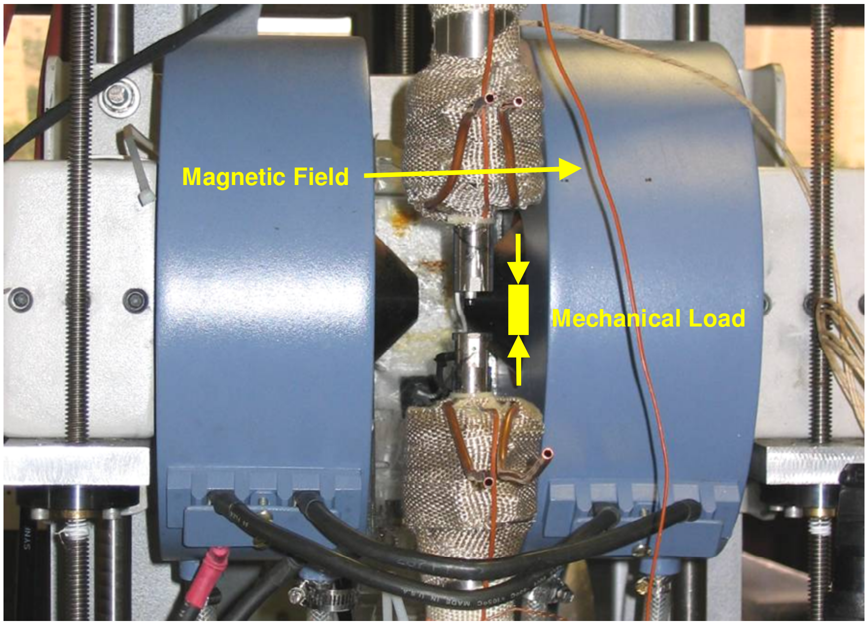

Figure II.9. Lake Shore model EM4-CS water cooled electromagnet.

The magnetic field measurements are performed by a LakeShore model 450 gaussmeter utilizing a LakeShore high sensitivity cryogenic transverse Hall probe with a resolution of ±0.00001 Tesla within ±30 Tesla range. The probe is positioned away from the specimen lying perpendicular to the magnetic field lines in between the pole pieces of the electromagnet. The gaussmeter and Hall probe sensor can be seen in Figure II.10.

Figure II.10. LakeShore 450 Gaussmeter and cryogenic transverse Hall Probe used to provide feedback and control the electromagnet.

II.2.1.6 Custom Design Electric Motor Driven Carrier Frame

As specimen size and/or the test type (tension or compression) changes, the location of the specimen also moves substantially with respect to the reference frame of the test platform. Therefore, the applied field must also be aligned, both vertically and horizontally, in tandem with the new location of the specimen so that the specimen can be embraced by the uniform magnetic flux. The electric motor driven custom design carrier frame was designed and manufactured with high degree of freedom to provide the user of MTM with versatility. While bearing the weight of the magnet, as shown in Figure II.11, the frame is capable of sliding back and forth in the X direction so that the grips (i.e., the load train) can remain in between the pole pieces of the magnet.

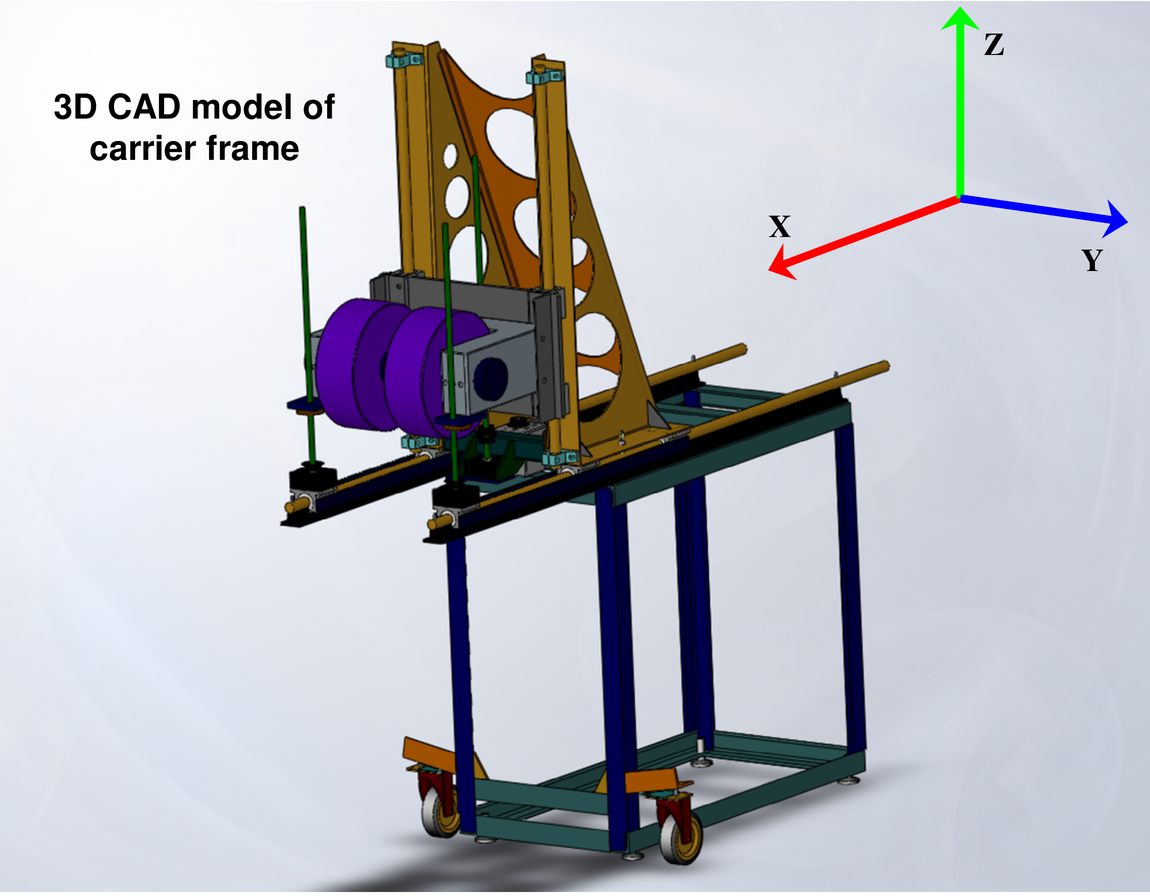

Figure II.11. High degree of freedom, electric motor driven custom design carrier frame is seen in 3D CAD model with the electromagnet mounted on it.

A remote controlled electric motor driven chain-sprocket mechanism shown in Figure II.12, precisely ascends and descends the magnet in the Z direction (Figure II.11) by means of three square profile threaded rods so that the specimen in between the grips can be exactly located in the homogeneous flux of the applied field.

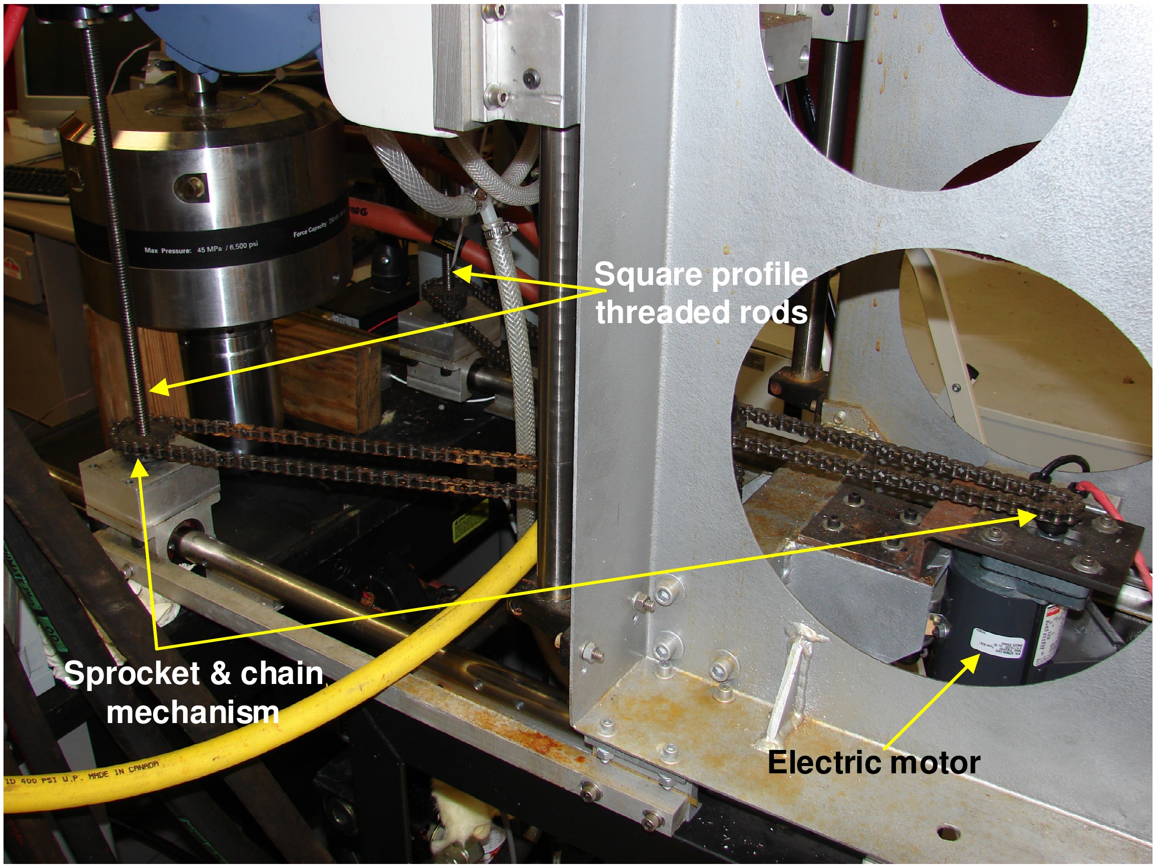

Figure II.12. Remote controlled electric motor drives the chain-sprocket mechanism shown allowing precise up and down movement of the magnet by means of three square profile threaded rods.

II.2.1.7 Cryogenic Grade Capacitive Displacement Sensor

A nonmagnetic capacitive displacement probe, Capacitec model HCP-75-21943, with a linear range of 0-1.25 mm is attached to the grip head in use to measure the change in length between the end points of the specimen (Figure II.13). The precision of the measurements is ±0.001 mm. Strain is calculated by dividing the change in length to the initial length of the sample.

The capacitive displacement sensor provides an input signal to the conditioner box unit which is connected to an analog input of the designated computer. This computer is the same one which controls the MTM system hydraulics; hence the processed analog signal from the conditioner directly goes into the commanding software and can be observed/processed for further use. Figure II.13 shows the sensor as it is attached to the upper grip head.

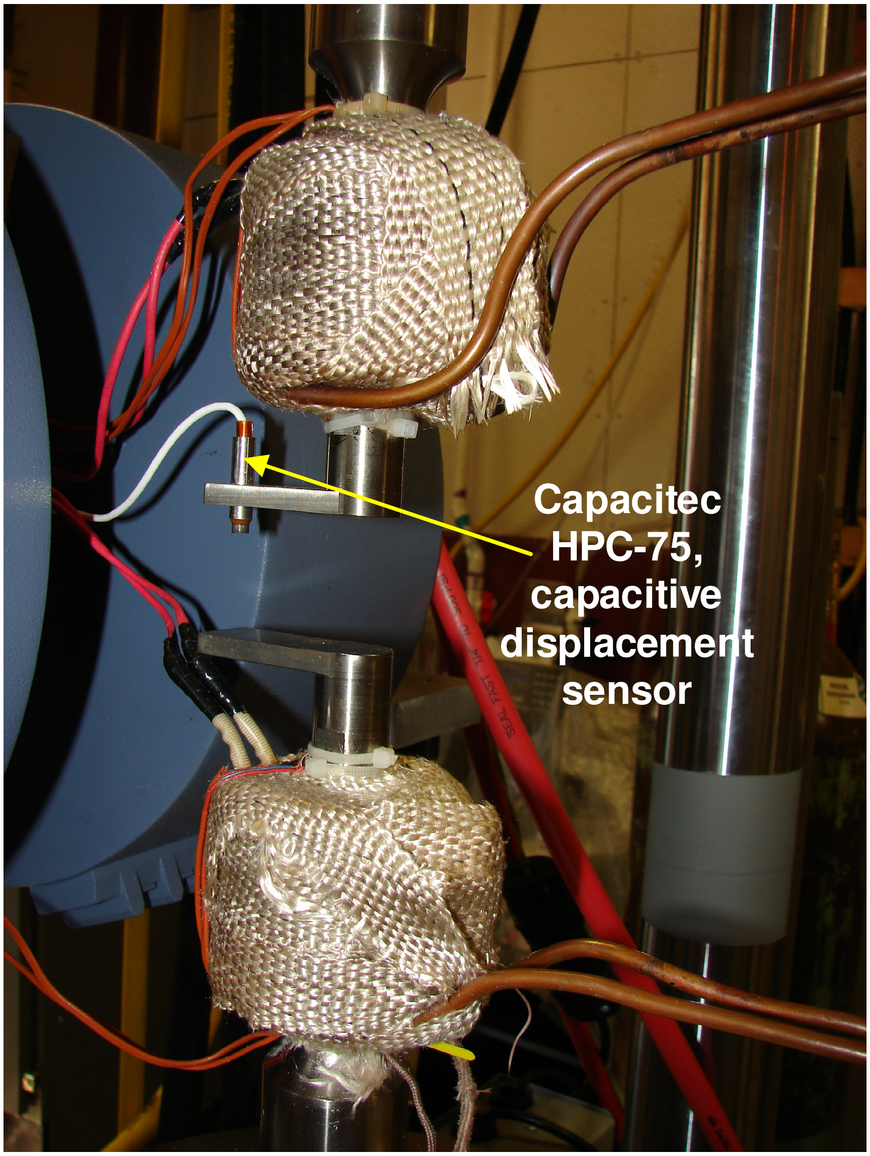

Figure II.13. The capacitive displacement sensor attached to the grip head.

II.2.2 Experiments Conducted by Means of the Macroscopic MTM System

The macroscopic MTM system has been in service since early 2005 to investigate the conventional and magnetic SM behaviors of various MSMAs such as single crystalline NiMnGa, NiFeGa, CoNiGa, CoNiAl, NiFeGaCo, NiMnCoIn and polycrystalline NiMnCoAl and NiMnCoSn. All of the possible experiments which can be carried out by the macro MTM system are tabulated in Table II.1. Isobaric thermal cycling tests and isothermal pseudoelasticity tests, with/without magnetic field, are the most general two experiments. During thermal cycling and pseudoelasticity tests, the experimental data recorded includes actual time, MTS actuator displacement, force, capacitive sensor displacement, temperatures from both grips and the specimen and amplitude of applied magnetic field (Figure II.14).

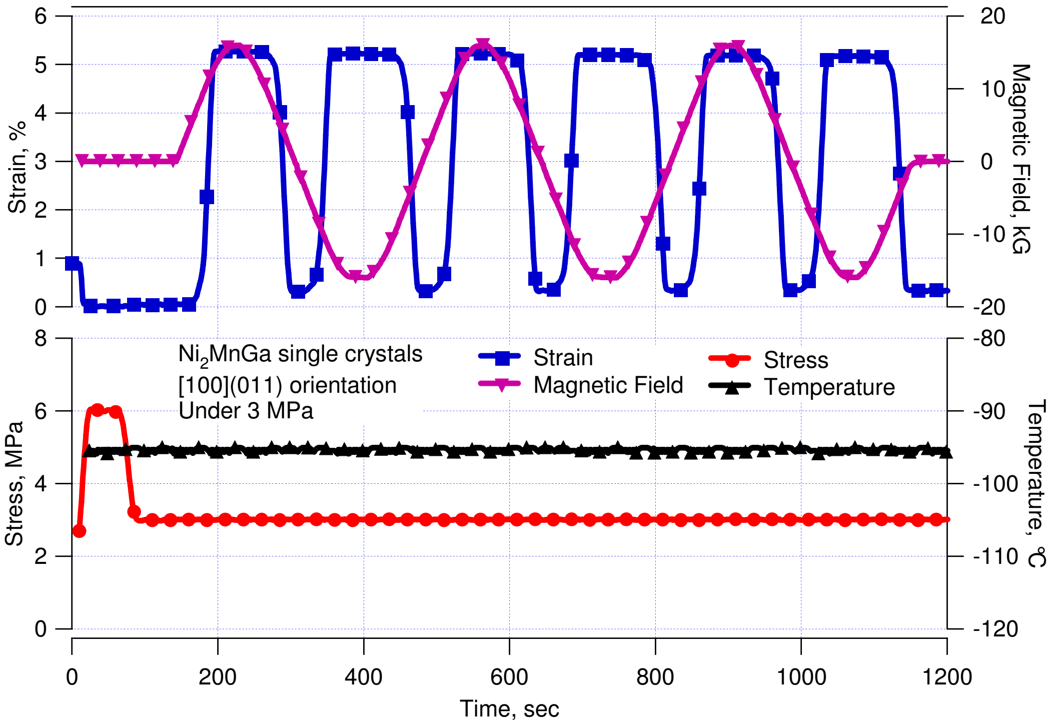

Figure II.14. A plot of the representative data obtained during the magneto-thermo-mechanical experiments by macroscopic MTM testing system.

For thermal cycling tests, the externally applied compressive stress is held constant, while the temperature is cycled at a constant rate of 10 °C/min. For pseudoelasticity tests, the temperature is held constant while the sample is loaded under displacement control at a strain rate of 0.004 mm/s and unloaded under force control at a rate of 25 N/s.

In all of the experiments conducted, a non-magnetic T-type thermocouple is attached to the outer surface of the specimen by wrapping with multithreaded nonmagnetic Cu wires. This thermocouple provides specimen temperature feedback to the Hotmux system for data logging purposes, as mentioned in the previous section in detail.

Figure II.15 shows a schematic representation of the typical experiment layout for the compression tests under magnetic field via macro MTM system. Note that the direction of applied stress and magnetic field are perpendicular to each other.

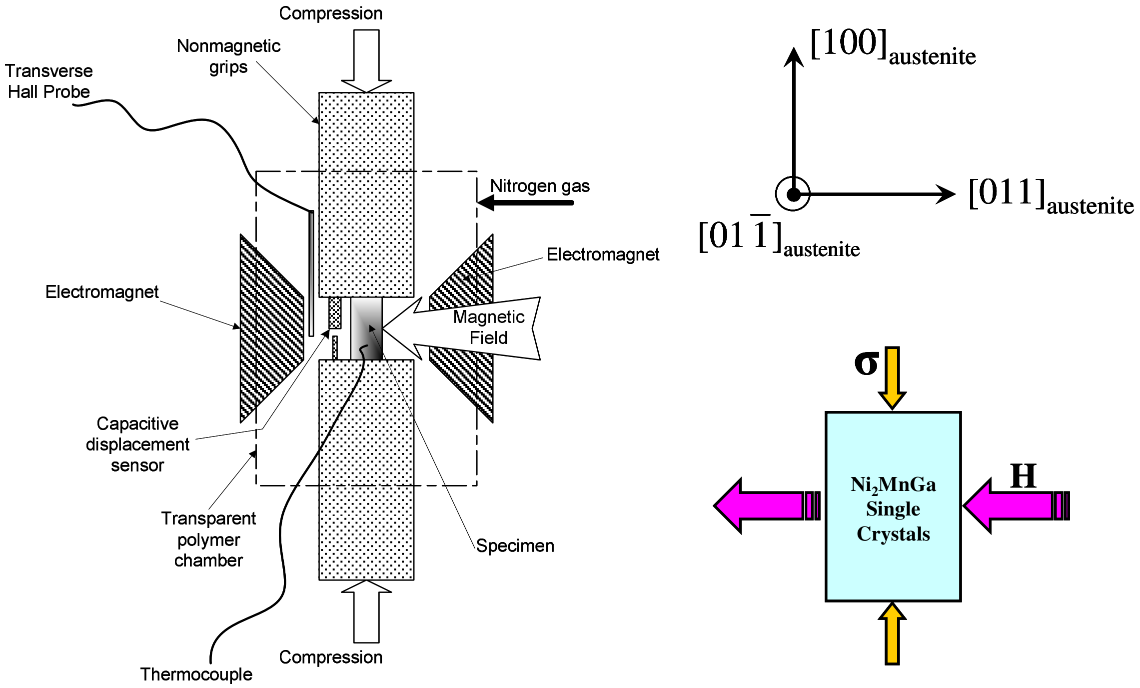

Figure II.15. The typical experiment layout for the compression tests (isobaric thermal cycling and isothermal pseudoelasticity) under magnetic field via macro MTM system.

Table II.1. Text matrix showing the possible experiments that could be performed using the macroscopic magneto-thermo-mechanical testing system and their targeted outputs. MFI: magnetic field induced, MFIPT: magnetic field induced phase transformation, VR: variant reorientation, σ: stress, H: magnetic field, ε: Strain, T: temperature, Ms: martensite start temperature, Mf: martensite finish temperature, As: austenite start temperature, Af: austenite finish temperature, PE: Pseudoelasticity.

	Temp	**σ**	**H**	**ε**	**T**	**done**	**Target Output**
1	$<M_f$ or $<A_s$	Fixed	Variable	Measured	Fixed	Yes	Butterfly curves
2	$<M_f$ or $<A_s$	Variable	Fixed	Measured	Fixed	Yes	Magnetoelastic response
3	$<M_f$ or $<A_s$	Fixed	Variable $f(\acute{R})$	Measured	Fixed	Yes	Magnetic Field Rate Effect
4	$<M_f$ or $<A_s$	Measured	Variable	Fixed	Fixed	No	Magnetostress
5	$>A_f$	Fixed	Variable	Measured	Fixed	Yes	MFI phase transformation
6	$>A_f$	Variable	Fixed	Measured	Fixed	Yes	Effect of H on PE Curves
7	$>A_f$	Measured	Variable	Fixed	Fixed	No	Magnetostress
8		Fixed	Fixed	Measured	Variable	No	Magnetic Field vs. T and Stress vs. T Phase Diagrams
9	$>A_f$	Variable	Fixed	Incremental	Fixed	No	Effect of Strain on Hysteresis (mechanical training)
10	$M_s<T<A_f$	Variable	Fixed	Measured	Fixed	Yes	MFIPT VR

II.2.3 Magneto-Thermo-Mechanical Microscopic Testing System

The second system designed and manufactured is the ***microscopic-magneto-thermo-mechanical testing system*** (micro MTM), shown as in Figures II.16 and II.17.

This gadget consists of a precipitation hardened nonmagnetic Cu-Be body and inner components (refer to figure on page 70 for details). It is meant to apply compressive stress on a 2x2x4 mm^3 specimen by means of SS302 type Belleville springs so that the level of stress remains nearly constant during phase transformation. A 0.5 mm pitch screw mechanism is driven by an amount of displacement which corresponds to the desired stress level to be applied on the specimen as acquired from compression calibration tests on the springs. The micro MTM system was designed to harbor a custom made miniature (OD 3mm) capacitive sensor, Capacitec model HPC40-27601(L3-15') (Figure II.17a), to directly measure transformation strains during magnetic field induced phase transformation (FIPT) of NiMnCoIn alloys.

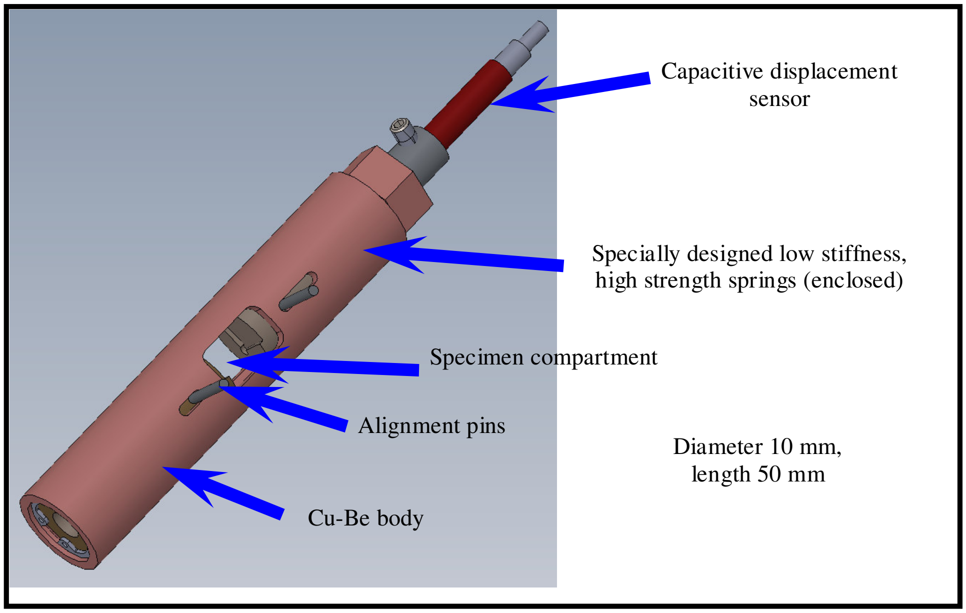

Figure II.16. 3D CAD model of micro MTM system, and its integrated 3mm diameter miniature-capacitive-displacement-sensor. This assembly was exclusively built to fit in the 18 Tesla extraction type magnetometer.

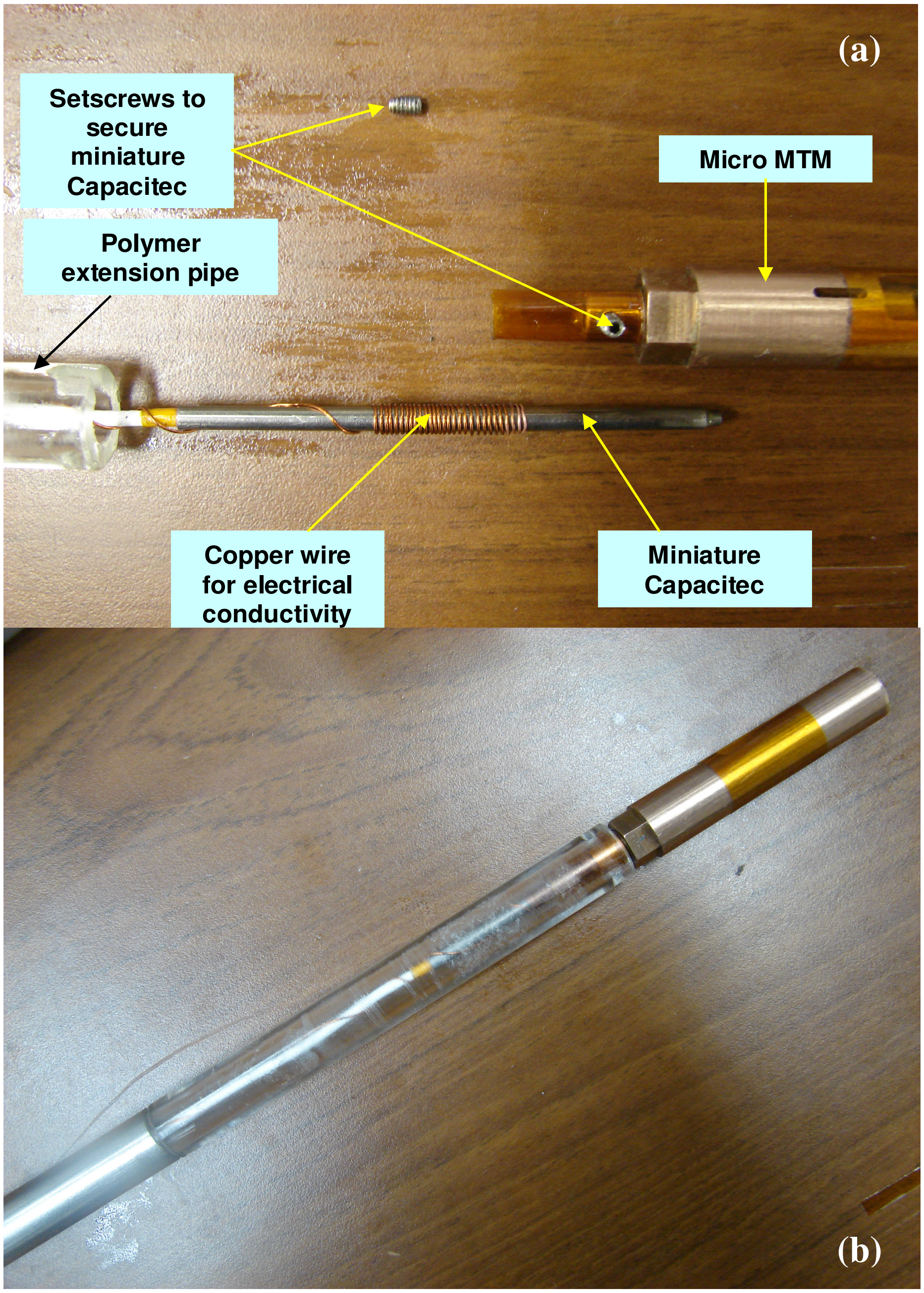

Figure II.17. (a) Micro MTM and its miniature-capacitive-displacement-sensor. (b) Displacement sensor is set inside the micro MTM and the micro MTM is secured to the extraction train of the 18 Tesla magnetometer.

This whole system (Figure II.17b) was employed in a custom built extraction-type high-field magnetometer which is capable of magnetic fields as high as 18 Tesla shown in Figure II.18. Micro MTM system was built since the macro MTM system was not capable of reaching the high magnetic field values required for the NiMnCoIn alloy to display reversible FIPT.

Figure II.18. 18 Tesla extraction type magnetometer in High Field Laboratory for Superconducting Materials, Institute for Materials Research, Tohoku University, Japan.

Figure II.20b shows the electronics used to log the displacement data acquired by the miniature capacitive sensor. The analog signal conditioner unit of Capacitec (not shown) is connected to an HP high sensitive voltmeter via the A/D converter. Then, the converted digital signal (in volts) is processed by the LabView software in the laptop computer and logged as displacement data. The same software is also capable of simultaneous logging of change in magnetic field by means of an extra connection between the laptop and the computer that governs the magnetometer.

The 18 Tesla magnetometer testing system consists of the following major components:

1) 18 Tesla field capable superconducting magnet (Figure II.18),
2) PID controlled DC power supply to govern the applied field,
3) Stepper motor to stimulate the extraction train up and down so that the specimen oscillates between a pair of pickup coils in the magnetic field (Figure II.18),
5) Auxiliary electronic units (stepper motor controller, A/D signal converter, specimen temperature controller, gain control for the pickup coils, Figure II.20a),
6 Computer to run the control software of the system and for magnetization/magnetic field data logging (Figure II.20a).

A detailed discussion regarding the working principles, components and functional features of the magnetometer can be found elsewhere [71, 72].

Once the compression specimen is put under the desired level of compressive stress, the miniature Capacitec is set inside the micro MTM at an optimum distance from the Cu-Be plunger that bears the specimen (displacement referencing) and secured by the setscrews. Then, the micro MTM is retrofitted into the polymer extension at the end of the stainless steel pipe, which altogether constitute the extraction train of the 18 Tesla magnetometer. Having the end that has the micro MTM go first, this long assembly is inserted through the guide piping and immersed into the liquid He filled well which also harbors the 18 Tesla capable superconducting magnet. Next, the portion of the extraction train (the stainless steel pipe) that extrudes out of the guide piping is linked to the stepper motor so that the motor can drive the extraction train up and down, hence having the specimen oscillate between the pickup coils in the magnetic field. As the test specimen rests inside the micro MTM, the relative location of the specimen with respect to the reference frame of the magnetometer needs be arranged to coincide with the midpoint of the pickup coils located at the end of the guide pipe inside the well. After the referencing of specimen location, the temperature can be set to the desired level and the magnetic field is cycled at a rate of 70 mA/s (≈ 50 Gauss/s).

In order to attain the real magnetization response of the specimen, the effect of the micro MTM and the miniature displacement sensor must be excluded from the total magnetization response picked up by the coils. For this reason, a calibration routine is carried out prior to the actual magnetization vs. magnetic field (M-H) experiments. First, a nickel specimen with given weight and volume is tested and its magnetization response is recorded by the magnetometer while it is confined in a polymer specimen holder. Having achieved the pure response from the nickel specimen, next step is installing it to the micro MTM and get the combined response of both. Hence, the subtraction of nickel's response from the combined leaves us with the pure response of the micro MTM and the miniature capacitive sensor system.

II.3 Other Test Systems Used for Materials Characterization

The magnetic properties of MSMAs were determined by the Quantum Design Superconducting Quantum Interference Device (SQUID) model MPMS-XL magnetometer.

A PerkinElmer differential scanning calorimeter (DSC) was used to determine the martensitic transformation temperatures.

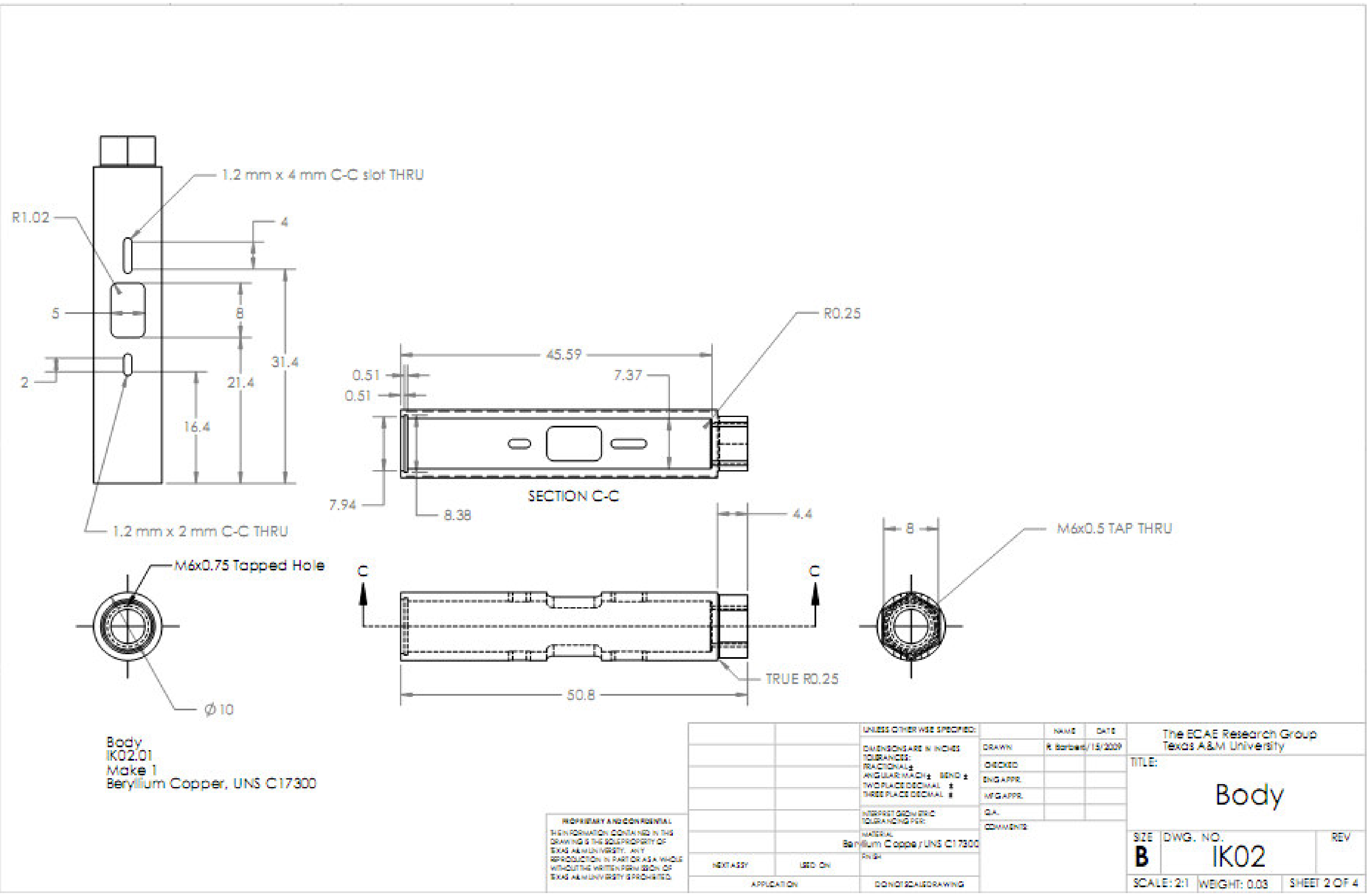

Figure II.19. CAD technical drawing of the micro MTM providing the manufacturing details.

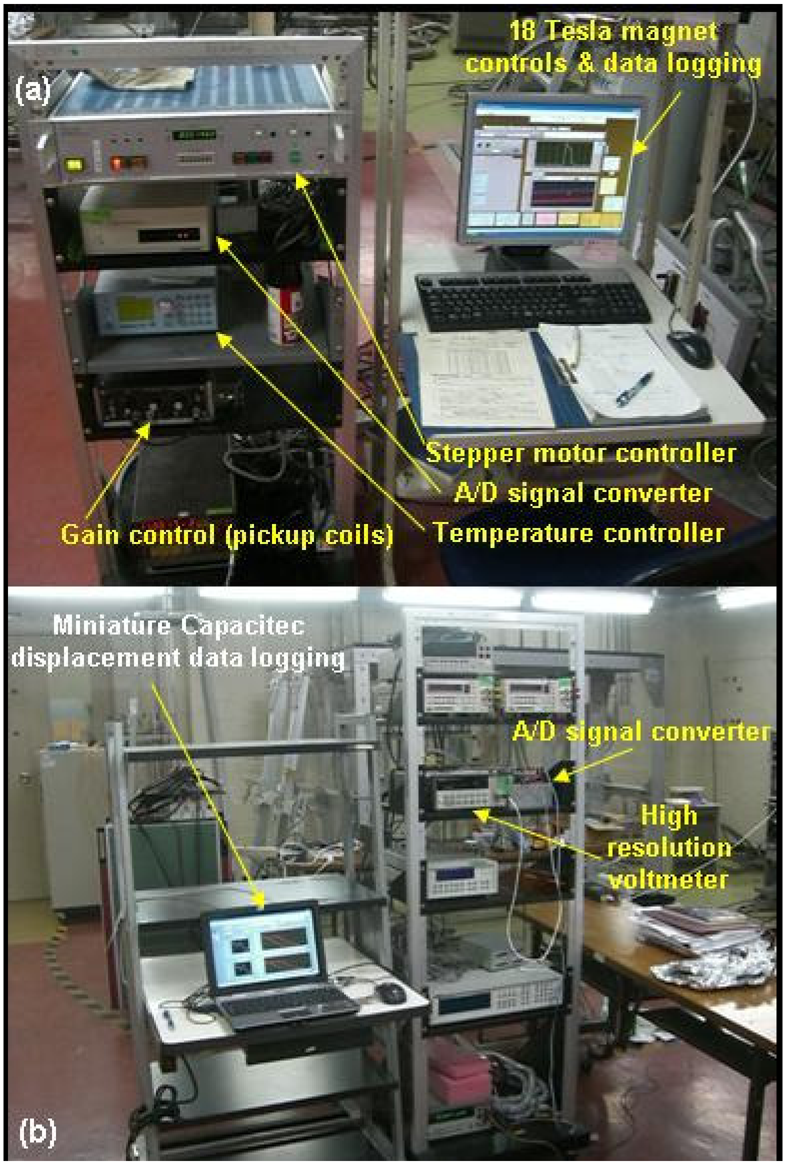

Figure II.20. (a) Electronics of 18 Tesla magnetometer for superconducting magnet and stepper motor control and data logging. (b) Electronics used for miniature Capacitec displacement data logging.

CHAPTER III

MAGNETIC FIELD-INDUCED MARTENSITE VARIANT REORIENTATION IN Ni_2MnGa MSMAs

In this chapter, the first of the two mechanisms to achieve magnetic field induced strain (MFIS), martensite variant reorientation (VR), is explained. Besides MFIS, the other two major parameters for actuation performance in MSMAs, namely; blocking stress and magnetostress are also defined. Results of magnetic field-induced strain by martensite variant reorientation under constant stress and stress-induced martensite variant reorientation under constant magnetic field tests are reported in a comparative manner with those from the literature to better understand the effect of alloy composition and test temperature on the magneto-thermo-mechanical response of NiMnGa MSMAs, including workout put.

III.1 Magnetic Field-Induced Variant Reorientation

Rearrangement of martensite variants or detwinning by the application of magnetic field is the most common mechanism in MSMAs yielding magnetic field induced strain [19, 73-75]. Due to their low detwinning stress and high magnetocrystalline anisotropy energy, NiMnGa alloys attracted quite an attention [74, 76] as compared to other MSMAs among which are FePt [77], FePd [73, 78], CoNiAl [79-81], CoNiGa [82], CoNi [83], NiFeGa [84, 85], NiFeGaCo [86].

Unless there is an external magnetic field, magnetization direction of magnetic domains tend to remain parallel to the easy axis of magnetization in NiMnGa MSMAs. However, upon application of a field along a direction other than the easy axis, the domains will have their magnetization directions rotate from their easy axis towards the direction of the applied field. Magnetocrystalline anisotropy energy (MAE) is defined as the energy required for the magnetization rotation from the easy axis to the applied field.

In MSMAs, provided the MAE is higher than the energy needed for detwinning to occur, the field-induced variant reorientation can take place. As a consequence, the variant with its easy axis of magnetization parallel to the direction of the applied field is favored and it grows at the expense of the other variants, resulting in a net shape change which is termed as magnetic field-induced strain (MFIS) [75].

A schematic representation of field induced variant reorientation mechanisms in MSMAs is presented in Figure III.1a.

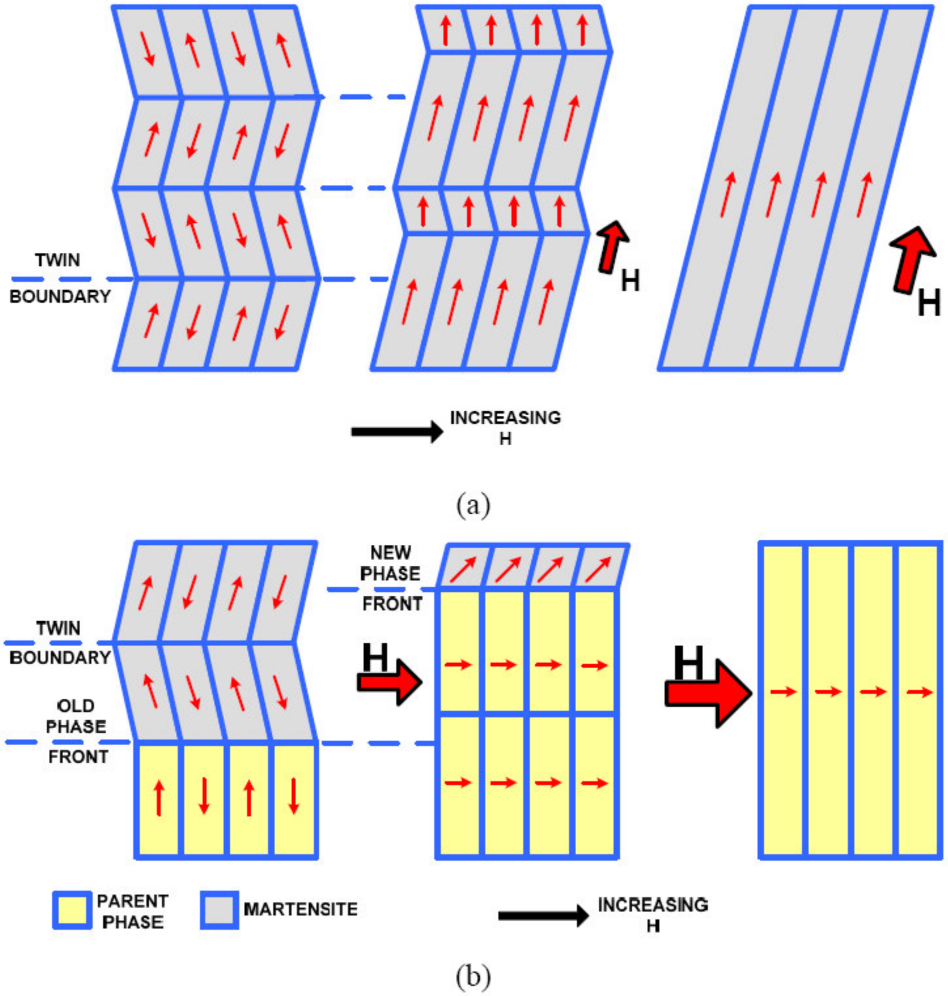

Figure III.1 Schematic representation of effect of applied magnetic field, H, (a) on the reorientation of the martensite twin variants and (b) on phase transformation in MSMAs [87].

With the application of an increasing magnetic field, assuming the MAE is higher than the energy needed for detwinning; twin motion occurs instead of the competing magnetization rotation, so that the magnetization directions of the domains arrange themselves to be parallel with the magnetic field direction.

Let's assume that our martensite has a tetragonal crystal structure with its easy magnetization axis parallel to its shorter c-axis. As a result of the twin motion (i.e., detwinning) external shape change occurs and the microstructural product is a single variant of martensite, magnetization direction of which is parallel with applied magnetic field, provided that the applied field strength is sufficiently high. In a single crystalline NiMnGa specimen, maximum MFIS can be attained if the reorientation takes place between a single martensite variant with its c-axis parallel to the application direction of compressive stress and another single variant with its c-axis along the application direction of the magnetic field, where the field and stress are applied perpendicular to each other.

Besides MFIS, two other major parameters can be mentioned as figures of merit in MSMAs:

a) Blocking stress (a.k.a. maximum actuation stress); which can be described as the external stress level above which magnetic field-induced strain through variant reorientation is not possible.

b) Magnetostress, which can be defined as the increase in stress required for detwinning under a constant magnetic field.

In MSMAs, low blocking and magnetostress levels (<2 MPa) [88, 89] come forward as the main issues for applications where high actuation forces are required. The maximum MFIS of NiMnGa alloys reported to date is approximately 6% in 10M martensite [88, 89] and 10% in 14M martensite [90]. Provided that the stress and magnetic field are applied perpendicular to each other or alternatively the field is applied along two perpendicular axes in a plane, MFIS via variant reorientation in NiMnGa can be easily reversed upon the removal of the applied magnetic field. In literature, methodical investigations on the reversible MFIS response of NiMnGa alloys under different applied stress levels are presented [52, 88, 91]. Tickle [91] reported 2% MFIS with a blocking stress of 4-6 MPa at -18 ˚C. Murray *et al.* [88] and Heczko *et al.* [52] reported 6% MFIS with a blocking stress of 2 MPa at 25 ˚C.

III.2 Magnetization Response

The magnetization response of $Ni_{51.1}Mn_{24.0}Ga_{24.9}$ as a function of temperature under a low applied magnetic field of 200 Gauss (G) is detected using SQUID magnetometer as shown in Figure III.2. Forward transformation (*A*→*M*) takes place with decreasing temperature. Upon heating, back transformation (*M*→*A*) occurs. The hysteretic form of magnetization vs. temperature is the characteristic of martensitic transformations in SMAs.

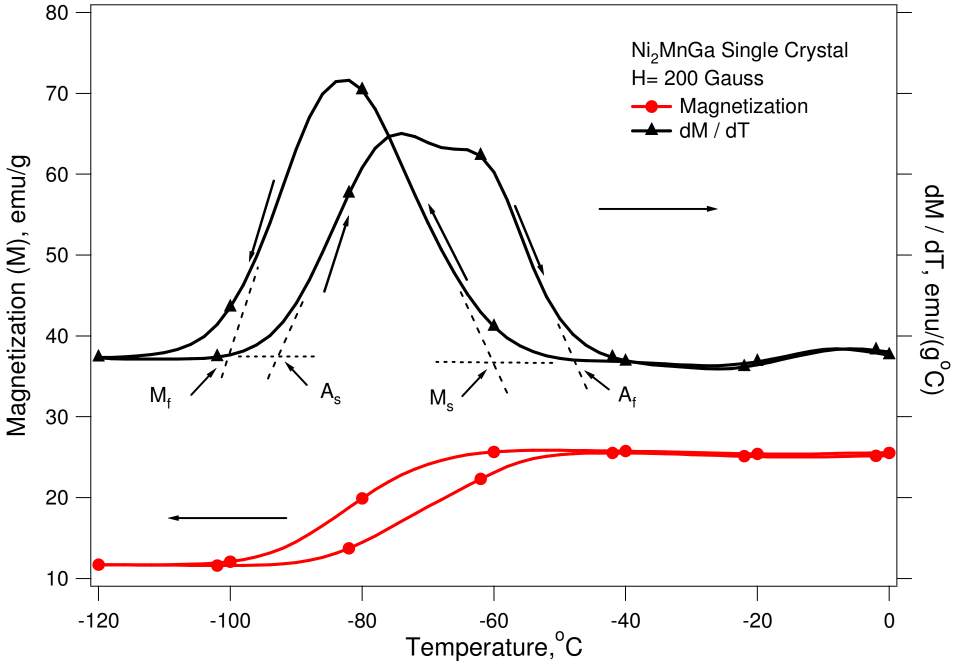

Figure III.2 Magnetization as a function of temperature under magnetic field of 200 G. Determination of transformation temperatures for the parent to I-phase to 10M transformation carried out on the derivative curve.

It is noteworthy that martensite has a higher MAE than that of austenite. Magnetization response is differentiated with respect to temperature and the resulting dM/dT curve illustrates two separate phase transformations. The first one is from parent austenite to premartensitic I-phase, represented by the petty peak at high temperature. The low temperature, sharper peaks represent the phase transformation from the I-phase to 10M martensite or vice versa.

The magnetization response of the $Ni_{51.1}Mn_{24.0}Ga_{24.9}$ single crystals as a function of temperature under various constant fields is given in Figure III.3a. As applied field is increased, the transformation start and finish temperatures also increase (under 200 G, -60 °C and -100 °C; under 10 kG at -58 °C and -88 °C).The drop in magnetization upon cooling in the courser of forward transformation (*A →M*) under low magnetic field is due to the higher magnetic anisotropy of martensite [92]. Under a higher magnetic field of 10 kG, however, the magnetization increases during the forward transformation. This increase might be because of the higher saturation magnetization of martensite than that of austenite at the same temperature. Figure III.3b shows the magnetization vs. applied magnetic field response of $Ni_{51.1}Mn_{24.0}Ga_{24.9}$ single crystal, in fully austenite (at 25 ˚C) and in fully martensite (at -125 ˚C) phases. As clearly seen, saturation magnetization and critical field values to reach saturation magnetization are higher for martensite than those of austenite because of the low test temperature and high MAE of martensite. The arrows in the figure may indicate start and finish of field-induced martensite reorientation, respectively.

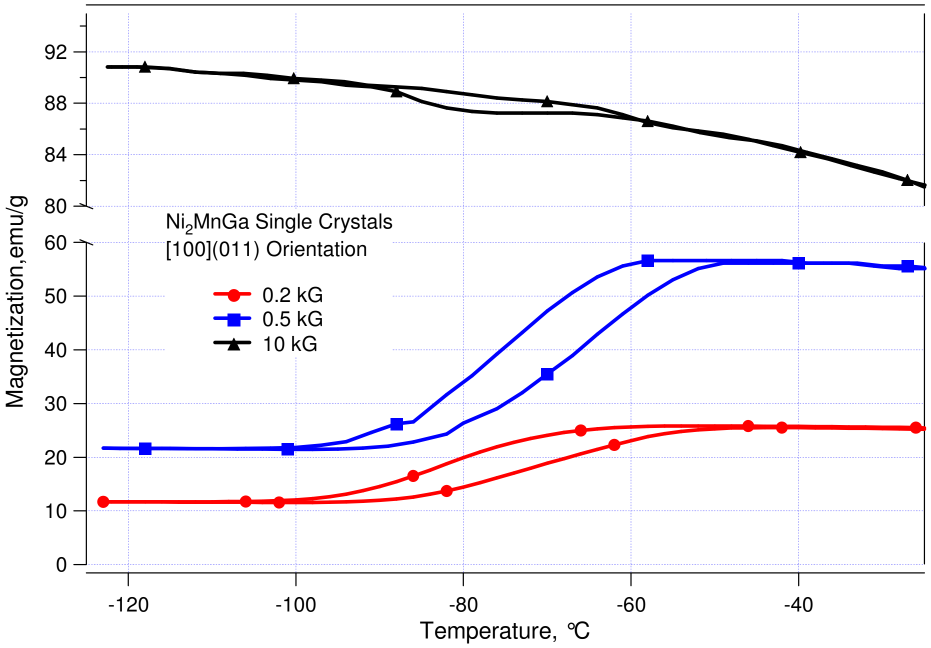

(a)

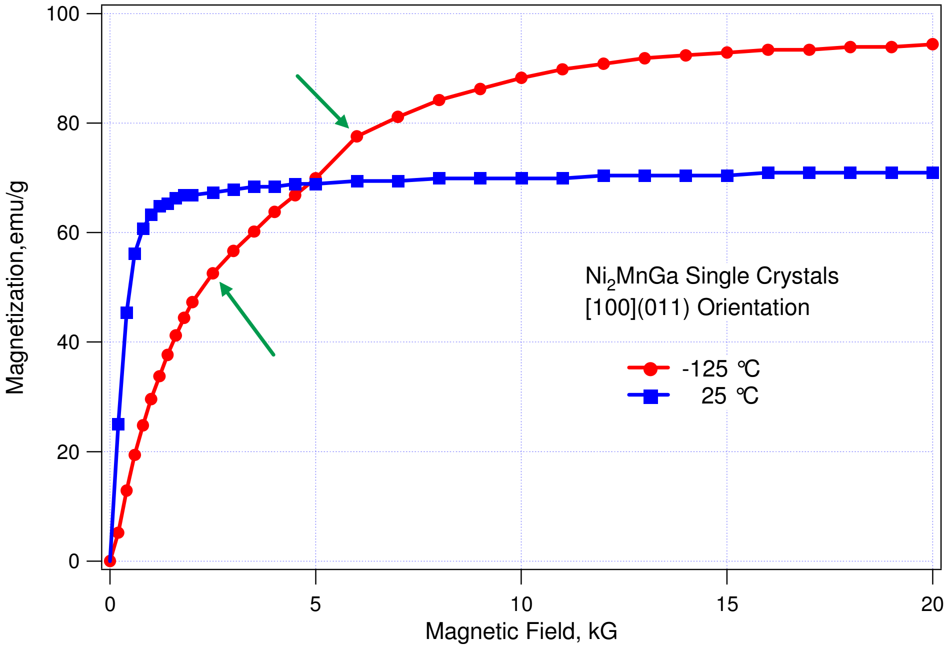

(b)

Figure III.3 (a) Magnetization response as a function of temperature under constant magnetic fields of 200 G, 500 G and 10 kG. (b) Trend in magnetization as applied magnetic field changes at -125 °C and 25 °C constant temperatures.

III.3 Conventional Shape Memory Effect in NiMnGa

Thermal cycling under stress results in the selection of certain martensitic variants and yields external strain. Figure III.4 shows cooling/heating response of a $Ni_{51.1}Mn_{24.0}Ga_{24.9}$ single crystal where 10 MPa is applied along the [100] orientation initially at 25 ˚C (fully austenite) without magnetic field. The detwinning stress of 10M martensite is relatively low, so 10 MPa is enough to form single variant of tetragonal martensite with its short c-axis along the applied compressive stress and this results in a strain of 3.8 % under 10 MPa, however, application of higher stress values do not increase the strain magnitude. From the figure, the M_S temperature is found to be around -80 ˚C while the A_S temperature is close to -67 ˚C.

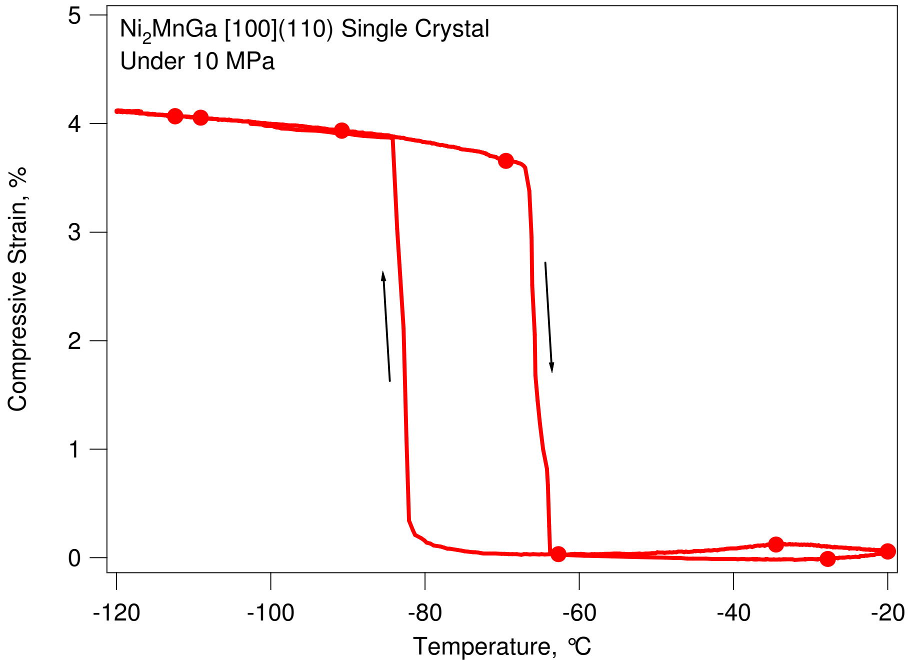

Figure III.4 Cooling/heating response of $Ni_{51.1}Mn_{24.0}Ga_{24.9}$ single crystal under a compressive load of 10 MPa along the [100] orientation.

III.4 Magnetic Field-Induced Strain via Field–Induced Martensite Variant Reorientation under Constant Stress

The evolution of MFIS in $Ni_{51.1}Mn_{24.0}Ga_{24.9}$ as a function of applied magnetic field under constant compressive stress and temperature are shown in Figures 5a and 5b. These curves are known as butterfly curves. 6 MPa bias stress was applied at room temperature while the specimen was in austenite phase and cooled under stress to obtain single variant martensite morphology and then unloaded to the desired stress level. A total of three magnetic field cycles were applied between 16 kG and -16 kG at each stress level. Subsequent to the completion of three magnetic cycles, the stress level was increased to 6 MPa to assure the sample had again stress biased single martensite variant morphology before the stress was lowered to the next test level and another set of three magnetic cycles was applied. The response under both increasing and decreasing stress levels are presented to show that there is no significant change in the strain and hysteresis trends.

In Figure III.5, there is a significant difference between the first and second cycle responses although the difference between the second and third cycles is negligible under all stress levels. This is attributed to the difficulty of nucleation of a new variant during the first cycle which vanishes with field training.

The MFIS response in the form of butterfly curves is also observed in ferroelectric crystals [93]. These curves are symmetric since the magnetic force on a twinning dislocation is insensitive to the sign of the magnetic field [94]. With increasing magnetic field, MFIS starts to evolve when a critical field value is reached and then saturates at a maximum. Increasing the field further does not make any changes on the maximum MFIS level. Applied stress level dictates the maximum MFIS level and the critical field values to start and finish the variant reorientation. As it can be observed in Figure III.5, when the applied stress level increases, MFIS decreases. This is expected since the magnetic energy provided by the applied field (MAE) needs to overcome the total mechanical energy demanded by the applied stress and the twin boundary motion. The higher the opposing mechanical energy by external stress, the lower the energy used for detwinning. Depending on the applied stress level, when the magnetic field is reduced and switched off, martensite variant favored by the field reorients back to the original variant favored by the stress. From Figure III.5b, we can see that 1 MPa is not enough for the reorientation of field biased variant back to stress biased variant in full; at least 3 MPa is needed. Therefore, the detwinning stress can be estimated between 1-3 MPa.

For each level of applied stress, the maximum MFIS for the first cycle is always greater than the one for the second cycle. The blocking stress is determined to be about 5 MPa. The irrecoverable MFIS, the MFIS difference between the first cycle and the second cycle, diminishes with stress level and vanishes completely for the stress levels of 5 MPa. It is also obvious that the critical magnetic field needed for martensite reorientation increases with stress magnitude.

The measured first and second cycle MFIS data are used to construct a maximum MFIS vs. applied stress plot shown in Figure III.6 along with previously reported MFIS levels from the literature for comparison [43, 52, 88, 91]. The highest MFIS of approximately 6.0 % was reported by Murray et al. [88], under 0.8 MPa, while in the present study the maximum MFIS of about 5.8% was measured under 1 and 2 MPa. In general, all the first cycle MFIS values decrease with increasing stress levels. This tendency holds until the blocking stress level is reached where no strain related to variant reorientation can be induced by the applied magnetic field. For the second cycle, MFIS increases from 3.2% to 4.9% in the present alloy as the stress increases from 1 MPa to 2 MPa. MFIS values under 2 and 3 MPa are the same and additional increase in stress decreases the MFIS. For stress levels higher than 4 MPa, the first and second cycle responses are almost identical. The difference in the MFIS between the first and second cycle can be due to the stress levels not being sufficient for a full reverse reorientation upon unloading the field following the first cycle. The MFIS magnitudes around 4-6 % under 2-4 MPa in our study are the highest reported so far in the literature [43, 52, 88, 91].

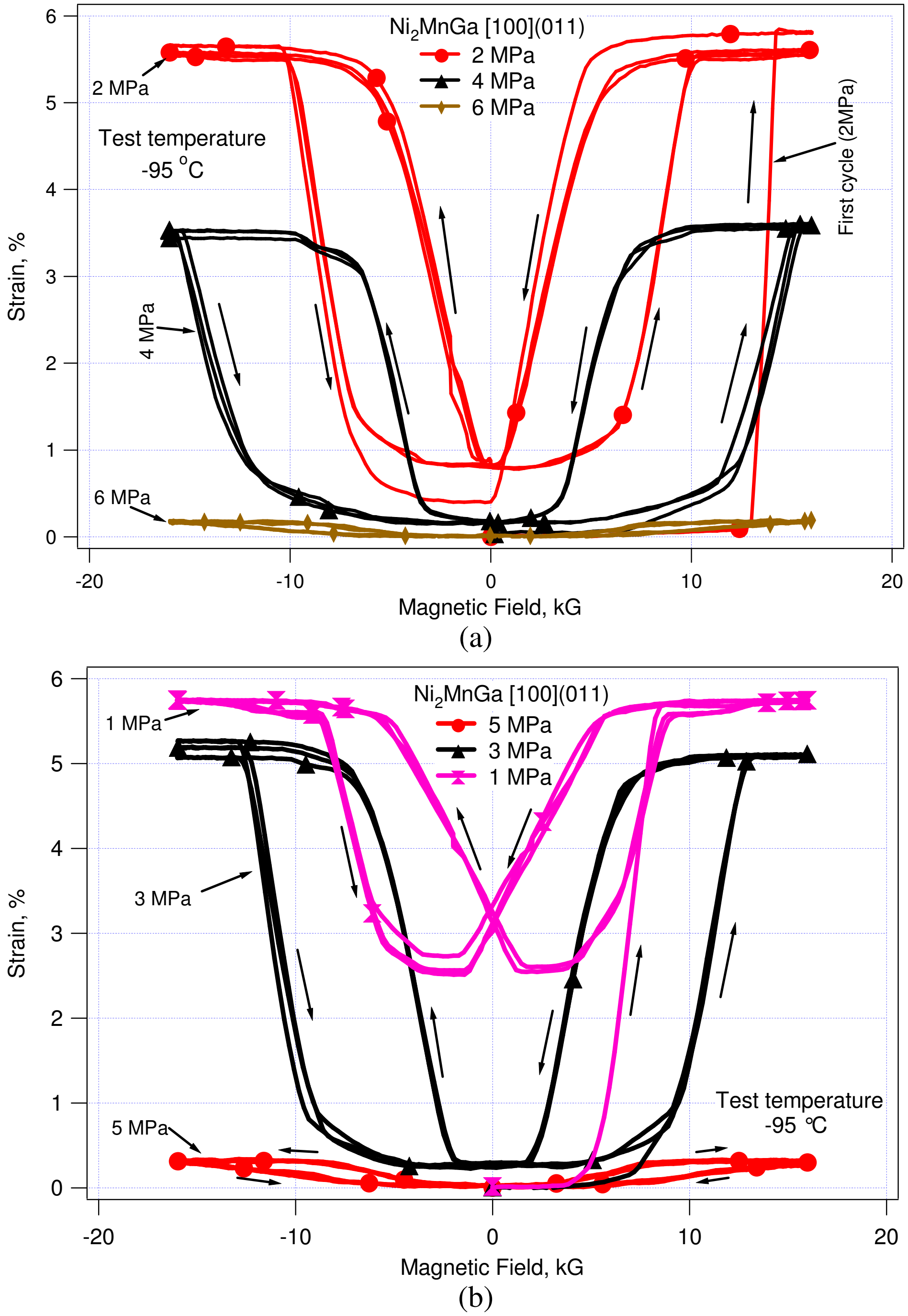

Figure III.5 Magnetic field-induced strain in the $Ni_{51.1}Mn_{24.0}Ga_{24.9}$ single crystals as a function of magnetic field under different constant compressive stress levels at -95 °C. Three cycles are shown; (a) Stress levels from 2 to 6 MPa, (b) Stress levels from 5 MPa to 1 MPa [95].

In the present study, the blocking stress is around 6 MPa where for the experiments conducted at room temperature by Murray *et al.* [88] and Heczko *et al.* [52] was reported to be around 2 MPa. The results reported by Tickle *et al.* [91] show a similar blocking stress level but the maximum MFIS of 2% is significantly lower. The blocking stress, however, cannot be easily identified, since at very low strain levels ordinary magnetostriction of MSMA materials is harder to be neglected [73, 96].

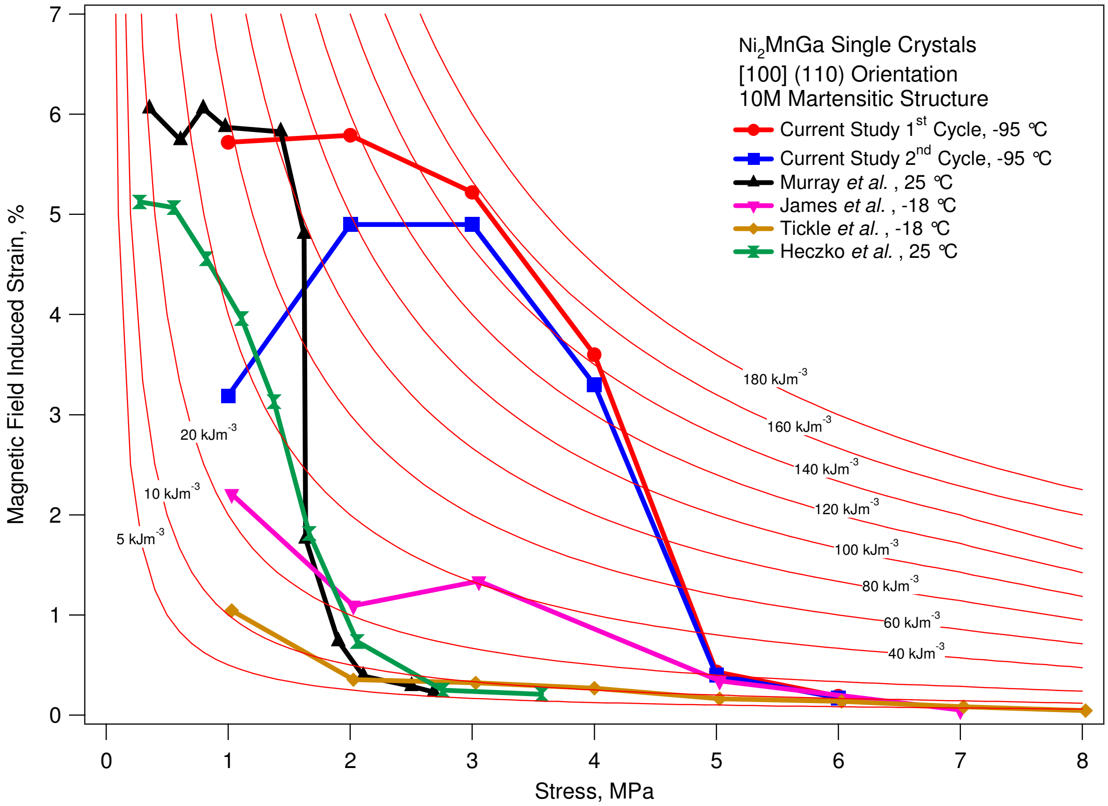

Figure III.6 Comparison of maximum MFIS as a function of stress for the current study and literature data. A grid of constant actuation work output hyperbolas ranging from 10 to 180 $\mathrm{kJm^{-3}}$ has been superimposed [97].

The aforementioned stress levels and maximum MFIS provide limited information about the actuation performance of MSMAs. Actuation work output per unit volume, $W = \sigma \times MFIS_{max}$, can be a better means of performance assessment. Here, σ is the constant applied stress during the experiment, and $MFIS_{max}$ is the maximum strain level attained at that specific stress. The actuation performances of some of the published NiMnGa MSMA compositions are given in comparison with our present results in Figure III.6 in terms of the mechanical work output per unit volume.

The maximum work output for the present composition is calculated to be 157 kJm^{-3} and 147 kJm^{-3} for the first and second cycles, respectively, showing an increase in the actuation work output of more than 100 % in the present study compared to the compositions studied by Murray *et al.* [52, 88, 91], Heczko *et al.* [52] and Tickle *et al.* [52, 88, 91]. This enhancement in performance can be related to the following: The major difference between our NiMnGa specimen and those of the prior studies in literature comes from the differences in the operating temperature (T_o) and M_S temperature. The compositions of the alloys can be slightly different; nevertheless, the saturation magnetization and Curie temperature, T_c, do not change drastically with composition in near Heusler compositions of NiMnGa [98, 99]. It is believed that detwinning stress levels are not very different as the detwinning stress in the present work is somewhat high for what has been generally reported for NiMnGa alloys. In our specimens, there is a large gap between T_c and T_o as compared to the [T_c-T_o] window in the previous studies. This brings in mind that the MAE must be significantly higher in our case. Besides, the T_o is right below M_F temperature, and thus, the detwinning stress is at its minimum possible value. Since the applied magnetic field has to overcome the externally applied stress and detwinning stress, the minimum detwinning stress maximizes the blocking stress with the available stored MAE. Being a schematic representation, Figure III.7 helps to identify the blocking stress levels for two cases with the same Curie temperature but different M_S and operating temperatures. In Figure III.7a M_S is high and T_o is chosen close to M_S so that the detwinning stress is minimized. The red curve represents the detwinning stress; it increases as temperature decreases. The blue curve represents the magnetostress which is calculated through dividing the MAE, K_u, by the transformation strain, ε_0. MAE is known to increase as temperature decreases since the saturation magnetization increases as temperature decreases [56, 57]. In this case both the [T_c -T_o] and [M_s-T_o] differences are small. This means low magnetostress, σ_{mag}, and low detwinning stress, σ_{detwin}. By definition, the blocking stress is [σ_{mag}- σ_{detwin}] and shown in the figure as the operating stress range. It is clear that, as far as (σ_{mag}> σ_{detwin}) MFIS can be obtained. Also, it is evident that with decreasing temperature the blocking stress decreases due to a more rapid increase in detwinning stress compared to that in magnetostress. Below a certain temperature MFIS cannot be obtained, therefore, only decreasing the temperature cannot improve blocking stress levels. Figure III.7b shows the schematic for a sample with the same T_c but lower M_S and T_o. In this case [T_c -T_o] difference is larger and [M_S -T_o] difference is smaller. This means a higher σ_{mag} and lower σ_{detwin}, resulting in a higher blocking stress compared to the previous case. It is important to mention the assumption that T_c was considered constant while M_S was shifted to a lower temperature. Thus, the magnetostress curve remains constant while detwinning stress curve is shifted to lower temperatures. Indeed, such change in M_S can be achieved in NiMnGa system with compositional variation without affecting T_c as T_c is not sensitive to the composition near Heusler Ni_2MnGa alloys. This approach is what we have followed and shown as a notable improvement in the actuation work output.

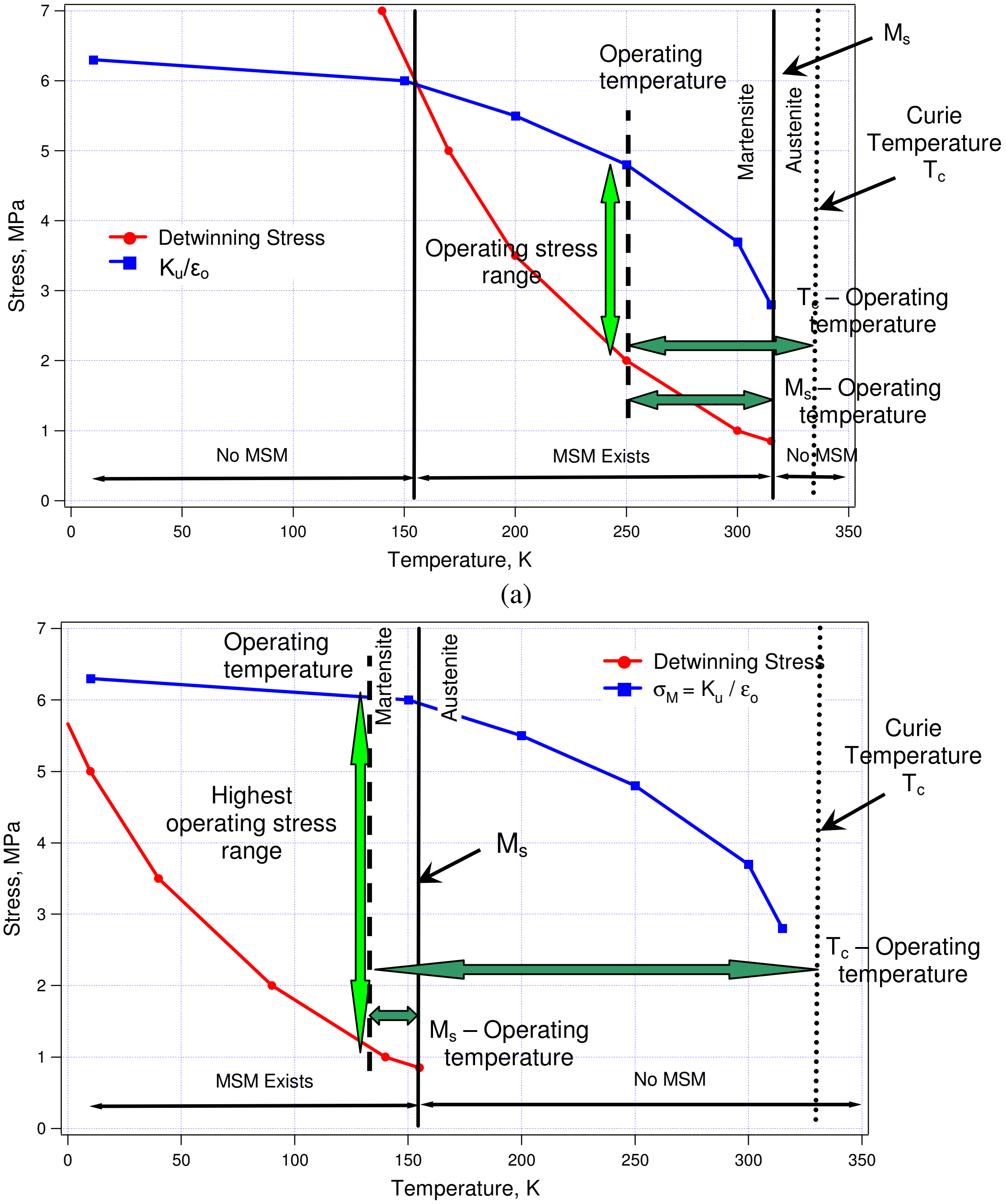

(a)

(b)

Figure III.7 Two schematics to identify the blocking stress levels for two cases with the same T_c but different M_S and operating temperatures. (a) M_S temperature is high and (b) M_S temperature is low, T_o is kept close to M_S. Stress and temperature ranges are hypothetical and not to scale.

III.5 Stress-Induced Martensite Variant Reorientation under Constant Magnetic Field

In this section, compressive stress is applied under different constantly applied magnetic fields. Figure III.8 shows the effect of magnetic field on the stress-strain behavior of martensite at -95 ºC. Prior to each experiment, single variant martensite was obtained by applying 16 kG under 1MPa as a reference. Then the magnetic field was set to the desired field magnitude and compressive stress was gradually applied to reach a maximum of 14 MPa for each case. The applied magnetic field magnitude was decreased 2 kG for each successive test. For the sake of clarity only selected responses are shown in the figure. Starting strains for the 4 kG and 0 G cases are not at zero. The reason is the variant reorientation from field biased variant to stress biased variant du to 1 MPa stress kept on the sample during decreasing the magnetic field from 16 kG to 4 kG and 0 kG.

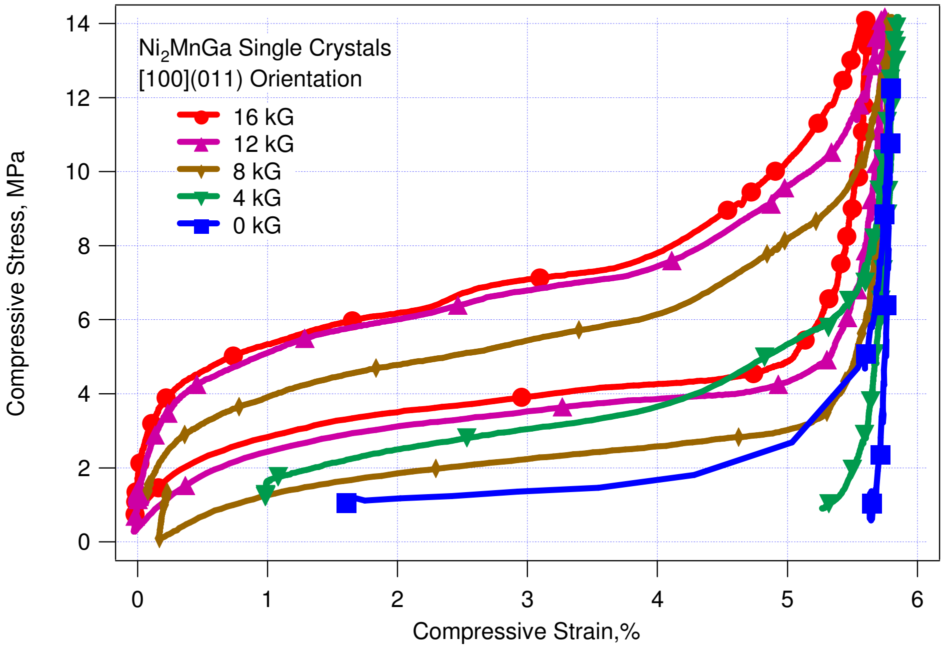

Figure III.8 The effect of magnetic field on the stress-strain response the $Ni_{51.1}Mn_{24.0}Ga_{24.9}$ single crystals during martensite reorientation. The test temperature was -95 °C [95].

In Figure III.8, upon the application of stress, the single variant martensite elastically deforms first, then the reorientation to the stress biased variant follows (plateau region) and the elastic deformation of the same variant finalizes the loop as is it starts undergoing elastic deformation.

Obviously, the applied field shifts the stress levels up. The stress-strain behavior under magnetic fields at and above 8 kG is similar to the rubber-like or pseudoelastic response of shape memory alloys. The incomplete back transformation under 4 kG and 0 kG cases are completed when a magnetic field of 16 kG is applied after unloading.

The resulting strain due to stress-induced variant reorientation (rubber-like behavior) is 5.7%. This value is almost the same as the strain magnitude obtained by magnetic field induced variant reorientation under constant stress (butterfly curves). Conforming strain levels in these different tests are an indication of complete and repeatable reorientations since the field and the applied stress competitively favor different variants with short axes along their respective applied directions. As will be discussed in the next chapter, aforementioned variant favoring by stress and magnetic field gives way to the utilization of the rubber-like behavior in Ni_2MnGa for energy harvesting applications.

Magnetostress, by definition, is the difference in the critical stress levels to start detwinning with and without magnetic field. Here, we take it as the difference in the flow stress levels with and without magnetic field at 3% applied strain.

Figure III.9 shows the magnetostress obtained from Figure III.8 where other reported MFIS levels are also included for comparison [74, 89, 100, 101]. The magnetostress increases with magnetic field up to 14 kG in our results and then saturates. The maximum magnetostress observed is 5.7 MPa.

The magnetocrystalline anisotropy energy can be determined using [101];

$$K_u = \sigma_{mag} \times \varepsilon_0 \qquad \text{(Eqn. III.1)}$$

where σ_{mag} is the magnetostress and ε_o is the reorientation strain. If ε_o is taken as 5.8 % and σ_{mag} as 5.7 MPa , K_u is calculated as 3.30 x10^5 J/m^3. Our NiMnGa single crystals have a greater MAE than what has been reported in the literature (~2.65x10^5 J/m^3) [89] supporting our explanation in section III.4 and Figure III.7. The difference in magnetostress levels between the present study and previous works is due to the high MAE originating from the low operating temperature of our single composition.

It can be inferred from Figure III.9 that magnetostress is linearly proportional to the magnetic field up to 10 kG. An empirical linear relation can be written to determine the change in stress as a function of magnetic field for MSMAs considering the MAE, reorientation strain and saturation magnetic field, as [95]:

$$\frac{\Delta\sigma_m}{\Delta H} = \frac{K_u}{\left(H^S * \varepsilon_0\right)} \qquad \text{(Eqn. III.2)}$$

where $\Delta\sigma_m$ is the change in stress with applied field (magnetostress), ΔH is the change in magnetic field and H^S is the saturation magnetic field.

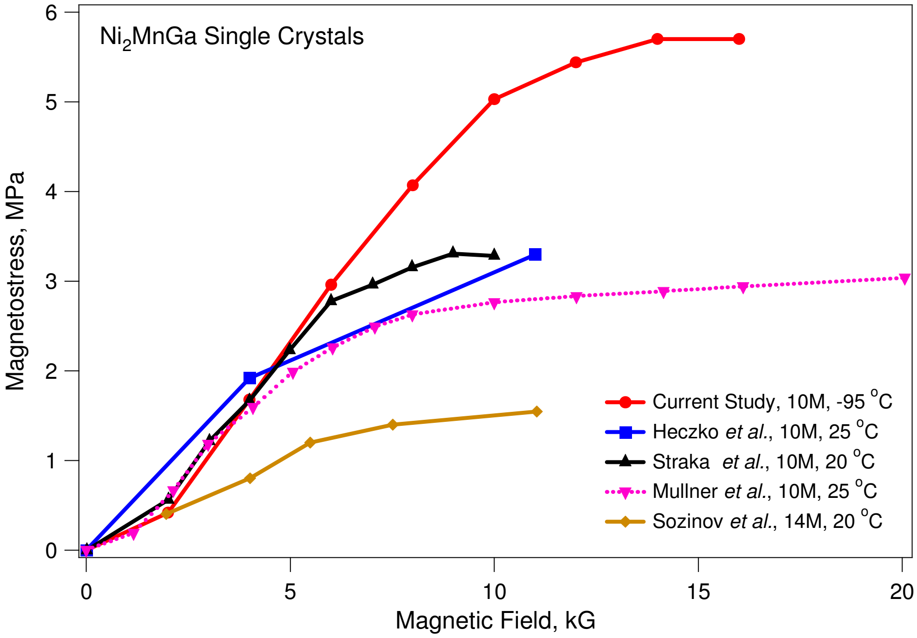

Figure III.9 Magnetostress as a function of applied magnetic field for NiMnGa single crystals with different martensite modulation [74, 89, 100, 101].

The slopes of the linear regions in Figure III.9 for all NiMnGa compositions with 10M martensitic structure is close to 0.55 MPa/kG. Additionally, the slope of the linear region in the figure for the NiMnGa single crystals with 14M martensite structure (0.23 MPa/kG) is lower than that for the 10M martensite cases which can be attributed to the higher reorientation strain of the 14M martensite (ε_0 ~ 10%, Eqn. III.2) [90]. This observation indeed indicates that there is basically no substantial difference between the present alloy and the others reported in the literature, but the difference in M_S temperatures. In our alloy, we simply take advantage of increasing K_u and H^S with decreasing temperature

CHAPTER IV

STRESS-ASSISTED FIELD-INDUCED PHASE TRANSFORMATION IN Ni_2MnGa SINGLE CRYSTALS

In this chapter, the second of the two mechanisms to achieve magnetic field induced strain (MFIS), field induced phase transformation (FIPT), is explained. The conditions to realize the cyclic magnetic field-induced phase transformation by stress assistance in NiMnGa is elaborated following the demonstration of successful test results. Using the data from pseudoelastic (PE) stress vs. strain and isobaric strain vs. temperature test results, a stress vs. temperature phase diagram is constructed to shed light on the multistage phase transformations phenomenon in NiMnGa alloys. Starting with effect of magnetic field on PE response, the required condition to achieve reversible FIPT is also identified.

IV.1 Magnetic Field-Induced Phase Transformation

In addition to magnetic field-induced martensite variant reorientation, an alternative mechanism to achieve significant MFIS is the magnetic field-induced phase transformation. This mechanism is schematically depicted in Figure III.1b; upon application or removal of the magnetic field, the phase front between martensite and austenite moves and phase transformation takes place provided the amount of the magnetic energy is adequate to drive the phase front. Iron based alloys such as Fe-C and Fe-Ni [77, 102-104] were reported to demonstrate irreversible field-induced martensitic phase transformation under very high fields (>15 Tesla), nevertheless without any report on the MFIS levels. Applied magnetic field is known to cause alterations in the temperatures, behavior and structures of the mutually transforming phases [104]. Under high pulsed magnetic fields (up to 30 Tesla) Fe-Ni-Co-Ti was found to undergo reversible field-induced martensitic transformation [77]. If the austenite is paramagnetic and the martensite is ferromagnetic, application of magnetic field can increase the transformation temperatures of NiMnGa and following this observation Cherechukin *et al.* [105] obtained irreversible MFIS by phase transformation mechanism. Realization of field-induced reversible phase transformation in NiMn(In,Sn) based alloys was reported, lately [59, 61, 62]. For this mechanism to work in these alloy systems in a reversible manner, it is necessary for the applied magnetic field to suppress the transformation temperatures to an extent that is greater than the thermal hysteresis observed without applied magnetic field [59, 61, 62]. In other words, austenite finish temperature under applied field, A_F^H , should be below martensite start temperature under zero field, M_S . However, the required magnetic field for phase transformation was reported to be more than 4 Tesla and still remains as a major obstacle in front of practical applications since the most potent permanent magnets are known to reach around 2 Tesla.

IV.2 Stress-Assisted Magnetic Field-Induced Phase Transformation in MSMAs

As a function of their chemical composition, single crystal orientation, and the test temperature, NiMnGa alloy family may display a complete or partial (up to) four stage transformation sequence:

$L2_1$ parent → Intermediate (I) → 10M tetragonal martensite → 14M orthorhombic (or monoclinic) martensite → Non-modulated 2M tetragonal martensite [106, 107].

The stress levels that come from the available magnetic energy in MSMAs are only a few MPa and they are enough to induce motion of phase front [88, 91]. The critical stresses required for stress–induced phase transformation are usually a few tens of MPa. Figure IV.1 compares the stress induced variant reorientation and phase transformation in NiMnGa single crystal via stress versus strain response at -90 and -40 °C, respectively. The prospect of inducing phase transformation via magnetic field has been overlooked due to the large difference between these two aforementioned stress levels. Only in a few studies, mechanical stress and magnetic field were applied simultaneously to induce phase transformation [108, 109] and the specimens, at first in austenitic phase, were mechanically loaded until partial stress induced martensitic transformation occurred and this was followed by application of magnetic field and hence MFIS was observed. Murray *et al.* [108] reported 0.2% strain by martensite to “ferromagnetic” austenite phase transformation under 108 MPa in polycrystalline specimens. Jeong *et al.* [109] reported 0.82% strain, which was not recovered upon the removal of the magnetic field, by “paramagnetic” austenite to martensite phase transformation under 126 MPa also in polycrystalline NiMnGa alloys. In our study, it will be shown that the applied field can result in austenite to martensite phase transformation (or vice versa), depending on the saturation magnetization, MAE and directions of applied magnetic field and compressive stress.

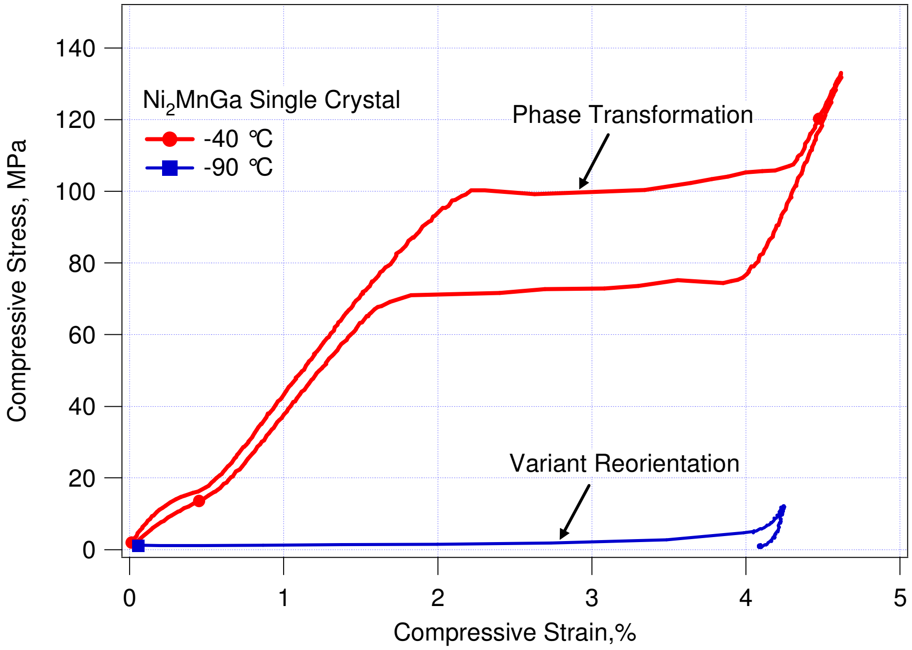

Figure IV.1 Stress-induced phase transformation and variant reorientation response of Ni_2MnGa single crystal of the present work at -40 and -90 °C, respectively.

Figure IV.2a shows the reversible phase transformation response in conventional SMAs under applied stress. The high temperature phase, austenite, transforms to martensite as temperature decreases and since a bias stress is applied, certain martensite variants are selected among others; resulting in an external macroscopic strain. Upon heating, martensite transforms back to austenite and strain is recovered fully in the absence of plastic deformation.

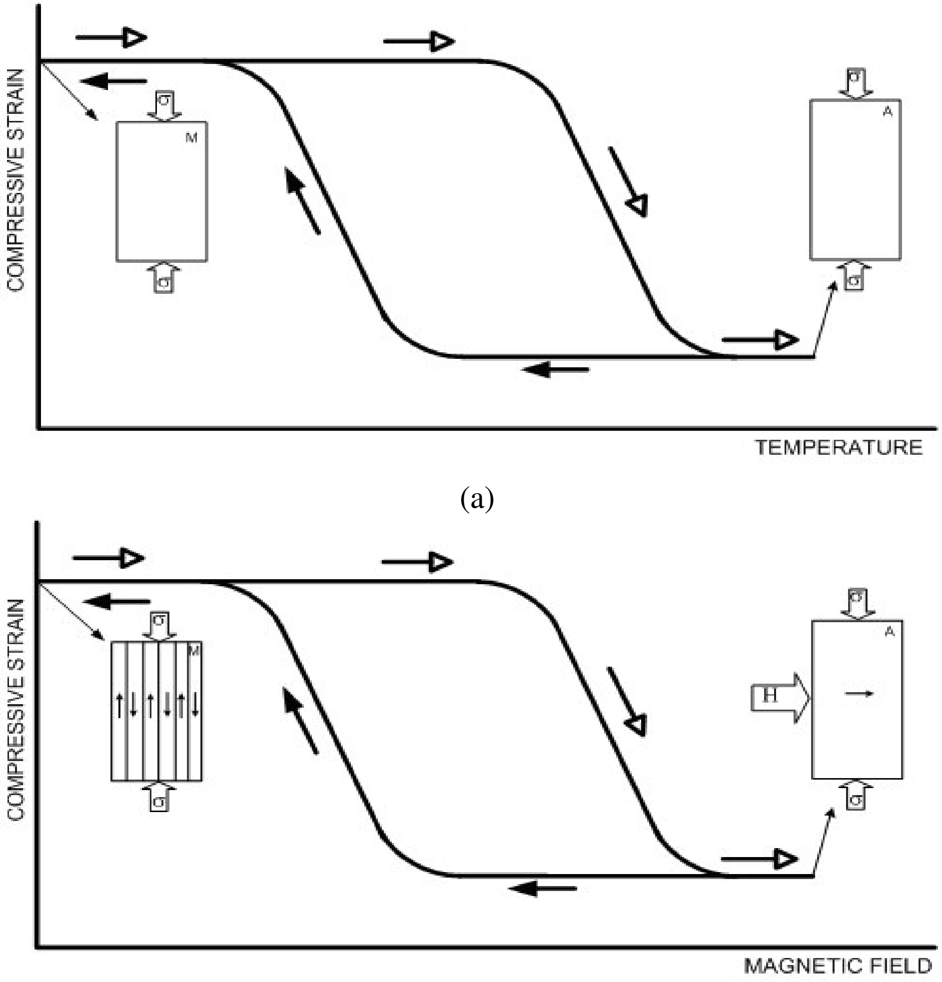

(a)

(b)

Figure IV.2 Schematics of reversible martensitic phase transformation upon cycling, (a) temperature in conventional shape memory alloys and (b) magnetic field in magnetic shape memory alloys due to field-induced phase transformation. In both cases the stress is kept constant during the phase transformation [87].

The main goal of working with MSMAs is to replace the effect of temperature on phase transformation by a magnetic field, and thus, obtain the same response under stress by variation in magnetic field, which would lead to a much faster response. Under a constant stress and temperature, phase transformation can be induced by a magnetic field in Ni_2MnGa single crystals, which results in a response as shown in Figure IV.2b. As the applied field decreases, single magnetic domain austenite transforms into multi domain martensite and vice versa. This phenomenon is termed stress-assisted field-induced phase transformation and is analogous to stress-assisted thermally-induced phase transformation as shown in Figure IV.2a.

IV.3 Pseudoelastic Response

Figure IV.3 portrays the pseudoelastic (stress vs. strain) response of the $Ni_{51.1}Mn_{24.0}Ga_{24.9}$ single crystals under compression along the [100] orientation as a function of temperature without any magnetic field applied. A two-stage martensitic transformation is observed in the course of loading within a temperature window of -70 to -40 ˚C. For this temperature interval, the initial phase is the intermediate I-phase (please refer to the magnetization results in Figure III.2). Subsequent to the elastic deformation of the I-phase, a two-stage stress-induced martensitic transformation takes place during loading. These martensitic phases fully recover upon unloading, hence leading to pseudoelasticity.

A similar stress-strain response of Ni_2MnGa single crystals was observed by Kim *et al.* [110]. The first stage was reported to be from the I-phase to an unknown martensitic phase (X-phase) and the second stage from X-phase to the 10M tetragonal martensite. The I phase is thermally induced between the parent and 10M tetragonal martensite [111]. The X-phase, on the other hand, shows up under stress only and demonstrates some peculiar behavior. Its crystallographic structure has not been revealed so far. At -80 ˚C, I-phase transforms to 10M martensite without transforming first to the X-phase (not shown in the figure).

At temperatures above -20 ˚C, the two stage transformation disappears and parent austenite (*A*) to 10M martensite take place upon mechanical loading. With increasing temperature, the critical stress for I-phase to X-phase transformation decreases whilst critical stresses for X-phase to 10M martensite and parent phase to 10M martensite both increase.

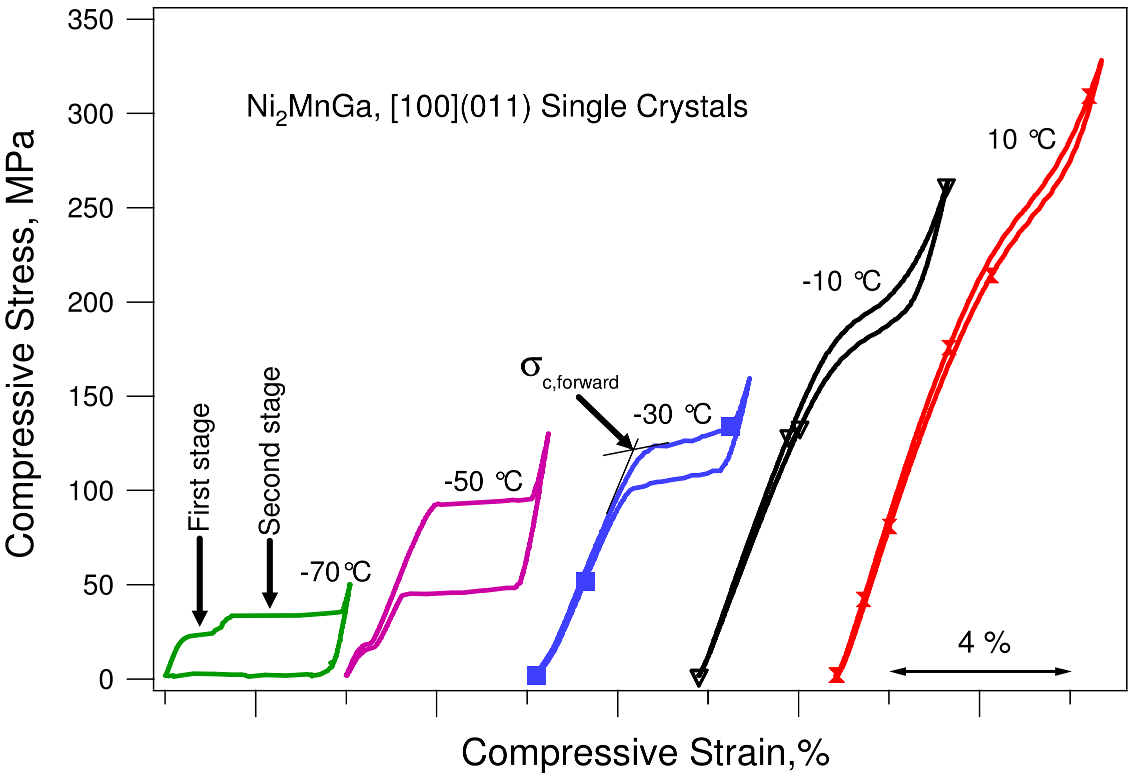

Figure IV.3 Pseudoelastic response of $Ni_{51.1}Mn_{24.0}Ga_{24.9}$ single crystals as a function of temperature under compression along the [100] orientation. The critical stress for SIM formation increases with temperature for the second stage while it decreases for the first stage [87].

IV.4 Isobaric Thermal Cycling

Thermal cycling experiments were conducted at stress levels ranging from 5 MPa up to 100 MPa to determine the phase transformation strain and temperature as a function of applied stress. It was observed that the transformation temperature for the I-phase to 10M martensite transformation increases with increasing bias stress, resulting in a positive Clausius-Clapeyron slope. The X-phase to I-phase transformation occurs at stress levels at or below 20 MPa, while the X-phase to 10M martensite transformation occurs above 25 MPa. The temperatures for X-phase to I-phase transformation decrease with increasing stress level, up to about 25 MPa resulting in a negative Clausius-Clapeyron slope. On the other hand, the transformation temperatures for parent phase to X-phase and I-phase to 10M martensite increase with increasing stress levels.

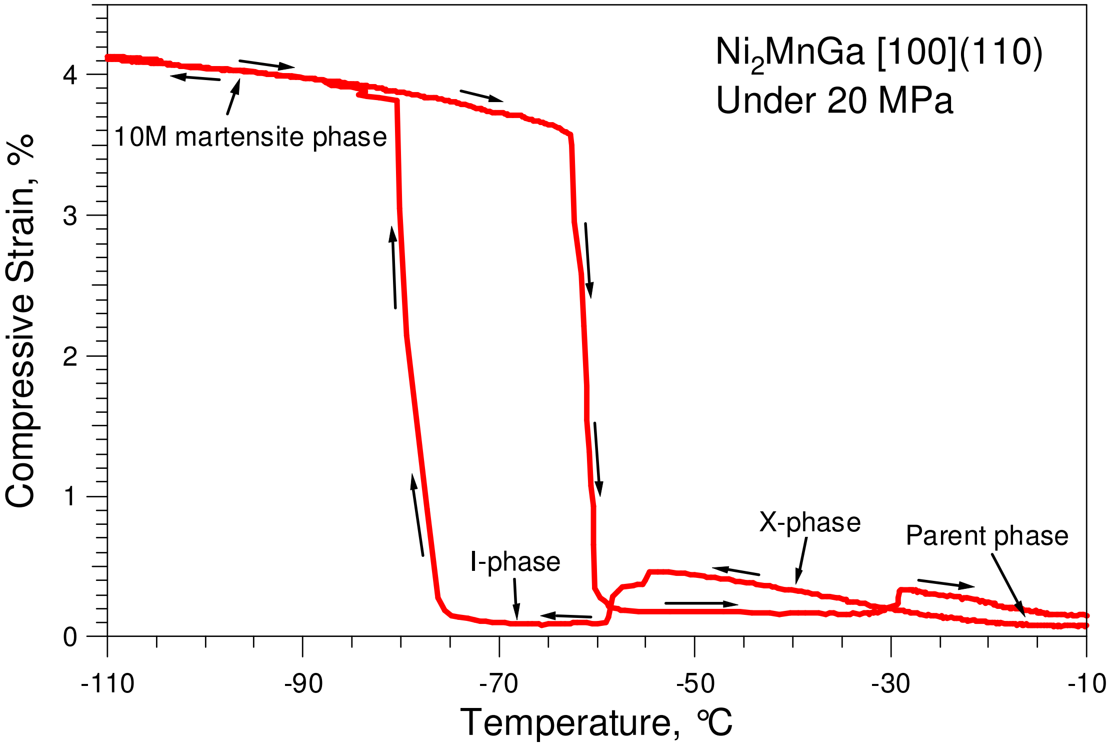

Figure IV.4 Parent phase to X-phase to I-phase to 10M martensite transformation sequence under 20 MPa compressive stress in the course of isobaric thermal cycling [112].

The multiple phase transformation sequence that occurs in $Ni_{51.1}Mn_{24.0}Ga_{24.9}$ under 20 MPa is shown in Figure IV.4 [112].Upon cooling, the specimen transforms from the parent phase to the X-phase, first. This transformation is evident by the slight increase in strain. Then, specimen transforms from the X-phase to the I-phase. However, as the specimen transforms to the I-phase, the strain obtained from the prior transformation, diminishes. This is due to the fact that the I-phase is similar in structure to the parent phase, thus the X-phase to I-phase transformation results in a tensile strain. At last, when the level of cooling suffices, the specimen transforms from the I-phase to 10M martensite and gives the major transformation strain.

IV.5 Construction of Stress-Temperature Phase Diagram

By combining the results from pseudoelasticity and thermal cycling under constant stress experiments, the stress-temperature phase diagram for $Ni_{51.1}Mn_{24.0}Ga_{24.9}$ shown in Figure IV.5 is constructed. The isobaric cooling/heating experiments are used to determine the following transformation temperatures as a function of externally applied compressive stress: Martensite start (M_S), X-phase start (X_s), and the I-phase start (I_s) temperatures. Critical stress levels for phase transformation start (σ_c) are extracted from pseudoelasticity experiments as shown in Figure IV.3. All of these are compiled and combined to construct the phase diagram in Figure IV.5 which represents the Clausius-Clapeyron relationship of each phase transformation. The solid markers represent data from isobaric thermal cycling and hallow markers represent data from the pseudoelasticity experiments, respectively.

Figure IV.5 allows us to determine the stable phase for a given pair of stress and temperature. The slopes (rate of increase in the critical stress level) for the X-phase to 10M transformation and parent phase to X-phase transformation are positive; 2.0 and 8.1 MPa/°C, respectively. On the contrary, the slope for the I-phase to X-phase transformation is negative; -0.4 MPa/°C. Kim *et al.* [110] reported similar values of 2.0 MPa/°C for the X-phase to 10M and -0.25 MPa/°C for the I-phase (or parent phase) to X-phase transformations.

The transformation sequence during stress loading at a given temperature can be clearly followed by the stress-temperature phase diagram in Figure IV.5. For temperatures lower than -90 ˚C, martensite reorientation takes place in 10M martensite. I-phase transforms directly to 10M martensite for the temperature range between -90 ˚C and -70 ˚C. I phase transforms to X-phase and then 10M martensite within the temperature range of -70 ˚C to -20 ˚C. Austenite transforms to X-phase and then 10M martensite at temperatures between -20 ˚C and 0 ˚C, while at temperatures above 0 ˚C austenite transforms to 10M martensite directly.

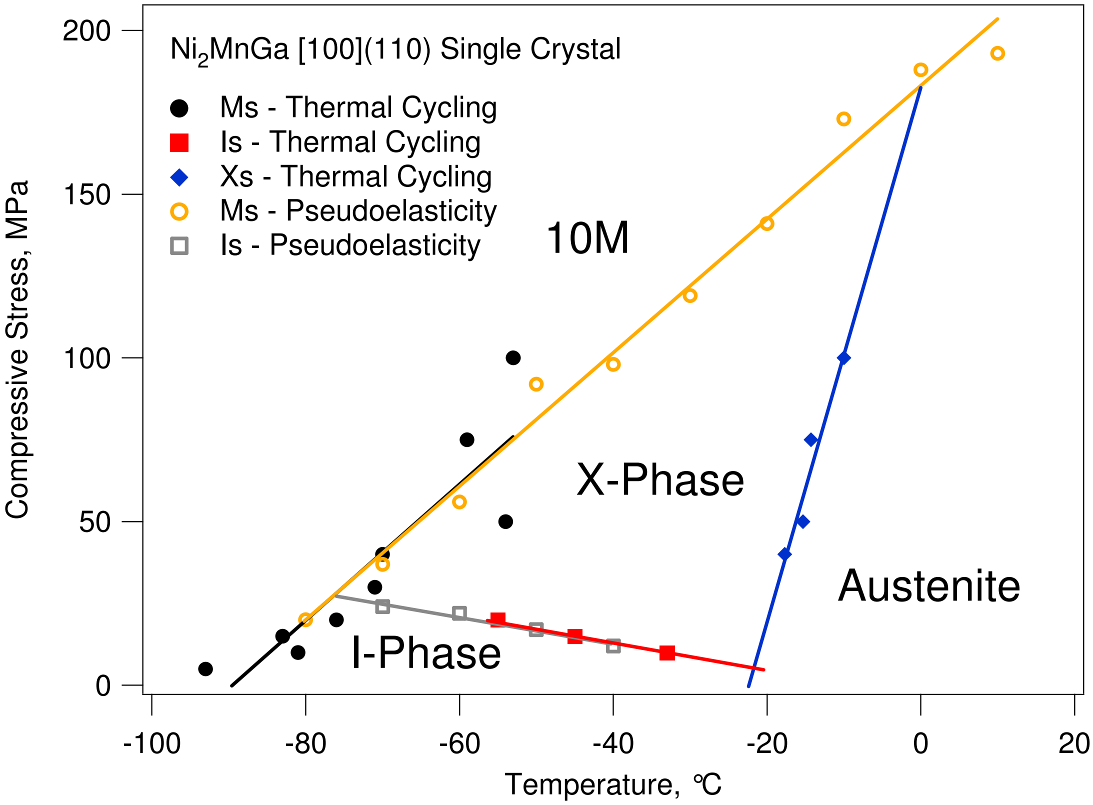

Figure IV.5 Stress-temperature diagram for $Ni_{51.1}Mn_{24.0}Ga_{24.9}$ illustrating the multiple stage phase transformations.

IV.6 Effect of Magnetic Field on Pseudoelastic Response

Figure IV.6 shows the effect of magnetic field on the pseudoelastic response at -70 ˚C. Prior to loading, the magnetic field was applied along the [011] direction, which is perpendicular to the [100] loading direction and kept constant during the test. For each subsequent stress cycle, the applied field was increased by a step of 0.1 Tesla, finally reaching 1.6 Tesla (16 kG) for the last cycle (for the sake of clarity, selected results are given in figure). When complete pseudoelasticity was not observed at this temperature (e.g., under 0, 0.2, and 0.4 Tesla), the field was increased to 1.6 Tesla following unloading in order to recover the residual strain and then reduced down to the field under which the next test was conducted.

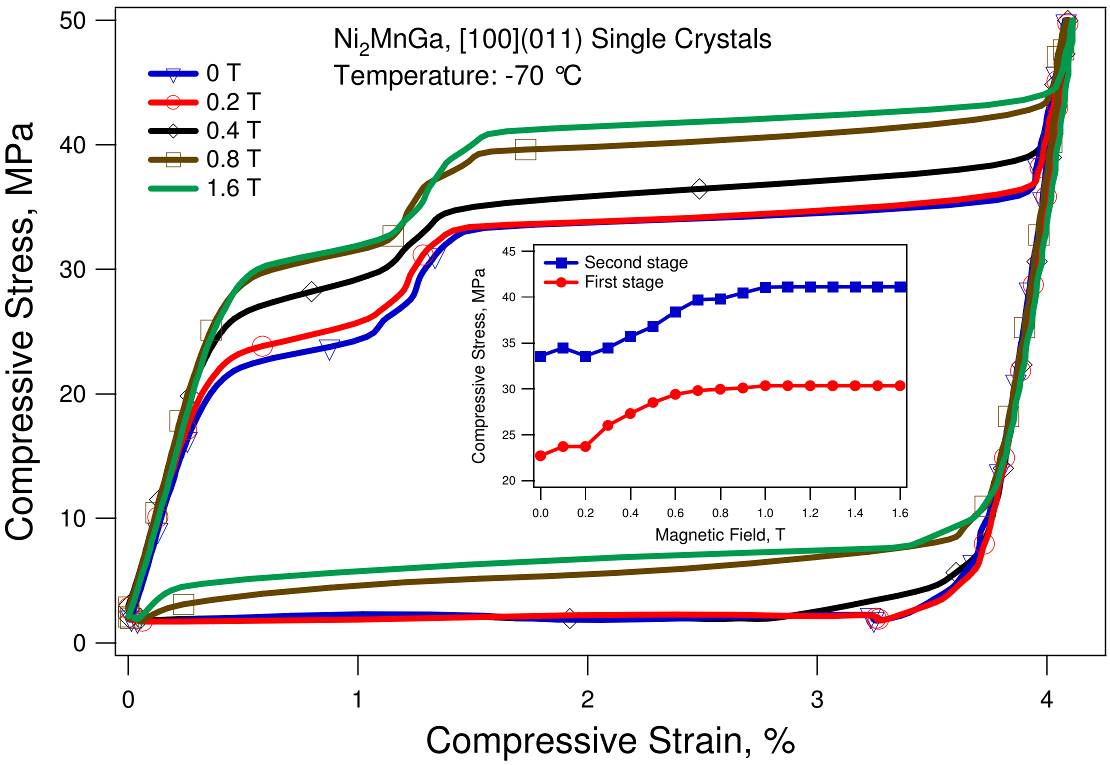

Figure IV.6 Effect of magnetic field on the pseudoelastic response of the $Ni_{51.1}Mn_{24.0}Ga_{24.9}$ single crystals at -70 ˚C. The critical stress levels for inducing the phase transformation increase with field up to a certain level and saturate at higher fields. The inset shows the change in the critical stresses with applied magnetic field for the first and second stages.

The critical stress levels for phase transformation in both first and second stages increase with the magnetic field up to a certain level and then stay constant at higher fields. The inset in the figure demonstrates the tendency of the critical stress values for phase transformation to start with applied magnetic field for the first and second stages.

Magnetostress is defined as the difference between the plateau stress levels with and without magnetic field in the pseudoelastic loops. The magnetostress levels for both the first and second stages are determined to be around 8 MPa at -70 °C. The critical stresses start increasing at magnetic fields above 0.2 Tesla and the rate of increase for the first stage is higher than that of the second stage (see inset in Figure IV.6). While the critical stress reaches saturation at 0.7 T for the first stage transformations, so does it at 1.0 T for the second stage transformations. This difference can be attributed to the dissimilar magnetization behavior along the respective hard axes of the mutually transforming phases.

Figure IV.7 shows the effect of temperature on the compressive stress-strain response of the single crystals under zero and 1.6 Tesla. Obviously, the critical stress required to induce the phase transformation is shifted to higher levels by the applied field, *i.e.* magnetic field stabilizes the initial phase (either X, I or P phases), without having a substantial effect on the stress hysteresis and the transformation strain. In Figure IV.7, for the loops without magnetic field, the critical stresses to start forward and reverse transformations are depicted by $\sigma_{\mathrm{c,forward}}$ and $\sigma_{\mathrm{c,reverse}}$, respectively, whereas $\sigma^{\mathrm{H}}_{\mathrm{c,forward}}$ and $\sigma^{\mathrm{H}}_{\mathrm{c,reverse}}$, mark the critical stresses to start forward or reverse transformations under magnetic field. The effect of magnetic field on the stress levels fades away with increasing temperature. Therefore, the magnetostress and the transformation strain both decrease with increasing temperature. At higher temperatures, the compatibility (the measure of elastic lattice mismatch between transforming phases) between the parent and product phases increases, which could result in an increase in the stress required for phase front propagation and thus, yield to nucleation of multi martensite phase fronts. The decrease in transformation strain with increasing temperature can be attributed to incomplete transformation/detwinning process under the present applied stress levels.

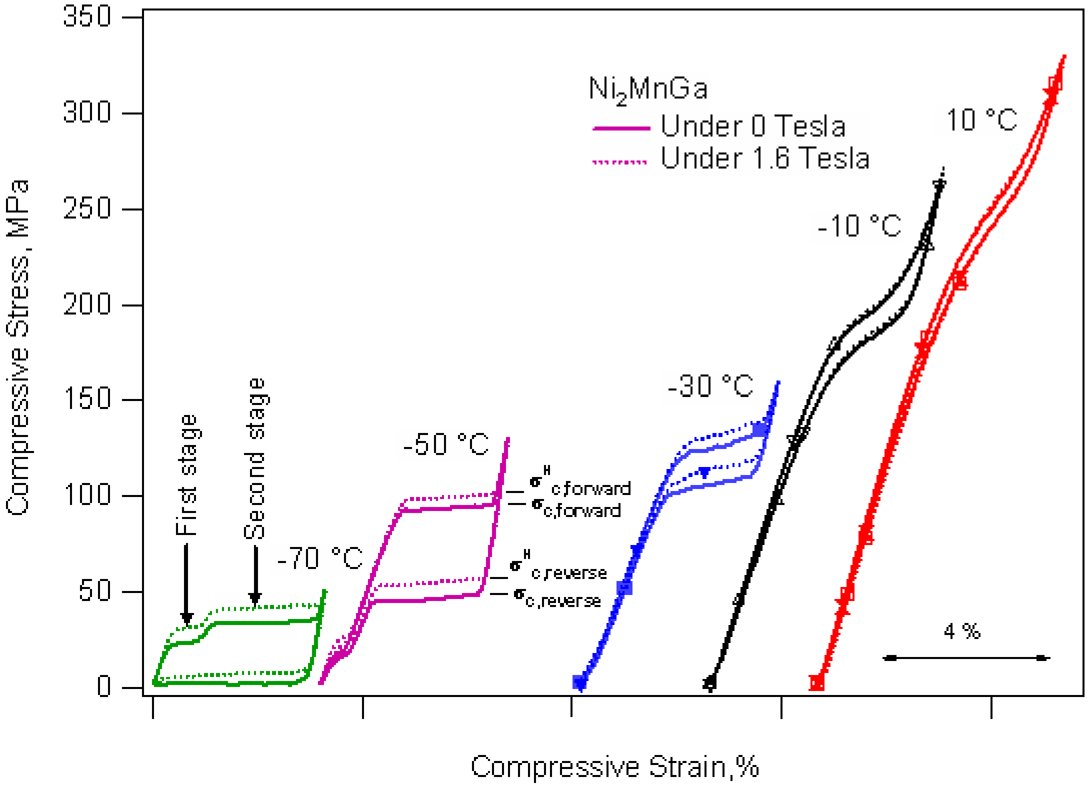

Figure IV.7 Pseudoelastic response of $Ni_{51.1}Mn_{24.0}Ga_{24.9}$ single crystals as a function of temperature and magnetic field under compression along the [100] orientation. σ_c: Critical stress at the onset of phase transformation [87].

Figure IV.8 intends to demonstrate the differences in the pseudoelastic response between the first and the second stages (at -60 °C) with and without applied magnetic field. For both stages, the applied field shifts the pseudoelastic loops to higher stress levels. When the first stage transformation is completed, upon unloading, a pseudoelastic loop with very small stress hysteresis is observed.

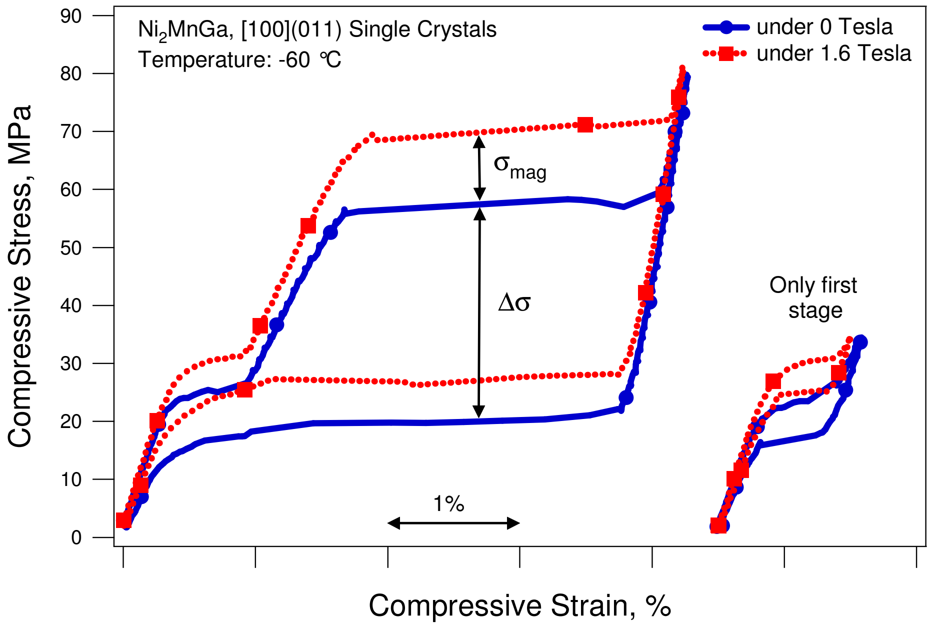

(a)

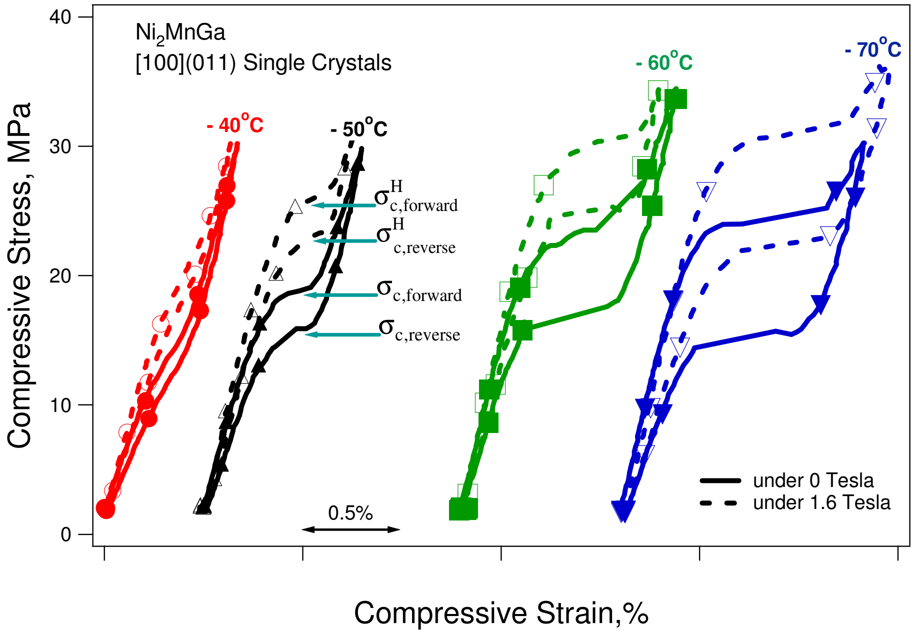

(b)

Figure IV.8 (a) Comparison of the pseudoelastic response in $Ni_{51.1}Mn_{24.0}Ga_{24.9}$ at -60 ˚C under zero (solid lines) and 1.6 T applied magnetic field (broken lines), (b) Temperature dependence of the critical stress levels and stress hysteresis during the first stage transformation only, with and without magnetic field [87].

In the first stage, the magnetic field and the resulting magnetostress are sufficient to completely separate the pseudoelastic loop with the magnetic field from the one without magnetic field (see Figure IV.8b). On the other hand, for the second stage, σ_{mag} level is not sufficient to realize a complete separation of the loops due to the large stress hysteresis (depicted by $\Delta\sigma$ in the figure). The effect of magnetic field on the first stage transformation as a function of temperature is clearly observed in Figure IV.8.b as the field separates the pseudoelastic loops in a certain temperature interval. The separation is possible whenever the magnetostress is larger than the stress hysteresis [87].

IV.7 Magnetic Field-Induced Phase Transformation during the First Stage Transformation

The full separation observed between the pseudoelastic loops of the first stage with and without magnetic field is an indication of the capability to induce reversible transformation among the aforementioned phases (refer to Figure IV.5) by switching the field on and off under constant applied stress. We call this phenomenon as stress-assisted reversible field-induced martensitic phase transformation. It can be realized by loading the single crystalline specimen under a magnetic field to a stress level which is lower than $\sigma^{\mathrm{H}}_{\mathrm{c,reverse}}$ but higher than $\sigma_{\mathrm{c,forward}}$. Upon removal of the magnetic field, forward transformation takes place since the parent phase (the I-phase in this case) is not stable at that stress level without the support of magnetic field. Following this route, the forward and reverse transformations can be induced in a cyclic manner by switching the field on and off within the stress range limited between $\sigma_{\mathrm{c,forward}}$ and $\sigma^{\mathrm{H}}_{\mathrm{c,reverse}}$.

Likewise, a magnetic field-induced reverse transformation can also be induced, provided that the crystal is loaded without magnetic field to a stress magnitude greater than $\sigma_{\mathrm{c,forward}}$ allowing forward transformation to take place. Then, this stress level is kept steady between the $\sigma^{\mathrm{H}}_{\mathrm{c,reverse}}$ and $\sigma_{\mathrm{c,forward}}$, and upon the application of the magnetic field the reverse transformation happens because the martensite (the X-phase in this case) is not stable at that stress under the applied magnetic field. Figure IV.9a demonstrates an example of this alternative mechanism. Figure IV.9b shows the MFIS vs. magnetic field response at -55 °C to better explain the alternative mechanism. Here, the specimen was loaded from point zero till the stress reached up to #1 ($>\sigma_{c,forward}$) yielding to I→X forward transformation and then unloaded to #2 ($<\sigma^{H}_{c,reverse}$) without any magnetic field applied. At #2, the stress magnitude was stabilized at 22 MPa and the magnetic field was applied, to start the reverse transformation X→I at around 0.7 Tesla in the first cycle and at 0.5 Tesla in the subsequent cycles.

Switching the field on and off continuously induces forward and reverse transformations without noteworthy modification in the critical magnetic field values (loops between #3 & #6) therefore allowing the magnetic field to do work against stress levels above 20 MPa. Due to the low transformation strain along the [100] orientation, the MFIS accompanying the I→X transformation turned out to be 0.5%. When the stress was reduced, the field necessary to trigger the forward and reverse transformations decreased, accordingly. For example, at 18 MPa (#7 in Figure IV.9), the field only induced reverse transformation at 0.2 Tesla because the stress level was smaller than $\sigma_{c,forward}$.

In addition, the critical magnetic field values to induce reverse transformation decrease with decreasing applied constant stress level. In accord with this observation, it can be inferred that under higher stress levels, magnetic field needs to provide more energy to overcome the barrier to bring phase transformation.

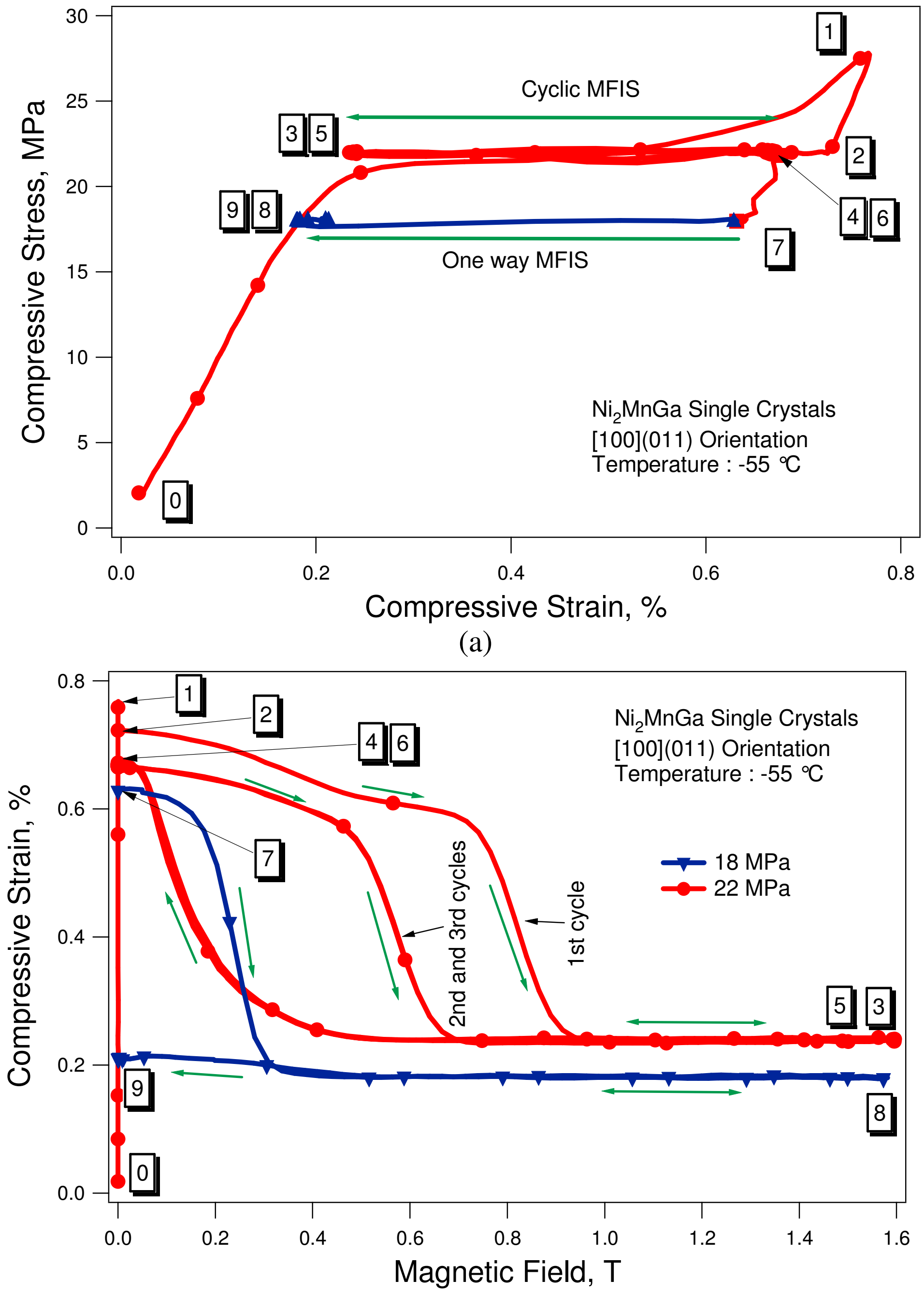

(a)

(b)

Figure IV.9 The stress-assisted reversible (cyclic) field-induced phase transformation at low field magnitudes at -55 ˚C. (a) Stress vs. Strain and (b) Strain vs. magnetic field, data presented are from the same experiment. The numbers (#) are meant to describe the loading path.

From other test results not shown here, at 18, 20 and 22 MPa applied stress, the critical magnetic field values for the reverse transformations to start are reported approximately as 0.15, 0.23 and 0.32 Tesla, respectively. The transformation strain and the critical stress levels to for the first stage transformation increase as temperature decreases, whilst the differences between $\sigma^{H}_{c,reverse}$ and $\sigma_{c,forward}$ decrease. For example, at -70 ˚C, $\sigma_{c,forward}$ is already greater than $\sigma^{H}_{c,reverse}$, therefore only allowing one-way field-induced phase transformation to be accomplished Reversible MFIS levels were found to be less than 0.1% above 26 MPa and attributed to magnetostriction or elastic strain as observed in other NiMnGa MSMAs [3]. Even though the recoverable magnetic field induced strain magnitude is relatively small compared to the phase transformation strain, it is still big enough compared to that of other magnetostrictives [3, 113].

IV.8 Magnetic Field-Induced Phase Transformation during the Second Stage Transformation

Figure IV.10a and Figure IV.10b demonstrate the stress vs. strain and strain vs. magnetic field responses during the second stage transformation, X→10M martensite, at -60 ˚C. The field-induced one way shape memory effect was accomplished by loading the sample to 64 MPa under 1.6 Tesla (depicted by #1 in figure). Here, 64 MPa was chosen since it is below $\sigma^{H}_{c,forward}$ but above $\sigma_{c,forward}$.Then, the magnetic field was taken away whereas the stress was kept constant. The forward phase transformation was observed along with a 2.4% strain (#2) as the magnetic field diminished from 0.7 to 0.5 Tesla. However, upon re-application of the magnetic field, reverse transformation was not induced at this stress level (#3). Following the forward transformation, the sample was unloaded to 24 MPa (#5) without magnetic field. Here, 24 MPa was chosen since it is between $\sigma^{H}_{c,reverse}$ and $\sigma_{c,reverse}$. Then, the magnetic field was applied and a MFIS 3.1 % (#6) was observed sourcing from the reverse transformation starting at 0.1 Tesla and ending at 0.6 Tesla.

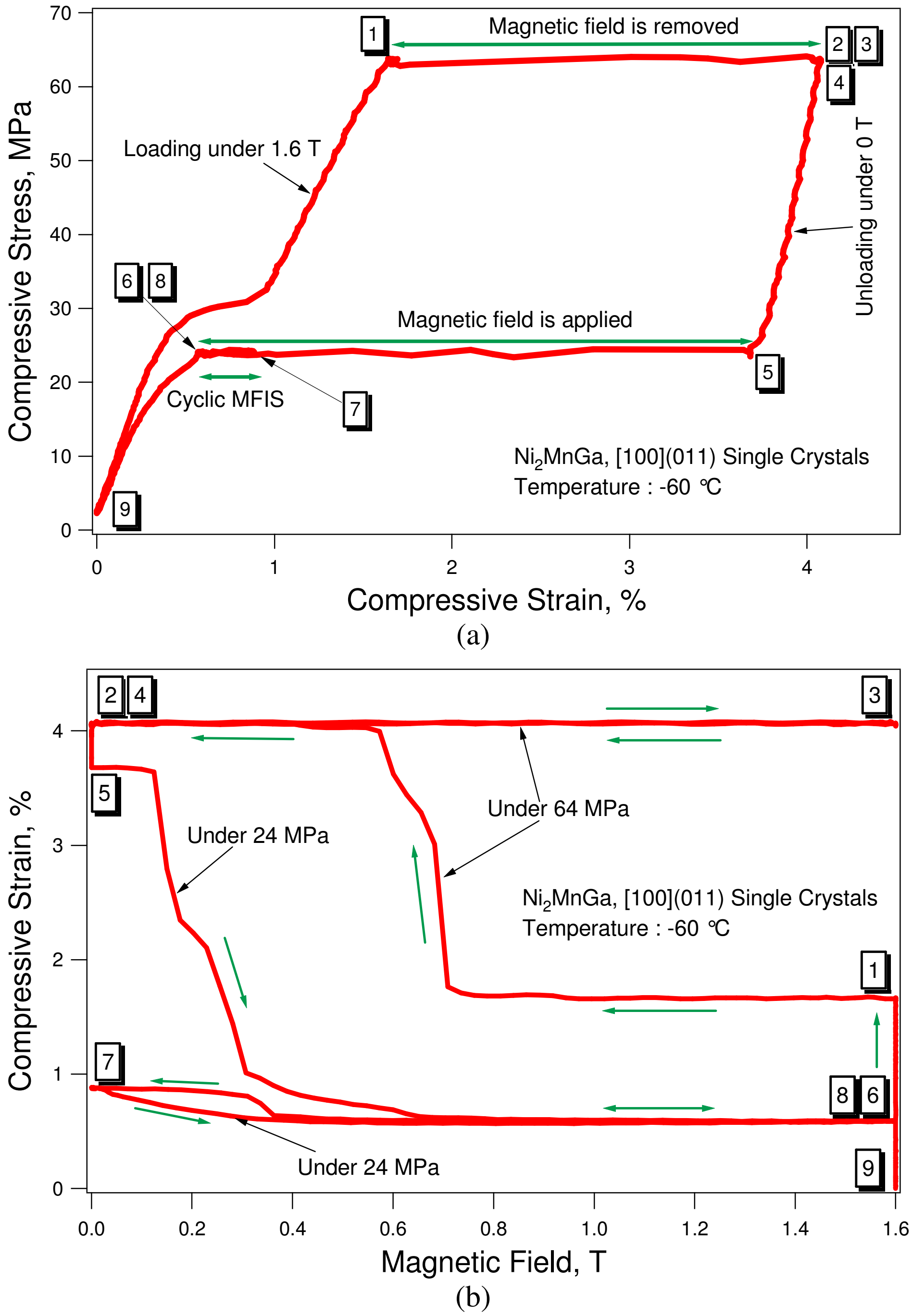

Figure IV.10 Demonstration of the field-induced one-way shape memory effect via X to 10M martensitic transformation or vice versa at low field magnitudes. Data in (a) and (b) are from the same experiments. The number sequence demonstrates the loading path [87].

Furthermore, upon the cycling of magnetic field between 0 and 1.6 Tesla under a constant stress value of 24 MPa, a fully reversible MFIS of 0.3% was accomplished related to the reversible field-induced I←→X martensitic phase transformation since 24 MPa is between $\sigma_{c,\mathrm{forward}}$ and $\sigma^{H}_{c,\mathrm{reverse}}$ for the I←→X transformation (the first stage). Unloading the load under 1.6 Tesla field brings the pseudoelastic cycle to completion (#9). The phenomena detailed in Figure IV.10 is the proof that activation of both reversible and one-way field-induced phase transformations in one pseudoelastic cycle is possible depending on the level of applied stress.

IV.9 Work Output in NiMnGa

As mentioned in the previous section, 28 MPa is the maximum stress level for the reversible field-induced phase transformation to occur in the course of the first stage transformation of our NiMnGa single crystalline specimen. This value is almost 10 times greater than the blocking stress levels observed for the field-induced martensite variant reorientation in the same specimen. Mechanical work output per unit volume can be employed as a measure of performance in order to compare the actuation performance of previously reported Ni_2MnGa compositions with our present results, and is plotted in Figure IV.11 [87]. In the case of the stress-assisted field-induced phase transformations, the work output values reflect the contributions from both magnetic ($W^{\mathrm{mag}} = \sigma_{\mathrm{mag}} \times \mathrm{MFIS}_{\max}$) and mechanical energy ($W^{\mathrm{mech}} = \sigma \times \mathrm{MFIS}_{\max}$) terms [Ersin's dissertation]. Therefore, actuation performance by the stress-assisted field-induced phase transformation is considered as the total work output response of the material, activated in a reversible fashion by the applied magnetic field.

Figure IV.11 presents three main groups enclosed by ellipses: The first ellipse on the left hand side shows the actuation stress and work output levels by field-induced martensitic variant reorientation which was introduced in Chapter III [43, 52, 88, 91]. The second ellipse at the lower right hand corner displays our results for the reversible field-induced phase transformation in the first transformation stage (I → X). The work output in this region is similar to that from the field-induced variant reorientation (the first ellipse); however, the actuation stress is almost 10 times higher than that of the former. The third ellipse at the upper right hand corner shows the actuation stress, MFIS, and work output levels from the one-way field-induced phase transformation (one-way shape memory effect) in the second transformation stage of the present alloy (between -80 and -40 °C). Here, the work output ranges from 660 to 1848 kJm^{-3} while the temperature increases from -80 to -40 ˚C. This means that one-way field-induced phase transformation is likely to achieve more than one order of magnitude higher work output and actuation stress when compared to those by field-induced variant reorientation. The third ellipse also covers the region of anticipated performance which may be achieved by future compositions and phase structures in NiMnGa and in other MSMAs to provide us with separated pseudoelastic stress hysteresis loops with and without field, as discussed in the previous section (refer to Figure IV.8). A work output of 115 kJm^{-3} was obtained for the cyclic MFIS in the first stage transformation under 24 MPa actuation stress. The maximum work output of 1848 kJm^{-3} was obtained in the second stage phase transformation at -40 ^{o}C under 84 MPa. It is important to note that these values are considerably higher than those of currently available ferroelectrics and magnetostrictives [6, 87, 113, 114].

It is a fact that in various NiMnGa alloys composition, orientation and stress state dependent multi-stage martensitic transformations have been reported [106]. The multi-stage phase transformations in off-stoichiometric Ni_2MnGa alloys can be a part of the four stage transformation sequence [106]. However, our alloy composition demonstrates just the first two stages and, only the first stage can be realized in a reversible fashion by application of magnetic field. In this study, pseudoelastic stress hysteresis and magnetostress levels were demonstrated to evolve in different ways with temperature for two different martensitic transformations (first stage, I←→X and second stage, X→10M martensite). This outcome is enough to imply the importance of temperature dependence of the material properties. Even though the multi-stage martensitic transformation is not a requisite for the field-induced phase transformation to occur, studying it is beneficial to get a grasp of the supplementary parameters to modify, and thus increase the possibility of reversible field-induced phase transformation realization.

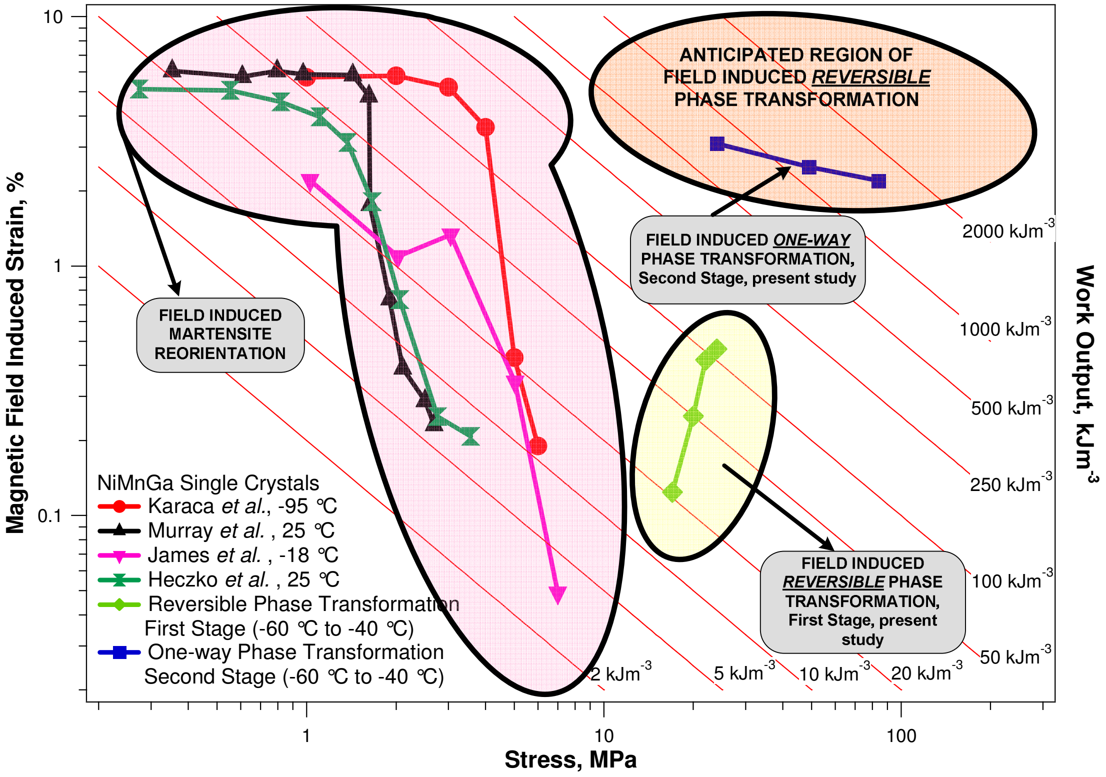

Figure IV.11 MFIS and total work output vs. the actuation stress plots showing the literature data obtained to date utilizing field-induced martensite reorientation mechanism and the present results of field-induced reversible and irreversible phase transformations in NiMnGa MSMAs [87].

CHAPTER V

INVESTIGATION OF POWER HARVESTING CAPABILITY IN Ni_2MnGa MSMAs

Harvesting power from waste mechanical vibrations using smart materials has been of interest since it would allow self sustainment to autonomous systems in terms of energy supply. Prototypes working with piezoelectric and magnetostrictive materials have already been under trial. This chapter reports a preliminary study on the feasibility of NiMnGa magnetic shape memory alloys as a promising alternative in power harvesting applications.

V.1 Power Harvesting via Smart Materials

In Chapter I, it was explained in detail how magnetic shape memory alloys (MSMAs) have the capability to convert mechanical, thermal, and magnetic stimuli into each other for potential applications in actuation, sensing, and power generation. Magnetic field-induced strain via reorientation of martensite variants mechanism [19, 115, 116] in MSMAs can result in reversible strain levels as high as 10% [34],which are about two orders of magnitude higher than those of Terfenol-D, Galfenol, and piezoelectrics [117]. MSMAs are metallic materials, thus, they can be reshaped easier than brittle piezoelectrics. They also cost less compared to piezoelectrics and Terfenol-D. Some MSMAs can be used under tension with large strain outputs [118]. Recently discovered Galfenol has also good tensile strength but its high permeability results in eddy current generation even at low frequencies which limits its utility in energy harvesting applications [117].

MSMAs have mainly been investigated for conversion of magnetic stimuli into mechanical response. However, the effect of external mechanical stimuli on the magnetic behavior of MSMAs has received limited attention [100, 116, 119, 120]. Strain induced changes in the flux density have been determined in NiMnGa single crystals under constant bias magnetic field [100, 116]. Suorsa et al. [119] reported magnetization measurements at various discrete levels ranging from 0% to 6% for strain and from 5 to 120 kA/m for magnetic field. Sarawate and Dapino [120] determined the bias field for maximum recoverable flux density change in a commercial NiMnGa. The investigations on the potential of these materials in energy harvesting are, however, still lacking. Moreover, there has been no report on the voltage or power output due to cyclic martensite variant reorientation which has the potential to convert free vibrations to electrical power.

V.2 Experimental Setup & Testing Methodology

In order to fill this gap, a set of power harvesting experiments was conducted on 4x4x16 mm^3 $Ni_{51.1}Mn_{2}4Ga_{24.9}$ single crystal compression specimens. Our macro MTM testing system (Figure V.1a) is combined with a copper pickup coil of 1000 turns (Figure V.1b), and an analogue oscilloscope.

The long axes of the specimens are along the $[100]$ orientation of the high temperature L2$_1$ austenite phase while the other two perpendicular orientations are $[011]$ and $[0\bar{1}1]$. Compressive load is applied along the long axis and bias field is applied perpendicular to the compression axis. A Hall sensor is used to measure the bias field. Note that in a practical application, instead of an electromagnet, a permanent magnet would be used to provide the bias field, as in the case of magnetostrictive energy harvesters.

The single crystal specimen was cooled down to -90 °C under 6 MPa to obtain a single variant tetragonal martensite with its short axis along the stress direction (variant 1) shown by #1 in Figure V.2. The room temperature phase is a cubic L2$_1$ phase (#0 in Figure V.2). Upon application of a bias field of 1.6 T, the field induced variant reorientation formed another martensite variant (variant 2), the long axis of which is parallel to the compression direction, shown by #2. While the field was being kept constant, the sample was loaded up to 20 MPa during which variant 2 reoriented into variant 1, (#4 in Figure V.2).

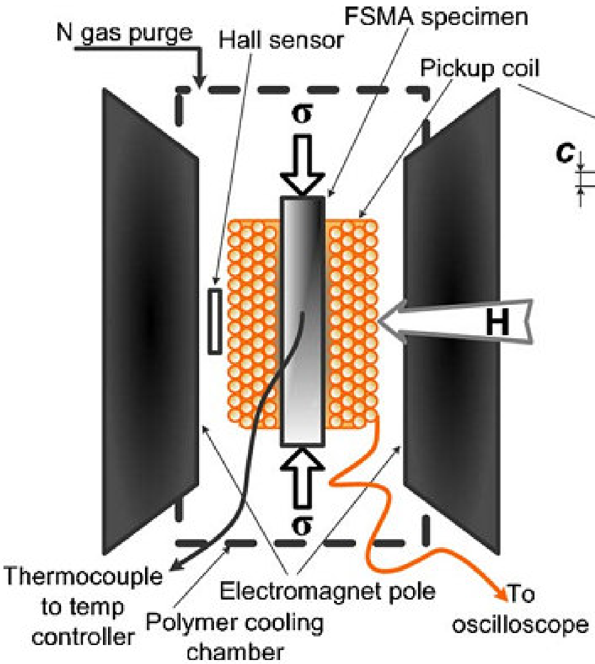

Figure V.1a Schematics of the experimental setup and pickup coil. *c,* diameter of the wire in the pickup coil, *D*, diameter of the MSMA specimen, l_c, length of the pickup coil, *T*, thickness of the coil [121].

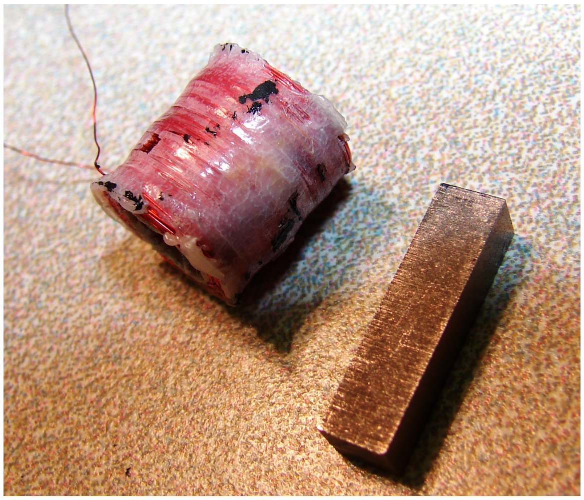

Figure V.1b Actual photo of the 1000 turn pickup coil and 4x4x16 mm^3 $Ni_{51.1}Mn_24Ga_{24.9}$ single crystal compression specimen.

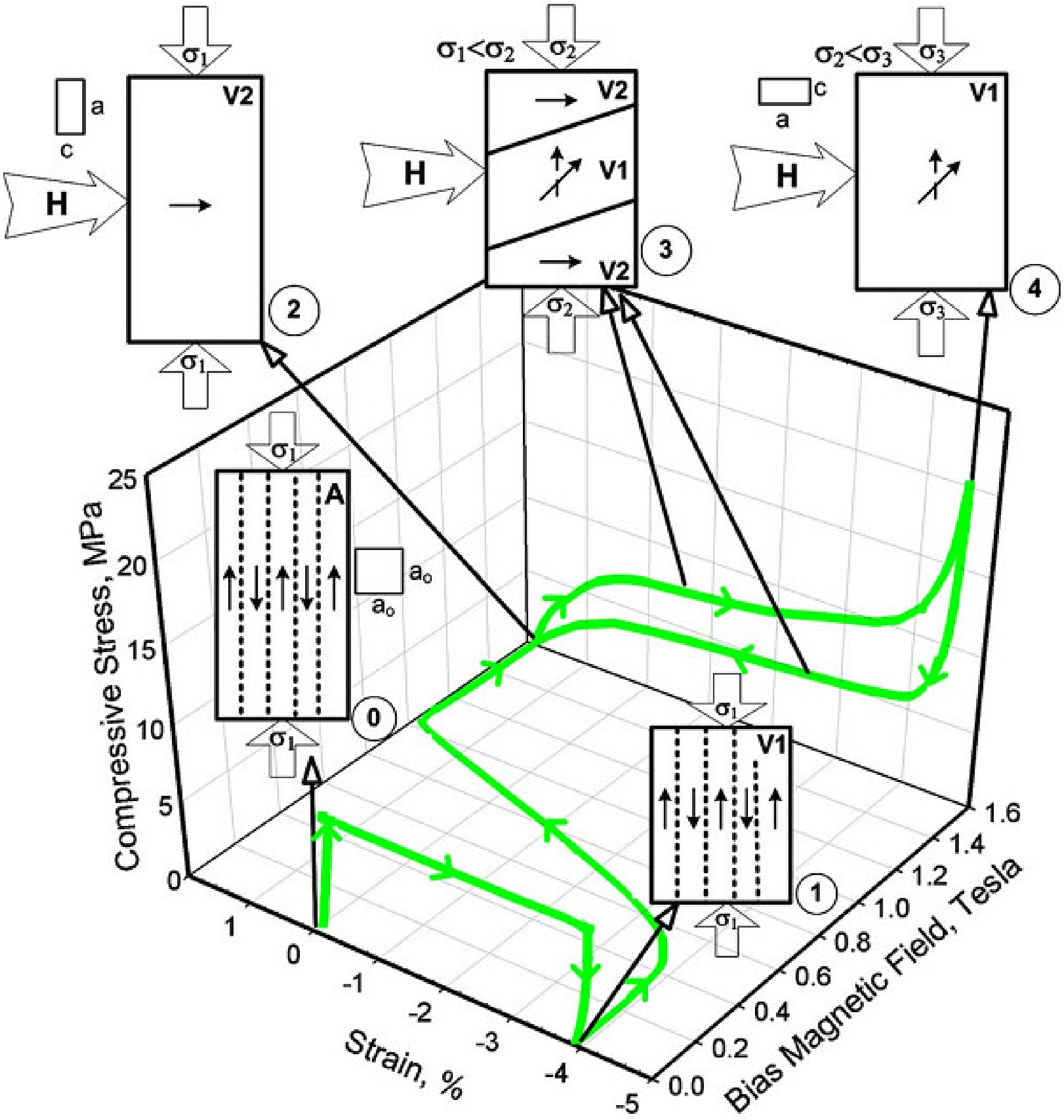

Figure V.2 Compressive stress-strain-bias magnetic field response of [100] oriented $Ni_{51.1}Mn_{2}4Ga_{24.9}$ single crystal at -90 °C. *A*, austenite; V_1 and V_2, martensite variants; a_0 lattice parameter of austenite; *a* and *c,* lattice parameters of martensite [121].

In the course of unloading, variant 1 reoriented back to variant 2 due to the bias field, #3 in Figure V.2. The corresponding stress versus strain (magnetoelastic) response is portrayed in Figure V.2 with the schematics representing the ongoing magneto-microstructural evolution. The detailed magnetoelastic response of these single crystals can be found in section III.5 of this dissertation.

V.3 Experimental Results

In MSMAs, reorientation from one variant to another under a bias field yields a change in magnetization since the easy magnetization direction of the variants is along their short axes. The magnitude of this change depends on the difference in magnetization of the hard and easy axes of martensite under the given bias field. Such change in magnetization and magnetic flux leads to voltage generation which can be detected using an oscilloscope. Utilizing this fact, several experiments were conducted by systematically changing the bias field, applied strain range (i.e., the amount of reoriented material volume), and loading frequency in the region where both martensite variants existed in the microstructure (#3 in Figure V.2). Figure V.3 shows the peak induced voltage output as a function of the bias field for a strain range of 1.25% under the loading frequencies of 1 and 5 Hz. As frequency increases, induced voltage output increases. Similarly, increasing bias field increases the voltage output up to 60 mV under 5 Hz but then decreases with further increase. The reason for this nonlinear behavior is the different critical magnetic fields of the easy and hard axes to reach saturation magnetization (M^S). Initially, the difference between the magnetizations of these axes increases with the increasing bias field where the magnetization along the easy axis as a function of magnetic field has a higher slope. After M^S is reached along the easy axis, a further increase in the bias field results in a decrease in the magnetization difference. From Figure V.3, the critical field to reach M^S along the easy axis is determined to be 1.2 T. This is much higher than expected, since demagnetization has a substantial effect on the real material behavior due to the experimental setup. Kiefer and Lagoudas [122] calculated the demagnetization factor as 0.65 for a sample with an aspect ratio of 2:1:1

under the present experimental conditions. The demagnetization factor is expected to be slightly smaller for the samples with the aspect ratio of 4:1:1. If a demagnetization factor of 0.6 is used, the field inside the sample under the external bias field of 1.2 T would be 0.65 T, showing that the material itself requires much lower fields to saturate.

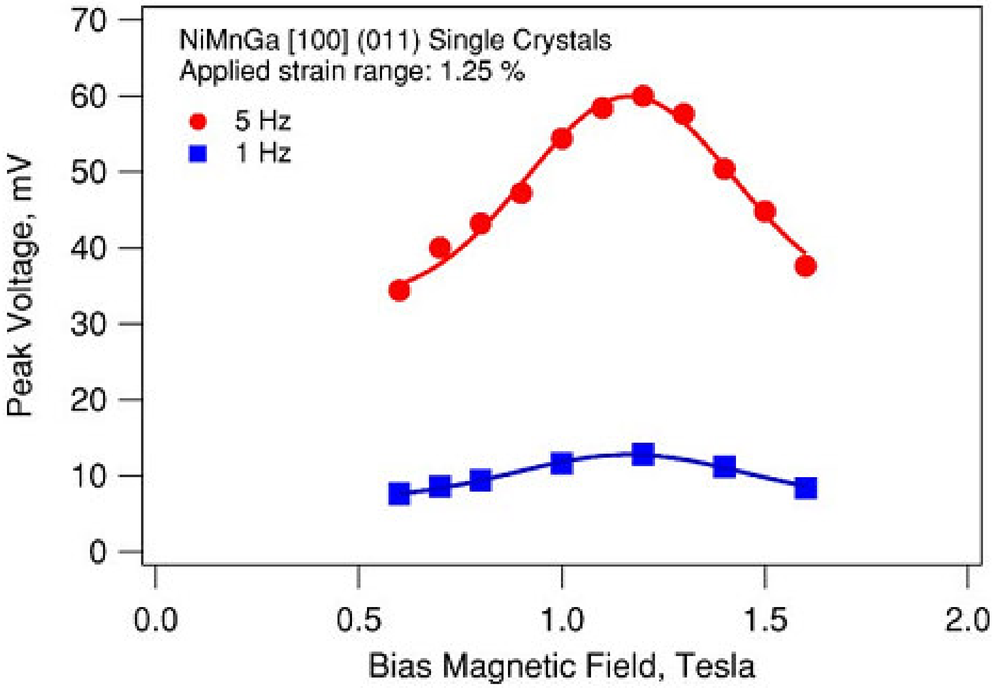

Figure V.3. Peak induced voltage output as a function of bias magnetic field under the loading frequencies of 1 and 5 Hz at a constant applied strain range of 1.25% [121].

Figure V.4 shows the direct readings of the peak voltage output from the oscilloscope as a function of strain range (a) and excitation frequency (b) under the bias field of 1.6 T. Figure V.5a presents the combined 3D plot of Figures V.4a and V.4b. Strain ranges up to 4.9% were applied in the form of sinusoidal excitation with frequencies ranging from 0.5 to 10 Hz. The observed increase in voltage with strain (Figure V.4b) is due to the increase in the fraction of the material that undergoes variant reorientation, resulting in higher total magnetization change.

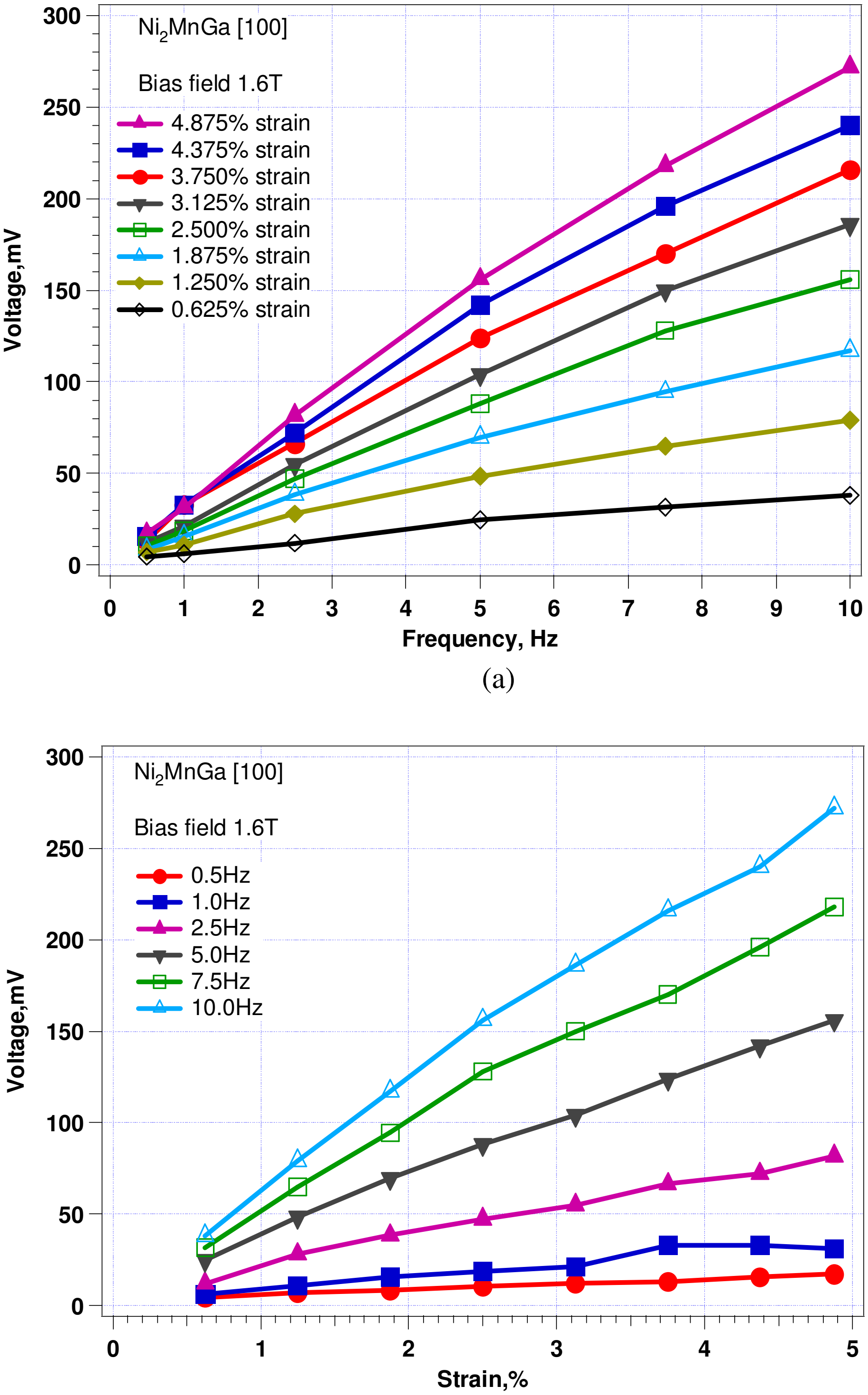

(a)

(b)

Figure V.4. Direct readings of the peak voltage output as a function of strain range (a) and excitation frequency (b) under the bias field of 1.6 Tesla.

Also, as frequency increases, the rate of change of magnetization increases which, in turn, affects the output voltage (Figure V.4a). The maximum voltage of 280 mV is obtained with the strain range of 4.9% at 10 Hz frequency under 1.6 T. However, as seen in Figure V.3, a higher voltage level would have been expected under 1.2 T. To predict the power outputs that could possibly be achieved in the present alloy, the maximum reversible magnetic flux density change upon full martensite reorientation is taken to be 0.2 T [120]. Referring back to Figure V.1, if the volume of the coil is fixed by appropriate choices of *D, l_c,* and *T*, the number of turns *N* in the coil can be approximated as $N \approx \frac{l_c T}{c^2}$ where l_c is the length, T is the thickness and *D* is the inner diameter of the coil, and c is the wire diameter. Resistance of the coil can be calculated, assuming that the wire is made of copper with the resistivity of (1/6)x10^{-7} Ωm, as

$$R \approx \frac{N\pi D}{\pi (c/2)^2 (6\times 10^7)} = \left(66.67\times 10^{-9} \frac{l_c T D}{c^4} \right) \qquad \text{(in } \Omega\text{)} \qquad \text{(Eqn. V.1)}$$

whereas the peak voltage induced in the coil can be found as

$$V = N\frac{d\phi}{dt} = NA\frac{dB}{dt} = \frac{l_c T}{c^2}\pi\left(\frac{D}{2}\right)^2 \frac{dB}{dt} = 0.785\frac{l_c T D^2}{c^2}\frac{dB}{dt} \qquad \text{(in V)} \qquad \text{(Eqn. V.2)}$$

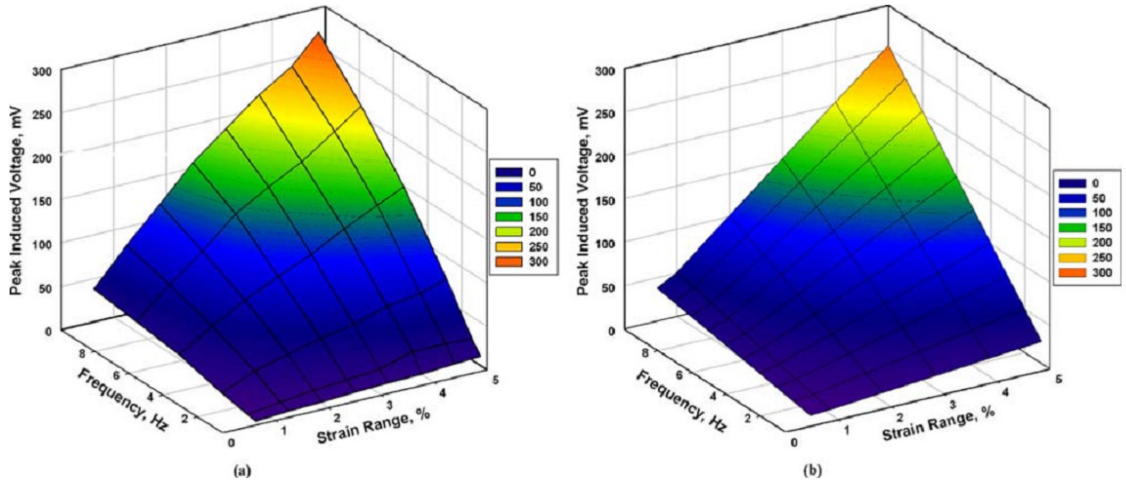

Figure V.5. Comparison of experimental (a) and computed (b) peak induced voltage outputs as a function of strain range under the bias field of 1.6 T for different excitation frequencies [121].

Assuming a sinusoidal excitation, the change in the magnetic induction can be modeled by $B = B_0\, r \sin(\omega t)$ where B_0 is half of the reversible magnetic flux density change upon martensite reorientation and r is the volume fraction of the material undergoing reorientation which is defined as $\varepsilon / \varepsilon_{\max}$ is the applied strain range and $\varepsilon_{\max}$ is the maximum reorientation strain for the present crystals which is measured as 5%. Since B_0 depends on applied strain range, [120] the term r is explicitly included in the formulation. It is important to note that B_0 is also a function of bias magnetic field [120] which can be deduced from Figure V.3. Bias magnetic field dictates what the maximum B_0 would be when the variant reorientation is complete. Using Eqn. V.2 and $B = B_0\, r \sin(\omega t)$, the rms voltage generated can be expressed as

$$V_{rms} = 3.488 \frac{l_c T D^2 B_0 r f}{c^2} \qquad \text{(in V)} \qquad \text{(Eqn. V.3)}$$

where *f* is the excitation frequency. If N is known for pickup coils, then the peak induced voltage can be found using

$$V_{peak} = N\pi^2 f B_0 r \frac{D^2}{2} \qquad \text{(Eqn. V.4)}$$

The rms power delivered to a matching electrical load impedance can then be calculated as

$$P_{rms} = 45.62 \times 10^6 l_c T D^3 B_0^2 r^2 f^2 \qquad \text{(in W)} \qquad \text{(Eqn. V.5)}$$

Figure V.5b shows the peak induced voltage output predicted using Eqn. V.4 and the current materials and pickup coil parameters (B_0 =0.1 T, N=1000 turns, and D=7 mm). The predictions agree well with the experimental results, confirming the validity of the above approach at least for the low frequency range used. As a comparison, similar voltage output levels were detected under 7–15 MPa in Terfenol-D and Galfenol at a frequency of about 60 Hz using a 3000 turn pickup coil [117]. In similar hardware and frequency conditions, the present alloy could result in much larger voltage outputs according to Eqn. V.4. To reveal the potential of the present NiMnGa alloy for power generation, Eqn. V.3 and Eqn. V.5 were used to calculate the V_{rms} and P_{rms} values as functions of wire diameter and excitation frequency for the experimental pickup coil parameters of D=7 mm, T=5 mm, and l_c =12 mm. It is clear in Figure V.6 that at relatively low frequencies around 200 Hz, it might be possible to achieve power outputs above 1 W.

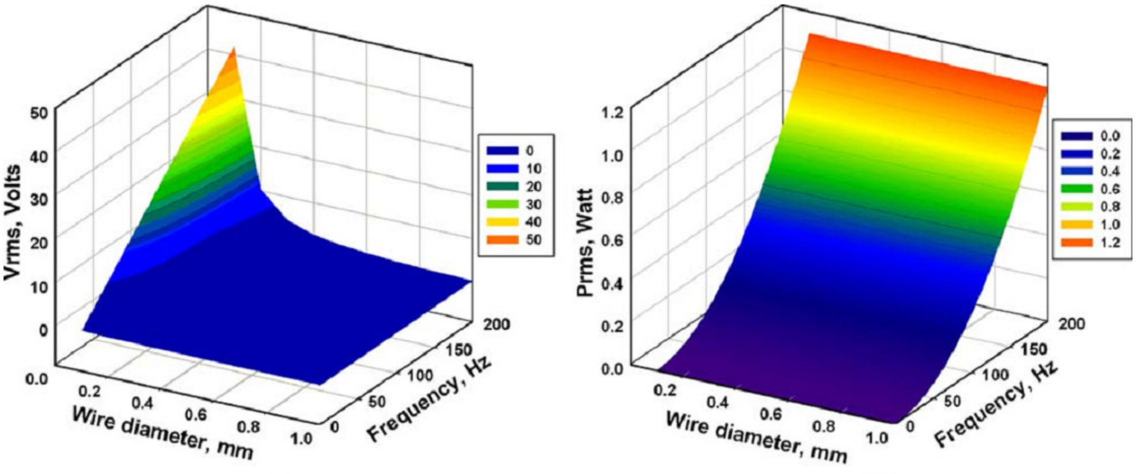

(a)

(b)

Figure V.6. Predicted induced voltage (a) and power outputs (b) in NiMnGa MSMA power harvesters, with fixed specimen and coil volume as shown in Figure V.1 as a function of wire diameter and excitation frequency [121].

Although the power delivered to a matching electrical load is independent of the wire diameter as seen in Figure V.6, the inductance and the resistance of the coil primarily depend on *c*. This provides flexibility during the optimization of coil parameters and allows maximum power transfer to a given electrical load impedance. However, we did not attempt to enhance the coil parameters in this study. Similarly, the above calculations do not consider optimized power conditioning circuitry which, together with the enhanced conversion unit, could make it possible to achieve power outputs as high as 1 W below 100 Hz. As a conclusion, power harvesting experiments on NiMnGa MSMA single crystals demonstrated that it is possible to obtain a few milliwatt power output utilizing martensite reorientation mechanism under slowly fluctuating loads (10 Hz). This can be increased over 1 W at frequencies over a hundred hertz by optimizing the power conversion hardware which would make these materials comparable and possibly better energy harvesters than magnetostrictive and piezoelectric materials at low frequencies. There is an optimum bias field where induced voltage and power output maximize. Voltage generation increases linearly with excitation frequency and strain range, and decreases linearly with the square of wire diameter.

CHAPTER VI

ULTRA HIGH MAGNETOSTRESS & MAGNETIC WORK OUTPUT IN NiMnCoIn METAMAGNETIC SMAs VIA MAGNETIC FIELD-INDUCED PHASE TRANSFORMATION

This chapter reports the effects of the applied magnetic field on the transformation temperatures, magnetization and pseudoelasticity (PE) responses of $Ni_{45}Mn_{36.5}Co_5In_{13.5}$ single crystalline metamagnetic shape memory alloys via magnetization measurements as a function of temperature or magnetic field, isobaric thermal cycling and isothermal mechanical loading experiments. In the light of these findings, magnetic field-induced phase transformation mechanism (FIPT) in NiMnCoIn results in much higher magnetic work outputs as compared FIPT and magnetic field-induced variant reorientation (VR) observed in NiMnGa alloys.

VI.1 Magnetic Field-Induced Phase Transformation in NiMn*X* Alloys

As it was already explained comprehensively in Chapter III, magnetic field-induced martensite variant reorientation (VR) is one of the two main mechanisms utilized for magnetic field-induced shape change in MSMAs. Although NiMnGa can display a magnetic field-induced strain (MFIS) of ~10% via magnetic field-induced VR mechanism [34], its actuation stress remains at best around 10 MPa even with the contribution of size effect [123]. In Chapter IV, a necessary condition for realization of FIPT was identified as the pseudoelasticity (PE) stress hysteresis being lower than the magnetostress. Likewise, transformation thermal hysteresis should be lower than the change in transformation temperatures under the field. Fulfilling these conditions, our NiMnGa composition demonstrated a FIPT which yielded in an actuation stress on the order of 20 MPa accompanied by a cyclic MFIS of 0.5% with stress assistance (Figure IV.9 in Chapter IV) [87]. Since the actuation stress in NiMnGa is intrinsically limited by the limited magnetocrystalline anisotropy energy (MAE) of martensite, new alternatives have been sought for to replace the NiMnGa system. NiMn*X* (*X*= *In, Sn, Sb, Al*) [67, 124] alloy families were introduced as promising alternatives where the replacement of *Ga* with *In*, *Sb*, *Al* or *Sn* in appropriate amounts results in the overlap of the magnetic and martensitic transformations and leads to weakly magnetic martensitic phases. In these new alloys, FIPT is observed as the main mechanism for the shape change between a ferromagnetic austenite parent phase (*A*) and a paramagnetic/antiferromagnetic martensite phase (*M*) for which the Zeeman energy serves as the driving energy source. This kind of magnetic FIPT is called as "***metamagnetic phase transition***" and was previously reported in other alloys systems such as MnAs, FeSiLa, etc. [125] besides NiMnCoIn [61]. In the NiMnGa system, on contrary to metamagnetic SMAs, the magnetocrystalline anisotropy energy (MAE) is responsible for the magnetic field induced twin boundary motion which in turn amounts to a net shape change. While the MAE is sensitive to crystal orientation and limited with the saturation magnetization (M^S) of martensite; the Zeeman energy is not as orientation dependent and can continuously increase with the increasing applied field since it depends on the magnetization difference between austenite and martensite phases [126]**.** Figure VI.1 schematically demonstrates the differences between magnetocrystalline anisotropy energy and Zeeman energy. The aforementioned distinction of NiMn*X* alloys seem to be promising in utilizing polycrystals as potential actuator materials and achieving much higher actuation stress levels than those of NiMnGa alloys. Cobalt has the highest Curie point, 1120 ^{o}C, of any known material [127]. Addition of *Co* is found to increase the Curie temperature and saturation magnetization of parent austenite in Ni-Mn-In [61], NiMnSn [128], and NiMnAl [129]. Among the members of NiMnCo*X* family, *X*= *In* is the easiest one to grow in single crystalline form resulting in the largest transformation strain (6.3%) with a moderate magnetic hysteresis (an average of 3 Tesla for the range of 150 to 250 K without bias stress), where *X*= *Sn* is only possible to fabricate in polycrystalline form with a comparatively limited performance. Despite having a single crystalline structure, *X*= *Al* displays a large transformation hysteresis [129] hence is not desirable for actuation applications. After Kainuma *et al* [61] showed that in NiMnCoIn, 4 Tesla field was sufficient to recover 3% of pre-applied strain in martensite at room temperature, many studies on metamagnetic SMAs which mainly focused on the magnetocaloric properties and compositional effects on the transformation temperatures followed [130-141]. Kainuma *et al* also [61] predicted that the magnetostress levels in NiMnCoIn alloys should be on the order of tens of MPa, but there has been no systematic experimental study to prove this prediction. Wang *et al.* [141] reported reversible FIPT under 50 MPa with the application of 5 Tesla in $Ni_{45}Mn_{36.6}Co_5In_{13.4}$ alloys with unknown MFIS values using in-situ high energy XRD measurements. The actuation stress level achieved in the study of Wang *et al.* [141] is an order of magnitude higher than that in Ni-Mn-Ga alloys obtained via field-induced martensite reorientation [95]. Investigating the conventional shape memory properties of $Ni_{45}Mn_{36.5}Co_5In_{13.5}$ single crystals along the [100] orientation, we recently reported fully reversible pseudoelastic response with strain levels more than 6% accompanied with large stress and temperature hystereses [68] as the details of which will be provided later in this chapter. It is a must to have an applied magnetic field at a critical level:

a) To be able to induce the phase transformation,
b) To have martensite completely transform into austenite,
c) To obtain MFIS levels as high as the transformation strain levels.

It should be kept in mind that the critical levels of magnetic field which mark the start and finish of forward and back transformations are functions of temperature. Apparently, the necessary magnetic field for FIPT in NiMnCoIn alloys is still high for practical applications due the large transformation hysteresis. There are some microstructural factors influencing conventional shape memory properties [142] that can be engineered to decrease the hysteresis of these alloys. However, this initially requires a systematic work on the shape memory and pseudoelastic response of MSMAs to assess hysteretic transformation behavior. Without a proper understanding of the SMA characteristics, it is not possible to fully comprehend their magnetic shape memory response.

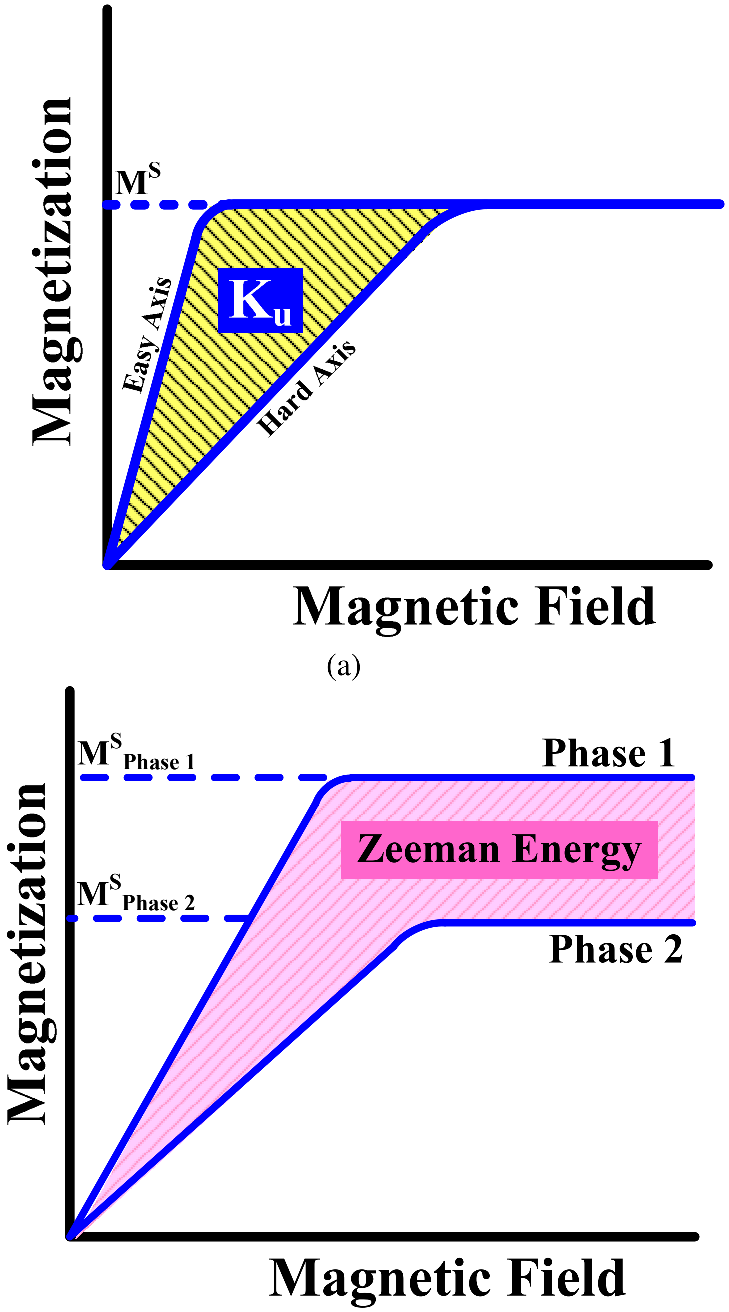

(a)

(b)

Figure VI.1. Schematics showing (a) the maximum magnetocrystalline anisotropy energy (K_u) for ferromagnetic martensite in Ni_2MnGa responsible for the field-induced martensite variant reorientation, b) Zeeman energy difference between two phases which reversibly transform into each other, can be responsible for field-induced phase transformation. M^S: Saturation magnetization.

Thus, one of the aims of the study reported in this chapter is to reveal the shape memory response of NiMnCoIn single crystal characterized along the $[100]$ orientation. The effects of stress and/or temperature on the transformation temperatures, strain and hysteresis were investigated, along with the critical stress for transformation. The $[100]$ orientation was chosen since, in similar alloys, transformation strain and resistance against plastic deformation are relatively high in this orientation under uniaxial loading [80].

VI.2 Isobaric Thermal Cycling & Isothermal Pseudoelastic Responses of NiMnCoIn

Figure VI.2 shows the results of isobaric cooling/heating experiments which were conducted [68] in order to determine the shape memory response and the effect of applied stress on the transformation temperatures. The stress was isothermally applied in austenite and the sample was thermally cycled between a temperature below M_F and a temperature above A_F at the given stress level. After the completion of the cycle, the stress was increased further and thermal cycling was repeated. It is worth to note that the transformation strain (ε_{tr}) increases with stress from 0.2% under 10 MPa to 5.4% under 125 MPa.

This type of evolution in ε_{tr} is a consequence of the evolution of martensite variants as a function of external stress. In the course of cooling under low stresses, the measured low ε_{tr} levels imply that the stress is not enough to bias the formation and propagation of only a single martensite variant, and a self-accommodating martensite structure forms partially. Under high stress levels, the volume fraction of the stress-biased martensite variant increases, so does the ε_{tr} level [68]. The possible evolution of martensite variants in two cases, *i.e.,* under bias stresses of 50 MPa and 125 MPa, during the forward transformation is also depicted in Figure VI.2.

As mentioned earlier in Chapter II, analysis of the nominal composition $Ni_{45}Mn_{36.5}Co_5In_{13.5}$ vacuum induction melted ingot by SEM revealed the presence of second-phase particles inherited from the as-grown crystals. These were not possible to be eliminated by the selected heat treatment. Wavelength-dispersive spectroscopy (WDS) was utilized to find the composition of the matrix and the second phase as $Ni_{45.7}Mn_{35.6}Co_{4.8}In_{13.8}$ and $Ni_{42.0}Mn_{40.3}Co_{16.0}In_{1.6}$, respectively [126]. Note that the second-phase particles do not transform.

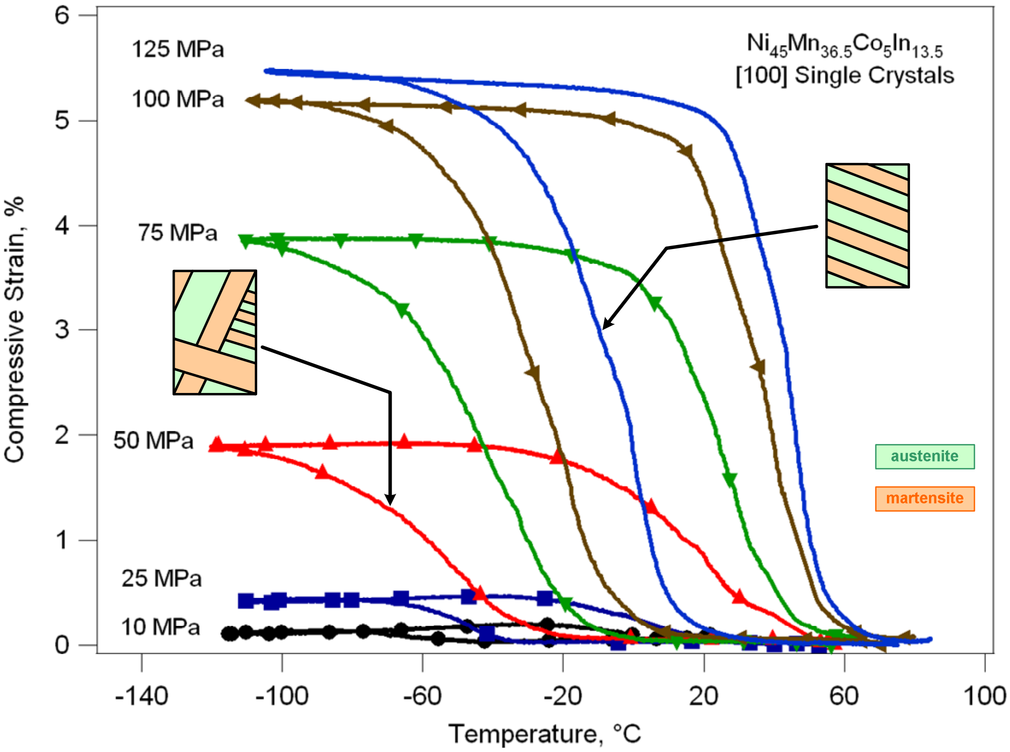

Figure VI.2. The strain vs. temperature response of $Ni_{45}Mn_{36.5}Co_{5}In_{13.5}$ single crystals under constant compressive stress levels applied along the [100] orientation. The insets show the possible microstructural evolution under the different stress levels as discussed in the main text [68].

Pseudoelastic response of the present NiMnCoIn single crystals along the $[001]$ orientation at 0 °C, 20 °C and 50 °C are shown in Figure VI.3a. The experiments were conducted above A_F temperature, resulting in a transformation strain of about 5.2 % in the plateau region at 0 °C which is in good agreement with ε_{tr} detected in Figure VI.2. If the initial part of the unloading curve is extrapolated to zero stress, transformation strain can be determined as 6.3 %. As the stress increases, austenite ($L2_1$ cubic phase) deforms elastically and then transforms to martensite (6 layered modulated structure [126]) with notable hardening in the plateau region, followed by further transformation of remnant austenite and simultaneous elastic deformation of martensite. Upon unloading, martensite relaxes elastically and transforms back to austenite before the elastic relaxation of austenite takes place. The stress hysteresis is approximately 110 MPa at 0 ^{o}C and increases with temperature [68].

Figure VI.3b presents the M_S temperature as a function of applied stress, determined from the isobaric thermal cycles in Figure VI.2 and also the critical stress for the forward transformation as a function of test temperature, extracted from Figure VI.3a. It is clear that the critical stress for the transformation increases linearly with temperature, with a rate of 2.1 MPa/^{o}C. The linear dependence between the critical stress and temperature can be expressed following the Clausius-Clapeyron (CC) relation:

$$\frac{\Delta\sigma}{\Delta T} = -\frac{\Delta H_{enth}}{T_o \varepsilon_{tr}^{\max}} \qquad \text{(Eqn. VI.1)}$$

where $\Delta\sigma$ is the change in the critical stress, ΔT is the change in temperature, ΔH_{enth} is the transformation enthalpy, T_o is the equilibrium temperature, and ε_{tr}^{max} is the transformation strain from a single crystal austenite to a single variant martensite.

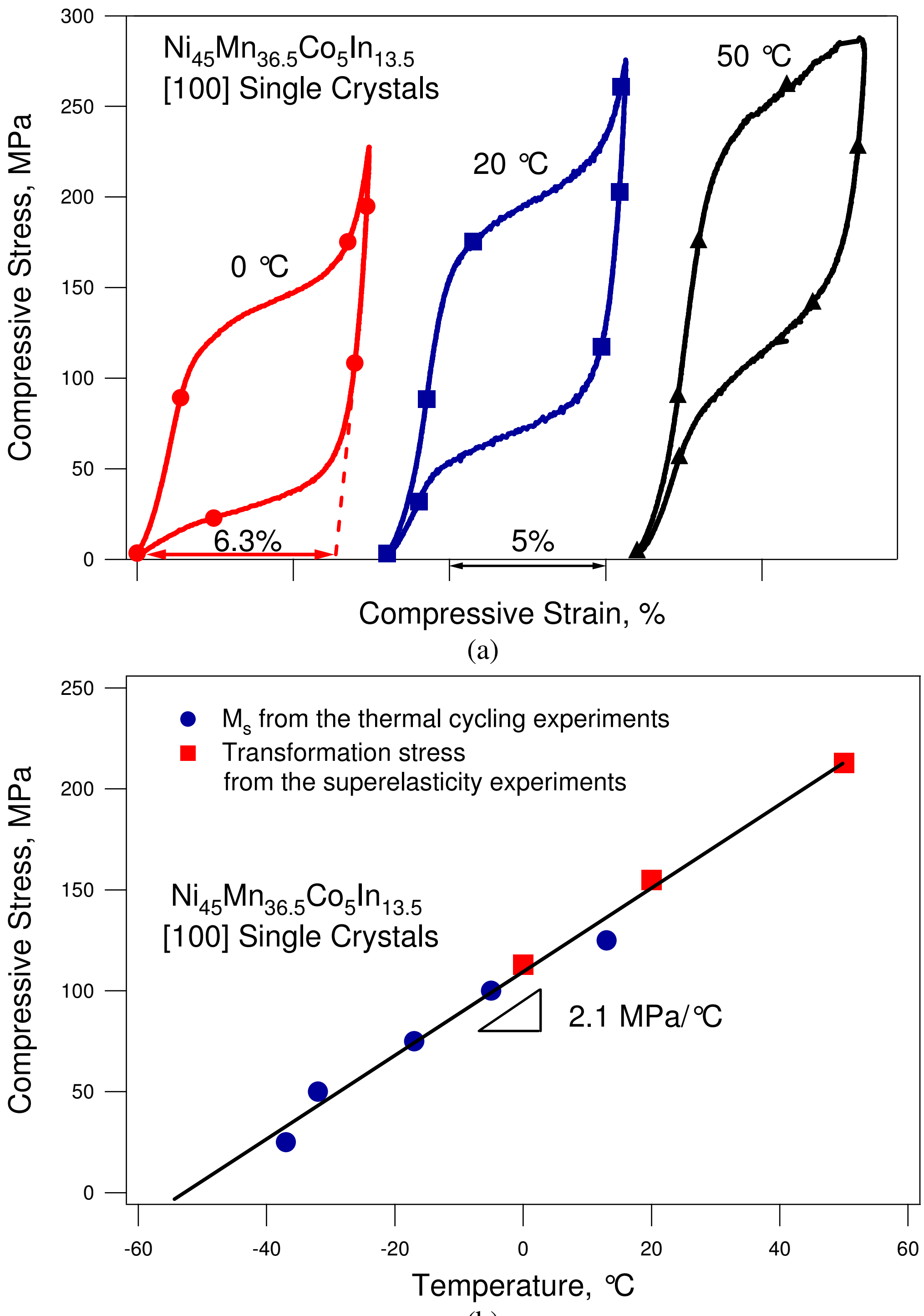

(a)

(b)

Figure VI.3. (a) Superelastic response of the $Ni_{45}Mn_{36.5}Co_5In_{13.5}$ single crystals along the [100] orientation under compression at 0˚C, 20˚C and 50˚C. (b) Critical stress for phase transformation vs. temperature phase diagram constructed using the data extracted from Figures VI.3a and VI.2 [68].

The CC slope for the $[100]$ orientation (2.1 MPa/°C) matches the CC slope of the austenite to 10M martensite transformation in Ni_2MnGa single crystals along the same orientation for similar transformation temperatures. However, ε_{tr}^{max} of the NiMnCoIn (5.4%) is greater than that of Ni_2MnGa (4%), suggesting a larger ΔH_{enth} in the NiMnCoIn crystals. ε_{tr} and thermal hysteresis as a function of stress were determined from the thermal cycling experiments and are depicted in Figure VI.4.

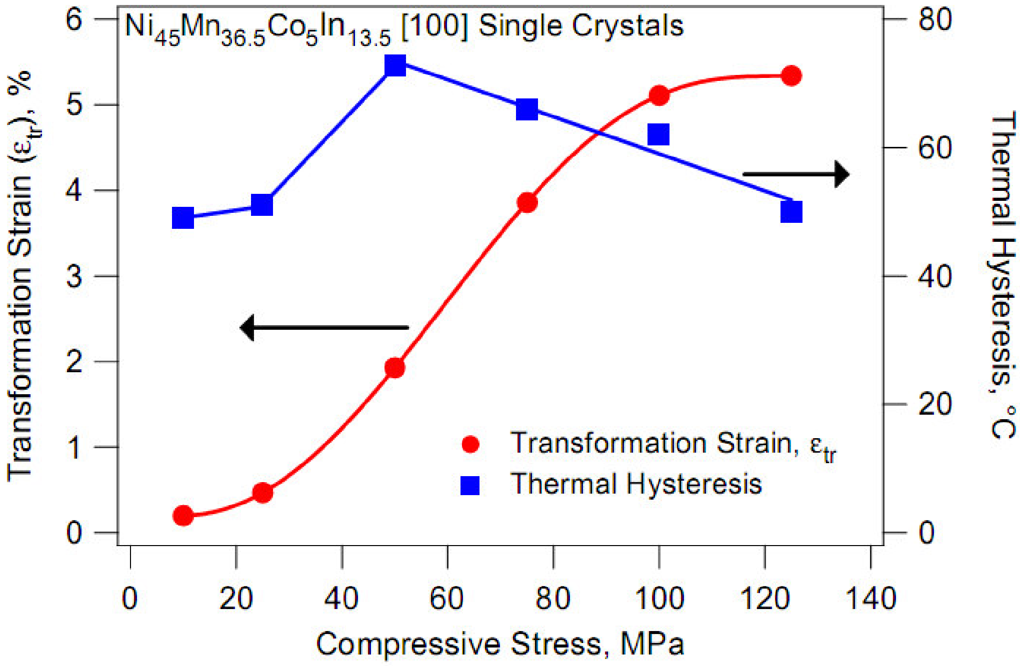

Figure VI.4. Transformation strain (left axis) and temperature hysteresis (right axis) of $Ni_{45}Mn_{36.5}Co_5In_{13.5}$ single crystals along the [100] orientation as a function of applied stress [68].

ε_{tr} increases with stress and saturates above 100 MPa. Such progression in ε_{tr} can be a consequence of the evolution of martensite variants as a function of external stress. During cooling under low stresses, the measured low ε_{tr} levels imply that the stress is not sufficient to bias the formation of one single variant; hence, a self-accommodating martensite structure partially forms. The phase front propagation seems to be hard, most likely because of the second-phase particles and defect generation as a result of lattice incompatibility between austenite and martensite. Under high stress levels, a stress-biased martensite variant must have formed and grown hindering propagation of other variants' nuclei since the attained 5.4% of stain is near the calculated theoretical ε_{tr} level (6.61% for $[100]$ orientation [126]).

The possible evolution of martensite variants in two cases, at 50 and 125 MPa, are depicted as simple schematics in Figure VI.2. At 50 MPa, multiple variants form. However, at 125 MPa, only one variant favored by the external stress can grow thanks to the stress being high enough to bias the propagation.

The observed ε_{tr} saturates above 100 MPa which is really high as compared to the corresponding 6 MPa in Ni_2MnGa [95]. Possible factors that may be responsible for such a large difference are higher lattice friction in NiMnCoIn alloys due to solid solution hardening and off stoichiometry, more defect generation during transformation due to larger lattice incompatibility between transforming phases, and local internal stress near precipitates, which do not exist in Ni_2MnGa.

Thermal hysteresis in Figure VI.4 also increases with stress up to 50 MPa and then decreases with further increase in stress. The hysteresis was determined to be between 50 and 75 ^{o}C, depending on the stress level, which is large compared with those of other MSMAs, such as NiFeGa [143]. Large hysteresis or high-energy dissipation in SMAs arises from structural defect formation, such as dislocations, during transformation and frictional energy spent on the movement of phase fronts and on multiple phase front interactions. The individual contributions of these factors on the hysteresis depend on the lattice compatibility between transforming phases, their elastic moduli and strength, and the lattice friction, which is dictated by the crystal structure and stoichiometry. If phases are relatively soft, lattice incompatibility would be mainly accommodated with irreversible local defects increasing hysteresis [142]. If they are strong, it could be accommodated elastically or with internal twin formation. Since, in the present case, there is no irrecoverable strain during thermal cycling, we conclude that the transforming phases have high strength with negligible irrecoverable defect generation. Then, the frictional loss can be expected to be more prominent in the present material, which is also supported by the large thermal hysteresis of 50 ^{o}C under stress-free conditions.

Moreover, multiple phase fronts and their interactions associated with self-accommodating morphology should increase frictional energy dissipation. Macro segregation during the single crystal growth using the Bridgman technique can be another reason for high lattice friction due to the formation of second-phase particles. The presence of second-phase particles can strongly influence the hysteresis and the stress dependence of ε_{tr} [142]. The large particles, as in the present case, are likely to be incoherent without any notable coherency stress. However, under applied stress, modulus mismatch between the particles and matrix can initiate local internal stress, which in turn can oppose external stress and bias martensite variants other than the one favored by external stress. Interactions between these variants increase the dissipation and hysteresis. Furthermore, large untransformed particles in a transforming matrix can delay the relaxation of stored elastic energy of transformation due to the need to accommodate the large transformation shape change around the untransformed second-phase particles. This should lead to additional dissipation, contributing to the overall hysteresis. Thus, in Figure VI.4, thermal hysteresis increases to 75 ^{o}C with increasing stress up to 50 MPa. Upon further stress increase, the number of variant interactions is reduced, as is the dissipation and hysteresis, since most of the sample transforms to a single martensite variant. In addition, the local internal stress around the particles cannot sufficiently oppose the high external stresses in biasing the single variant. Therefore, for stresses 100 MPa and higher, the sample transforms to a single variant and the maximum ε_{tr} is reached [68].

The relaxation of elastic energy due to the non-transforming second-phase should not increase with stress once a complete single variant morphology is reached, since the shape change to be accommodated does not change further. On the other hand, the decrease in hysteresis with stresses above 100 MPa, even though ε_{tr} saturates, can be attributed to the uneven change in lattice parameters of the phases with increasing stress and temperature. Lattice parameters are a function of composition, temperature and stress, and can vary differently with temperature and stress for martensite and parent phases [143]. The compatibility between transforming phases is usually dictated by lattice parameters and crystal structures of these phases [144]. Since elastic moduli of transforming phases are quite different from each other in many SMAs, increasing stress alters the lattice parameters of the phases disproportionately, leading to a change in compatibility. The change usually occurs in a positive manner, and thus brings about a reduction in thermal hysteresis with increasing stress, until plasticity or some other dissipative mechanisms become more pronounced.

One way to reduce thermal hysteresis in SMAs is to improve the lattice compatibility with compositional modifications and enhance the strength to suppress defect-induced dissipation. For instance, off stoichiometric alloy compositions in SMAs in general, possess higher strength levels than the stoichiometric ones due to solid-solution hardening. Coherent precipitates can both increase strength and help bias single variant martensite via aligned coherency stress field [68].

VI.2.1 Effect of Magnetic Field on Pseudoelastic Response of NiMnCoIn

As mentioned earlier in sections IV.4 and IV.7 of Chapter IV, there are two ways to realize reversible FIPT in MSMAs:

(i) Separation of thermal cycling loops, and/or

(ii) Separation of isothermal pseudoelastic loops, both with and without an applied field.

Once one of these is achieved, it is possible to find a temperature or stress window at which martensite is the stable phase under no magnetic field and austenite is the one under the field. Cycling the field in this window would then result in reversible FIPT with an associated external strain. Large thermal or stress hysteresis, however, increases the critical magnetic field required for the complete separation of these loops. The change in M_S temperature for the present material is measured as 13 ^{o}C/Tesla using a superconducting quantum interference device (refer to figure on page 140) Thus at least 4 Tesla field would be required to separate the loops hysteresis values of which are shown in Figure VI.4.

In order to reveal the effect of a magnetic field on the compressive superelastic response, the compressive behavior along the $[100]$ orientation was investigated under constant magnetic fields at 0 ^{o}C, as well. The field was applied prior to the loading, and kept constant throughout the experiment along the $[011]$ orientation, perpendicular to the direction of the applied stress. Field magnitudes ranging from 0 Tesla to 1.6 Tesla with increments of 0.4 Tesla were applied in order to capture the magnetostress levels as a function of magnetic field magnitude as depicted in Figure VI.5a. It is clear that the superelastic response exhibited a shift to higher stress levels with increasing magnetic field magnitudes. The magnitude of this shift is determined at 4% strain (the center of the superelastic loop) and plotted as a function of the field level in Figure VI.5b. The crystal exhibits approximately 30 MPa magnetostress under 1.6 Tesla which is much higher than other MSMAs (2 to 6 MPa for NiMnGa alloys [87]). The magnetostress increases from 2.5 MPa to 30 MPa when the applied magnetic field increases from 0.4 Tesla to 1.6 Tesla. In these alloys, the magnetization of martensite and austenite saturates at an applied field of around 0.5 Tesla (refer to figure on page 144). In order to determine the rate of increase in the transformation stress with field without considering the initial non-linear region due to saturation, the points for 0.4 Tesla and above are taken into account and the transformation stress (or magnetostress) vs. magnetic field ($\Delta\sigma / \Delta H$) slope is determined as 22.9 MPa/Tesla. In other words, up to the saturation field, the difference between MAEs of austenite and martensite is responsible for magnetostress. On the other hand, above the saturation field, field dependence is expected to be linear as can be seen in Figure VI.1 due to the Zeeman energy being the responsible energy contribution for the increase in transformation stress level.

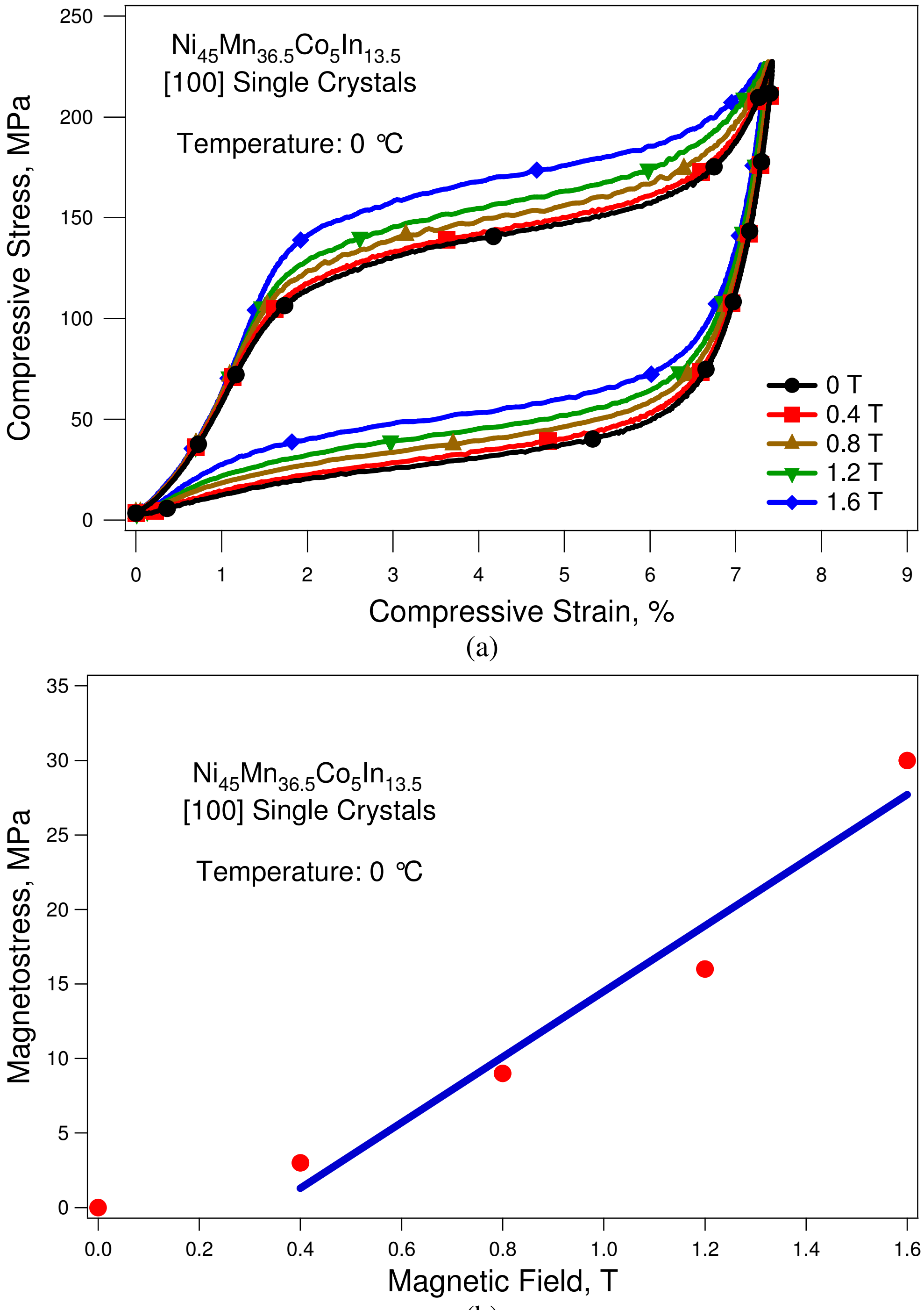

(a)

(b)

Figure VI.5. Effect of magnetic field on PE response of $Ni_{45}Mn_{36.5}Co_5In_{13.5}$. The magnetic field was applied along [011] orientation, perpendicular to the applied stress direction of [100], prior to loading and kept constant throughout the experiment. (a) Experimental results at 0 ^{o}C, and (b) the increase in transformation stress (determined at 4% strain) vs. magnetic field plot [126].

VI.3 Magnetization Response under Isothermal & Constant Applied Field Conditions

Figure VI.6a shows the effect of applied magnetic field on the magnetization response of $Ni_{45}Mn_{36.5}Co_5In_{13.5}$ single crystals as a function of temperature. A magnetic field of 0.05 Tesla was applied at 390 K and the sample was cooled down to 100 K and heated back to 390 K. Then, the field was increased to 3, 5 and 7 Tesla and the thermal cycling was repeated in each case. Under 0.05 Tesla, the forward *A*→*M* transformation starts at 230 K (M_S) and finishes at 205 K (M_F) upon cooling. The reverse *M*→*A* transformation starts at 225 K (A_S) and finishes at around 250 K (A_F) upon heating. The transformation is reversible with a minute thermal hysteresis (~20 K). As the applied magnetic field increases, the transformation temperatures shift to lower temperatures, e.g. M_S decreases from 230 K to 165 K as the field increases from 0.05 to 5 Tesla. Here, the applied magnetic field favors the phase with the higher saturation magnetization (ferromagnetic austenite in this case). Additional undercooling is needed to supply the required chemical energy to overcome the magnetic energy opposing phase transformation.

Figure VI.6b shows the change in transformation temperatures as a function of magnetic field extracted from the experiments partially shown in Figure VI.6a. The change in A_S is approximately -12.6 K/Tesla. As a benchmark, the same value is around +6 K/Tesla for NiMnGa alloys [109] since martensite has slightly higher saturation magnetization than that of austenite in NiMnGa alloys which yields to a positive temperature change.

For applied magnetic fields higher than 3 Tesla, the magnetization of austenite is saturated and does not increase with the field at all temperatures. During forward transformation, the magnetization of the single crystal drops from 130 emu/g to 30 emu/g under 3 Tesla, and to 100 emu/g under 5 Tesla upon transformation. Under 7 Tesla, there was no change in magnetization for this particular sample and thus, no transformation down to 100 K.

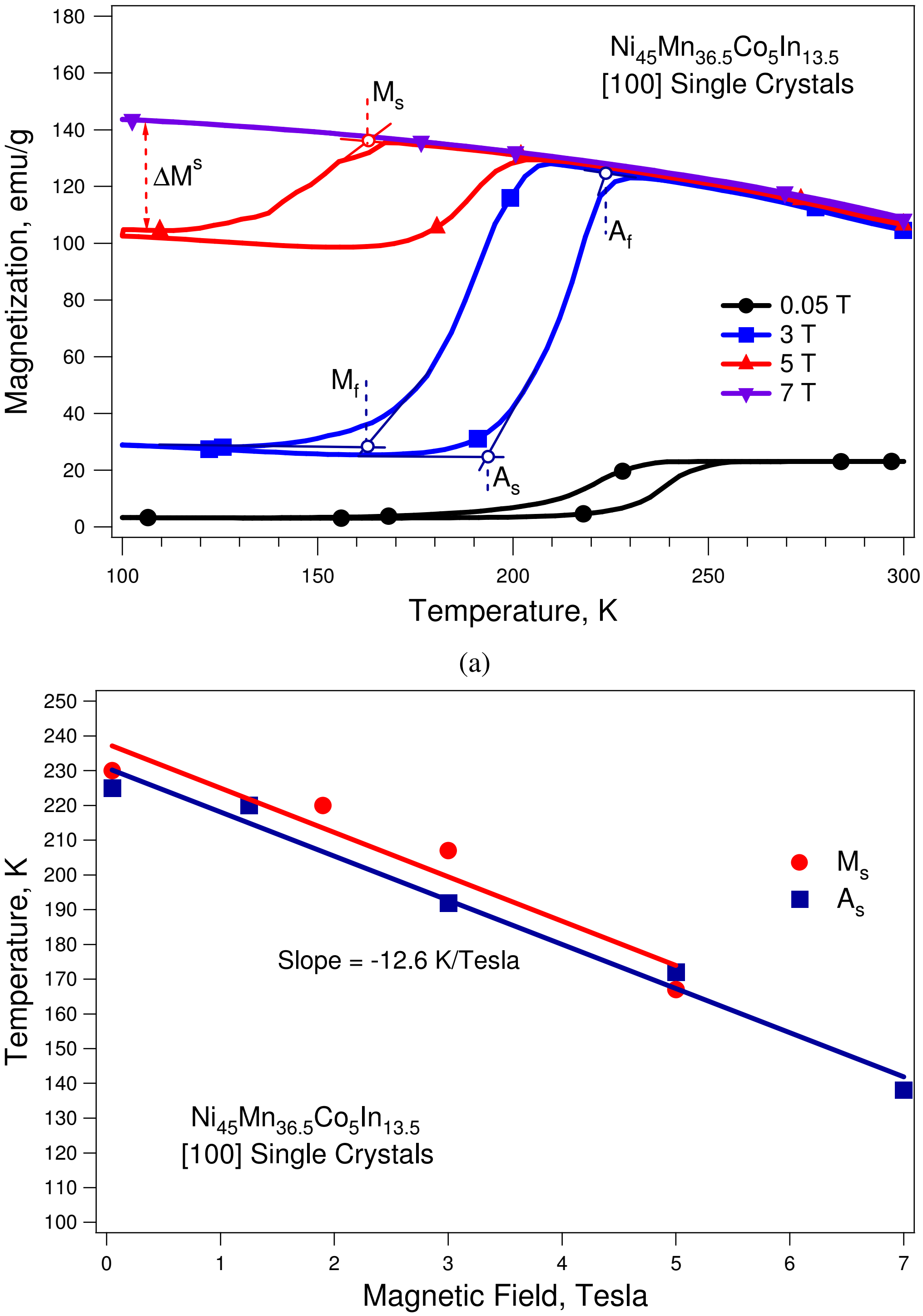

Figure VI.6. (a) Change in magnetization of $Ni_{45}Mn_{36.5}Co_5In_{13.5}$ single crystals oriented along the $[100]$ orientation as a function of temperature under different constant applied magnetic fields. (b) Change in transformation temperatures as a function of magnetic field extracted from the experiments partially shown in Figure VI.6a [126].

The increase in magnetization at low temperatures with increasing constant field upon the transformation can be due to either partial transformation of austenite to martensite or an anomalous increase in the magnetization of martensite. Ito *et al* [145] observed a similar behavior in a $Ni_{45}Mn_{36.7}Co_5In_{13.3}$ alloy and they attributed this behavior to the former, i.e. to the kinetic arrest of martensitic transformation. They argued that there is an abnormal change in entropy and extremely low mobility of phase interfaces, resulting in lack of complete phase transformation at low temperatures. Nevertheless, the reason for such low mobility under high fields and at low temperatures is not known.

A parallel study on $Ni_{50}Mn_{34}In_{16}$ polycrystals by Krenke *et al* [136] did not report a similar increase in low temperature magnetization after transformation under high magnetic fields. The degree of change in magnetization due to martensitic transformation (i.e. ΔM^S: the difference between the magnetization right below M_F and the magnetization right above M_S as shown in Figure VI.6a) continuously increases with increasing magnetic field in the $Ni_{50.3}Mn_{33.8}In_{15.9}$ alloy polycrystals and then it saturates above 1 Tesla as seen in Figure VI.7. However, it first increases and then decreases with increasing field in the present single crystals with *Co* addition due to the partial transformation of austenite to martensite. The comparison in Figure VI.7 indicates the strong influence of *Co* addition on the kinetic arrest of martensitic transformation in NiMnIn alloys which requires further investigation.

Figure VI.8a shows the magnetization vs. temperature cooling curve under 7 Tesla (the curve between #1 and #2) with only a small amount of martensitic transformation below 150 K. When the field is reduced down to 0 Tesla at 50 K, the magnetization vs. field curve (the curve between #2 and #3) in Figure VI.8b demonstrates that the magnetization starts to decrease at a field level considerably above the saturation fields of both austenite and martensite. Thus, this should be a consequence of an austenite to martensite phase transformation upon field removal. When the field is increased to 7 Tesla again at 50 K, the magnetization vs. field curve (between #3 and #4) shows a typical saturation curve of martensite. Heating the specimen to room temperature under 7 Tesla (the curve between the #4 and #6) causes martensite to austenite reverse transformation above 150 K with the austenite magnetization level being exactly the same as during the cooling response under 7 Tesla.

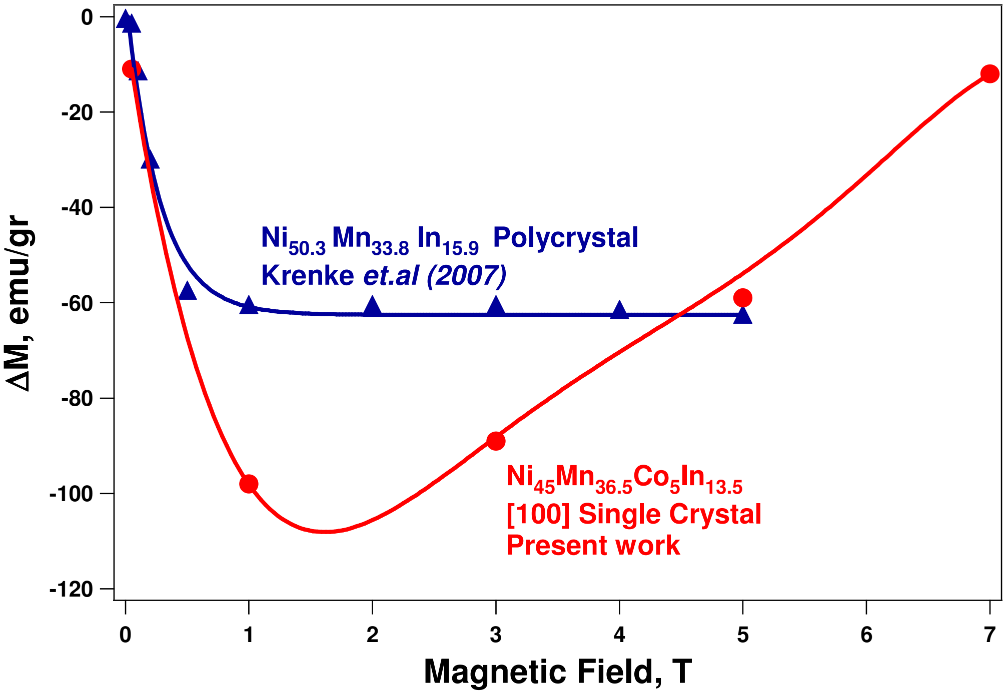

Figure VI.7. Comparison of change in magnetization between austenite and martensite upon transformation (defined in Figure VI.6a) in $Ni_{50.3}Mn_{33.8}In_{15.9}$ and $Ni_{45}Mn_{36.5}Co_5In_{13.5}$ alloys showing the effect of *Co* addition on the kinetic arrest of martensitic transformation [126].

Apparently, cooling under a field of 7 Tesla causes the kinetic arrest of the transformation even if the temperature level is much lower than what one would expect for the transformation start temperature under the field, according to Figure VI.6.

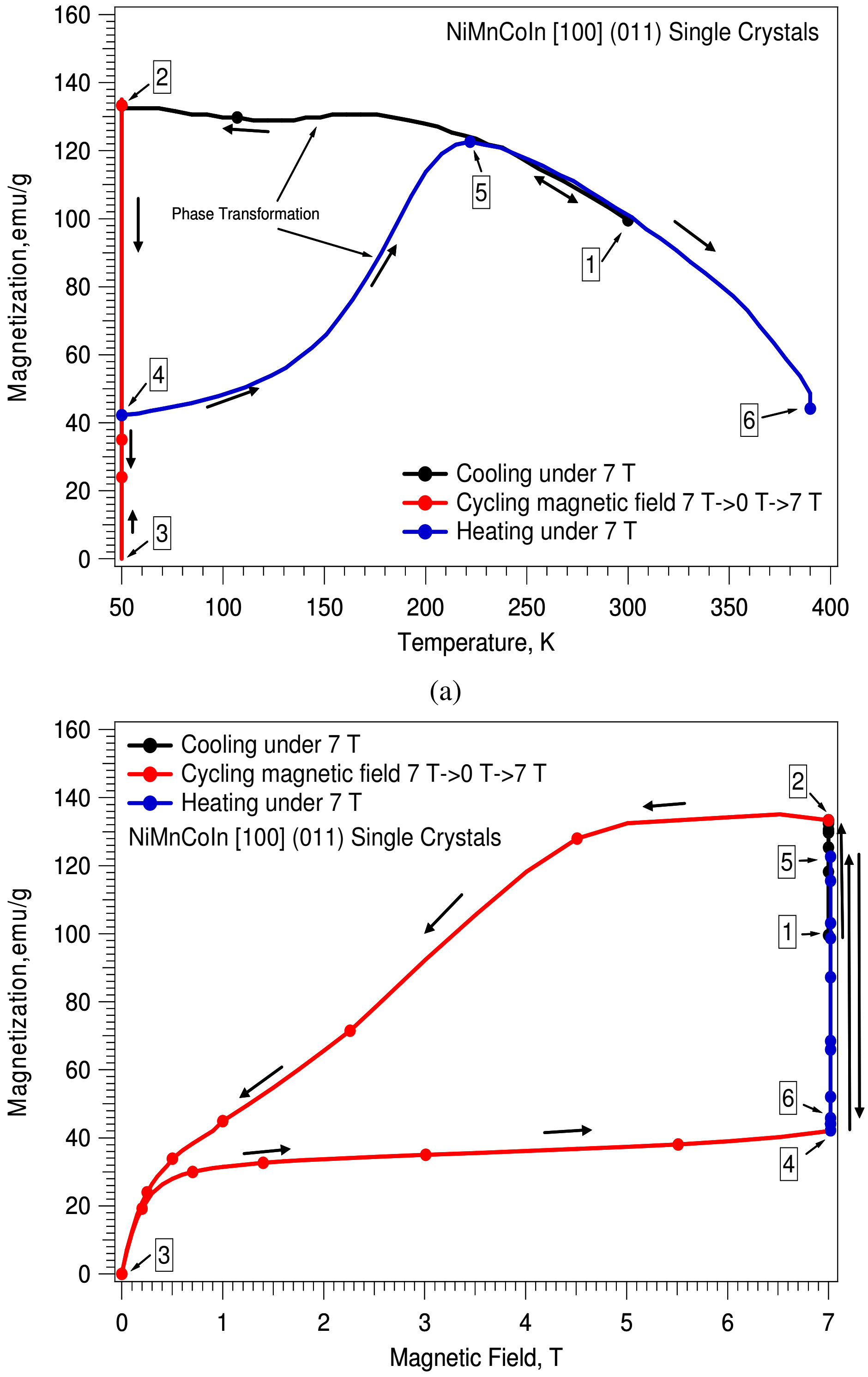

(a)

(b)

Figure VI.8 Change in magnetization of $Ni_{45.7}Mn_{35.6}Co_{4.8}In_{13.8}$ single crystal as a function of (a) temperature (b) magnetic field. Sample is cooled down from 300 K to 50 K. The sequence of numbers denotes the path of magnetic field application [126].

On the other hand, martensite happens to be the stable phase at that low temperature under zero field (upon removal of the magnetic field). Reloading up to 7 Tesla is not sufficient to induce the reverse transformation at 50 K. The reverse transformation temperature (A_S) upon heating under 7 Tesla is close to what one would expect from Figure VI.6b according to the linear slope.

The shift in transformation temperatures with magnetic field provides a distinguishing chance to induce reversible phase transformation within a certain temperature range. Figure VI.9 shows the change in magnetization of the $[100]$ single crystal as a function of applied magnetic field at 350, 250, 220 and 140 K.

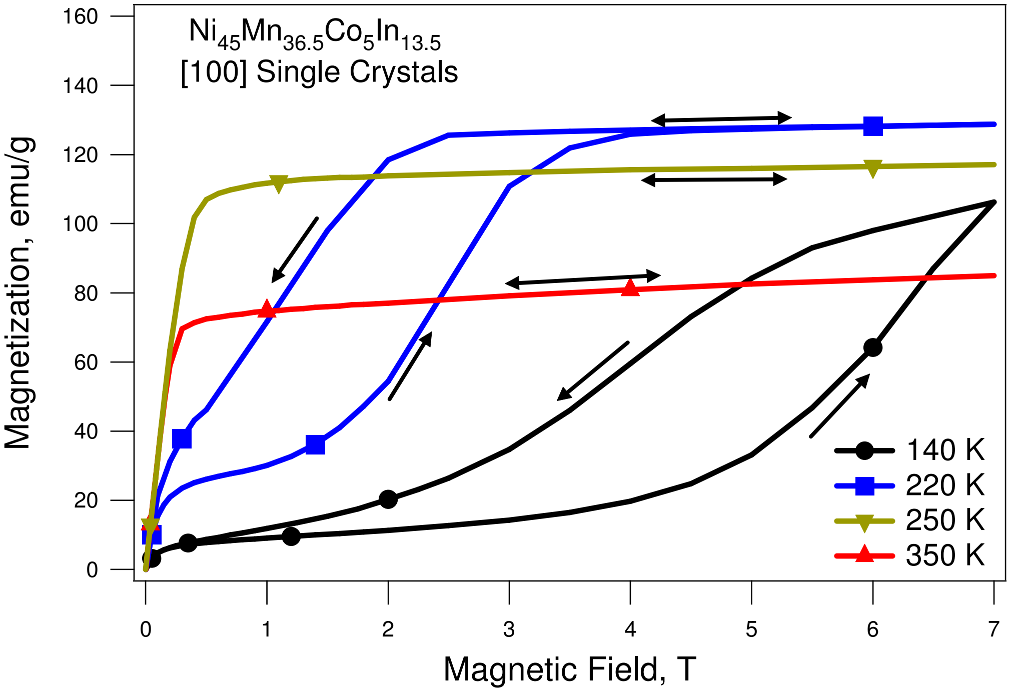

Figure VI.9. Change in magnetization of $Ni_{45}Mn_{36.5}Co_5In_{13.5}$ single crystals oriented along the $[100]$ orientation as a function of applied magnetic field at different temperatures demonstrating fully reversible magnetic field-induced phase transformation [126].

At 350 and 250 K, the single crystal is in the austenitic phase and it shows a typical response expected of a ferromagnetic material; i.e., the magnetization increases quickly and saturates at low fields (< 0.5 Tesla).

At 220 K, most of the material is in the martensite state with a small amount of coexisting austenite according to Figure VI.6a. The initial magnetization response up to 1 Tesla that seems to saturate at 25 emu/g is due to the magnetization of martensite and residual austenite. Further increase in the applied field results in a sudden alteration in magnetization due to $M \rightarrow A$ reverse transformation. At 4 Tesla, the magnetization saturates again where the structure becomes fully austenite. Removal of the magnetic field results in forward transformation $A \rightarrow M$ with a hysteresis of about 1.5 Tesla. At 140 K, the magnetization response is similar to the one at 220 K where the initial saturation magnetization is lower since the structure becomes fully martensite.

The necessary magnetic field for the reverse phase transformation at 140 K is higher than the one at 220 K since the sample temperature is much lower than the A_S under zero field and more magnetic energy is needed to initiate and support austenite formation. In this case, the reverse transformation is not complete up to 7 Tesla. Upon unloading, austenite to martensite transformation starts immediately, continues at a faster rate below 5.5 Tesla and is completed just below 1 Tesla. Clearly, loading-unloading of the magnetic field can trigger fully reversible phase transformation without any stress-assistance which is promising for actuator applications.

VI.4 Crystal Structure & Lattice Parameters of Single Crystalline $Ni_{45}Mn_{36.5}Co_5In_{13.5}$

In order to determine the crystal structure and lattice parameters of the austenite and martensite phases of our NiMnCoIn single crystals, 2D diffraction patterns were collected as a function of temperature using synchrotron high-energy x-ray diffraction (XRD) technique which provide *in-situ* tools for advancing the understanding of many physical processes such as deformation, phase transformation, and recrystallization [65].

Patterns covering a large reciprocal space confirmed that the austenite phase has $L2_1$ structure with Fm3m symmetry, as also reported in the literature [61, 130]. Through analysis of the peak positions seen in Figure VI.10, the austenite lattice constant was determined to be a= 0.5979 nm at room temperature.

The single crystal was then cooled down to 180 K ($< M_F$) where it became completely martensitic. The martensite demonstrated a modulated and more complex structure than austenite which was determined to be a (12M) six-layered monoclinic structure with lattice parameters of a= 0.439 nm, b= 0.557 nm, c= 2.593 nm, and β= 93.82^{o}[126].

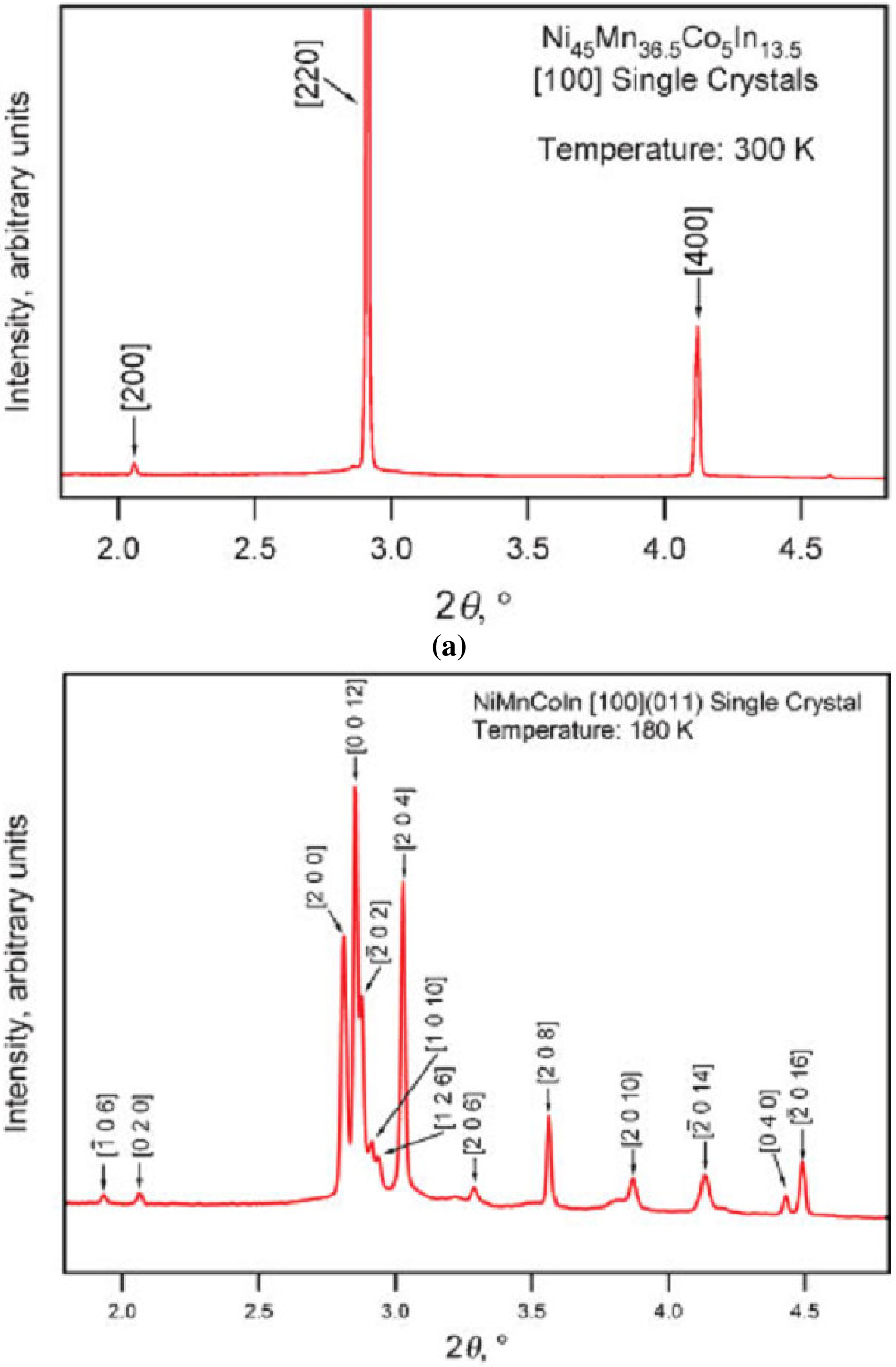

(a)

(b)

Figure VI.10. Intensity vs. 2θ graphs of $Ni_{45}Mn_{36.5}Co_5In_{13.5}$ single crystal in (a) austenite phase at 300 K with $L2_1$ cubic (b) martensite phase at 180 K with 6-layered monoclinic structures [126].

VI.5 Prediction of Magnetostress in NiMnCoIn Alloys

Actuation strain was mentioned before as a figure of merit on the performance of MSMAs when employed in actuator applications. In NiMnCoIn alloys, the actuation strain is a consequence of the phase transformation mechanism and orientation dependent as well. The orientation dependence of the shape memory strain is mainly due to the crystallographic relation between the applied stress direction and possible crystallographic transformation systems. A crystallographic system consists of a transformation shear plane (a.k.a. habit plane) and a shear direction which characterizes the deformation geometry during the parent to martensite transformation. Using “Energy Minimization Theory”, it is possible to determine habit plane and direction as well as twinning shear and direction for given lattice parameters and detailed discussions on the pertaining theoretical framework can be found elsewhere [146, 147].

In NiMnCoIn alloys, parent phase has $L2_1$ structure while martensite has 5-layered (10M) or seven-layered (14M) modulated monoclinic or 6-layered (12M) modulated orthorhombic crystal structures [61, 66, 126]. There are total of 12 variants for cubic to monoclinic phase transformation [146]. It is important to note that for NiMnGa alloys (Chapter IV, Figure IV.1) the stress required for detwinning is very low compared to NiMnCoIn [112] and NiTi [146], and for these alloys it is better to compare the experimental results with the theoretical results with detwinning.

The lattice parameters determined from high energy X-ray diffraction [126] are used to determine volume fraction, habit plane normal, transformation shear and twinning direction and the achieved results on the experimental and calculated theoretical transformation strains are summarized in Table VI.1 [126].

Table VI.1 Comparison of experimentally observed and theoretically calculated phase transformation strains of $Ni_{45}Mn_{36.5}Co_5In_{13.5}$ single crystals under compression along four orientations [126].

	% Strain for $L2_1$ → 12M phase transformation		
	Experimental	**Theoretical**	
	SME	**Transformation**	**Detwinned**
$[100]$	6.5	6.61	6.61
$[123]$	---	4.04	4.14
$[110]$	---	3.25	3.47
$[111]$	---	1.22	1.22

Provided that the change of critical stress with temperature (the slope of CC curves) and the change of transformation temperature with applied field are known, it is probable to calculate the magnetostress as a function of applied magnetic field. Recalling Eqn. VI.1, the change in critical stress with temperature is written as;

$$\frac{\Delta\sigma}{\Delta T} = -\frac{\Delta H_{enth}}{T_o \varepsilon_{tr}^{\max}} \qquad \text{(Eqn. VI.1)}$$

where ΔH_{enth} is the change in enthalpy during transformation, T_o is the chemical equilibrium temperature, and $\varepsilon_{tr}^{\max}$ is the transformation strain. The transformation strains of single crystals can be calculated or can be determined from pseudoelasticity and/or isobaric thermal cycling experiments. The change in transformation temperatures with applied field can be determined from the magnetization results as shown in Figure VI.6. Then the magnetostress as a function of field can be determined as;

$$\frac{\Delta\sigma}{\Delta H} = \frac{\Delta\sigma}{\Delta T} x \frac{\Delta T}{\Delta H} \qquad \text{(Eqn. VI.2)}$$

Calculated values of the compressive transformation strains for the $[100]$, $[123]$ $[110]$ and $[111]$ orientations are listed in Table VI.1. The theoretical strain value of 6.61% for the $[100]$ direction is in good agreement with our experimental result [68] reported in the previous section, in Figures VI.3 and VI.4. From Figure VI.3b, the change in critical stress with temperature can be determined as 2.1 MPa/K. CC slopes for other orientations can be calculated assuming the same enthalpy and chemical equilibrium temperature for all samples since they are not a function of orientation. The change in transformation temperatures as a function magnetic field can be determined from Figure VI.6 as -12.6 K/Tesla. This value is considered to be orientation independent as well, thus neglecting the effect of MAE. Table VI.2 shows the calculated magnetostress per unit field as a function of orientation. The calculated $\frac{\Delta\sigma}{\Delta H}_{theoretical}$ for the $[100]$ orientation is 26.6 MPa/Tesla, and it is fairly close to $\frac{\Delta\sigma}{\Delta H}_{\exp erimental}$ of 22.9 MPa/Tesla from Figure VI.5b [126].

Table VI.2 Orientation dependence of magnetostress as a function of applied field. The symbol * indicates experimental values where all others are theoretical values [126].

	$\varepsilon_{tr}^{\max}$ %	$\frac{\Delta\sigma}{\Delta T}$ **MPa/K**	$\frac{\Delta T}{\Delta H}$ **K/Tesla**	$\frac{\Delta\sigma}{\Delta H}_{theoretical}$ **MPa/Tesla**	$\frac{\Delta\sigma}{\Delta H}_{\exp erimental}$ **MPa/Tesla**
$[100]$	6.61	2.1*	12.6*	26.5	22.9*
$[123]$	4.14	3.35	12.6*	42.2	---
$[110]$	3.47	4.0	12.6*	50.4	---
$[111]$	1.22	11.3	12.6*	143.4	---

The difference between the experimental and theoretical values is attributed to the demagnetization effect that would result in a lower magnetic field inside the material and to the difference between the theoretical calculations and experimental observations of the transformation strain [126]. It is important to note that the value for $\frac{\Delta\sigma}{\Delta H}_{theoretical}$ along the $[111]$ orientation (143.4 MPa/Tesla) is more that 5 times larger than that in the $[100]$ orientation (26.5 MPa/Tesla). However, the transformation strain along the $[100]$ orientation (6.61%) is more than 5 times larger that along the $[111]$ orientation (1.22%). In the light of these comparisons, it can be inferred that, specific to the demands of application, an orientation with superior actuation stress or actuation strain can be chosen among the listed above.

VI.6 Evaluation of Magnetostress & Work Output Levels of NiMnCoIn as Compared to Other Active Materials

Magnetostress is one of the key parameters to assess the potential of MSMAs for actuator applications. Furthermore, it is directly related to the actuation stress and is defined by the change in the critical stress levels for phase transformation (or for martensite variant reorientation in the case of NiMnGa) upon the application of magnetic field. Figure VI.11 displays a comparison on the magnetostress levels as a function of magnetic field. Compared data are from our present study for phase transformation along the $[100]$ (experimental) and $[111]$ (predicted) orientations in the NiMnCoIn alloy, and from the literature on NiMnGa alloys for both phase transformation and variant reorientation [52, 74, 95, 100, 148-150]. In the case of NiMnGa alloys, magnetostress increases linearly with the field at first and then saturates above a certain field value. The reason for this is the MAE being the driving force behind the magnetostress (see Figure VI.1). Since MAE is limited with the saturation field so is the magnetostress. However, in the case of NiMnCoIn alloys, magnetostress always increases with applied magnetic field since there is no limit for the contribution of the ZE (refer to Figure VI.1). Figure VI.11 shows that for magnetic fields above 0.7 Tesla, magnetostress of NiMnCoIn alloys is larger than those of the other MSMA systems. When a magnetic field of 1.6 Tesla is applied, the magnetostress for phase transformation in the NiMnCoIn alloy is 30 MPa. On the other hand, at the same magnetic field level, it is 5.7 MPa [95] and 1.5 MPa [149] through variant reorientation in the 10M and 14M martensites of NiMnGa alloys, respectively. Also, for the phase transformation from austenite to 10M martensite in the $Ni_{51.1}Mn_{24}Ga_{24.9}$ alloy, magnetostress is 7.6 MPa [148, 151].

The magnetic work output per unit volume, $W = \sigma \times \varepsilon$, where σ is the magnetostress and ε is the strain induced by the magnetic field, is the next figure of merit for the actuation performance of MSMAs . The maximum work output for variant reorientation in NiMnGa alloys was reported to be 156 kJm^{-3} by Karaca *et al.* [151]. The work outputs for the field-induced two-stage martensitic phase transformation in the $Ni_{51.1}Mn_{24}Ga_{24.9}$ alloy were determined as 36.4 kJm^{-3} and 160 kJm^{-3}, respectively for each stage, in our recent work [148]. In NiMnGa alloys, magnetostress stems from the MAE of martensite, only. Regardless of whether the variant reorientation or phase transformation mechanism is in action, the maximum work output will be similar. Because the saturation magnetization levels of austenite and martensite phases are about the same, it can be assumed that the ZE is negligible in the NiMnGa alloys family.

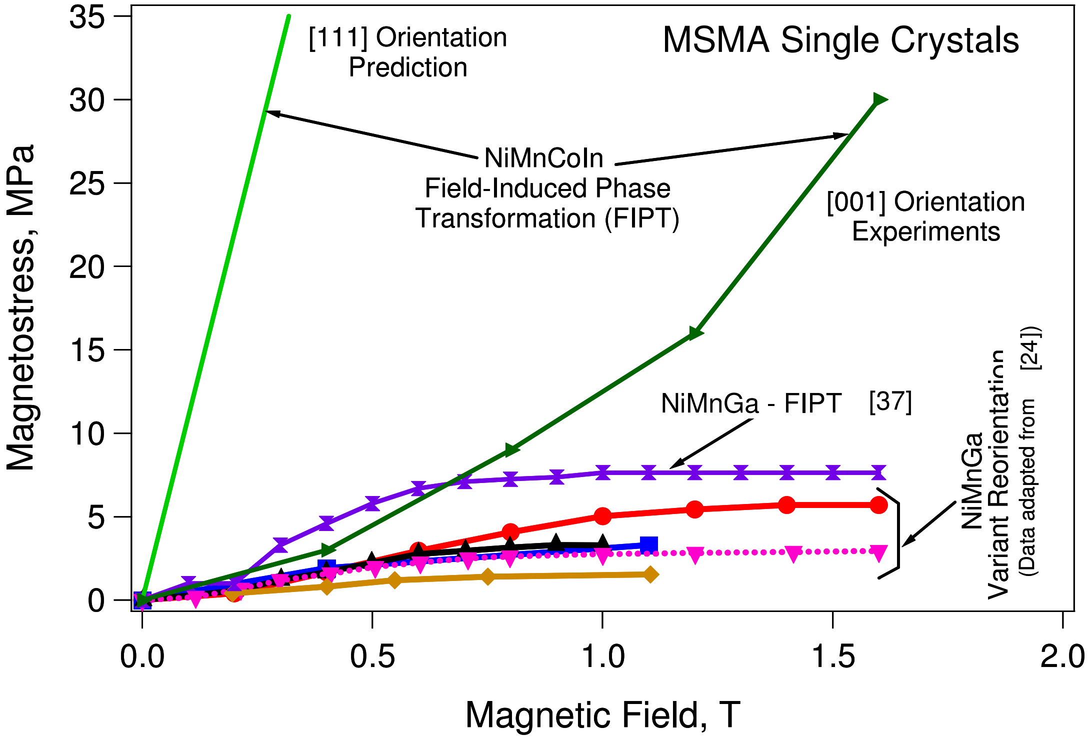

Figure VI.11. Magnetostress levels as a function of applied magnetic field for the martensitic phase transformation in the present $Ni_{45}Mn_{36.5}Co_5In_{13.5}$ single crystals, obtained from Figure VI.5 and the predictions introduced in Table VI.2, and for the phase transformation and variant reorientation of 10M and 14M martensite structures in several NiMnGa alloys extracted from the literature [52, 74, 95, 100, 148-150]. Adapted from [126].

The magnetic work output of the present NiMnCoIn alloy, on the other hand, is about 1600-1800 kJm^{-3} which is one order of magnitude higher than the work output of NiMnGa alloys [148].

Figure VI.12 provides the benchmark among the aforementioned magnetostress, MFIS, and magnetic work output levels for NiMnGa alloys from the literature and the present $Ni_{45}Mn_{36.5}Co_5In_{13.5}$ single crystals [43, 52, 88, 95, 148, 152]. It is obviously seen that the NiMnCoIn alloy demonstrates a drastically enhanced work output level, which very promising for MSMAs in actuator applications.

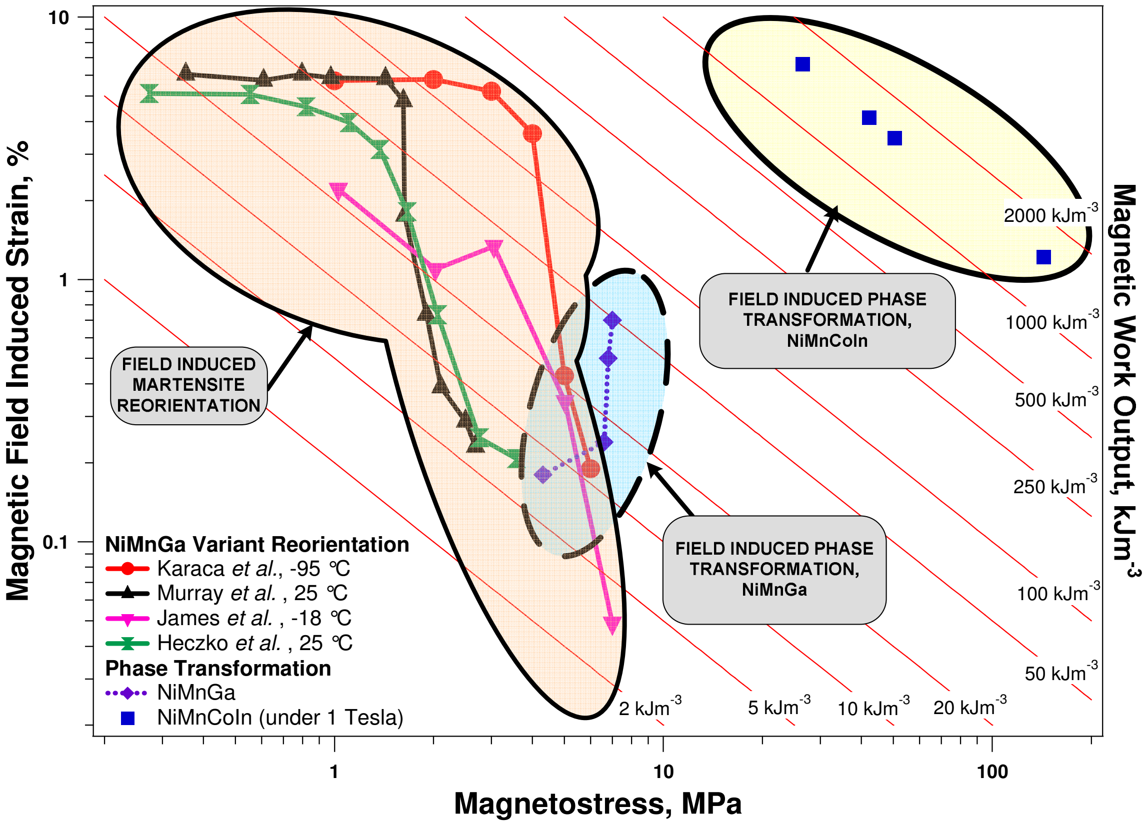

Figure VI.12. MFIS and magnetic work output vs. the magnetostress plots showing the literature data obtained to date in NiMnGa MSMAs utilizing field-induced martensite reorientation and field-induced phase transformation mechanisms, and the present results on the $Ni_{45}Mn_{36.5}Co_5In_{13.5}$ single crystals. A grid of constant magnetic work output hyperbolas ranging from 2 and 2000 kJ m^{-3} has been superimposed. Logarithmic scale is used for both axes for easy comparison. Adapted from [126].

Figure VI.13 compares the experimentally reported actuation stress, strain, and work outputs for the several different actuator materials including MSMAs. The data presented in this figure for the materials other than MSMAs are adapted from [153] and [154].

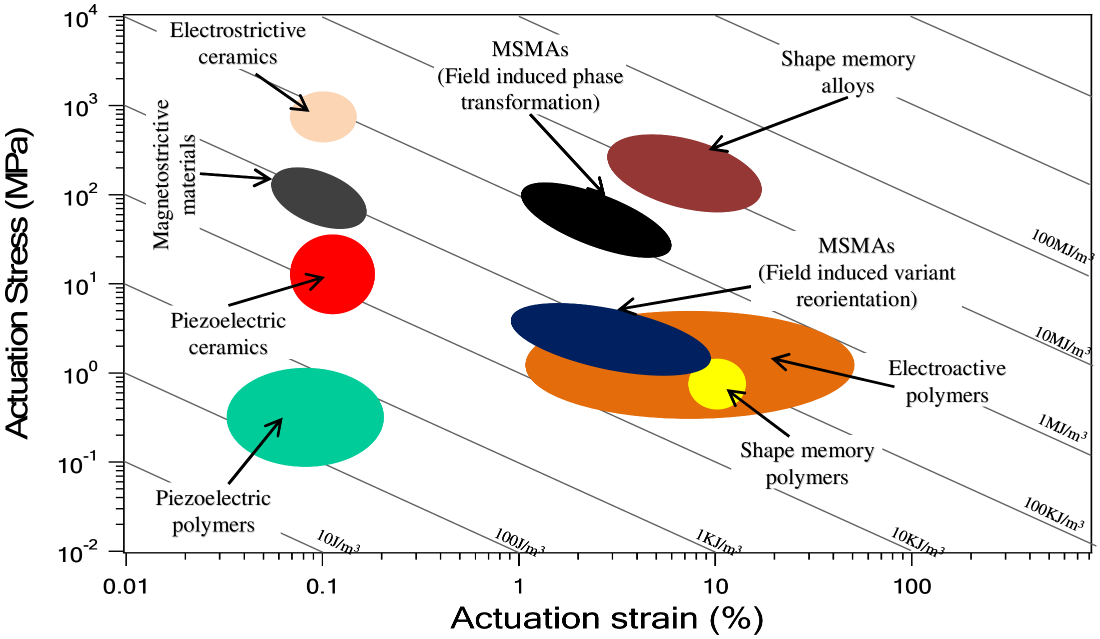

Figure VI.13. Comparison of actuation stress, actuation strain, and actuation work output levels that are reported for different active materials [153, 154] with those from MSMAs. The values resulting from the field-induced variant reorientation and phase transformation are presented separately. The results for the MSMAs showing field-induced phase transformation include experimental observations in NiMnGa alloys and the realistic estimates for the new NiMnCoIn alloys which are predicted in the present work. Adapted from [126].

We have also included in this figure, magnetostress level, MFIS, and magnetic work output for the NiMnCoIn alloy for 1 Tesla applied field. The work output levels for the NiMnCoIn alloy are not the experimental actuation work outputs but instead the magnetic work output per 1 Tesla observed in the present study. Part of the magnetic work output would be spent for dissipation during the forward and reverse phase front motion, and the remaining could be used as mechanical work output. Considering that slightly higher magnetic field levels can be applied to overcome the dissipation, the work output levels for the NiMnCoIn alloy in Figure VI.13 show a realistic estimate of the actuation work output levels that can be easily achieved in these new alloys.

In the figure, MSMAs utilizing the field-induced phase transformation mechanism for actuation fill a gap between conventional SMAs and other actuator materials. It should be kept in mind that, one advantage of MSMAs over conventional SMAs is notably faster actuation frequency which makes these materials prime candidates for high work output, high stroke, and medium frequency actuators of the future.

CHAPTER VII

SHAPE MEMORY CHARACTERISTICS OF $Ni_{40}Mn_{33}Co_{10}Al_{17}$ & $Ni_{43}Mn_{39}Co_7Sn_{11}$ POLYCRYSTALLINE METAMAGNETIC SMAs

In this chapter, isobaric thermal cycling and isothermal pseudoelastic responses of polycrystalline bulk $Ni_{40}Mn_{33}Co_{10}Al_{17}$ and polycrystalline sintered compacted-powder $Ni_{43}Co_7Mn_{39}Sn_{11}$ alloys are reported in the search of inexpensive alternatives to replace NiMnCoIn single crystalline metamagnetic shape memory alloys. Using the experimental data, stress vs. transformation temperatures phase diagrams are constructed for both materials. A detailed comparison between calculated figures of merit for actuation performance via Clausius-Clapeyron slopes from the phase diagram is presented.

VII.1 Polycrystalline Bulk $Ni_{40}Mn_{33}Co_{10}Al_{17}$ MSMA

Newly discovered Ni-Mn-*X* (*X*= *In, Sn* and *Sb*) family Heusler alloy systems where the magnetization of the martensite (*M*) phase is considerably smaller than that of the parent austenite (*A*) phase [63], and especially the *Co*-doped NiMnIn and NiMnSn quaternary alloys, attracted a lot of attention due to showing drastic changes in magnetization response in the course of martensitic transformations [61, 128, 134]. Furthermore, it was revealed that the martensitic transformation temperatures of these alloys drastically decreased by the application of magnetic fields and both alloys showed magnetic field-induced reverse transformation. An almost perfect shape memory effect induced by magnetic field (which is called as 'metamagnetic shape memory effect') was observed in NiMnCoIn single crystalline and the NiMnCoSn polycrystalline alloys near room temperature [61, 128]. In $Ni_{45}Mn_{36.5}Co_5In_{13.5}$ single crystals, oriented along $[100]$ direction of the parent phase, as reported in Chapter VI of this dissertation, a transformation strain of 5.4% via thermal cycling under 125 MPa compressive stress was realized. We also demonstrated in Chapter VI that actuation stress and work output levels in the NiMnCoIn alloys is at least one order magnitude higher than those in the conventional MSMAs. Moreover, accompanying this martensitic transformation, giant magnetoresistance (GMR) [145, 155, 156] and large magnetocaloric effects (MCE) [131, 157] have also been reported by other researchers. Thus, these alloys deserve more research for being promising candidates in actuation applications.

Regardless of being single or polycrystalline, NiMnCoIn alloys are costly due to the expensive *In* element. Brittle natures of both NiMnCoIn and NiMnCoSn alloys (especially in polycrystalline form when obtained by conventional melting) are among the major drawbacks in front of their employment in practical applications. Furthermore, the thermal hysteresis and interval during the martensitic transformation are too broad. In the line of the efforts made to address these issues, Kainuma *et al.* [129] have recently replaced *In* and *Sn* with *Al* and showed that NiMnCoAl quaternary alloys demonstrate magnetic field induced reverse phase transformation between a paramagnetic *M* phase with $L1_0$ structure and a ferromagnetic *A* phase with *B*2 structure.

Another effort made to overcome the abovementioned difficulties pertaining polycrystal structure was synthesizing of NiMnCoSn via powder metallurgy techniques [70], characterization efforts details of which will be provided in the subsequent section.

To evaluate the full potential of these new alloys for actuation applications, first, it is necessary to reveal their conventional shape memory characteristics such as transformation strain levels and stress vs. temperature phase diagram. Therefore, in this chapter, we are reporting the shape memory effect via isobaric thermal cycling and isothermal pseudoelastic response of $Ni_{40}Mn_{33}Co_{10}Al_{17}$ polycrystalline bulk and $Ni_{43}Mn_{39}Co_7Sn_{11}$ polycrystalline compacted-powder metamagnetic shape memory alloy specimens.

The $Ni_{40}Mn_{33}$ $Co_{10}Al_{17}$ (at.%) specimen was prepared by induction melting under an argon atmosphere. The polycrystalline ingot was annealed at 1373 K for 168 hours in vacuum and quenched in ice water. Several compression specimens with dimensions near to $3.0\times2.5\times5.5$ mm^3 were cut out of the annealed ingot by wire-electrical discharge machining. The latent heat of the martensitic transformation was determined using the differential scanning calorimetry (DSC) measurements, where the heating and cooling rate was 10 K/min [69].

Figure VII.1 shows the strain vs. temperature response during thermal cycling under various compressive stresses across the phase transformation temperature interval in $Ni_{40}Mn_{33}Co_{10}Al_{17}$ polycrystalline bulk specimen. The application of stress was executed at 473 K in the parent phase for all tests and the temperature was cycled between 283 and 473 K under this designated constant stress level. The level of applied compressive stress was started from 10 MPa and incrementally (by 25 MPa steps) raised for each thermal cycle up to 200 MPa.

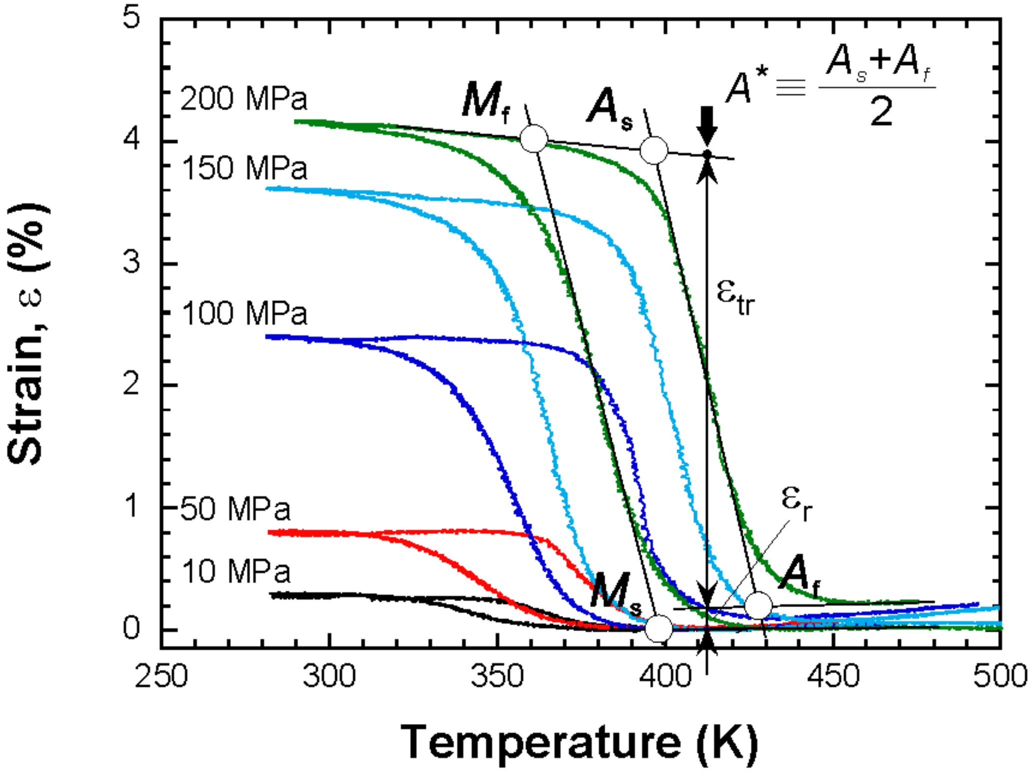

Figure VII.1 Strain vs. temperature response of the $Ni_{40}Co_{10}Mn_{33}Al_{17}$ polycrystalline alloy under various constant compressive stresses across the phase transformation temperature interval, figure adapted from [69].

In Figure VII.1, only selected data are shown for the sake of clarity. The drastic change in strain due to the transformation is observed at every stress level and the strain change increases monotonically with increasing stress. In the experiments under high stress levels, it is apparent that there is a noticeable residual strain subsequent to each thermal cycle. The martensitic transformation temperatures for $A \rightarrow M$ forward transformation (M_S and M_F) and $M \rightarrow A$ reverse transformation (A_S and A_F) were determined for each stress level, as demonstrated on the curve under 200 MPa in Figure VII.1. These transformation temperatures are plotted in Figure VII.2 for $Ni_{40}Mn_{33}Co_{10}Al_{17}$. It is important to note that for the martensitic transformation temperatures under 0 MPa, the data was acquired from other tests [129] conducted by means of a SQUID magnetometer. The data for each transformation temperature can be easily represented by a line due to its linear tendency. The slope of 4.1 MPa/K is almost the same for M_F, A_F and A_S fit lines. On the other hand, the slope of the fit line (5.6 MPa/K) for M_S turned out to be slightly greater compared to that of the others.

Similarly, the transformation strain ε_{tr} and the residual strain ε_r were defined at the temperature $A^* \equiv (A_S + A_F)/2$ using the base lines method in A and M phase regions as demonstrated on the 200 MPa curve in Figure VII.1 for $Ni_{40}Mn_{33}Co_{10}Al_{17}$. The data extracted from Figure VII.1 for ε_{tr} and ε_r are plotted in Figure VII.3a and VII.3b, respectively. ε_{tr} increases with increasing stress and saturates at around 3.6% under 200 MPa and ε_r starts to drastically increase at about 150 MPa. Therefore, the maximum transformation strain obtained from this specimen is about 3.6%.

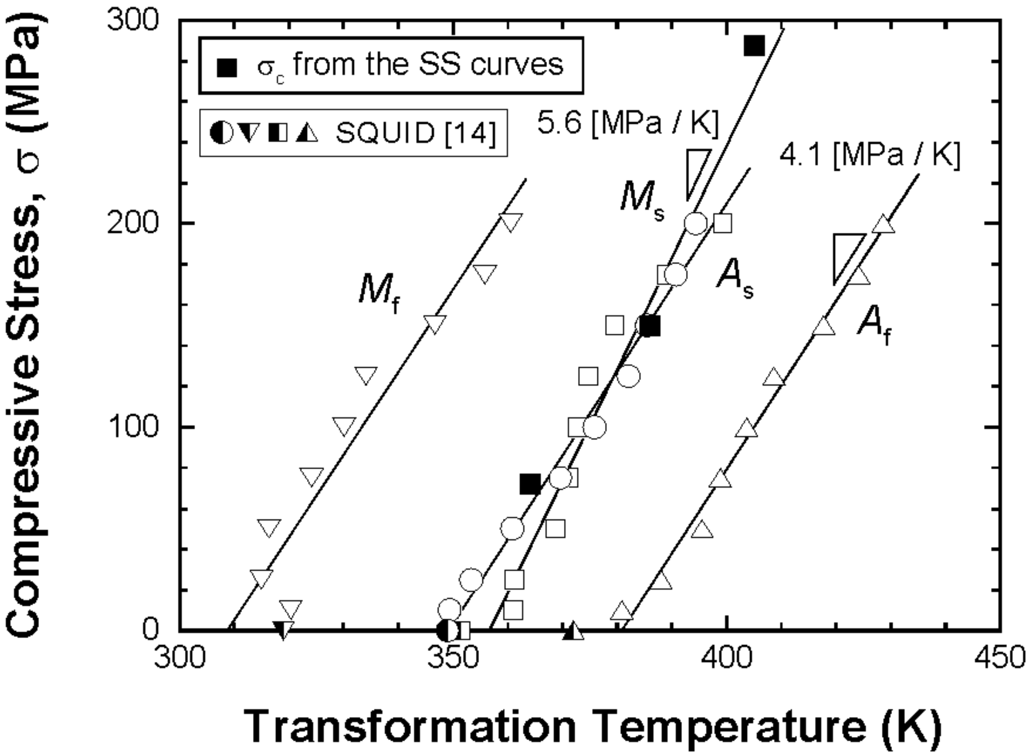

Figure VII.2 Compressive stress vs. transformation temperatures phase diagram of the $Ni_{40}Co_{10}Mn_{33}Al_{17}$ polycrystalline alloy. The values for each point were extracted from the experiments in Figure VII.1 [69].

In the case of the uniaxial stress-induced martensitic transformation, the slope of the critical stress for the onset of the transformation is given by the Clausius-Clapeyron equation [132]:

$$\frac{\partial \sigma_c}{\partial T} \approx \frac{\Delta S}{\Delta \varepsilon \cdot V_m} \qquad \text{(Eqn VII.1)}$$

where ΔS is the change in transformation entropy, $\Delta \varepsilon$ is the change in strain in the corresponding direction during the transformation and V_m is the molar volume of the specimen.

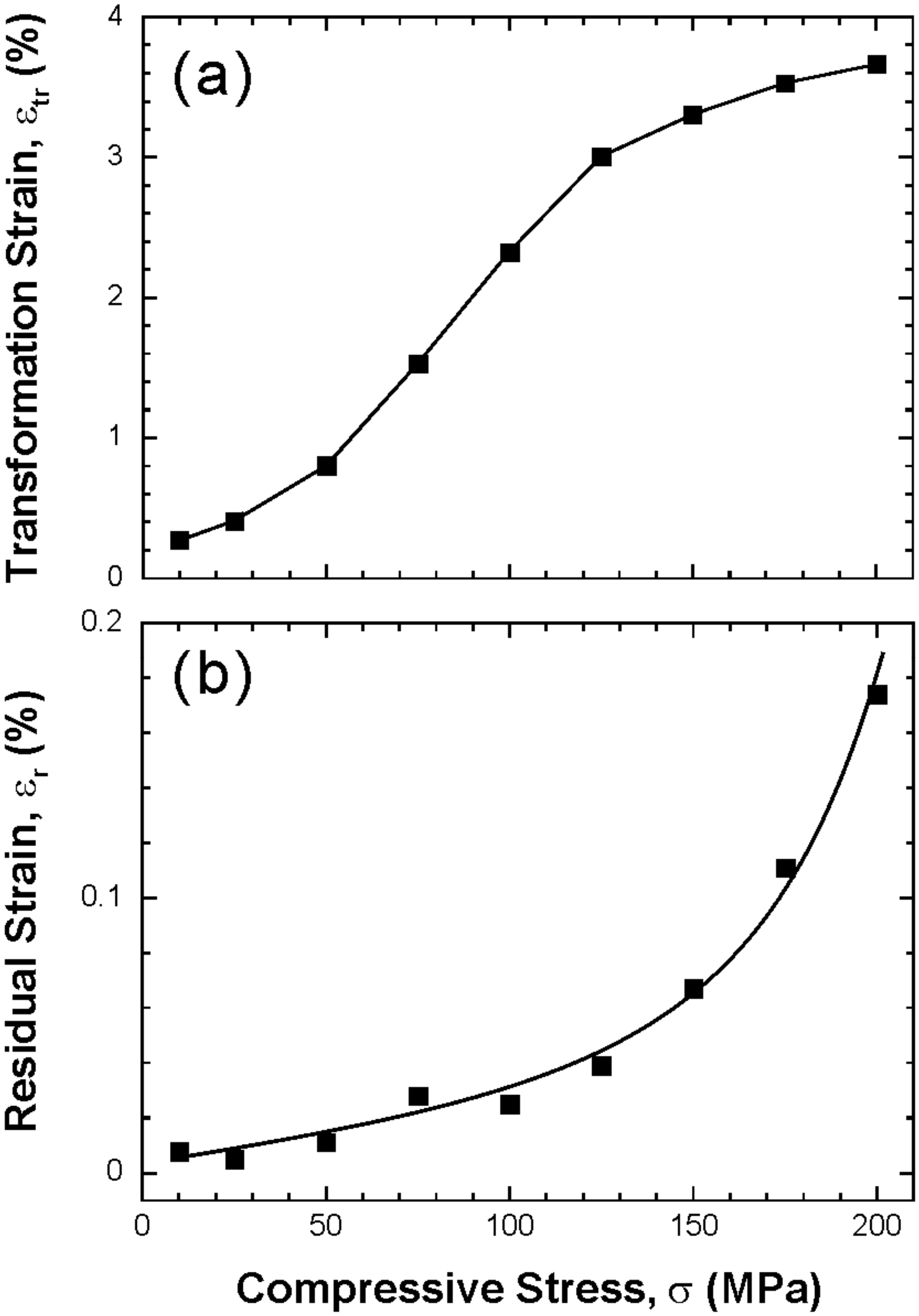

Figure VII.3 Transformation strain ε_{tr} (a) and the residual strain ε_r (b) as a function of stress level for the $Ni_{40}Co_{10}Mn_{33}Al_{17}$ polycrystalline specimen, figure adapted from [69].

For the $Ni_{40}Co_{10}Mn_{33}Al_{17}$ polycrystalline alloy in hand, a value of 4.5 MPa/K can be obtained for $\partial\sigma_c/\partial T$ from Eqn G.1 by substituting ΔS (= 1.21 J mol^{-1} K^{-1}) which is experimentally determined by $\Delta S = L/T^*$ using the latent heat L (= 463 J mol^{-1}) and the reverse transformation peak temperature T^* (= 383 K) obtained from the DSC heating curve. It is in good agreement with the experimental value 4.1 MPa/K for A_F, A_S and M_F. The reason why the slope for the M_S temperature is larger than that of the others is not clear.

The slopes of the stress vs. transformation temperature phase diagram are important in practice if the materials are to be used as magnetic actuators. For instance, if the desired actuation strain level and the temperature range of actuation are known, it would be possible to determine the magnetic field required for the onset and completion of the magnetic field induced transformation under a particular stress level. It is also possible to predict the magnetostress level achievable in this material using the following relation [126]:

$$\frac{\partial\sigma_c}{\partial H} = \frac{\partial\sigma_c}{\partial T}\cdot\frac{\partial T}{\partial H} \qquad \text{(Eqn. VII.2)}$$

where H is the magnetic field applied to the specimen. In the present case, $\partial\sigma_c/\partial T$ (= 4.1 MPa/K) has already been determined in the phase diagram (Figure VII.2) and the $\partial T/\partial H$ (= 3.6 K/Tesla) can be estimated using the previously published data from the thermal cycling experiments in SQUID magnetometer under the magnetic fields of 0.05 and 7 Tesla [129]. From these values, the magnetostress $\partial\sigma_c/\partial H$ is estimated to be 14.8 MPa/Tesla for the $Ni_{40}Mn_{33}Co_{10}Al_{17}$ polycrystalline bulk specimen. This magnetostress level, a direct indication of the achievable actuation stress per unit applied field in this material, is significantly higher than what is reported for NiMnGa single crystalline MSMAs, i.e. < 5MPa [95], where the field-induced martensite reorientation is the mechanism responsible for MFIS. Furthermore, it is surprisingly close to magnetostress levels of the $[100]$ oriented NiMnCoIn single crystalline MSMAs at 20 MPa/Tesla [126].

Figure VII.4 shows the stress vs. strain pseudoelastic curves for the NiMnCoAl polycrystalline specimen, where a compressive strain of about 2.5% was applied at 364, 386 and 405 K. At every temperature, an almost perfect pseudoelastic behavior with full recovery of the applied strain is confirmed. The critical stress σ_c for the stress-induced martensitic transformation increases with increasing temperature, being consistent with the plot of the M_S temperature under the fixed stress levels shown in Figure VII.2.

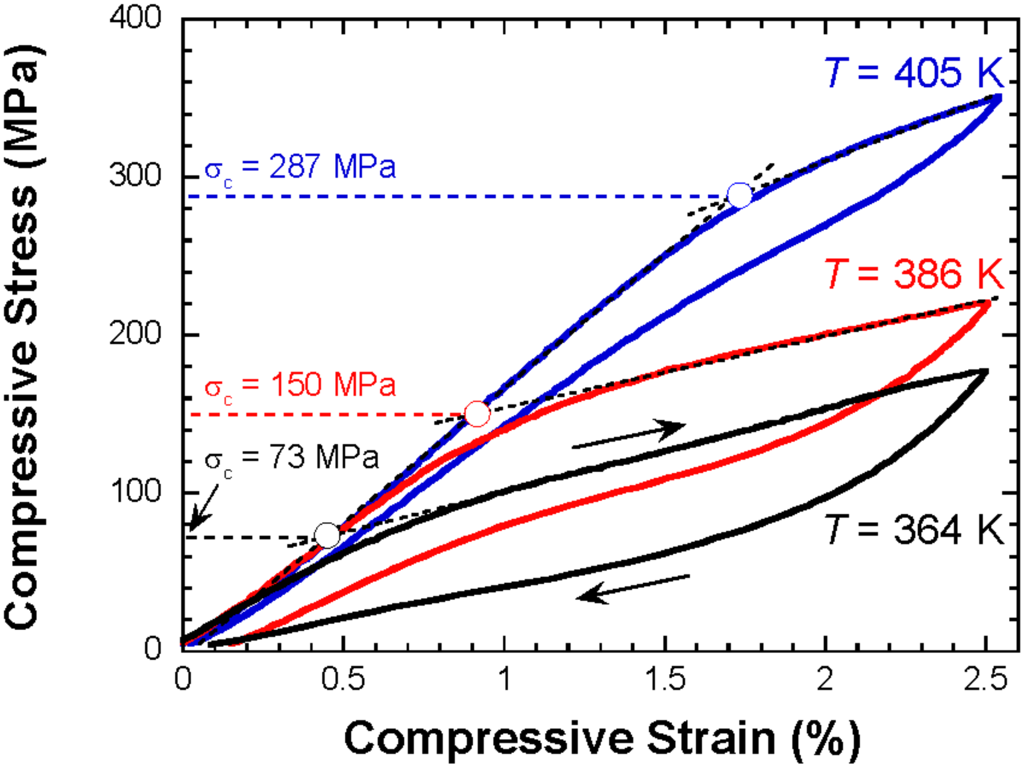

Figure VII.4 Compressive stress-strain response of the $Ni_{40}Co_{10}Mn_{33}Al_{17}$ polycrystalline specimen at 364, 386 and 405 K showing almost perfect pseudoelastic behavior, figure adapted from [69].

Figure VII.5 demonstrates the trend in thermal hysteresis as a function of applied compressive stress in the course of isobaric thermal cycling tests. The temperature hysteresis was evaluated at the mid point of transformation strain value on each heating cooling curve. As clearly seen in Figure VII.5, temperature hysteresis increases following a linear trend from 10 MPa to 100 MPa, then saturates between 100 MPa and 150 MPa. Finally, with the further increasing stress level, it starts declining.

As explained in detail in Chapter VI, large hysteresis or high-energy dissipation in SMAs arises from structural defect formation, such as dislocations, during transformation and frictional energy spent on the movement of phase fronts and on multiple phase front interactions. The individual contributions of these factors on the hysteresis depend on the lattice compatibility between transforming phases, their elastic moduli and strength, and the lattice friction, which is dictated by the crystal structure and stoichiometry. If transforming phases are relatively soft, lattice incompatibility would be mainly accommodated with irreversible local defect generation which increase thermal hysteresis [142]. If they are strong, it could be accommodated elastically or with internal twin formation in martensite. Since, in the present cases, there is some irrecoverable strain during thermal cycling, we conclude that the transforming phases have relatively lower strength with some irrecoverable defect generation. In addition, multiple phase front interactions, especially around grain boundaries, can be expected to be more prominent in the present polycrystalline materials and increase frictional energy dissipation. Furthermore, different levels of volume fractions in neighboring grains may delay the relaxation of stored elastic energy of transformation due to the need to accommodate the large transformation shape change allover the polycrystalline specimen when compared to single crystalline materials. This should lead to additional dissipation, contributing to the overall hysteresis.

Thus, in Figure VII5, thermal hysteresis increases from around 20 ^{o}C to 40 ^{o}C with increasing stress from 10 MPa to 125 MPa. Upon further stress increase, the number of variant interactions is reduced, as is the dissipation and hysteresis, since most of the sample transforms to single martensitic variant structures within each respective grain.

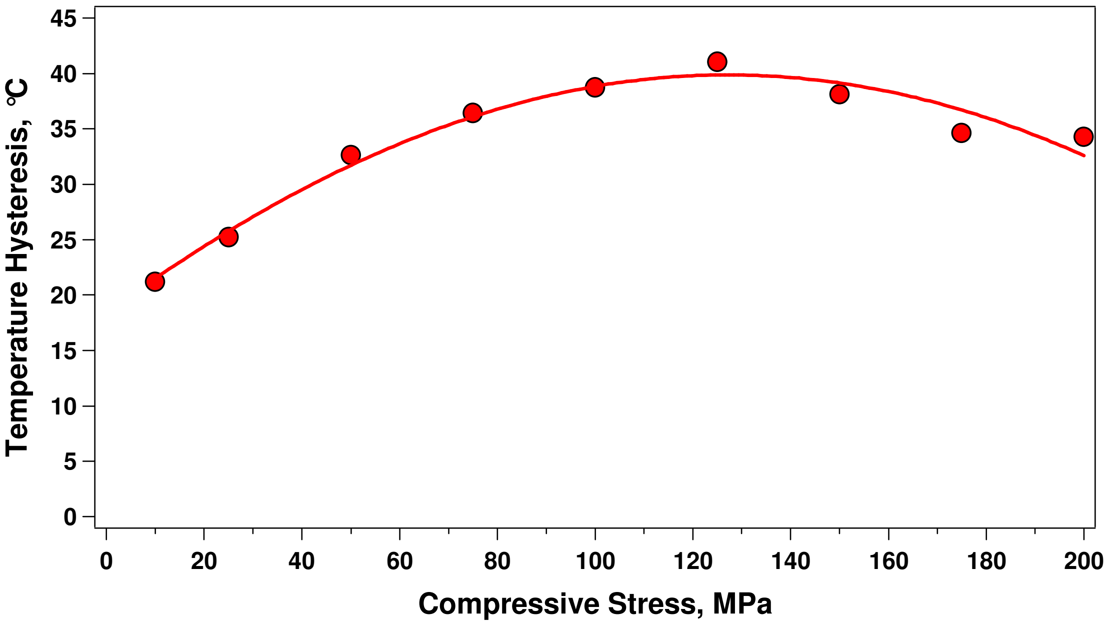

Figure VII.5 Change in temperature hysteresis as a function of compressive bias stress in $Ni_{40}Co_{10}Mn_{33}Al_{17}$ polycrystalline bulk specimen. The values for each point were derived from the thermal cycling experiments.

In addition, the local internal stresses within each grain cannot sufficiently oppose the high external stresses in biasing the single variant. Therefore, for stresses 125 MPa and higher, the sample transforms to a single variant and the maximum ε_{tr} is reached. The decrease in hysteresis with stresses above 125 MPa, even though ε_{tr} saturates (see Figure VII.3a), can be attributed to the uneven change in lattice parameters of the phases with increasing stress and temperature. Lattice parameters are a function of composition, temperature and stress, and can vary differently with temperature and stress for martensite and parent phases [143]. The compatibility between transforming phases is usually dictated by lattice parameters and crystal structures of these phases [144]. Increasing stress alters the lattice parameters of the phases disproportionately thus leading to a change in compatibility and a reduction in thermal hysteresis with increasing stress, until plasticity or some other dissipative mechanisms become more pronounced.

In summary, the stress vs. strain curves in Figure VII.4 indicate that the NiMnCoAl polycrystalline alloys have some ductility, much better than those in the polycrystalline NiMnCoIn and NiMnCoSn [62, 69] alloys, and exhibit not only shape memory effect, but also perfect pseudoelasticity. The NiMnCoAl alloy, in which the magnetic field-induced reverse transformation has been confirmed [129], is expected to display metamagnetic shape memory effect, as well. The NiMnCoAl polycrystalline alloys sound potent in providing a relatively inexpensive and more ductile alternative to single crystalline NiMnCoIn metamagnetic shape memory alloys.

VII.2 Characterization Results for $Ni_{43}Mn_{39}Co_7Sn_{11}$ Polycrystalline Compacted-Powder MSMA

The $Ni_{43}Mn_{39}Co_7Sn_{11}$ (at%) polycrystalline compacted-powder specimen was prepared through a process which consisted of multiple steps. The first step was melting of the ingot by high frequency induction. Next, the powders with particle diameters of 10 to 250 μm were obtained using conventional nitrogen gas atomization under argon atmosphere (1.5 to 5 MPa pressure). For the present study, a powder with particle sizes between 25 to 63 μm was compacted into pellets by pressure application. The compacted powder was sealed in quartz tubes under argon atmosphere and annealed at 1173 K for 6 days and then quenched in ice water. Several compression specimens with dimensions close to $3.0\times2.5\times5.5$ mm^3 were cut out of the sintered pellets by wire-electrical discharge machining [70].

Figure VII.6 depicts the strain vs. temperature response during thermal cycling under various compressive stresses across the phase transformation temperature interval for the $Ni_{43}Mn_{39}Co_7Sn_{11}$ polycrystalline compacted-powder specimen. The application of stress was executed at 155 ^{o}C in the parent phase for all tests and the temperature was cycled between -40 ^{o}C and 140 ^{o}C under this designated constant stress level. The level of applied compressive stress was started from 10 MPa and incrementally (by 25 MPa steps) raised for each thermal cycle up to 175 MPa. Change in transformation strain with applied compressive stress and some accompanying irrecoverable strain are clearly seen in Figure VII.6 and the related tendencies are portrayed separately in detail (see Figure VII.8).

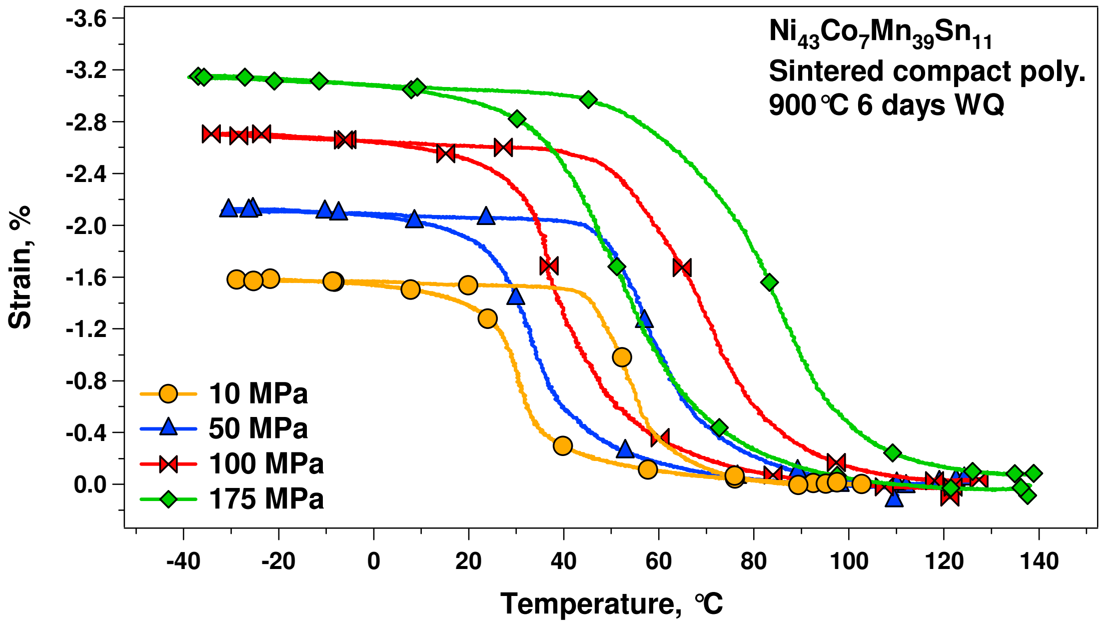

(a)

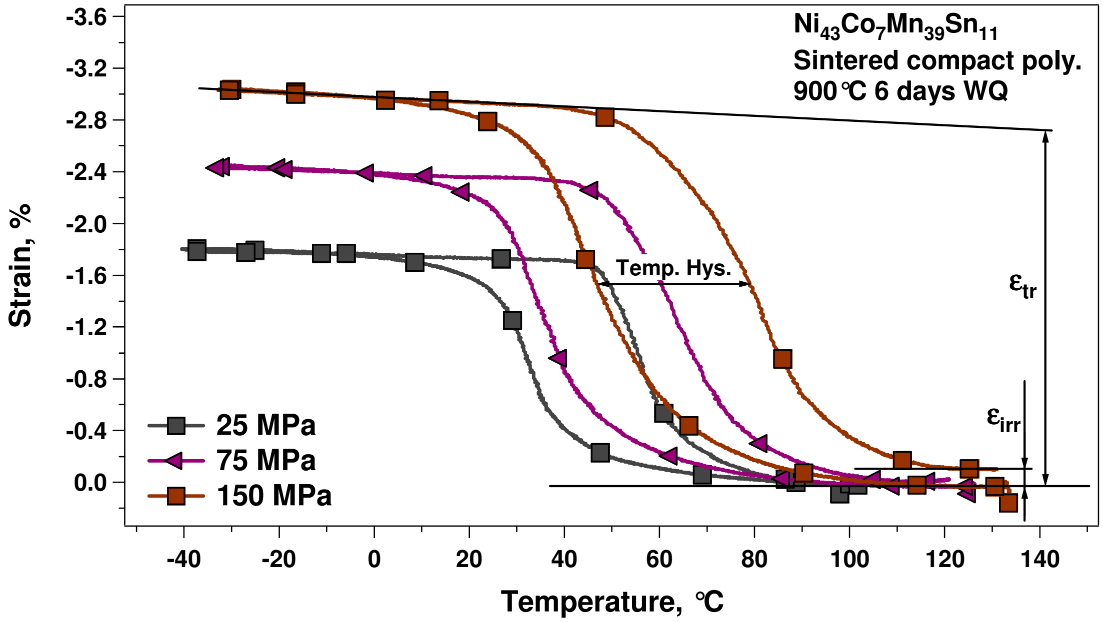

(b)

Figure VII.6 Strain vs. temperature response of the $Ni_{43}Mn_{39}Co_7Sn_{11}$ polycrystalline compacted-powder specimen under various constant compressive stresses across the phase transformation temperature interval.

The transformation temperatures of $Ni_{43}Mn_{39}Co_7Sn_{11}$ polycrystalline compacted-powder specimen for forward and reverse transformations are derived from the heating/cooing curves in Figure VII.6 and compiled as functions of applied compressive stress to construct a stress vs. transformation temperatures phase diagram as shown in Figure VII.7.

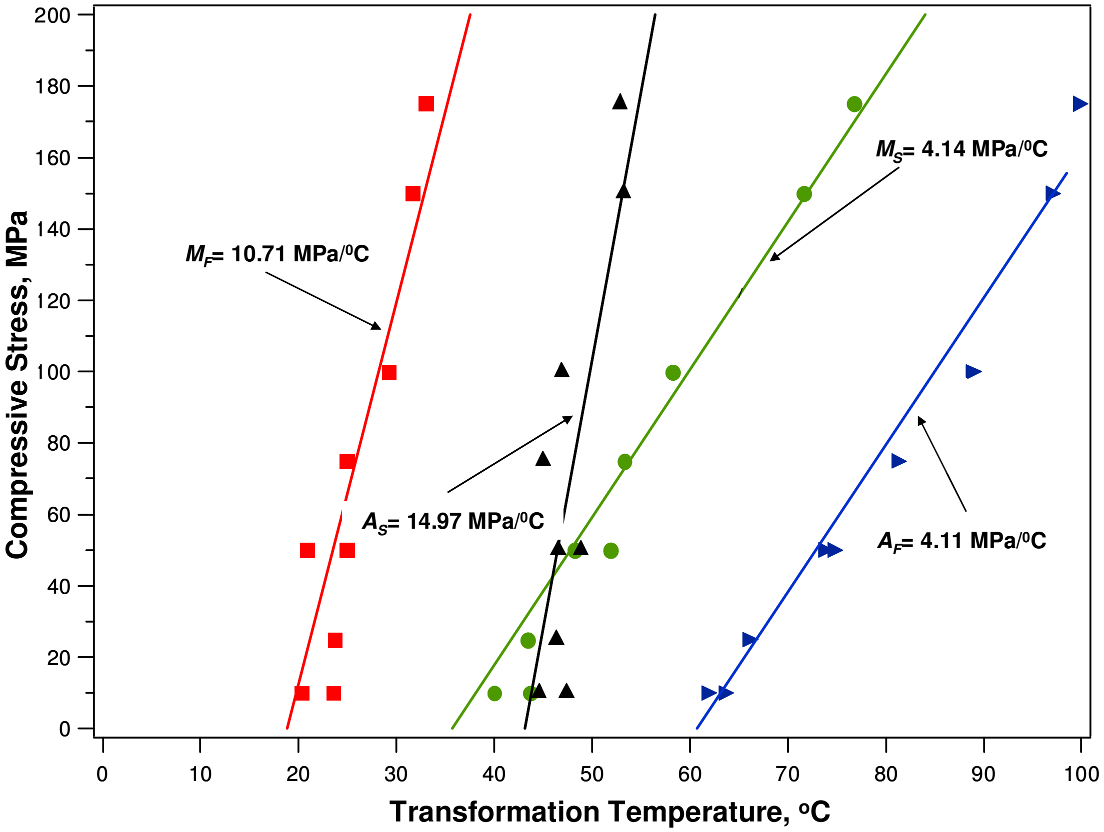

Figure VII.7 Compressive stress vs. transformation temperatures phase diagram of $Ni_{43}Mn_{39}Co_7Sn_{11}$ polycrystalline compacted-powder specimen. The values for each point were extracted from the experiments in Figure VII.6.

In Figure VII.7, the slopes of the fitted lines for M_S, M_F, A_S and A_F temperatures are 4.14, 10.71, 14.97 and 4.11 MPa/^{o}C, respectively.

For the $Ni_{43}Mn_{39}Co_7Sn_{11}$ polycrystalline compacted-powder specimen, $\partial\sigma_c/\partial T$ value is acquired as 4.14 MPa/^{o}C (slope of the M_S fit line in the figure above). $\partial T/\partial H$ (= 3.8 ^{o}C/Tesla) can be estimated using the previously published data from the thermal cycling experiments in SQUID magnetometer under the magnetic fields of 0.05 and 4 Tesla [70]. Plugging these values into Eqn. VII.2 allows us to estimate the magnetostress $\partial\sigma_c/\partial H$ as 15.5 MPa/Tesla for the $Ni_{43}Mn_{39}Co_7Sn_{11}$ polycrystalline compacted-powder specimen, which is interestingly close to that of the $Ni_{40}Mn_{33}Co_{10}Al_{17}$ polycrystalline bulk specimen (14.8 MPa/Tesla, [69]) and NiMnCoIn single crystalline bulk specimen (20 MPa/Tesla, [126]).

Figure VII.8 displays the transformation strain, ε_{tr}, and the irrecoverable (residual) strain, ε_{irr}, as a function of compressive bias stress applied in the course of isobaric thermal cycling tests. ε_{tr} increases exponentially with increasing stress and saturates at around 3 % under 175 MPa and ε_r shows a linear increase from 10 MPa to 175 MPa with a maximum value of 0.2%.

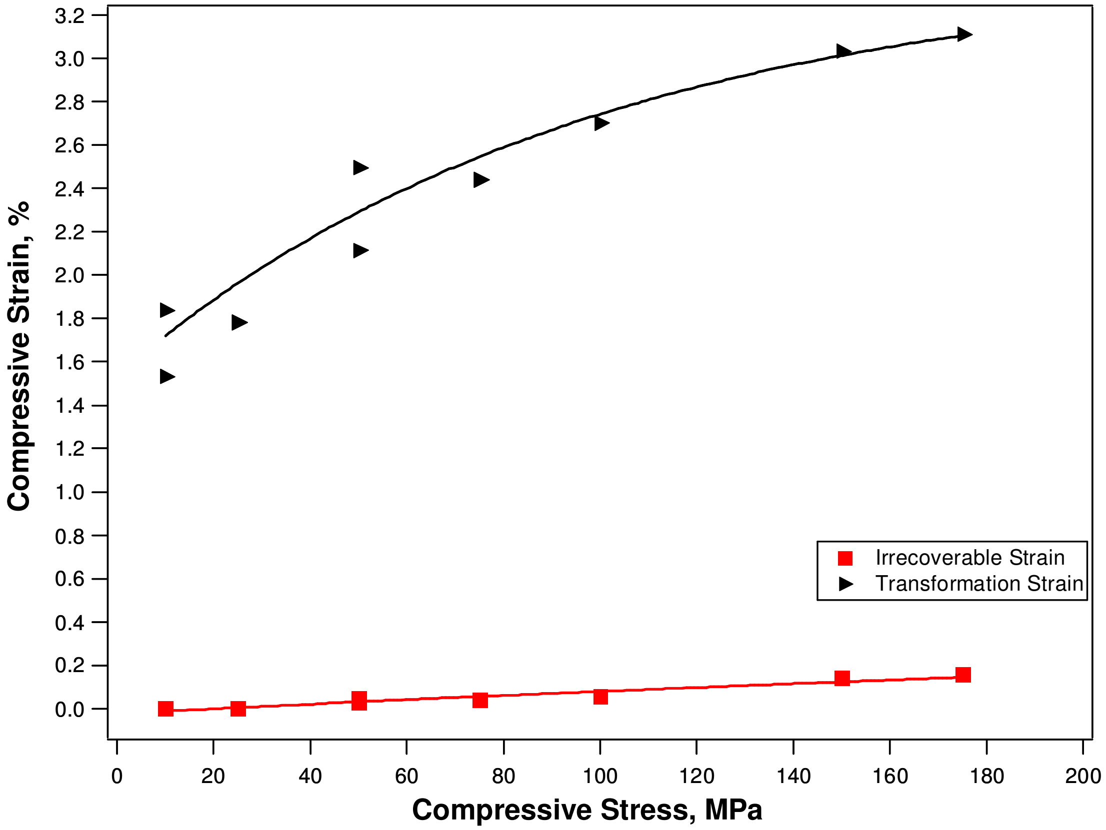

Figure VII.8 Transformation strain ε_{tr} and the irrecoverable (residual) strain ε_{irr} as a function of stress level for the $Ni_{43}Mn_{39}Co_7Sn_{11}$ polycrystalline compacted-powder specimen. The values for each point were extracted from the heating/cooling experiments in Figure VII.6.

The stress vs. strain plots of pseudoelastic behavior for the $Ni_{43}Mn_{39}Co_7Sn_{11}$ polycrystalline compacted-powder specimen, where a compressive strain of about 3% was applied at 70 ^{o}C is shown in Figure VII.9. Almost perfect pseudoelastic loops with full recovery of the applied strain are confirmed. There is no clear plateau region in any of the curves. Right after the critical stress σ_c for the stress-induced martensitic transformation is reached, a continuous hardening is evident from the almost linearly increasing stress level as deformation proceeds. Also, σ_c decreases with the increasing number of cycles indicating a softening phenomenon in the compacted and sintered structure of the powder specimens.

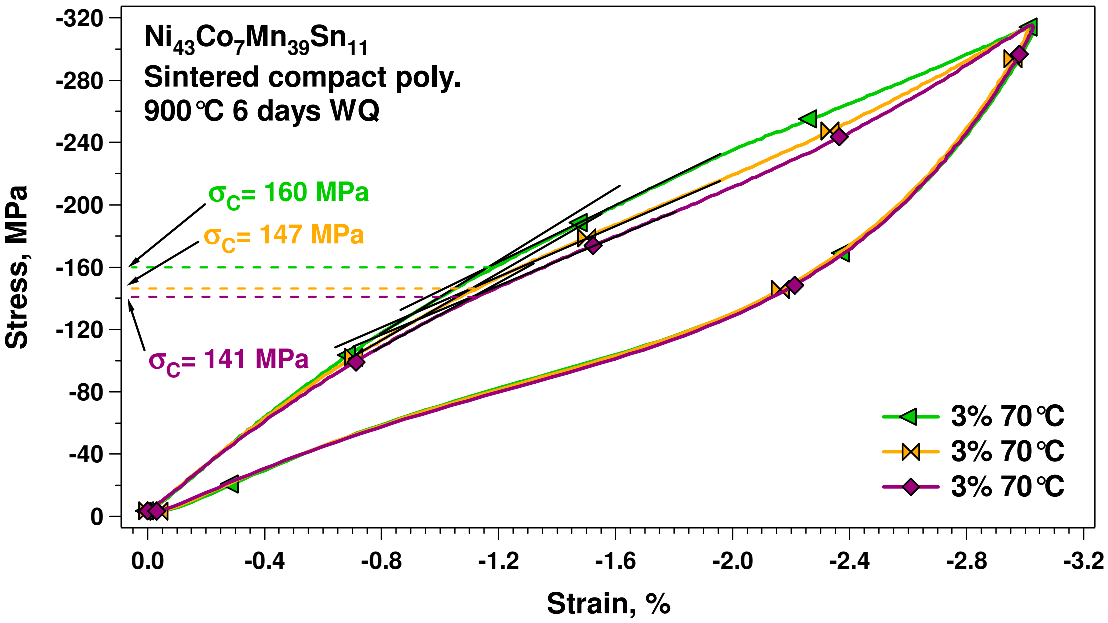

Figure VII.9 Compressive stress vs. strain response of the $Ni_{43}Mn_{39}Co_7Sn_{11}$ polycrystalline compacted-powder specimen at 70 °C showing almost perfect pseudoelastic behavior. As the number of tests increase, softening is pronounced more, evident by the decreasing values of σ_C.

Figure VII.10 demonstrates the trend in thermal hysteresis as a function of applied compressive stress in the course of isobaric thermal cycling tests. The temperature hysteresis was evaluated at the mid point of transformation strain value on each heating cooling curve. As clearly seen in Figure VII.10, temperature hysteresis increases following an almost linear trend from 10 MPa to 150 MPa, then starts declining with the further increasing stress level.

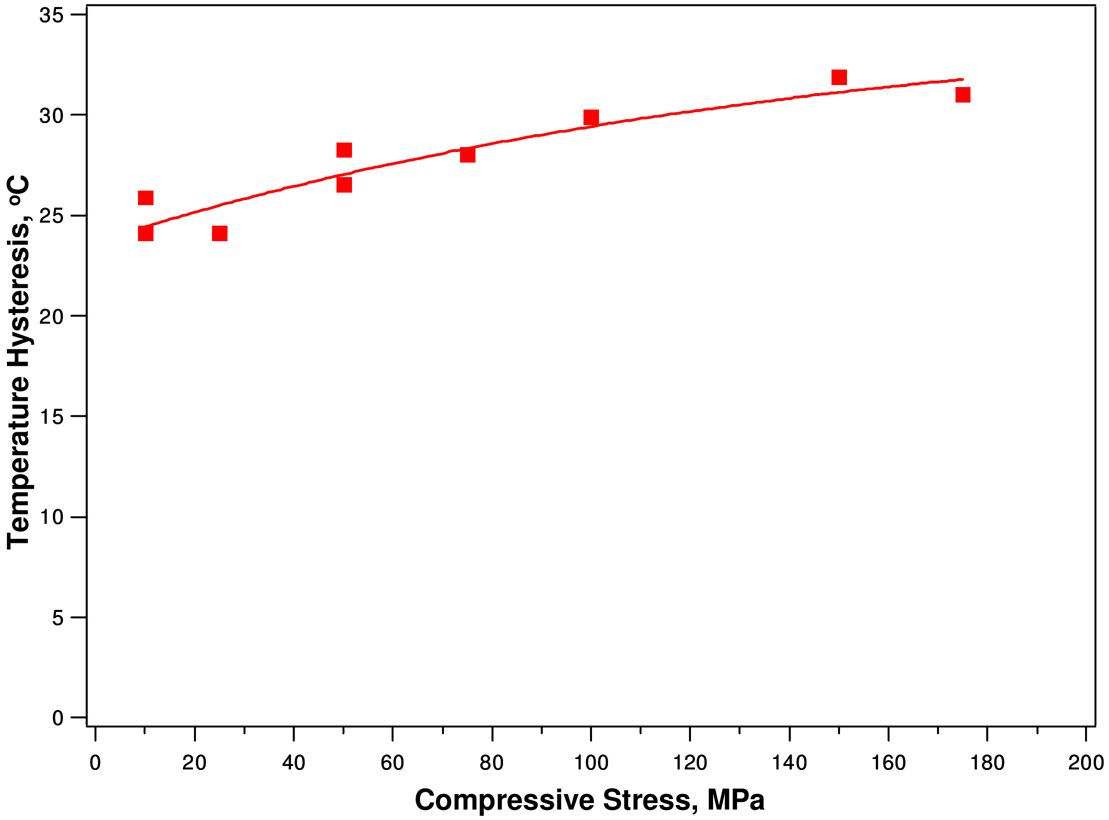

Figure VII.10 Change in temperature hysteresis as a function of compressive bias stress in $Ni_{43}Mn_{39}Co_7Sn_{11}$ polycrystalline compacted-powder specimen. The values for each point were derived from the heating/cooling experiments in Figure VII.6.

CHAPTER VIII

EFFECT OF EXTERNAL BIAS STRESS ON MAGNETIC FIELD-INDUCED PHASE TRANSFORMATION & DIRECT MEASUREMENT OF REVERSIBLE MAGNETIC-FIELD-INDUCED STRAIN IN NiMnCoIn METAMAGNETIC SMAs

This chapter reports the direct measurement results of reversible magnetic-field-induced strain (MFIS) on a single crystalline $Ni_{45}Mn_{36.5}Co_{5}In_{13.5}$ metamagnetic shape memory alloy which were successfully attained for the first time in literature by means of our custom designed microscopic magneto-thermo-mechanical testing system. Magnetization response and MFIS levels are reported as functions of temperature, applied magnetic field and external bias stress. Also, at various temperatures starting with 150 K, kinetic arrest phenomenon of austenite phase was confirmed in the course of forward transformation under magnetic field.

VIII.1 Effect of External Stress on Magnetic Field-Induced Phase Transformation Behavior in NiMnCoIn

In conventional SMAs, in order to observe an external shape change, martensitic structure formation during phase transformation must be biased either by an applied external stress or internal residual stresses. Zero stress thermal cycling through transformation temperatures will not result in large external shape changes typical of SMAs although the material can completely transform to another phase. Temperature cannot bias specific martensite variants, hence, either prior thermo-mechanical training should be performed or a constant external stress should be applied during thermal cycles to bias a martensite variant. This very same principle ought to be valid for field-induced phase transformation in metamagnetic SMAs during magnetic cycling. Since the MAE of the weakly magnetic martensite is negligible in the present NiMnCoIn alloy, applied magnetic field should neither favor any specific martensite variant nor yield an external strain. As a result, to be able to obtain reversible field-induced phase transformation accompanied with MFIS, either of the following requirements should be fulfilled: a) Development of internal local stresses through thermo-mechanical and/or magneto-mechanical training, b) Application of a simultaneous stress which is high enough to bias a variant [68]. Furthermore, it is a must to have an applied magnetic field at a critical level: a) To be able to induce the phase transformation, b) To have martensite completely transform into austenite, c) To obtain MFIS levels as high as the (thermally driven) transformation strain levels. Here, it should be kept in mind that the critical level of magnetic field is function of temperature [126].

From this point of view, a magnetic field in the case of the present metamagnetic NiMnCoIn alloy is analogous to temperature, as both do not have a significant effect on the microstructure formation of martensite, but martensite transforms to austenite when they are increased, and austenite transforms back to martensite when they are reduced.

Up to date, no systematic study has been conducted to understand the effects of simultaneously applied magnetic field and stress on FIPT in any metamagnetic SMA system as well as in NiMnCoIn. In an actuator application utilizing this alloy, magnetic field has to do work against external load. While the magnetic field makes the martensitic transformation temperatures diminish, on the contrary, the external stress increases them. Therefore, as this alloy is a prospective actuator material with a large actuation work output, it is of utmost importance to characterize this metamagnetic shape memory alloy under simultaneously applied magnetic field and external stress through evaluation of its transformation temperatures, transformation hysteresis and magnetization response and understand the effect of bias stress levels on its field-induced phase transformation behavior during field cycling.

VIII.1.1 Effect of Magnetic Field on Martensitic Transformation Temperatures

Figure VIII.1a shows the change in magnetization as a function of temperature under different magnetic field levels obtained from the magnetization vs. temperature (M-T) curves measured using a SQUID magnetometer. Under 0.05 T, the austenite to martensite transformation started at 260 K (M_S: martensite start temperature) and finished at 238 K (M_F: martensite finish temperature) upon cooling.

The reverse transformation started at 254 K (A_S: austenite start) and finished at around 277 K (A_F: austenite finish) upon heating. The transformation is reversible with a small thermal hysteresis (~20 K, see Figure VIII.2a). As the applied magnetic field increased, the transformation temperatures were reduced; e.g., M_S decreased from 260 to 168 K as the field increased from 0.05 to 7 T. This is due to the fact that the applied magnetic field favors the phase with the higher saturation magnetization (austenite in this case). Additional undercooling is needed to supply the required chemical energy to overcome the magnetic energy opposing the forward phase transformation. Figure VIII.1b shows the change in A_S, A_F, and M_S temperatures as a function of magnetic field, extracted from the experiments shown in Figure VIII.1a. The level of change in A_S as a function of bias field is -10.6 K/Tesla. Other transformation temperatures, M_S and A_F, show a similar trend as they decrease with magnetic field at the rates of 10.2 K/Tesla and -9.8 K/Tesla, respectively.

Suppression of the transformation temperatures and the separation of the M-T curves under different field levels is an indication of the possibility of reversible FIPT in the metamagnetic SMAs [63]. The reason for the shift in transformation temperatures is the requirement of additional undercooling which in turn supplies the required chemical energy to overcome the magnetic energy opposing the forward phase transformation since the applied magnetic field favors austenite.

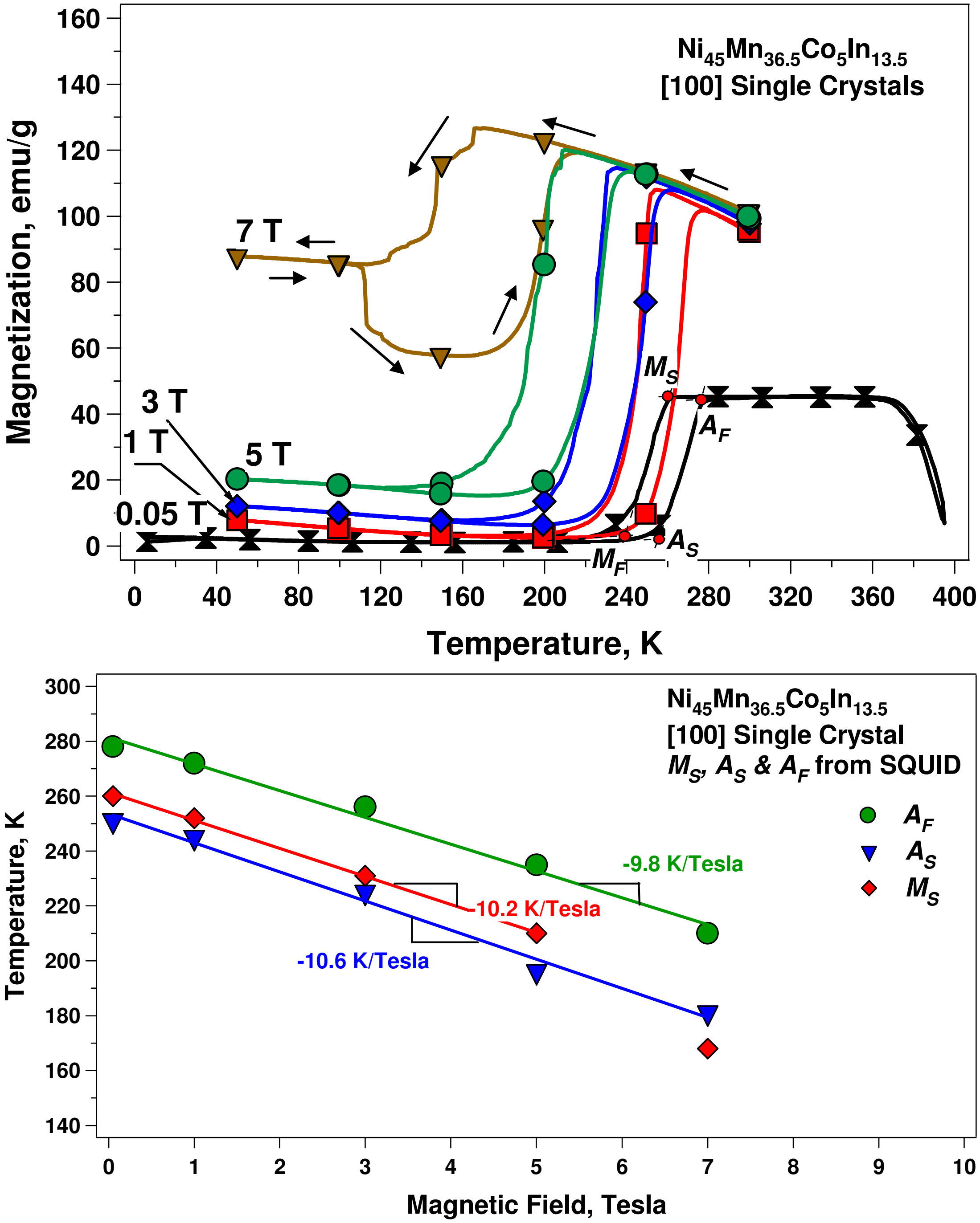

Figure VIII.1. (a) Magnetization vs. temperature response of Ni$_{45}$Mn$_{36.5}$Co$_5$In$_{13.5}$ single crystals under different constant applied magnetic field levels and (b) the transformation temperatures as a function of these field levels extracted from (a).

The variation in saturation magnetization of martensite for each curve under different levels of applied field is also noteworthy in Figure VIII.1a. The reason for this variation is the fact that upon cooling under relatively high magnetic fields, the forward transformation is not completed even though the temperature reaches much below the "apparent" M_F. We have confirmed the existence of austenite at very low temperatures using neutron diffraction measurements when cooled under high magnetic fields (not shown here). This phenomenon is known as kinetic arrest of martensitic transformation, reason of which is not clear at this point [158].

It was stated before that magnetic field favored ferromagnetic austenite and opposed forward transformation ($A \rightarrow M$) by making it harder for the weakly magnetic martensite to nucleate and its phase front to propagate. During reverse transformation ($M \rightarrow A$) magnetic field aligns and eventually merges the magnetic domains in the ferromagnetic austenite so that the austenite phase reaches saturation magnetization, M^S. The martensitic phase in NiMnCoIn has been termed as antiferromagnetic/paramagnetic [61] or weakly magnetic (showing an antiferromagnetic to ferromagnetic transformation) [145]. Therefore, it sounds logical that magnetic field may not impose as much a pronounced effect on martensite as it does on austenite. At that point, temperature change (also the external stress as it will be discussed later) remains to be the only driving force which favors martensite for forward transformation to take place. On the other hand, it was also argued that the martensitic variants in Ni-Mn-*X* (*X*= *In, Sn, Sb*), when acquired upon cooling beyond M_S under applied field, can nucleate and grow along a preferred orientation within the austenitic matrix in tandem with the direction of the applied field and the direction of magnetization easy axis which belongs to that specific martensitic variant. It is reported that easy magnetization axis in martensite is parallel to the long axis in NiMnSb and NiMnIn systems while in NiMnSn it is either along a short axis or in the plane bounded by the short axes [159].

Directly derived from the SQUID M-T curves (Figure VIII.1), Figure VIII.2a depicts the change in the temperature hysteresis (ΔT) as a function of applied magnetic field. Temperature hysteresis was taken as the difference between A_F and M_S temperatures.

Along with the certain fraction of kinetically arrested austenite, the transformation temperature hysteresis increases with increasing applied field as shown in Figure VIII.2a. Obviously, the hysteresis does not alter much up to 5 Tesla along with the increasing applied field. However, at 7 Tesla, it exhibits an abrupt change. Hysteresis is a measure of lattice incompatibility between austenite and martensite phases and in NiMnCoIn one of the reasons it could be associated with is the internal friction sourcing from the movement of phase fronts and their interactions to some extent. We mentioned earlier that the magnetic field, energy wise, favors the ferromagnetic austenite and makes it harder for weakly magnetic martensite to nucleate and propagate, thus deteriorate the compatibility in between.

Therefore, the sudden increase in ΔT can be taken as a sign of the magnetic field reaching a critical point where incompatibility between magnetic field favored austenite phase and temperature favored martensite phase gets much more pronounced due to this briefly mentioned mechanism. However at this time, it is not certain whether this increase in hysteresis is due to kinetic arrest of austenite or low temperature levels increasing the lattice friction, or even due to high magnetic field levels changing the compatibility between austenite and martensite thru magnetostriction and thus, transformation hysteresis.

Figure VIII.2b shows the relative change in magnetization as a function of decreasing temperature between M-T loops under 7, 5 and 3 Tesla vs. the loop under 1 Tesla. Change in magnetization is directly related to the volume fraction of remnant austenite in the course of forward ($A \rightarrow M$) transformation. The increase in ΔT could be explained by the interaction between multiple martensite and austenite fronts due to the austenite stabilization and the associated dissipation there in. Austenite stabilization might be coming from the pinning of phase boundaries by the magnetic domain walls which in turn leading to additional dissipation, i.e., increase in ΔT. This phenomenon is somewhat similar to martensite stabilization in conventional SMAs such as CoNiGa

[160] where once detwinning occurs in martensite, it requires further energy to go back to austenite due to the need for martensite to twin prior to reverse transformation ($M \rightarrow A$).

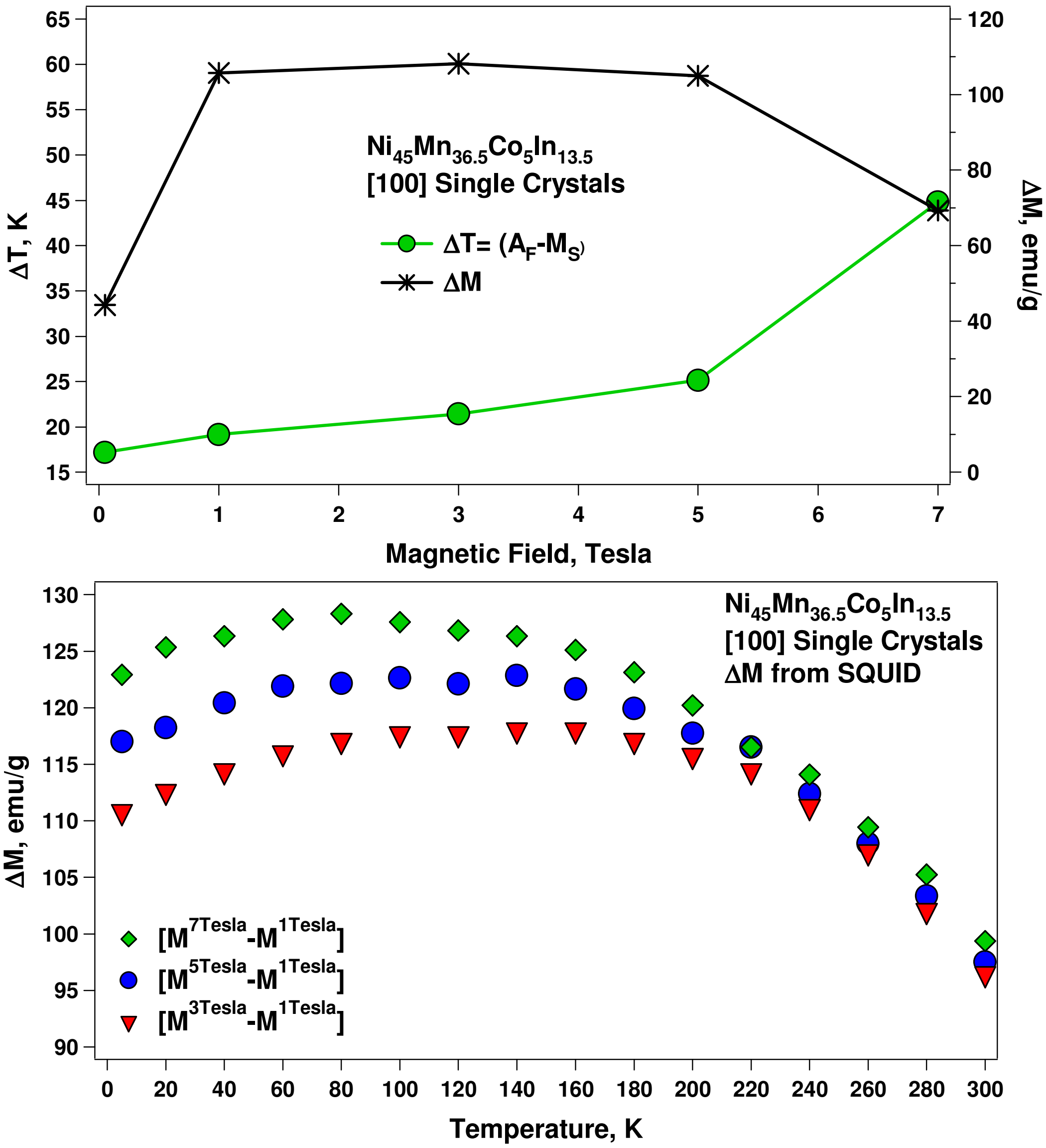

Figure VIII.2. Trends of change in **(a)** Temperature Hysteresis (A_F-M_S) and Magnetization Hysteresis as a function of applied field **(b)** Magnetization Hysteresis as a function of temperature. Graph is deduced from SQUID measurements in Figure VIII.1.

VIII.1.2 Effect of External Bias Stress on Magnetization Response as Functions of Applied Field & Temperature

Following the SQUID experiments, the $Ni_{45}Mn_{36.5}Co_5In_{13.5}$ metamagnetic shape memory specimen was subjected to a series of experiments by using the microscopic MTM testing system in order to observe its magnetization response under different stress levels (0, 75 and 125 MPa) at different temperatures so that we could construct stress vs. magnetic field and magnetic field vs. temperature phase diagrams. The experiments were conducted at fixed temperatures of 4.2, 50, 100, 150, 180, 200, 230 and 245 K. During each test, the magnetization response of the specimen was recorded while the applied magnetic field was increased from a minimum of 0.5 Tesla to a maximum of 18 Tesla (or lower depending on the completion of the reverse ($M \rightarrow A$) transformation). Upon reaching the maximum, the field then was unloaded to 0.05 Tesla. In order to guarantee the full recovery of the M-H curves which indicates a complete ($A \rightarrow M$) transformation, prior to reapplication of magnetic field for the next test, the specimen was first cooled down to 100 K and then heated up to the designated test temperature under zero field, to restore the fully martensitic structure.

Figure VIII.3 represents the magnetization response of NiMnCoIn single crystal with increasing field at different temperatures under 0 MPa (Figure VIII.3a) and 75 MPa (Figure VIII.3b). For the sake of clarity, not all but only a few of curves representing the aforementioned test temperatures are given here. Results for 125 MPa were not shown since the trends they followed in terms of stress effect are similar to that of 75 MPa curves as will be presented in figure on page 185. All curves in Figure VIII.3 reveal metamagnetic transformation behavior in association with a reversible FIPT between austenite and martensite phases. Upon increasing magnetic field, reverse transformation ($M \rightarrow A$) takes place. It can be seen that the saturation magnetization of austenite decreases with increasing temperature, as expected. The trend is in good agreement with that of SQUID results shown in Figure VIII.1. As the test temperature gets closer to the Curie temperature, the capability of austenite to get magnetized (i.e., the level of ferromagnetism) diminishes, thus decreases M^S.

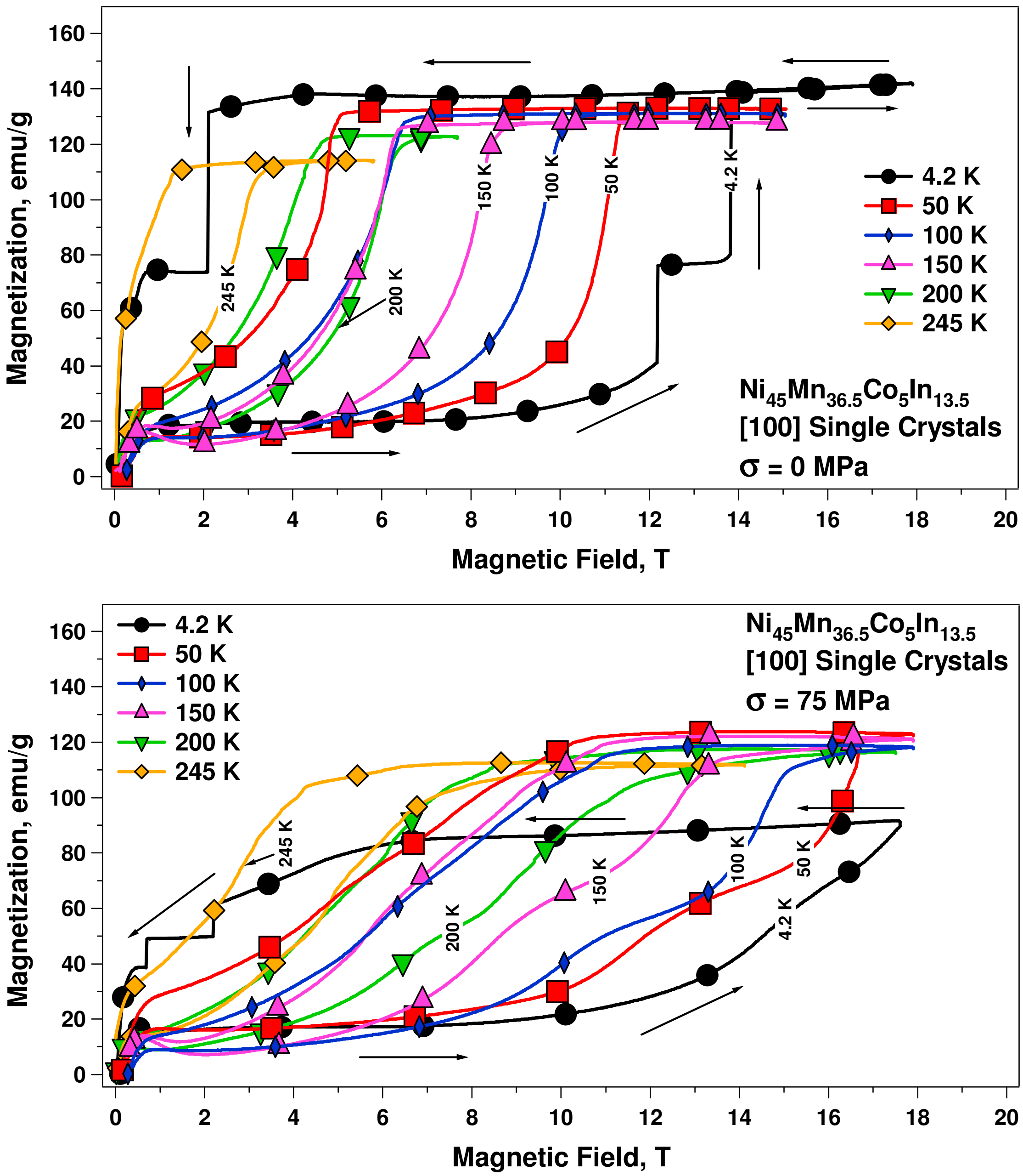

Figure VIII.3. Change in magnetization with applied magnetic field at different temperatures measured by 18 Tesla magnetometer. (a) under 0 MPa external stress, (b) under 75 MPa external stress.

It is very clearly seen in Figure VIII.3b that external stress increases the critical field value to start (*M*→*P*) transformation. This trend will be presented by means of Clausius-Clapeyron phase diagrams and discussed later in this section.

In the course of reverse transformation, over the portion of M-H curves prior to the critical magnetic field value H^{A_S}, the saturation magnetization level of martensite also reduces with decreasing test temperature following a monotonic trend, with the exception of the test at 4.2 K. This monotonic reduction may be explained in the light of the abovementioned behavior of magnetization easy axis of martensite under magnetic field: Due to the reduced symmetry of martensite compared to that of austenite, the number of easy axes can diminish, which in turn can be accompanied by an increase in magnetic anisotropy. The increase in anisotropy is reflected in the low field region of M-H curve where initial slope of the magnetization decreases with decreasing temperature [161, 162].

Under 75 MPa, the change in austenite saturation magnetization levels with increasing temperature is notably smaller in comparison with that of without stress. In Figure VIII.3b (not all temperatures are given for the sake of clarity), magnetization of austenite remains constant around 118 emu/g for 180 and 200 K loops. On the other hand, for loops at 230 and 245 K, the same quantity alleviates to 114 emu/g. This observation can be attributed to the effect of stress which energy vise promotes martensitic nucleation and propagation. Saturation magnetization levels of austenite ranges between 125-114 emu/g at temperatures 180-245 K, respectively for austenite free of applied stress (Figure VIII.3a). Combined with the effect of test temperatures getting closer to the Curie temperature which diminish the ferromagnetism of austenite, introduction of stress obviously stabilizes the presence of martensite in the portion of the M-H curves after the critical point of magnetic field where reverse transformation (*M*→*A*) is supposed to be 100% completed. Under stress, decreasing test temperature shifts up the critical magnetic-field-levels of reverse and forward transformations, H^{A_S}, H^{A_F}, H^{M_S} and H^{M_F}, as well, just like it did on the stress free experiments. A comparative picture of this trend will be given by magnetic field vs. temperature phase diagrams in Figure VIII.4.

The M-H curves at 4.2 K, with and without external stress both indicate different characteristics in comparison with the others at higher temperatures. In Figure VIII.3a, M-H curve at 4.2 K reaches a higher magnetization of 140 emu/g accompanied with a burst type, intermittent progression both for reverse and back transformations. It is well known that thermal energy causes misalignment in the directions of magnetic moments within the magnetic domains, i.e., spontaneous magnetization within a magnetic domain decreases as temperature increases above 0 K. Since 4.2 K is very close to absolute zero, the higher level of magnetization of ferromagnetic austenite can be related to the lowered thermal energy [34]. Moreover, the same burst type phenomenon was reported in other publications and was explained by the hindrance on the mobility of habit planes (martensite/austenite interphase) due to low temperatures since martensitic transformation occurs on a basis of a thermally activated process [145, 163]. In Figure VIII.3b, for 75 MPa, the M-H curve at 4.2 K obviously looks far from attaining saturation magnetization of the austenite phase. It requires a higher value of magnetic field well beyond 18 Tesla which is the magnetic field application limit of the test setup. This is a clear indication of the substantial suppression effect on austenite nucleation and propagation by the external stress.

Figure VIII.4 shows the magnetic field vs. temperature phase diagrams (Clausius-Clapeyron relationship) which represent the effect of external stress on the critical magnetic-field-levels of reverse and forward transformations. Decreasing test temperature shifts all *critical magnetic-field-levels for forward and reverse transformations* up, which are H^{A_S}, H^{A_F}, H^{M_S} and H^{M_F} for austenite start, austenite finish, martensite start and martensite finish, respectively. This is expected due to the same phase-favoring-mechanism acting on austenite and martensite, summarized to explain the M-T curves from SQUID results. Since the difference in the chemical free energies of martensite and austenite increases with decreasing temperature favoring martensite, reverse transformation (*M→A*) requires a greater field value to start, thus occurs the aforementioned shift.

Initial regions of the 0, 75 and 125 MPa curves above 150 K; show an almost linear trend in Figure VIII.4. For the 0 MPa curves, these portions include data points from Figure VIII.1 as well, to complement the data derived from 18 Tesla M-H curves under zero stress. The good match between the data from SQUID M-T and 18 Tesla magnetometer M-H curves indicates the repeatability of our test results. Stress, obviously, translates the critical magnetic-field-points of transformation to higher values, although their rates of change with temperature (slopes of initial regions as indicated on each curve in Figure VIII.4) remain close to each other for the cases with and without stress.

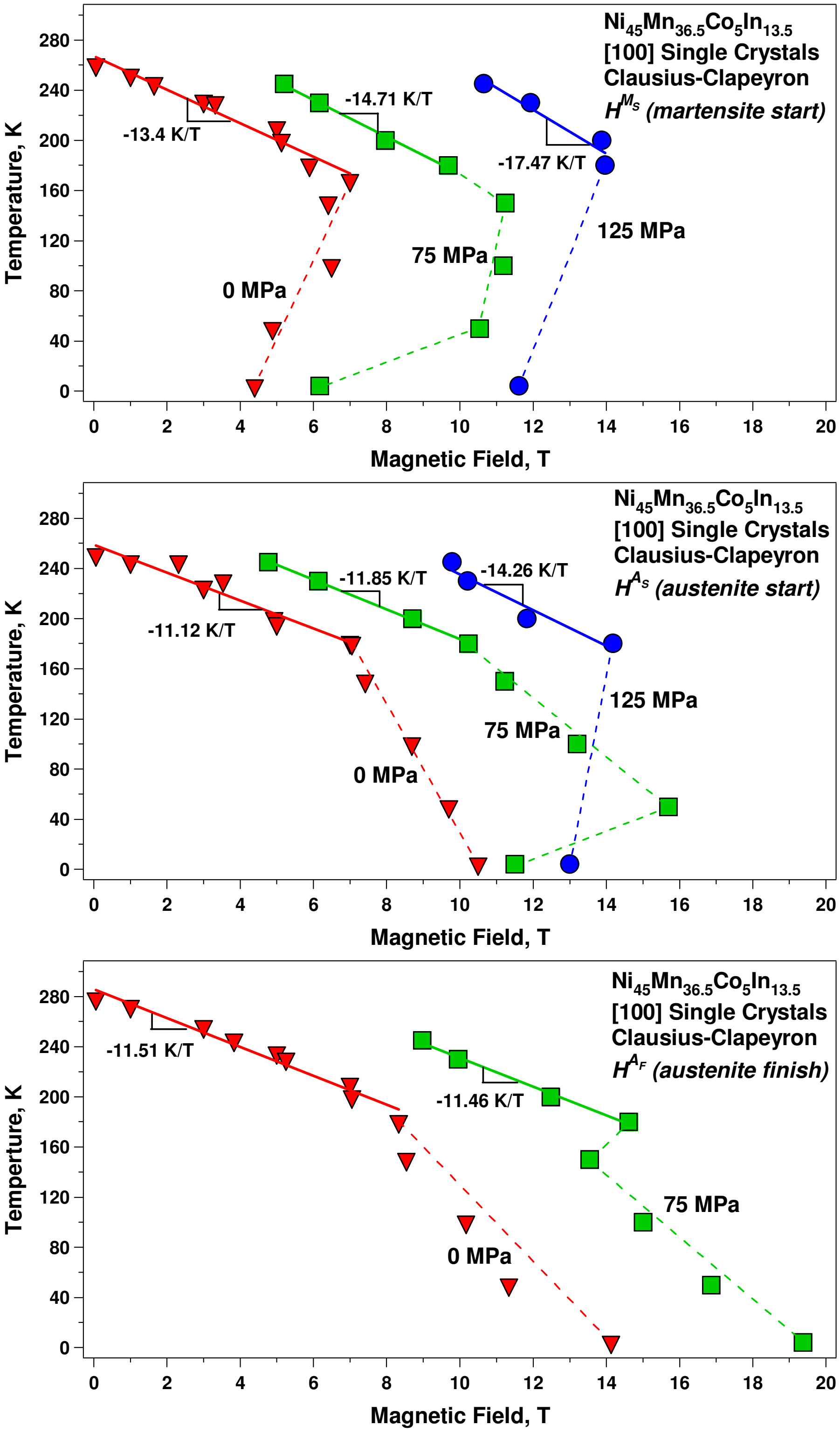

Figure VIII.4. Magnetic field vs. temperature phase diagrams showing the effect of stress on the critical magnetic-field-levels of reverse & forward transformations.

Figure VIII.5 reflects the effect of external stress up to 125 MPa on the magnetization response of NiMnCoIn single crystalline bulk specimen to applied magnetic field at various temperature levels. Regardless of the test temperature, applied stress opposes the nucleation and progression of the austenite phase, yielding an incomplete ($M \rightarrow A$) transformation as indicated by the diminishing saturation magnetizations as stress level increases. Also with stress, the distance between manganese atoms (Mn-Mn distance) changes and this can be another reason for smaller saturation magnetization levels up to 18 Tesla magnetic field.

Magnetic field hysteresis observed in this metamagnetic shape memory alloy is an indication of the field-induced martensitic transformation taking place between the (ferromagnetic) austenite and (weakly magnetic) martensite phases. As can be clearly seen in Figure VIII.3, the magnetic field hysteresis in the course of FIPT increases with decreasing temperature. At lower temperatures, especially lower than 150 K, this behavior was thought be linked to kinetic arrest of austenite [134, 145]. Application of external stress amplifies this trend. At low temperatures, the thermal component of the dissipation process is expected to be less effective; hence its athermal component must be dictating the increasing magnetic field hysteresis, in our case. There is a need to study magnetic domain and structure interaction and kinetics of FIPT as a function of temperature to shed light on the contribution of athermal component of energy dissipation.

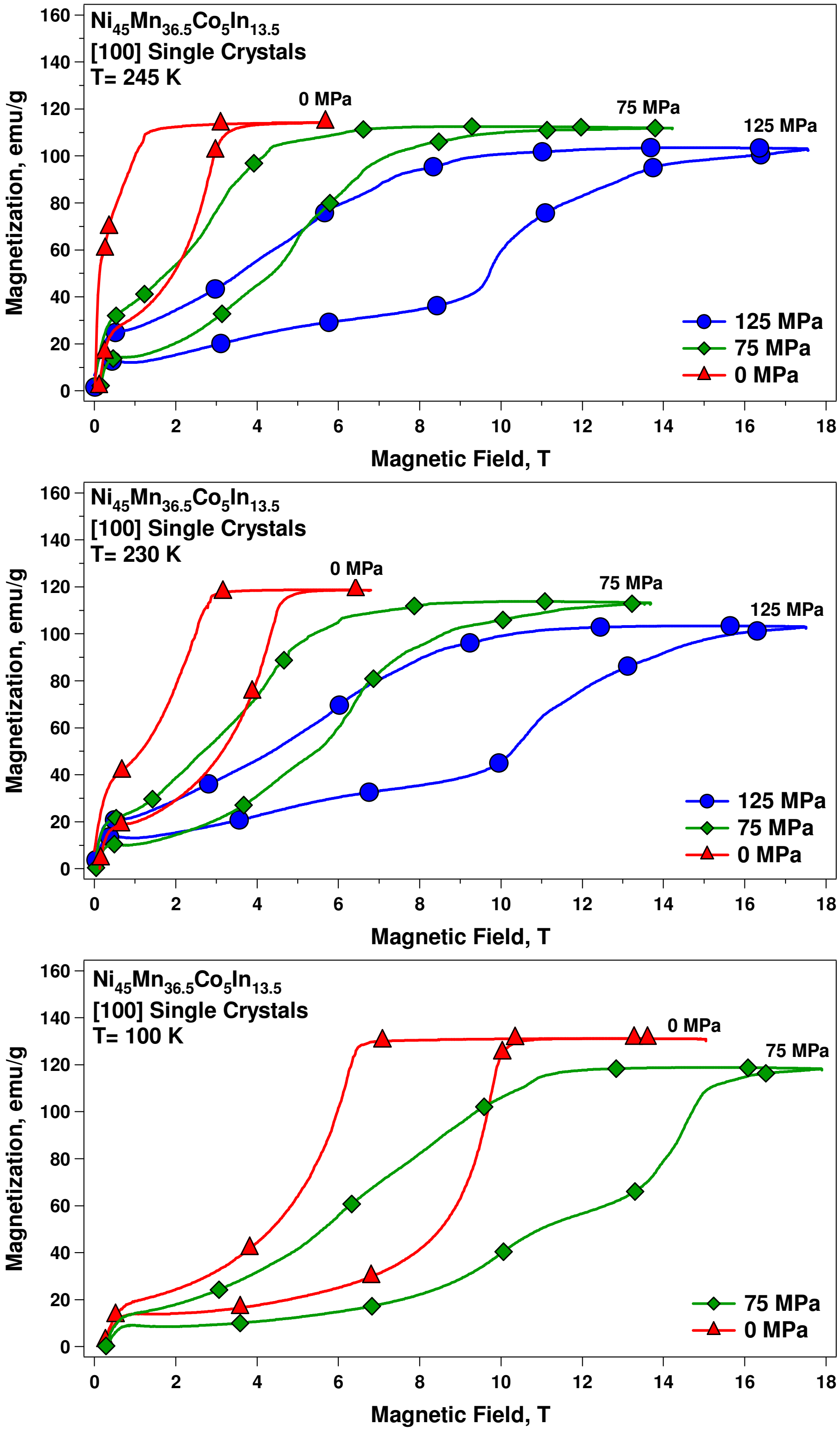

Figure VIII.5. Change in magnetization response simultaneously applied magnetic field and external stress at 245, 230, 100, 50 and 4.2 K.

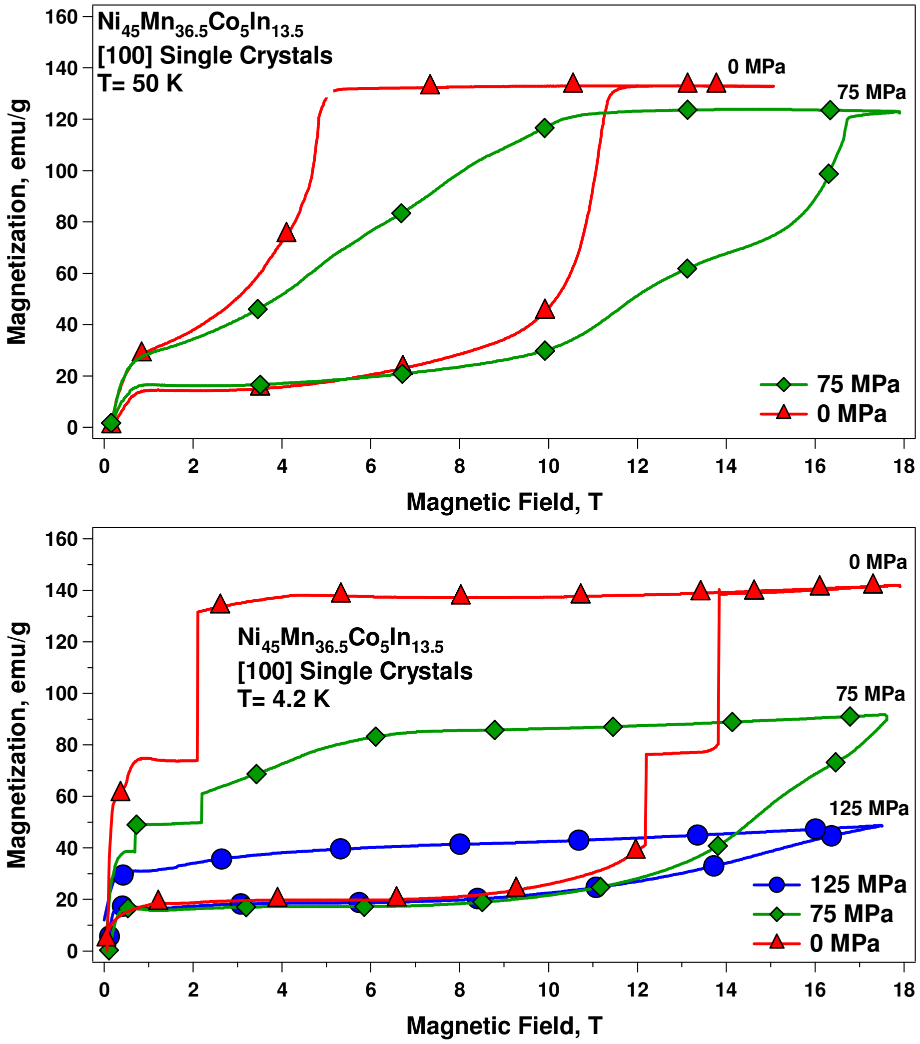

Figure VIII.5 continued.

Figure VIII.6 is derived from Figure VIII.3 and portrays the trend in the variation of magnetic field hysteresis ($H^{A_F} - H^{M_S}$). Magnetic field hysteresis increases with decreasing temperature, however under the influence of simultaneously applied external stress, this decrease becomes more pronounced. Stress introduces imperfections such as dislocations which are known to pin down and deteriorate the mobility of the magnetic domain walls.

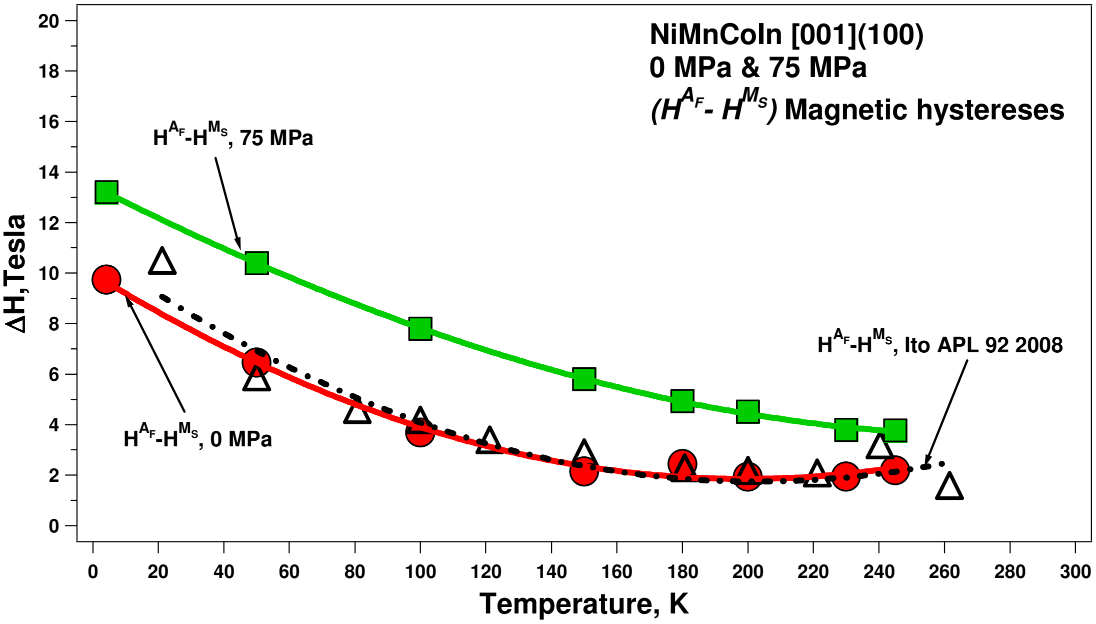

Figure VIII.6. Change in magnetic field hysteresis by $(H^{A_F} - H^{M_S})$ & midpoint methods for 0 MPa and 75 MPa taken from M-H curves.

Due to the magneto-mechanical coupling, interactions of domain walls with the above mentioned defects, impurities like precipitations and secondary phases, and also structural boundaries (e.g. of grains, twins, secondary phases) all manipulate the internal friction, hence its measure in magnetic terms; magneto-hysteresis. In Figure VIII.3, although not pronounced at 4.2 K, the increasing slopes along the reverse transformation portions of M-H curves for 230 and 245 K as ($M \rightarrow A$) evolves is an indication of the change in elastic moduli and the internal friction dynamics in the martensite/austenite mix.

VIII.2 Direct Measurement of Reversible Magnetic Field-Induced Strain in NiMnCoIn Metamagnetic SMAs

In magnetic shape memory alloy literature, besides indirect evidences through magnetization vs. magnetic field [134], magnetization vs. temperature [134], electrical resistivity vs. magnetic field [164, 165] and DSC measurements [134, 136], there exists no report in literature on reversible MFIS as a direct evidence of fully recoverable phase transformation in metamagnetic SMAs, up to date. By means of our microscopic MTM testing system integrated with a miniature capacitive displacement sensor, we succeeded to measure fully reversible magnetic field-induced strains in a metamagnetic shape memory alloy.

Figures VIII.7a and VIII.7b demonstrate direct measured MFIS response of the $Ni_{45}Mn_{36.5}Co_5In_{13.5}$ single crystalline specimen as a function of magnetic field at various test temperatures and under two different compressive bias stress levels, i.e., 75 and 125 MPa, respectively. These results provide the direct evidence of reversible MFIS utilizing FIPT mechanism, for the first time in literature. It should be noted that under zero stress level, there was no notable MFIS levels observed supporting our initial argument on the inability of magnetic field biasing a particular martensite variant. In Figure VIII.7, as the test temperature decreases, all the critical magnetic field values required to start and finish reverse $\left(H^{A_S}, H^{A_F}\right)$ and forward $\left(H^{M_S}, H^{M_F}\right)$ transformations are shifted towards higher field values since martensite is more stable at low temperatures and more magnetic energy is needed to reach the energy level of austenite. The sense of this shift is similar to the increase in transformation temperatures in conventional SMAs under constant stress, i.e. the higher the stress levels are applied, the more the transformation temperatures and critical magnetic fields shifts to higher levels.

The maximum MFIS achieved in this study was 3.13% at 250 K under 125 MPa with an irrecoverable strain of 0.26%. The reason for the irrecoverable strain is the incomplete forward transformation because 250 K is higher than the M_F temperature under zero field. Fully recoverable MFIS values were attained as 2.92% and 2.39% at 200K under 125 and 75 MPa, respectively. Figure on page 194 was constructed using the results in Figure VIII.7 and it depicts the trend in transformation strain and magnetic transformation hysteresis as a function of bias stress.

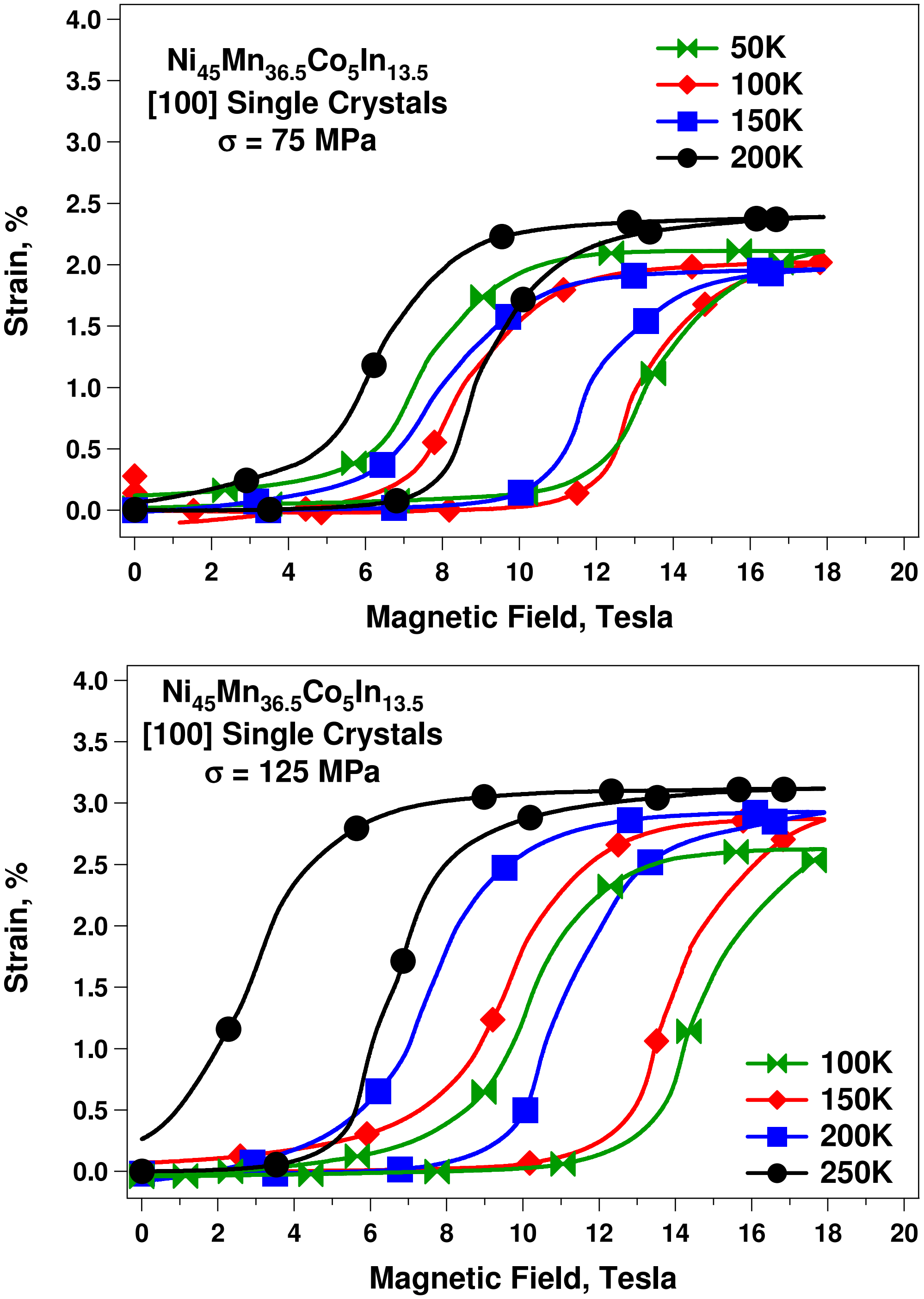

Figure VIII.7. Magnetic field induced strain vs. applied magnetic field response of $Ni_{45}Mn_{36.5}Co_5In_{13.5}$ single crystals oriented along the [100] direction under (a) 75 MPa and (b) 125 MPa compressive bias stress at different test temperatures in the course of metamagnetic phase transition.

The strain levels observed here is smaller than what we expect from this material theoretically, i.e. approximately 6.5% (see Chapter VI), if the austenite has $L2_1$ and the martensite has six layered monoclinic structure. However, in the present crystal, the austenite could be either B2 or $L2_1$ and the martensite can be a mixture of $L1_0$ and six-layered monoclinic structure according to the magnetization results in Fig. 3.a and following the recent study by Ito *et al.* [166] on the different structure of the transforming phases depending on the order heat treatments. Therefore, one of the reasons for the lower transformation strains than expected from our previous work might be due to the different heat treatment in the present crystal. To validate this argument, the structures of the transforming phases need be determined in the future.

In our previous work on the isobaric thermal cycling experiments of the same material which was narrated in Chapter VI, we reported the transformation strain to increase with bias stress and saturate above a certain stress level before it starts decreasing under high stress levels due to simultaneous plasticity. Such changes in transformation strain are a consequence of the evolution of martensite variants as a function of applied stress. During thermal or magnetic cycling under low stresses, the measured lower transformation strain levels imply that the applied stress may not be sufficient to bias a single variant martensitic structure; therefore a self-accommodating martensite structure may partially form. Difficulty of biasing a single variant martensite at low stress levels depends on the presence of second-phase particles and defect generation during phase transformation which is a direct consequence of lattice incompatibility between austenite and martensite phases. From the significant increase in the transformation strain (Figure VIII.8) when the stress increased from 75 to 125 MPa, it is reasonable to assume that maximum transformation strain and single variant martensite morphology will be reached above much higher stress levels. These stress levels are significantly larger than 6 MPa required for reaching maximum transformation strain in Ni_2MnGa [95]. Such a large difference in the saturation stress can originate from the second phase particles in the NiMnCoIn samples [68] and the higher lattice friction in NiMnCoIn alloys due to solid solution hardening and off-stoichiometry which in turn yields more defect generation during transformation. As a reminder, for the alloy used in this study, the composition of the matrix and the second phase were determined as $Ni_{45.7}Mn_{35.6}Co_{4.8}In_{13.8}$ and $Ni_{42.0}Mn_{40.3}Co_{16.0}In_{1.6}$, respectively using WDS [68].

The small variations in the MFIS levels under each bias stress at different test temperatures (Figure VIII.7) can be attributed to several different reasons: (1) a small change in the spring constant of the spring used in the micro MTM as a function of temperature, which in turn affects the level of stress, (2) the effect of temperature on the lattice parameters of austenite and martensite, thus on the transformation strain, (3) the effect of temperature dependent magnetostriction on lattice parameters of austenite and martensite, and (4) incomplete reverse transformation even under 18 T at low temperatures and under 125 MPa.

As shown in Figure VIII.8, the magnetic transformation hysteresis remains almost constant around 4 - 4.5 Tesla in the 125 MPa experiments for a temperature range of 100K to 250K, whereas it slowly declines under 75 MPa from 4.5 Tesla to 2.5 Tesla for the same temperate range. In the entire temperature range investigated, magnetic transformation hysteresis increases with decreasing temperature under 75 MPa. Applied stress also increases the field hysteresis at a given temperature (not shown here). This trend is opposite of what we observed during isobaric thermal cycling experiments where the transformation thermal hysteresis diminishes with increasing bias stress as discussed in Chapter VI (see Figures VI.2 and VI.4). Since transformation hysteresis is a measure of compatibility between the transforming phases and energy dissipation during the transformation, this discrepancy in the hysteresis trends is attributed to temperature dependent lattice friction and change in compatibility. It is well-known that Peierls-Nabarro stress is very high in bcc like structures, and at low temperatures this stress governs the lattice friction. Therefore, since magnetic field suppresses transformation temperatures, the phase transformation occurs at low temperatures, and the phase front motion has to move in the presence of high lattice friction causing large dissipation.

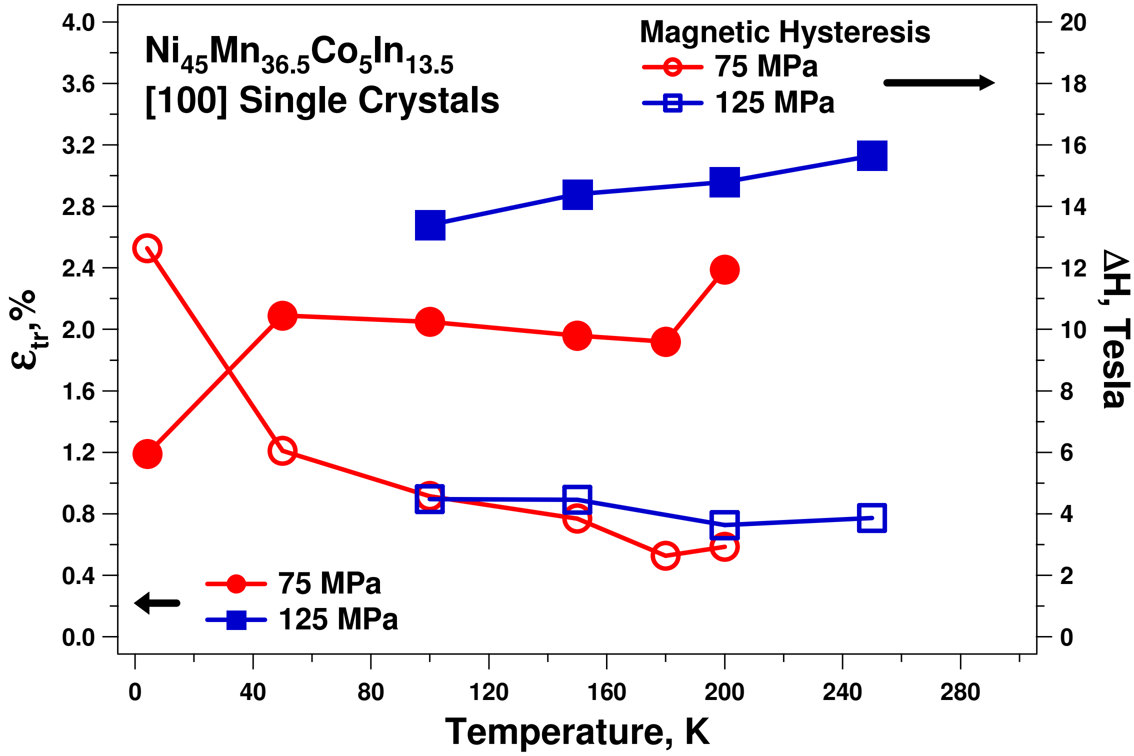

Figure VIII.8. Magnetic field-induced strain levels and magnetic transformation hysteresis in $Ni_{45}Mn_{36.5}Co_5In_{13.5}$ single crystals oriented along the [100] direction as a function of temperature under 75 MPa and 125 MPa compressive bias stresses.

From thermal cycling and pseudoelastic (PE) experiments on similar NiMnCoIn crystals, the rate of change in the critical stress for the onset of martensitic transformation (i.e. σ^{M_s}) was determined to be $\frac{d\sigma}{dT} = 2.1 MPa / K$ under zero magnetic field, in Chapter VI. From the magnetization response of the same material, the rate of change in M_S as a function of applied magnetic field is determined to be $\frac{dT}{dH} = -14.0 K / Tesla$ (Figure VIII.1b). Multiplying these two values gives us the shift in critical magnetic field required to start forward transformation as a function of applied bias stress as $\frac{dH}{d\sigma} = -0.034 Tesla / MPa$. Figure VIII.9 shows the change in critical magnetic field levels as a function of temperature under the influence of bias stress. In order to verify the increase in the critical field level for the onset of forward transformation as a function of stress, we can compare the predicted value, -0.034 Tesla/MPa, with the experimental results presented in Figure VIII.9. According to this prediction, there should be 2.55 Tesla difference between the 0 and 75 MPa curves. Indeed, the measured differences are 2.6 Tesla at 200 K and 2.8 Tesla at 175 K.

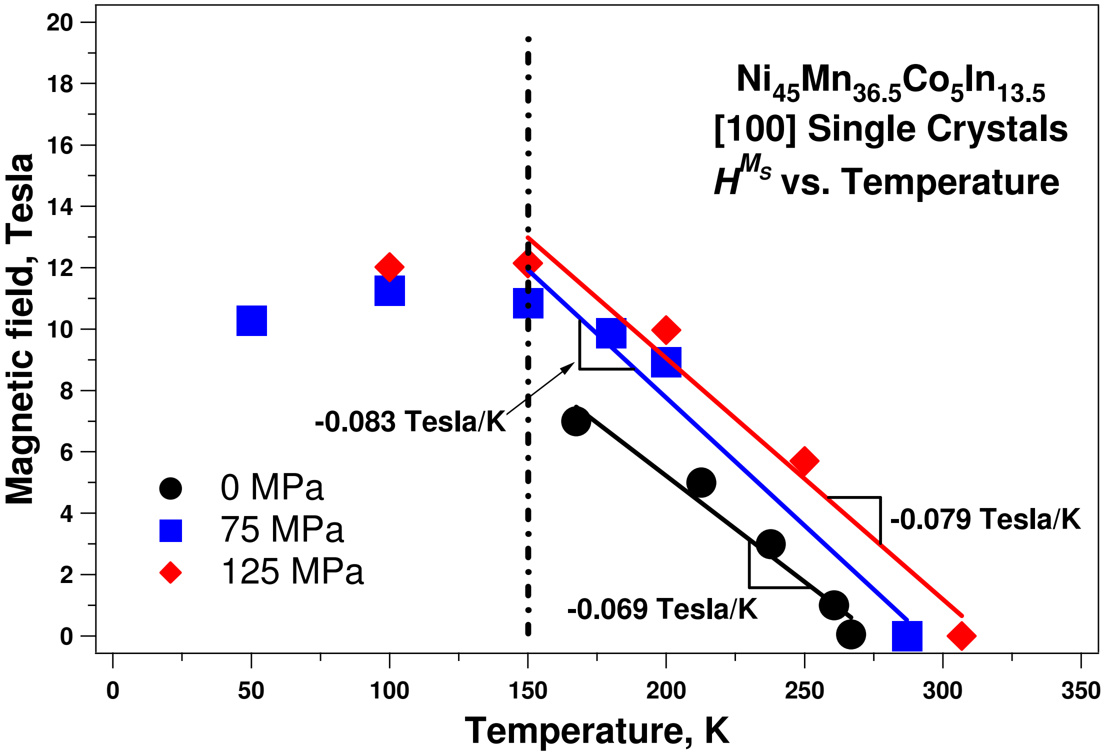

Figure VIII.9. Magnetic field vs. temperature phase diagram of $Ni_{45}Mn_{36.5}Co_5In_{13.5}$ single crystals oriented along the [100] direction under three stress levels, 0, 75, and 125 MPa.

Since these two values are close to the prediction, we can conclude that the results from the magnetization and conventional isobaric thermal cycling or pseudoelastic experiments can be used to roughly predict the change in required magnetic field values for the onset of transformation under different bias stress levels. If we use this simple approach, then it is possible to estimate the approximate value for the real stress level on the sample under 125 MPa at room temperature, which should be around 115 MPa at 200 K due mainly to the change in the spring constant with temperature and due to the transformation strain relaxing the spring force.

Figures VIII.10a and VIII.10b show the magnetic field vs. temperature phase diagram under 75 and 125 MPa bias stress levels, respectively. It is clearly observed that for both stress levels, the change in critical field values with temperature follow a linear trend down to 150 K. However, at temperatures lower than 150 K, this linear trend ceases and the field levels changes only slightly with reduction in temperature. The equilibrium magnetic field, H_O, where Gibbs free energies of austenite and martensite phases are equal, can be defined as the arithmetic mean of H^{M_S} and H^{A_F}. H_O gradually increases with decreasing temperature and saturates at temperatures lower than 150 K, while magnetic hysteresis continuously increases below 150 K.

If a bias stress is applied, both H_O and ΔH curves shift upwards to higher magnetic field values, indicating that stress makes it harder for reverse transformation to take place. Umetsu *et al*. [163] explained the aforementioned trends in H_O and ΔH curves by the diminishing transformation entropy during forward transformation which in turn yielding kinetic arrest of austenite making it thermodynamically more stable than martensite during cooling under magnetic field. The reason for the kinetic arrest is not clearly known at this point.

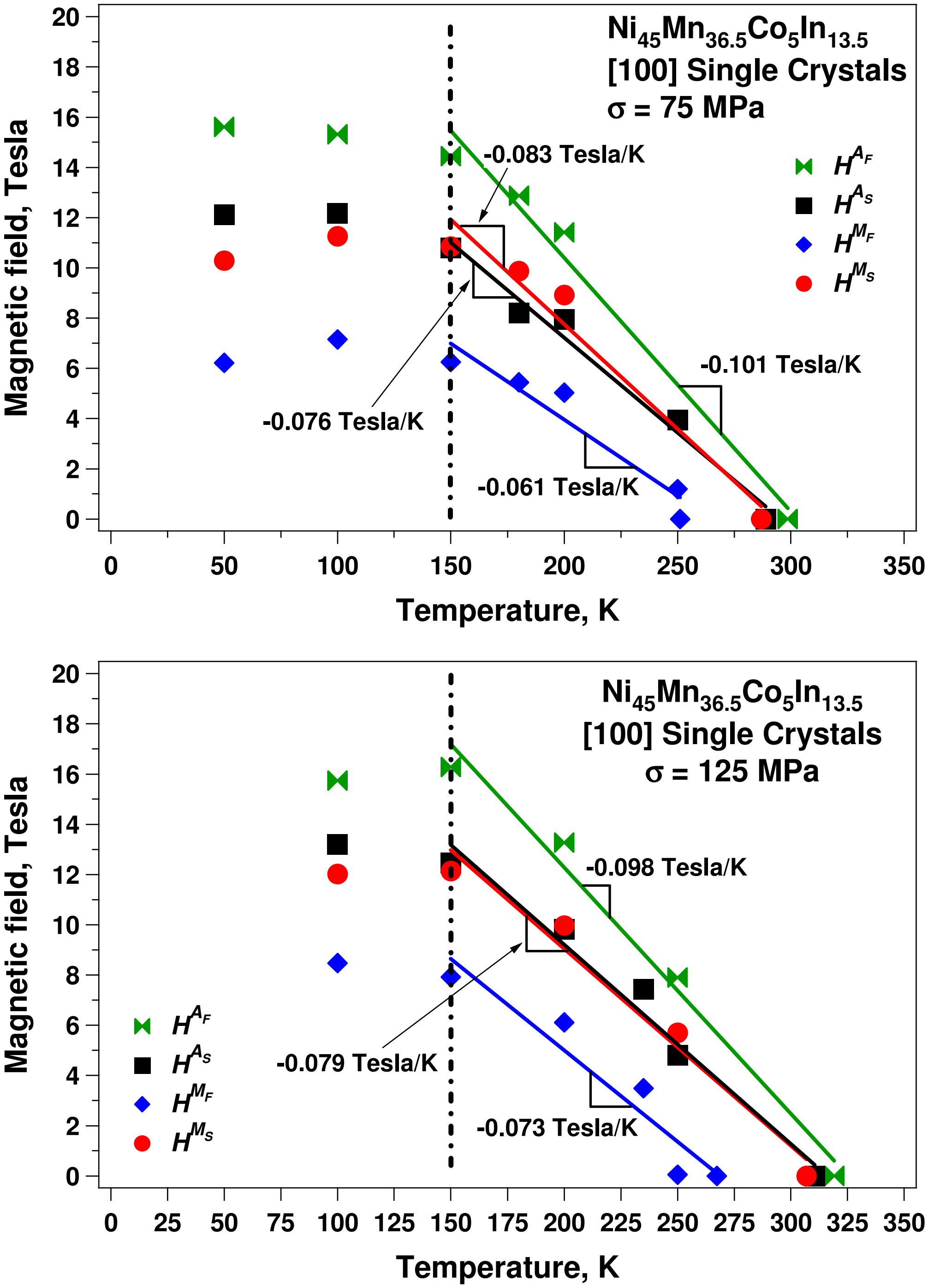

Figure VIII.10. Magnetic field vs. temperature phase diagram of $Ni_{45}Mn_{36.5}Co_5In_{13.5}$ single crystals oriented along the [100] direction under (a) 75 and (b) 125 MPa.

CHAPTER IX

SUMMARY & CONCLUSIONS

In this Ph.D. study, Magnetic Shape Memory Alloys (MSMAs) are put under investigation. This newly discovered class of smart materials combines the shape-change/deformation-recovery abilities of heat driven conventional shape memory alloys (SMA) and the magnetic field driven magnetostrictives through martensitic transformation. Besides being promising for actuation applications they can also be employed as sensors and/or power harvesters due to their capability to convert mechanical stimuli into magnetic response or vice versa. The coupled effects of stress, magnetic field and temperature on the magnetic field induced strain response and cyclic repeatability should be explored in detail to understand the underlying microstructural mechanisms for improved magneto-thermo-mechanical response.

To shed light on the aforementioned issues, it was necessary to design and build novel testing systems which would allow simultaneous magnetic, thermal and mechanical characterization of single crystalline and polycrystalline MSMAs in bulk form while maintaining complete control on simultaneously applied magnetic field and stress/strain in a wide and stable temperature range. Thus, the development of two distinct magneto-thermo-mechanical (MTM) testing systems, one macroscopic and one microscopic, was realized.

Extensive experimental work on MTM characterization of these materials enabled us to determine the effects of main parameters on reversible FIPT, such as magnetocrystalline anisotropy energy (MAE), Zeeman energy (ZE), stress hysteresis, thermal hysteresis, critical stress for the stress induced phase transformation and crystal orientation. The magnetic field and external stress were applied perpendicular to each other. Conventional shape memory alloy (SMA) characteristics of single crystalline Ni_2MnGa and NiMnCoIn oriented along the [100] direction, and polycrystalline NiMnCoAl and NiMnCoSn MSMAs were investigated using the macroscopic MTM testing system to reveal how these conventional properties were linked to magnetic-field-induced actuation. The actuation stress of 5 MPa and work output of 157 kJm^{-3} are obtained by the field-induced martensitic variant reorientation in NiMnGa alloys.

Both in Ni_2MnGa MSMA and in NiMnCoIn metamagnetic SMA, FIPT was investigated implying an alternative mechanism to field-induced martensite variant reorientation, as the governing mechanism of field-induced shape change. One-way and reversible (0.5% cyclic MFIS under 22 MPa) stress-assisted field-induced phase transformations in Ni_2MnGa single crystals were realized under low field magnitudes (< 0.7 Tesla) and resulted in at least an order of magnitude higher actuation stress levels compared to those previously reported in the literature. Magnetic field-induced phase transformation (FIPT) mechanism provided higher work output levels (at lower operating temperatures) than variant reorientation mechanism did in NiMnGa alloys.

Also, the possibility of harvesting waste mechanical work as electrical power by means of magnetic field induced martensite variant reorientation (rubber-like behavior) in NiMnGa MSMAs was explored.

For the first time in literature, a fully recoverable magnetic field-induced strain (MFIS) of 3% under 125 MPa was attained on single crystalline metamagnetic SMA NiMnCoIn by means of the microscopic MTM testing system to understand the evolution of FIPT under simultaneously applied magnetic field and stress.

Conventional SMA characteristics of polycrystalline bulk NiMnCoAl and sintered compacted-powder NiMnCoSn metamagnetic SMAs were investigated, with and without applied field, to discover their performance against that of their single crystalline counterparts, since polycrystalline alloys are relatively easier and inexpensive to synthesize.

The following conclusions can be drawn from this study:

1. The maximum MFIS level is a function of constant bias stress. In NiMnGa, increasing stress decreases the MFIS and no MFIS is observed above the blocking stress. The blocking stress in the present study was about 5 MPa two

times higher than the maximum MFIS reported in the literature. The maximum MFIS was 5.8% which is close to the theoretical maximum reorientation strain for the 10M tetragonal martensite.

2. In NiMnGa, the cyclic MFIS evolution is different than that of the first field cycle. Significant irrecoverable MFIS is possible during first cycle as a function of the bias stress level. This difference maybe due to the competition between the stress and magnetic field favored martensite variants in the course of magnetic field-induced reorientation. The MFIS in the first cycle is considerably higher compared to those of the subsequent cycles under low bias stress.
3. The stress induced martensite reorientation under constant magnetic field led to the observation of magnetoelasticity (rubber-like behavior). In other words this is recoverable magnetic field-induced martensite reorientation, similar to the stress induced martensite formation during pseudoelastic behavior conventional SMAs. When carried out under constant magnetic field, the critical stress for detwinning increased at the onset of reorientation, and the difference is named as magnetostress. 5.7 MPa magnetostress in the present study is the highest reported to date.
4. For 10M martensite NiMnGa alloys, the combination of magnetostress (5.7 MPa), blocking stress (5 MPa) and MFIS (5.8%) in this study is the highest reported to date. This was a consequence of two parameters: i) The large difference between the operating temperature (-95 °C) and the Curie temperature (means high MAE), ii) The small difference between the operating temperature and the martensite start temperature (means low detwinning stress). These together maximized the blocking stress and magnetostress. The magnetocrystalline anisotropy energy was calculated as 3.30 x 10^5 J/m^3 at -95 °C and was reported elsewhere as 2.65 x 10^5 J/m^3 at room temperature.
5. A magnetic field applied perpendicular to the compressive stress increases the flow stress levels during the two-stage phase transformation. The magnetostress levels were on the order of 7 to 10 MPa. The pseudoelastic stress hysteresis loops

with and without magnetic field were separated in the temperature range of -60 °C to -40 °C for the first stage transformation. The separation of the pseudoelastic loops with and without magnetic field was identified as the necessary mechanical condition for the reversible field-induced phase transformation in MSMAs.

6. Actuation stress and work output levels achieved by employing stress-assisted field-induced phase transformation in this study are more than one order of magnitude higher than the results previously reported for NiMnGa MSMAs.
7. The field-induced reversible phase transformation in NiMnCoIn alloys is determined by both measuring the change in magnetization and using high energy x-ray diffraction with *in situ* magnetic field capability. The required magnetic fields for reversible phase transformation were found to be high (>4 T) compared to field-induced variant reorientation and stress-assisted field-induced phase transformation in NiMnGa alloys (<1.5 T).
8. The crystal structure of austenite and martensite phases of NiMnCoIn single crystals used in this study is determined to be $L2_1$ and 12M, respectively. 12M structure is determined for the first time in NiMnCoIn alloys.
9. Direct measurement of magnetic field induced strains during metamagnetic phase transition was attained in a metamagnetic SMA, for the first time in literature, by means of novel microscopic MTM system integrated with a miniature capacitive displacement sensor. Up to 3% fully recoverable MFIS was confirmed at 125 MPa.
10. Magnetization vs. temperature behavior of $Ni_{45}Mn_{36.5}Co_5In_{13.5}$ single crystals oriented along the [100] direction were reported without bias stress where kinetic arrest of austenite was confirmed. Also, form magnetization vs. magnetic field behavior at various temperatures, it was found that increasing bias stress increased both magnetic field hysteresis and the critical magnetic field levels for forward and reverse phase transformations to start.

11. Shape memory effect and pseudoelastic response of polycrystalline $Ni_{40}Mn_{33}Co_{10}Al_{17}$ bulk and $Ni_{43}Mn_{39}Co_7Sn_{11}$ sintered compacted-powder alloys were investigated under compression. Transformation strains of 3.6% under 200 MPa and 3.2% under 175 MPa were observed for NiMnCoAl and NiMnCoSn specimens, respectively, during isobaric thermal cycling. 2.5% strain fully recoverable pseudoelasticity was confirmed in both specimens. It was confirmed that NiMnCoAl and NiMnCoSn polycrystalline alloys could provide relatively inexpensive and more ductile alternatives to single crystalline NiMnCoIn metamagnetic shape memory alloys.

REFERENCES

[1] Leo DJ. Engineering Analysis of Smart Material Systems. Hoboken, NJ: John Wiley & Sons, Inc.; 2007.

[2] Schwartz M. Encyclopedia of Smart Materials. New York: Wiley-Interscience; 2002.

[3] Faidley LE. Characterization and Modeling of Ferromagnetic Shape Memory Ni-Mn-Ga in a Collinear Stress-Field Configuration. PhD thesis: The Ohio State University, 2006.

[4] Tzou HS, Lee HJ, Arnold SM. Smart materials, precision sensors/actuators, smart structures, and structronic systems. Mechanics of Advanced Materials and Structures 2004;11:367.

[5] Cullity B, Graham C. Introduction to Magnetic Materials. Hoboken, NJ: Wiley/IEEE press, 1972.

[6] Kellogg RA, Flatau AB, Clark AE, Wun-Fogle M, Lograsso TA. Temperature and stress dependencies of the magnetic and magnetostrictive properties of Fe0.81Ga0.19. Journal of Applied Physics 2002;91:7821.

[7] Wayman CM. Shape memory alloys. MRS Bulletin 1993;18:49.

[8] Van Humbeeck J. Shape memory alloys: A material and a technology. Advanced Engineering Materials 2001;3:837.

[9] Porter DA, Easterling KE. Phase Transformations in Metals and Alloys. Cheltenham, England: Nelson Thornes Ltd.; 2001.

[10] Gharghouri MA, Elsawy A, Hyatt CV. Training of magnetic shape memory alloys. In: Chandra T, Torralba JM, Sakai T, editors, International Conference on Processing & Manufacturing of Advanced Materials Pt.3; Leganes, Madrid, Spain, 2003;426-432:2273.

[11] Liu Y, Liu Y, Van Humbeeck J. Two-way shape memory effect developed by martensite deformation in NiTi. Acta Materialia 1998;47:199.

[12] Van Humbeeck J, Stalmans R. Shape Memory Alloy Systems. In: Schwartz M, editor. Encyclopedia of Smart Materials, vol. 1. New York, NY: John Wiley & Sons, 2002, p.951.

[13] Buehler WJ, Wiley RC, Gilfrich JV. Effect of Low-Temperature Phase Changes on Mechanical Properties of Alloys near Composition TiNi. Journal of Applied Physics 1963;34:1475.

[14] Monner H. Smart materials for active noise and vibration reduction. Keynote paper. Novem – Noise and Vibration: Emerging Methods Saint-Raphael, France, 18-21 April 2005;1:1-17

[15] Funakubo H. Shape Memory Alloys. Amsterdam: Gordon & Breach Publishing Group, 1987.

[16] James R, Wuttig M. Altern ative smart materials. In: Varadan V, Chandra J, editors. Smart Structures and Materials 1996: Mathematics and Control in Smart Structures. Proceedings of SPIE - The International Society for Optical Engineering, vol. 2715, 1996, p. 420-426.

[17] Chernenko VA, Cesari E, Kokorin VV, Vitenko IN. The development of new ferromagnetic shape-memory alloys in Ni-Mn-Ga system. Scripta Metallurgica Et Materialia 1995;33:1239.

[18] Ullakko K. Magnetically controlled shape memory alloys: A new class of actuator materials. Journal of Materials Engineering and Performance 1996;5:405.

[19] Ullakko K, Huang JK, Kantner C, O'Handley RC, Kokorin VV. Large magnetic-field-induced strains in Ni2MnGa single crystals. Applied Physics Letters 1996;69:1966.

[20] Vasil'ev AN, Buchel'nikov VD, Takagi T, Khovailo VV, Estrin EI. Shape memory ferromagnets. Physics-Uspekhi 2003;46:559.

[21] Soderberg O, Ge Y, Sozinov A, Hannula SP, Lindroos VK. Recent breakthrough development of the magnetic shape memory effect in Ni-Mn-Ga alloys. Smart Materials and Structures 2005;14:S223.

[22] Webster PJ, Ziebeck KRA, Town SL, Peak MS. Magnetic Order and Phase-Transformation in Ni2mnga. Philosophical Magazine B-Physics of Condensed Matter Statistical Mechanics Electronic Optical and Magnetic Properties 1984;49:295.

[23] Venkateswaran SP, Nuhfer NT, De Graef M. Anti-phase boundaries and magnetic domain structures in Ni2MnGa-type Heusler alloys. Acta Materialia 2007;55:2621.

[24] Overholser RW, Wuttig M, Neumann DA. Chemical ordering in Ni-Mn-Ga Heusler alloys. Scripta Materialia 1999;40:1095.

[25] Khovailo VV, Takagi T, Vasilev AN, Miki H, Matsumoto M, Kainuma R. On order-disorder (L2(1) -> B2 ') phase transition in Ni2+xMn1-xGa Heusler alloys. Physica Status Solidi A-Applied Research 2001;183:R1.

[26] Martynov VV. X-ray diffraction study of thermally and stress-induced phase transformations in single crystalline Ni-Mn-Ga alloys. Journal de Physique IV, 1995;5:C8.91-C8.99.

[27] Manosa L, Planes A, Zarestky J, Lograsso T, Schlagel DL, Stassis C. Phonon softening in Ni-Mn-Ga alloys. Physical Review B 2001;64:024305.

[28] Wedel B, Suzuki M, Murakami Y, Wedel C, Suzuki T, Shindo D, Itagaki K. Low temperature crystal structure of Ni-Mn-Ga alloys. Journal of Alloys and Compounds 1998;290:137.

[29] Wedel B, Suzuki M, Murakami Y, Wedel C, Suzuki T, Shindo D, Itagaki K. Low temperature crystal structure of Ni-Mn-Ga alloys. Journal of Alloys and Compounds 1999;290:137.

[30] Pons J, Chernenko VA, Santamarta R, Cesari E. Crystal structure of martensitic phases in Ni-Mn-Ga shape memory alloys. Acta Materialia 2000;48:3027.

[31] Fritsch G, Kokorin VV, Chernenko VA, Kempf A, Zasimchuk IK. Martensitic transformation in Ni-Mn-Ga alloys. Phase Transitions 1996;57:233.

[32] Chernenko VA, Amengual A, Cesari E, Kokorin VV, Zasimchuk IK. Thermal and magnetic-properties of stress-induced martensites in Ni-Mn-Ga alloys. Journal de Physique IV, 1995;5:95.

[33] Heczko O, Lanska N, Soderberg O, Ullakko K. Temperature variation of structure and magnetic properties of Ni-Mn-Ga magnetic shape memory alloys. Journal of Magnetism and Magnetic Materials 2002;242-245:1446.

[34] Sozinov A, Likhachev AA, Lanska N, Ullakko K. Giant magnetic-field-induced strain in NiMnGa seven-layered martensitic phase. Applied Physics Letters 2002;80:1746.

[35] Chernenko VA, Segui C, Cesari E, Pons J, Kokorin VV. Sequence of martensitic transformations in Ni-Mn-Ga alloys. Physical Review B - Condensed Matter and Materials Physics 1998;57:2659.

[36] Chernenko VA, Cesari E, Pons J, Segui C. Phase transformations in rapidly quenched Ni-Mn-Ga alloys. Journal of Materials Research 2000;15:1496.

[37] Callister WD. Materials Science and Engineering: An Introduction. New York, NY: John Wiley & Sons; 2006.

[38] Askeland DR, Phule PP. The Science and Engineering of Materials. New York, NY: Thomson, Brooks/Cole; 2003.

[39] Spaldin N. Magnetic Materials: Fundamentals and Device Applications. Cambridge, England: Cambridge University Press; 2003.

[40] Jiles D. Introduction to Magnetism and Magnetic Materials. Boca Raton, FL: Chapman & Hall/CRC, 1998.

[41] O'Handley RC. Modern Magnetic Materials: Principles and Applications. New York, NY: John Wiley & Sons; 2000.

[42] Heczko O, Jurek K, Ullakko K. Magnetic properties and domain structure of magnetic shape memory Ni-Mn-Ga alloy. Journal of Magnetism and Magnetic Materials 2001;226-30:996.

[43] James RD, Tickle R, Wuttig M. Large field-induced strains in ferromagnetic shape memory materials. Materials Science and Engineering A 1999;273-275:320.

[44] Pan Q, James RD. Micromagnetic study of Ni2MnGa under applied field (invited). Journal of Applied Physics 2000;87:4702.

[45] Likhachev AA, Sozinov A, Ullakko K. Magneto-mechanical cycling and modeling the external stress effect on the magnetic-field-controlled strain response in Ni-Mn-Ga. Journal De Physique IV 2004:115:95.

[46] Ge Y, Heczko O, Soderberg O, Lindroos VK. Various magnetic domain structures in a Ni-Mn-Ga martensite exhibiting magnetic shape memory effect. Journal of Applied Physics 2004;96:2159.

[47] Venkateswaran SP, Nuhfer NT, De Graef M. Magnetic domain memory in multiferroic Ni2MnGa. Acta Materialia 2007;55:5419.

[48] De Graef M, Willard MA, McHenry ME, Zhu Y. In-situ Lorentz TEM cooling study of magnetic domain configurations in Ni2MnGa. IEEE Transactions on Magnetics 2001;37:2663.

[49] Park HS, Murakami Y, Shindo D, Chernenko VA, Kanomata T. Behavior of magnetic domains during structural transformations in Ni2MnGa ferromagnetic shape memory alloy. Applied Physics Letters 2003;83:3752.

[50] Solomon VC, McCartney MR, Smith DJ, Tang Y, Berkowitz AE, O'Handley RC. Magnetic domain configurations in spark-eroded ferromagnetic shape memory Ni-Mn-Ga particles. Applied Physics Letters 2005;86:1.

[51] Tickle R, James RD. Magnetic and magnetomechanical properties of Ni2MnGa. Journal of Magnetism and Magnetic Materials 1999;195:627.

[52] Heczko O, Sozinov A, Ullakko K. Giant field-induced reversible strain in magnetic shape memory NiMnGa alloy. IEEE Transactions on Magnetics 2000;36:3266.

[53] Shanina BD, Konchits AA, Kolesnik SP, Gavriljuk VG, Glavatskij IN, Glavatska NI, Soderberg O, Lindroos VK, Foct J. Ferromagnetic resonance in non-

stoichiometric Ni1-x-yMnxGay. Journal of Magnetism and Magnetic Materials 2001;237:309.

[54] Albertini F, Morellon L, Algarabel PA, Ibarra MR, Pareti L, Arnold Z, Calestani G. Magnetoelastic effects and magnetic anisotropy in Ni2MnGa polycrystals. Journal of Applied Physics 2001;89:5614.

[55] Heczko O, Straka L, Lanska N, Ullakko K, Enkovaara J. Temperature dependence of magnetic anisotropy in Ni-Mn-Ga alloys exhibiting giant field-induced strain. Journal of Applied Physics 2002;91:8228.

[56] Sozinov A, Likhachev AA, Ullakko K. Crystal structures and magnetic anisotropy properties of Ni-Mn-Ga martensitic phases with giant magnetic-field-induced strain. IEEE Transactions on Magnetics 2002;38:2814.

[57] Straka L, Heczko O, Ullakko K. Investigation of magnetic anisotropy of Ni-Mn-Ga seven-layered orthorhombic martensite. Journal of Magnetism and Magnetic Materials 2004;272-276:2049.

[58] Enkovaara J, Ayuela A, Nordstrom L, Nieminen RM. Magnetic anisotropy in Ni2MnGa. Physical Review B - Condensed Matter and Materials Physics 2002;65:1344221.

[59] Oikawa K, Ito W, Imano Y, Sutou Y, Kainuma R, Ishida K, Okamoto S, Kitakami O, Kanomata T. Effect of magnetic field on martensitic transition of Ni 46Mn41In13 Heusler alloy. Applied Physics Letters 2006;88:122507.

[60] Murakami Y, Yano T, Shindo D, Kainuma R, Oikawa K, Ishida K. Magnetic domain structure in a metamagnetic shape memory alloy Ni 45Co5Mn36.7in13.3. Scripta Materialia 2006;55:683.

[61] Kainuma R, Imano Y, Ito W, Sutou Y, Morito H, Okamoto S, Kitakami O, Oikawa K, Fujita A, Kanomata T, Ishida K. Magnetic-field-induced shape recovery by reverse phase transformation. Nature 2006;439:957.

[62] Kainuma R, Imano Y, Ito W, Morito H, Sutou Y, Oikawa K, Fujita A, Ishida K, Okamoto S, Kitakami O, Kanomata T. Metamagnetic shape memory effect in a

Heusler-type Ni43Co7Mn39Sn11 polycrystalline alloy. Applied Physics Letters 2006;88:192513.

[63] Sutou Y, Imano Y, Koeda N, Omori T, Kainuma R, Ishida K, Oikawa K. Magnetic and martensitic transformations of NiMnX(X=In, Sn, Sb) ferromagnetic shape memory alloys. Applied Physics Letters 2004;85:4358.

[64] Wachtel E, Henninger F, Predel B. Constitution and magnetic-properties of Ni-Mn-Sn alloys - Solid and Liquid-State. Journal of Magnetism and Magnetic Materials 1983;38:305.

[65] Wang YD, Ren Y, Huang EW, Nie ZH, Wang G, Liu YD, Deng JN, Zuo L, Choo H, Liaw PK, Brown DE. Direct evidence on magnetic-field-induced phase transition in a NiCoMnIn ferromagnetic shape memory alloy under a stress field. Applied Physics Letters 2007;90:101917.

[66] Krenke T, Duman E, Acet M, Wassermann EF, Moya X, Man?osa L, Planes A, Suard E, Ouladdiaf B. Magnetic superelasticity and inverse magnetocaloric effect in Ni-Mn-In. Physical Review B Condensed Matter and Materials Physics 2007;75:104414.

[67] Sutou Y, Imano Y, Koeda N, Omori T, Kainuma R, Ishida K, Oikawa K. Magnetic and martensitic transformations of NiMnX(X=In,Sn,Sb) ferromagnetic shape memory alloys. Applied Physics Letters 2004;85:4358.

[68] Karaca HE, Karaman I, Brewer A, Basaran B, Chumlyakov YI, Maier HJ. Shape memory and pseudoelasticity response of NiMnCoIn magnetic shape memory alloy single crystals. Scripta Materialia 2008;58:815.

[69] Ito W., Basaran B., Umetsu R.Y., Karaman I., Kainuma R., K. I. Shape memory response in the Ni40Co10Mn33Al17 polycrystalline alloy. To be submitted to Applied Physics Letters 2009.

[70] Ito K, Ito W, Umetsu RY, Nagasako M, Kainuma R, Fujita A, Oikawa K, Ishida K. Martensitic transformation in NiCoMnSn metamagnetic shape memory alloy powders. Materials Transactions 2008;49:1915.

[71] Koyama K, Hane S, Kamishima K, Goto T. Instrument for high resolution magnetization measurements at high pressures, high magnetic fields and low temperatures. Review of Scientific Instruments 1998;69:3009.

[72] Koyama K, Onodera H, Watanabe K. Magnetization measurements of DyB2C2 under high pressure and high magnetic fields. 2008:403:1607.

[73] James RD, Wuttig M. Magnetostriction of martensite. Philosophical Magazine A: Physics of Condensed Matter, Structure, Defects and Mechanical Properties 1998;77:1273.

[74] Mullner P, Chernenko VA, Kostorz G. A microscopic approach to the magnetic-field-induced deformation of martensite (magnetoplasticity). Journal of Magnetism and Magnetic Materials 2003;267:325.

[75] O'Handley RC. Model for strain and magnetization in magnetic shape memory alloys. Journal of Applied Physics 1998;83:3263.

[76] Marioni MA, O'Handley RC, Allen SM, Hall SR, Paul DI, Richard ML, Feuchtwanger J, Peterson BW, Chambers JM, Techapiesancharoenkij R. The ferromagnetic shape-memory effect in Ni-Mn-Ga. Journal of Magnetism and Magnetic Materials 2005;290-291:35.

[77] Kakeshita T, Takeuchi T, Fukuda T, Saburi T, Oshima R, Muto S, Kishio K. Magnetic field-induced martensitic transformation and giant magnetostriction in Fe-Ni-Co-Ti and ordered Fe3Pt shape memory alloys. Materials Transactions, JIM 2000;41:882.

[78] Muto S, Oshima R, Fujita FE. Relation of magnetic domain structure to fct martensite variants in Fe-Pd alloys. Scripta Metallurgica 1987;21:465.

[79] Karaca HE, Karaman I, Lagoudas DC, Maier HJ, Chumlyakov YI. Recoverable stress-induced martensitic transformation in a ferromagnetic CoNiAl alloy. Scripta Materialia 2003;49:831.

[80] Karaca HE, Karaman I, Chumlyakov YI, Lagoudas DC, Zhang X. Compressive response of a single crystalline CoNiAl shape memory alloy. Scripta Materialia 2004;51:261.

[81] Oikawa K, Wulff L, Iijima T, Gejima F, Ohmori T, Fujita A, Fukamichi K, Kainuma R, Ishida K. Promising ferromagnetic Ni-Co-Al shape memory alloy system. Applied Physics Letters 2001;79:3290.

[82] Oikawa K, Ota T, Imano Y, Omori T, Kainuma R, Ishida K. Phase equilibria and phase transformation of Co-Ni-Ga ferromagnetic shape memory alloy system. Journal of Phase Equilibria and Diffusion 2006;27:75.

[83] Liu Y, Zhou WM, Qi X, Jiang BH, Wang WH, Chen JL, Wu GH, Wang JC, Feng CD, Xie HQ. Magneto-shape-memory effect in Co-Ni single crystals. Applied Physics Letters 2001;78:3660.

[84] Oikawa K, Ota T, Sutou Y, Ohmori T, Kainuma R, Ishida K. Magnetic and martensitic phase transformations in a Ni54Ga27Fe19 alloy. Materials Transactions 2002;43:2360.

[85] Oikawa K, Ota T, Ohmori T, Tanaka Y, Morito H, Fujita A, Kainuma R, Fukamichi K, Ishida K. Magnetic and martensitic phase transitions in ferromagnetic Ni-Ga-Fe shape memory alloys. Applied Physics Letters 2002;81:5201.

[86] Imano Y, Omori T, Oikawa K, Sutou Y, Kainuma R, Ishida K. Martensitic and magnetic transformations of Ni-Ga-Fe-Co ferromagnetic shape memory alloys. Materials Science and Engineering A 2006;438-440:970.

[87] Karaca HE, Karaman I, Basaran B, Lagoudas DC, Chumlyakov YI, Maier HJ. On the stress-assisted magnetic-field-induced phase transformation in Ni2MnGa ferromagnetic shape memory alloys. Acta Materialia 2007;55:4253.

[88] Murray SJ, Marioni M, Allen SM, O'Handley RC, Lograsso TA. 6% magnetic-field-induced strain by twin-boundary motion in ferromagnetic Ni-Mn-Ga. Applied Physics Letters 2000;77:886.

[89] Heczko O, Straka L. Magnetic properties of stress-induced martensite and martensitic transformation in Ni-Mn-Ga magnetic shape memory alloy. Materials Science and Engineering A 2004;378:394.

[90] Sozinov A, Likhachev AA, Lanska N, Ullakko K. Giant magnetic-field-induced strain in NiMnGa seven-layered martensitic phase. Applied Physics Letters 2002;80:1746.

[91] Tickle R. Ferromagnetic Shape Memory Materials. PhD. thesis: University of Minnesota, 2000.

[92] Vasil'ev A, Bozhko A, Khovailo V, Dikshtein I, Shavrov V, Seletskii S, Buchelnikov V. Structural and magnetic phase transitions in shape memory alloys Ni2 + xMn1 - XGa. Journal of Magnetism and Magnetic Materials 1999;196-197:837.

[93] Lynch CS. The effect of uniaxial stress on the electro-mechanical response of 8/65/35 PLZT. Acta Materialia 1996;44:4137.

[94] Mullner P, Chernenko VA, Wollgarten M, Kostorz G. Large cyclic deformation of a Ni-Mn-Ga shape memory alloy induced by magnetic fields. Journal of Applied Physics 2002;92:6708.

[95] Karaca HE, Karaman I, Basaran B, Chumlyakov YI, Maier HJ. Magnetic field and stress induced martensite reorientation in NiMnGa ferromagnetic shape memory alloy single crystals. Acta Materialia 2006;54:233.

[96] Kiefer B. A Phenomenological Constitutive Model for Magnetic Shape Memory Alloys. Ph.D. thesis: Texas A&M University, 2006.

[97] Kiefer B, Karaca HE, Lagoudas DC, Karaman I. Characterization and modeling of the magnetic field-induced strain and work output in Ni2MnGa magnetic shape memory alloys. Journal of Magnetism and Magnetic Materials 2007;312:164.

[98] Albertini F, Pareti L, Paoluzi A, Morellon L, Algarabel PA, Ibarra MR, Righi L. Composition and temperature dependence of the magnetocrystalline anisotropy in Ni2+xMn1+yGa1+z (x+y+z=0) heusler alloys. Applied Physics Letters 2002;81:4032.

[99] Vasil'ev AN, Bozhko AD, Khovailo VV, Dikshtein IE, Shavrov VG, Buchelnikov VD, Matsumoto M, Suzuki S, Takagi T, Tani J. Structural and

magnetic phase transitions in shape-memory alloys Ni2+xMn1-xGa. Physical Review B - Condensed Matter and Materials Physics 1999;59:1113.

[100] Straka L, Heczko O. Superelastic response of Ni-Mn-Ga martensite in magnetic fields and a simple model. IEEE Transactions on Magnetics 2003;39:3402.

[101] Sozinov A, Likhachev AA, Lanska N, Soderberg O, Ullakko K, Lindroos VK. Stress and magnetic-field-induced variant rearrangement in Ni-Mn-Ga single crystals with seven-layered martensitic structure. Materials Science and Engineering A 2004;378:399.

[102] Hao XJ, Ohtsuka H. Phase transformation in Fe-based alloys in high magnetic fields. Materials Science Forum, 2005: 475-479:301.

[103] Kakeshita T, Shimizu K, Funada S, Date M. Composition dependence of magnetic field-induced martensitic transformations in Fe-Ni alloys. Acta Metallurgica 1985;33:1381.

[104] Shimizu Ki, Kakeshita T. Effect of magnetic fields on martensitic transformations in ferrous alloys and steels. ISIJ International 1989;29:97.

[105] Cherechukin AA, Dikshtein IE, Ermakov DI, Glebov AV, Koledov VV, Shavrov VG, Takagi T, Tulaikova AA. Reversible structural phase transition in Ni-Mn-Ga alloys in a magnetic field. International Journal of Applied Electromagnetics and Mechanics 2001;14:405.

[106] Chernenko VA, Pons J, Cesari E, Ishikawa K. Stress-temperature phase diagram of a ferromagnetic Ni-Mn-Ga shape memory alloy. Acta Materialia 2005;53:5071.

[107] Brown PJ, Crangle J, Kanomata T, Matsumoto M, Neumann KU, Ouladdiaf B, Ziebeck KRA. The crystal structure and phase transitions of the magnetic shape memory compound Ni2MnGa. Journal of Physics Condensed Matter 2002;14:10159.

[108] Murray SJ, Farinelli M, Kantner C, Huang JK, Allen SM, Handley RCO. Field-induced strain under load in Ni-Mn-Ga magnetic shape memory materials. Journal of Applied Physics 1998:83:7297.

[109] Jeong S, Inoue K, Inoue S, Koterazawa K, Taya M, Inoue K. Effect of magnetic field on martensite transformation in a polycrystalline Ni2MnGa. Materials Science and Engineering A 2003;359:253.

[110] Kim JH, Fukuda T, Kakeshita T. A new phase induced in Ni2MnGa by uniaxial stress. Scripta Materialia 2006;54:585.

[111] Zhao P. Magnetoelastic Coupling in NiMnGa Ferromagnetic Shape Memory Alloy. PhD thesis: University of Maryland, 2006.

[112] Brewer A. Shape Memory Response of Ni_2MnGa and NiMnCoIn Magnetic Shape Memory Alloys under Compression. M.S Thesis: Texas A&M University, 2007.

[113] Wun-Fogle M, Restorff JB, Leung K, Cullen JR, Clark AE. Magnetostriction of Terfenol-D heat treated under compressive stress. IEEE Transactions on Magnetics 1999;35:3817.

[114] Fan J, Stoll WA, Lynch CS. Nonlinear constitutive behavior of soft and hard PZT: experiments and modeling. Acta Materialia 1999;47:4415.

[115] Suorsa I, Tellinen J, Ullakko K, Pagounis E. Voltage generation induced by mechanical straining in magnetic shape memory materials. Journal of Applied Physics 2004;95:8054.

[116] Mullner P, Chernenko VA, Kostorz G. Stress-induced twin rearrangement resulting in change of magnetization in a Ni-Mn-Ga ferromagnetic martensite. Scripta Materialia 2003;49:129.

[117] Staley ME. Development of a Prototype Magnetostrictive Energy Harvesting Device. M.S. thesis: University of Maryland, 2005.

[118] Sutou Y, Kamiya N, Omori T, Kainuma R, Ishida K, Oikawa K. Stress-strain characteristics in Ni-Ga-Fe ferromagnetic shape memory alloys. Applied Physics Letters 2004;84:1275.

[119] Suorsa I, Pagounis E, Ullakko K. Magnetization dependence on strain in the Ni-Mn-Ga magnetic shape memory material. Applied Physics Letters 2004;84:4658.

[120] Sarawate N, Dapino M. Experimental characterization of the sensor effect in ferromagnetic shape memory Ni-Mn-Ga. Applied Physics Letters 2006;88.

[121] Karaman I, Basaran B, Karaca HE, Karsilayan AI, Chumlyakov YI. Energy harvesting using martensite variant reorientation mechanism in a NiMnGa magnetic shape memory alloy. Applied Physics Letters 2007;90:172505.

[122] Kiefer B, Lagoudas DC. Application of a magnetic SMA constitutive model in the analysis of magnetomechanical boundary value problems. Proceedings of SPIE - The International Society for Optical Engineering, vol. 6170, 2006, p.617017

[123] Yaniv G, Doron S, Thomas WS, Richard DJ. Breaching the work output limitation of ferromagnetic shape memory alloys. Applied Physics Letters 2008;93:122509.

[124] Morito S, Kakeshita T, Hirata K, Otsuka K. Magnetic and martensitic transformations in Ni50AlxMn50-x alloys. Acta Materialia 1998;46:5377.

[125] Gschneider KAJ. Rep. Prog. Phys. 2005; 68:1479.

[126] Karaca HE, Karaman I, Basaran B, Ren Y, Chumlyakov YI, Maier HJ. Magnetic field-induced phase transformation in NiMnCoIn magnetic shape-memory alloys-a new actuation mechanism with large work output. Advanced Functional Materials 2009;19:983.

[127] Bozorth RM. Ferromagnetism, New York, NY: D.V. Nostrand Co. Inc., 1953.

[128] Kainuma R, Imano Y, Ito W, Morito H, Sutou Y, Oikawa K, Fujita A, Ishida K, Okamoto S, Kitakami O. Metamagnetic shape memory effect in a Heusler-type Ni43Co7Mn39Sn11 polycrystalline alloy. Applied Physics Letters 2006;88:192513.

[129] Kainuma R, Ito W, Umetsu RY, Oikawa K, Ishida K. Magnetic field-induced reverse transformation in B2-type NiCoMnAl shape memory alloys. Applied Physics Letters 2008;93:091906.

[130] Oikawa K, Ito W, Imano Y, Sutou Y, Kainuma R, Ishida K, Okamoto S, Kitakami O, Kanomata T. Effect of magnetic field on martensitic transition of Ni46Mn41In13 Heusler alloy. Applied Physics Letters 2006;88.

[131] Krenke T, Duman E, Acet M, Wassermann EF, Moya X, Manosa L, Planes A. Inverse magnetocaloric effect in ferromagnetic Ni-Mn-Sn alloys. Nature Materials 2005;4:450.

[132] Kainuma R, Oikawa K, Ito W, Sutou Y, Kanomata T, Ishida K. Metamagnetic shape memory effect in NiMn-based Heusler-type alloys. Journal of Materials Chemistry 2008;18:1837.

[133] Han ZD, Wang DH, Zhang CL, Xuan HC, Gu BX, Du YW. Low-field inverse magnetocaloric effect in Ni50-xMn39+xSn11 Heusler alloys. Applied Physics Letters 2007;90:042507.

[134] Ito W, Imano Y, Kainuma R, Sutou Y, Oikawa K, Ishida K. Martensitic and magnetic transformation behaviors in Heusler-type NiMnln and NiCoMnln metamagnetic shape memory alloys. Metallurgical and Materials Transactions a-Physical Metallurgy and Materials Science 2007;38A:759.

[135] Koyama K, Igarashi T, Okada H, Watanabe K, Kanomata T, Kainuma R, Ito W, Oikawa K, Ishida K. Magnetic and thermoelectric properties of Ni50Mn36Sn14 in high-magnetic fields. Journal of Magnetism and Magnetic Materials 2007;310:E994.

[136] Krenke T, Duman E, Acet M, Wassermann EF, Moya X, Manosa L, Planes A, Suard E, Ouladdiaf B. Magnetic superelasticity and inverse magnetocaloric effect in Ni-Mn-In. Physical Review B 2007;75:104414.

[137] Sharma VK, Chattopadhyay MK, Kumar R, Ganguli T, Tiwari P, Roy SB. Magnetocaloric effect in Heusler alloys Ni50Mn34In16 and Ni50Mn34Sn16. Journal of Physics-Condensed Matter 2007;19:496207.

[138] Sharma VK, Chattopadhyay MK, Roy SB. Large inverse magnetocaloric effect in Ni50Mn 34In16. Journal of Physics D: Applied Physics 2007;40:1869.

[139] Liu J, Scheerbaum N, Lyubina J, Gutfleisch O. Reversibility of magnetostructural transition and associated magnetocaloric effect in Ni-Mn-In-Co. Applied Physics Letters 2008;93:102512.

[140] Khan M, Ali N, Stadler S. Inverse magnetocaloric effect in ferromagnetic Ni50 Mn37+x Sb13-x Heusler alloys. Journal of Applied Physics 2007;101:053919.

[141] Wang YD, Huang EW, Ren Y, Nie ZH, Wang G, Liu YD, Deng JN, Choo H, Liaw PK, Brown DE, Zuo L. *In situ* high-energy X-ray studies of magnetic-field-induced phase transition in a ferromagnetic shape memory Ni-Co-Mn-In alloy. Acta Materialia 2008;56:913.

[142] Hamilton RF, Sehitoglu H, Chumlyakov Y, Maier HJ. Stress dependence of the hysteresis in single crystal NiTi alloys. Acta Materialia 2004;52:3383.

[143] Karaca HE, Karaman I, Chumlyakov YI, Basaran B, Maier HJ. Compressive response of NiFeGa ferromagnetic shape memory alloys. (unpublished) 2007.

[144] Cui J, Chu YS, Famodu OO, Furuya Y, Hattrick-Simpers J, James RD, Ludwig A, Thienhaus S, Wuttig M, Zhang ZY, Takeuchi I. Combinatorial search of thermoelastic shape-memory alloys with extremely small hysteresis width. Nature Materials 2006;5:286.

[145] Ito W, Ito K, Umetsu RY, Kainuma R, Koyama K, Watanabe K, Fujita A, Oikawa K, Ishida K, Kanomata T. Kinetic arrest of martensitic transformation in the NiCoMnIn metamagnetic shape memory alloy. Applied Physics Letters 2008;92:021908.

[146] Sehitoglu H, Karaman I, Anderson R, Zhang X, Gall K, Maier HJ, Chumlyakov Y. Compressive response of NiTi single crystals. Acta Materialia 2000;48:3311.

[147] James RD, Hane KF. Martensitic transformations and shape-memory materials. Acta Materialia 2000;48:197.

[148] Karaca HE, Karaman I, Basaran B, Lagoudas DC, Chumlyakov Y, Maier H. On the stress-assisted magnetic field-induced phase transformation in Ni2MnGa ferromagnetic shape memory alloys. Acta Materialia 2007;55:4253.

[149] Sozinov A, Likhachev AA, Lanska N, Soderberg O, Ullakko K, Lindroos VK. Stress- and magnetic-field-induced variant rearrangement in Ni-Mn-Ga single crystals with seven-layered martensitic structure. Materials Science and Engineering A 2004;378:399.

[150] Meyer D, Maier HJ, Dadda J, Karaman I, Karaca HE. Thermally and stress-induced martensitic transformation in Co-Ni-Al ferromagnetic shape memory alloy single crystals. Materials Science and Engineering A 2006;438-440:875.

[151] Karaca HE, Karaman I, Basaran B, Lagoudas DC, Chumlyakov YI, Maier HJ. One-way shape memory effect due to stress-assisted magnetic field-induced phase transformation in Ni2MnGa magnetic shape memory alloys. Scripta Materialia 2006;55:803.

[152] Tickle R, James RD, Shield T, Wuttig M, Kokorin VV. Ferromagnetic shape memory in the NiMnGa system. IEEE Transactions on Magnetics 1999;35:4301.

[153] Lagoudas DC. Shape Memory Alloys: Modeling and Engineering Applications. New York: Springer, 2008.

[154] Leo DJ. Engineering Analysis of Smart Material Systems. Hoboken, NJ: John Wiley & Sons, 2007.

[155] Koyama K, Okada H, Watanabe K, Kanomata T, Kainuma R, Ito W, Oikawa K, Ishida K. Observation of large magnetoresistance of magnetic Heusler alloy Ni 50Mn36Sn14 in high magnetic fields. Applied Physics Letters 2006;89:182510.

[156] Yu SY, Liu ZH, Liu GD, Chen JL, Cao ZX, Wu GH, Zhang B, Zhang XX. Large magnetoresistance in single-crystalline Ni50 Mn 50-x Inx alloys (x=14-16) upon martensitic transformation. Applied Physics Letters 2006;89:162503.

[157] Han ZD, Wang DH, Zhang CL, Tang SL, Gu BX, Du YW. Large magnetic entropy changes in the Ni45.4Mn 41.5In13.1 ferromagnetic shape memory alloy. Applied Physics Letters 2006;89:182507.

[158] Sharma VK, Chattopadhyay MK, Roy SB. Kinetic arrest of the first order austenite to martensite phase transition in Ni50Mn34In16: dc magnetization studies. Physical Review B 2007;76:140401.

[159] Aksoy S, Krenke T, Acet M, Wassermann EF, Moya X, Manosa L, Planes A. Magnetization easy axis in martensitic Heusler alloys estimated by strain measurements under magnetic field. Applied Physics Letters 2007;91:251915.

[160] Chernenko VA, Pons J, Cesari E, Zasimchuk IK. Transformation behaviour and martensite stabilization in the ferromagnetic Co-Ni-Ga Heusler alloy. Scripta Materialia 2004;50:225.

[161] Aksoy S, Krenke T, Acet M, Wassermann EF, Moya X, Manosa L, Planes A. Tailoring magnetic and magnetocaloric properties of martensitic transitions in ferromagnetic Heusler alloys. Applied Physics Letters 2007;91:241916.

[162] Krenke T, Acet M, Wassermann EF, Moya X, Manosa L, Planes A. Ferromagnetism in the austenitic and martensitic states of Ni-Mn-In alloys. Physical Review B 2006;73:174413.

[163] Umetsu RY, Ito W, Ito K, Koyama K, Fujita A, Oikawa K, Kanomata T, Kainuma R, Ishida K. Anomaly in entropy change between parent and martensite phases in the Ni50Mn34In16 Heusler alloy. Scripta Materialia 2009;60:25.

[164] Chatterjee S, Giri S, Majumdar S, De SK. Metastability and magnetic memory effect in Ni2Mn1.4Sn0.6. Physical Review B 2008;77:012404.

[165] Chatterjee S, Giri S, Majumdar S, De SK. Thermomagnetic irreversibility in Ni2Mn1.36Sn0.64 shape-memory alloy. Physical Review B 2008;77.

[166] Ito W, Nagasako M, Umetsu RY, Kainuma R, Kanomata T, Ishida K. Atomic ordering and magnetic properties in the Ni45Co5Mn36.7In13.3 metamagnetic shape memory alloy. Applied Physics Letters 2008;93:232503.

VITA

Mr. Burak Basaran was born in Ankara, Turkey, in 1974. He graduated from Gazi Anatolian High School, Ankara in 1992. He graduated with a Bachelor of Science degree in mechanical engineering from Osmangazi University, Eskisehir, Turkey in 1996. Between 1997 and 2000, he was a graduate student and a research/teaching assistant at the Department of Mechanical Engineering, Gazi University, Ankara, Turkey where he acquired his first Master of Science degree. Upon receiving a Fulbright Scholarship, he came to the USA and enrolled in Texas A&M University, Department of Mechanical Engineering where he received his second Master of Science degree in 2003. Starting 2004, he worked as a research/teaching assistant and continued his Ph.D. studies in Materials Science and Engineering Interdisciplinary Graduate Program at Texas A&M University. He completed his Ph.D. in December 2009.

Mr. Basaran coauthored seven peer reviewed journal articles and more than ten conference papers/presentations.

He can be contacted through his academic advisor:

Dr. Ibrahim Karaman
Texas A&M University, Department of Mechanical Engineering,
College Station, TX, 77843-3123